



**OPTIMISING POLYMERSOMES FOR IMAGING  
TUMOUR AND ITS ENVIRONMENT**

**Adrian S. Joseph**

**Thesis submitted for the Degree of Doctor of Philosophy**

**Department of Oncology, University of Sheffield**

**2014**





**OPTIMISING POLYMERSOMES FOR IMAGING  
TUMOUR AND ITS ENVIRONMENT**

**Adrian S. Joseph**

**Thesis submitted for the Degree of Doctor of Philosophy**

**Department of Oncology, University of Sheffield**

**July 2014**



## **DECLARATION**

I hereby declare that no part of this thesis has previously been submitted for any degree or qualification of this, or any other University or Institute of learning



## ACKNOWLEDGEMENTS

First and foremost I want to thank my supervisors, Prof. Nicola Brown and prof. Giuseppe Battaglia. This work could have not been completed without their help and guidance. All their contributions and ideas helped me to complete this work. I am also extremely grateful to them for all the suggestions and corrections in the long writing stage.

I would also like to thank Cancer Research UK, Engineering and Physical Sciences Research Council and the Department of Health for the funding this work, and the PI of the project Prof. G. Tozer and Prof. M. Paley for their advices on the general direction of the work.

The completion of this multidisciplinary work was made possible only by the contribution of many people. I am grateful to Dr. Nick Warren and Dr. Jeppe Madsen from Prof. Steve Armes group for synthesising the co-polymers. I am also thankful to James Robertson and Dr. Denis Cecchin for their advices on polymersomes synthesis and characterisation and to Russell Pearson, Claudia Contini and Chris Hill for the help with transmission electron microscopy sample preparation and imaging. Coming from a biological background, none of the flow *in silico* simulations would have been possible without the precious help of Dr. Carla Pegoraro, who introduced me to the usage of Comsol Multiphysics, a key tool in the development of the flow bioincubator.

I am sincerely grateful to Matthew Fisher and Dr. Sarah-Jane Lunt for all the long hours spent in the filed lab during the *in vivo* work. Without their help it would have not been possible to complete any of the surgeries. I am also thankful to Colin Gray, whose help in setting up the microscope for intra-vital microscopy was crucial, and to Dr. Chryso Kanthou and Dr. Joanne Bluff for the advices with 10T1/2 and mouse fibrosarcoma cells culturing.

Completing this work was not only about experimental work. The process of writing, editing and correction of the manuscript was challenging, and I would like to thank again my supervisors Prof. Brown and Prof. Battaglia for their guidance. Furthermore, I am grateful to Gavin Fullstone and Dr. Claire Bennison, who kindly proofread part of the manuscript.

A sincere thank you to family and friends. They all have been supportive and understanding during the most difficult times, giving me the much needed extra strength to renew motivation and to replenish energies to continue with the work.

There is a long list of people who helped me during this time, both inside and outside the lab, just too long to be listed one by one. Even if you do not find your name listed above, to all of you goes my sincere thank you.

## ABSTRACT

Polymersomes are nano-meter sized vesicles made by the self assembly of amphiphilic co-polymers in water. This work presents the development of polymersomes as a tool for high resolution *in vivo* optical imaging. High resolution [Intra Vital Microscopy \(IVM\)](#) was made possible by the use of the [Window Chamber \(WC\)](#), a surgical procedure which allows observation of living tissues through an optically transparent glass replacing a section of skin. [WC](#) can be used to observe tumour growth and tumour vasculature development (angiogenesis). High resolution imaging of angiogenesis *in vivo* with polymersomes can give an useful insight in mechanism of angiogenesis, tumour response to anti-angiogenic therapy and the rationale behind the design of polymersomes for specific tumour targeting in therapy.

In this work we optimised a number of techniques and tools to characterise the interactions of two different polymersome formulation with three cell types relevant to the tumour microenvironment: tumour cells [Mouse Fibrosarcoma Cell \(MFC\)](#), endothelial cells [Small Vessel Endothelial Cells \(SVECs\)](#) and perivascular-like cells 10T1/2. The techniques used included [Reverse Phase-High Pressure Liquid Chromatography \(RP-HPLC\)](#), [Fluorescence Activated Cell Sorting \(FACS\)](#) and optical imaging. Furthermore, a flow bio-incubator was developed to study the effect of physiologically relevant flow rates on cellular polymersome uptake. Finally, formulations were tested *in vivo* to assess suitability for optical imaging and polymersomes distribution in tumour vasculature and stroma. Specific image analysis tool were developed to assist the analysis.

The results demonstrated that polymersomes can be used for optical imaging *in vivo* using a [WC](#). The *in vitro* techniques developed allowed us to quantify the interactions between polymersomes and cells, and the information gained can be translated *in vivo* to help predict the polymersomes distribution in tumour.

Taken together, the methods and results presented here provide a set of tools based on image analysis that allow rational design of polymersomes for *in vivo* application.

## PUBLICATIONS

### PUBLISHED ABSTRACTS

**Joseph A.S.**, Battaglia G., Tozer G., Brown N.J., Paley M., Polymersomes and imaging: A quantitative approach. *Technical Proceedings of the 2011 NSTI Nanotechnology Conference and Expo*, 3, 371-374, (2011)

### BOOK CHAPTER

Pearson R.T., Avila-Olias M., **Joseph A.S.**, Nyberg S., Battaglia G., Smart polymersomes: Formation, characterisation and applications. *RSC Smart Materials* 1(1), 179-207, (2013)

Robertson J.D., Patikarnmonthon N., **Joseph A.S.**, Battaglia G., Block copolymer micelles and vesicles for drug delivery, *WILEY Engineering polymer systems for improved drug delivery* 6, 164-188, (2014)

### OTHER WORKS

Cecchin D., **Joseph A.S.**, Nyberg S., Contini C., Akhtar A., Ruiz-Perez L., Madsen J., Ryan A.J., Fernyhough C., Armes S.P., Golestanian R., Battaglia G., Enzyme-driven chemotactic synthetic vesicles. *Submitted to 'Nature Nanotechnology'*

Chierico L., Rizzello L., Guan L., **Joseph A.J.**, Lewis A.L., Battaglia G., Ki-67 out of the box: the role of the two splice variants and its extranuclear pathway. *In preparation*

Chierico L., **Joseph A.J.**, Lewis A.L., Battaglia G., Live cell imaging of cytoskeleton interactions and membrane topology. *Scientific Reports* 4:6056 (2014)

<b>1</b>	<b>Introduction</b>	<b>1</b>
1.1	Cancer. General characteristics . . . . .	1
1.2	Angiogenesis . . . . .	2
1.2.1	Blood vessel anatomy . . . . .	2
1.2.2	Mechanisms of angiogenesis . . . . .	3
1.2.3	Tumour angiogenesis . . . . .	5
1.2.4	Tumour vasculature and tumour microenvironment . . . . .	6
1.2.5	Angiogenesis as a target in cancer therapy . . . . .	7
1.3	Imaging techniques . . . . .	9
1.3.1	Techniques and limitations: an overview . . . . .	9
1.4	Nanocarriers . . . . .	11
1.4.1	Background . . . . .	11
1.4.2	Targeting tumour with nanocarriers: basic principles . . . . .	11
1.4.3	Nanocarriers pharmacokinetics . . . . .	13
1.4.4	Nanocarriers self-assembly . . . . .	16
1.4.5	Polymersomes . . . . .	18
1.4.6	Polymersomes applications . . . . .	19
1.4.7	Co-polymers for <i>in vivo</i> applications . . . . .	21
1.4.8	Nanocarriers in <i>in vivo</i> imaging . . . . .	23
1.5	Aims . . . . .	24
<b>2</b>	<b>Methods</b>	<b>27</b>
2.1	Polymersomes . . . . .	27
2.1.1	Copolymers synthesis . . . . .	27
2.1.2	Polymersomes synthesis . . . . .	28
2.1.3	Polymersomes purification . . . . .	30
2.1.4	Polymersomes characterisation . . . . .	30

2.1.5	Polymersomes concentration . . . . .	32
2.1.6	Polymersomes functionalisation . . . . .	33
2.2	Tissue culture . . . . .	35
2.2.1	Routine subculture of Murine Fibrosarcoma cells . . . . .	35
2.2.2	Routine subculture of SVECs . . . . .	35
2.2.3	Routine subculture of C3H/10T1/2 . . . . .	35
2.2.4	Differentiation of 10T1/2 . . . . .	36
2.2.5	Fibronectin coating . . . . .	36
2.3	Pericyte markers expression quantification . . . . .	36
2.3.1	Immunocytochemistry (ICC) . . . . .	36
2.3.2	Western blot . . . . .	37
2.3.3	Quantitative size-based protein assay . . . . .	39
2.4	Polymersomes <i>in vitro</i> . . . . .	41
2.4.1	Static culture cells treatment . . . . .	41
2.4.2	Cytotoxicity . . . . .	41
2.4.3	FACS . . . . .	42
2.4.4	RP-HPLC . . . . .	43
2.5	In flow uptake studies . . . . .	45
2.5.1	Flow modelling . . . . .	45
2.5.2	Device sterilisation and preparation . . . . .	45
2.5.3	Cell seeding . . . . .	46
2.6	Polymersomes <i>in vivo</i> . . . . .	46
2.6.1	DSC . . . . .	46
2.7	Statistical analysis . . . . .	49
<b>3</b>	<b>Image analysis</b> . . . . .	<b>50</b>
3.1	Introduction . . . . .	50
3.2	Image segmentation . . . . .	51
3.2.1	Thresholding masking . . . . .	51
3.2.2	Difference of gaussians (DoG) . . . . .	52
3.2.3	Local threshold entropy (LTE) . . . . .	53
3.2.4	Mask post-processing . . . . .	54
3.3	Pericyte markers image analysis . . . . .	55
3.4	Image analysis for uptake <i>in static</i> conditions . . . . .	57
3.5	Image analysis for uptake <i>in flow</i> conditions . . . . .	58
3.5.1	BD Pathway 855 microscope set-up . . . . .	58
3.5.2	<i>In silico</i> well mapping segmentation . . . . .	60
3.5.3	Image analysis . . . . .	61
3.6	Image Analysis for <i>in vivo</i> experiments . . . . .	63

3.6.1	Masking . . . . .	63
3.6.2	Vessel mask segmentation: Isolating vessels to determine vascular diameter and diffusion profile . . . . .	66
3.7	Automatisation of image analysis . . . . .	70
<b>4</b>	<b>Polymersome up-take</b>	<b>73</b>
4.1	Introduction . . . . .	74
4.1.1	Uptake and <i>in vitro</i> screening . . . . .	74
4.1.2	Static and flow <i>in vitro</i> cell growth . . . . .	75
4.1.3	Effect of flow on cellular uptake . . . . .	75
4.1.4	Flow devices . . . . .	76
4.1.5	Aim . . . . .	77
4.2	Results . . . . .	77
4.2.1	Static conditions . . . . .	77
4.2.2	Flow bio-incubator . . . . .	80
4.3	Discussion . . . . .	95
<b>5</b>	<b><i>In vivo</i> imaging</b>	<b>100</b>
5.1	Introduction . . . . .	100
5.1.1	Window chamber . . . . .	100
5.1.2	Vascular Endothelial Growth Factor . . . . .	104
5.1.3	Single Vascular Endothelial Growth Factor (VEGF)-A iso- form producing tumours . . . . .	105
5.1.4	Nanoparticles extravasation in tumour . . . . .	105
5.1.5	Aim . . . . .	106
5.2	Results . . . . .	106
5.3	Discussion . . . . .	115
<b>6</b>	<b>Perivascular Cells Targeting</b>	<b>118</b>
6.1	Introduction . . . . .	119
6.1.1	Perivascular cells . . . . .	119
6.1.2	Perivascular cells <i>in vitro</i> models . . . . .	123
6.1.3	Transforming Growth Factor- $\beta$ 1 (TGF- $\beta$ 1) and perivascu- lar cells . . . . .	125
6.1.4	Immunoglobulin of the class G (IgG) structure . . . . .	127
6.1.5	Conjugation methods . . . . .	129
6.1.6	Aim . . . . .	133
6.2	Results . . . . .	134
6.2.1	Immunocytochemistry (ICC) . . . . .	134
6.2.2	Western Blotting . . . . .	145

6.2.3	Biotin/streptavidin conjugation . . . . .	149
6.2.4	Maleimide conjugation . . . . .	154
6.3	Discussion . . . . .	157
<b>7</b>	<b>Summary</b>	<b>162</b>
7.1	General discussion . . . . .	162
7.2	Future directions . . . . .	166
<b>8</b>	<b>List of material used</b>	<b>168</b>
8.1	General <i>in vitro</i> laboratory equipment and reagents . . . . .	168
<b>9</b>	<b>Annex</b>	<b>175</b>
9.1	Binding efficiency (BE) . . . . .	175
9.2	FACS for <i>in flow</i> uptake . . . . .	178
9.3	<i>In vivo</i> epifluorescence imaging . . . . .	180
	<b>List of figures</b>	<b>189</b>
	<b>List of tables</b>	<b>190</b>
	<b>Index</b>	<b>193</b>
	<b>Bibliography</b>	<b>219</b>

<b>Notation</b>	<b>Description</b>
$\alpha$ -SMA	$\alpha$ -Smooth Muscle Actin.
ADME	Administration, Distribution, Metabolism, Excretion.
AFM	Atomic Force Microscopy.
ALK-1	Activin receptor-like kinase 1.
ATCC	American Type Culture Collection.
ATRP	Atom Transfer Radical Polymerisation.
BCA	Bicinchoninic acid assay.
BE	Binding efficiency.
BME	Basal medium eagle.
BSA	Bovine serum albumine.
CAC	Critical Aggregation Concentration.
CAF	Cancer Associated Fibroblast.
CFD	Computational fluid dynamic.
CLSM	Confocal Laser Scanning Microscopy.
CNS	Central Nervous System.
CT	Computed Tomography.
DLS	Dynamic Light Scattering.
DMEM	Dulbecco's Modified Eagle's Medium.
DoG	Difference of gaussians.
DPA	2-(diisopropylamino)ethyl methacrylate).
DSC	Dorsal Skinfold Chamber.

Notation	Description
EC	Endothelial cell.
ECL	Enhanced chemiluminescence.
ECM	Extracellular Matrix.
EGF	Epidermal Growth Factor.
EGFR	Epidermal Growth Factor Receptor.
EMT	Epithelial-Mesenchymal Transition.
EndT	Endothelial-Mesenchymal Transition.
EPR	Enhanced Permeation and Retention.
FACS	Fluorescence Activated Cell Sorting.
FCS	Fetal calf serum.
FDA	Food and Drugs Administration.
FGF	Fibroblast Growth Factor.
GFP	Green Fluorescent Protein.
GPC	Gel Permeation Chromatography.
GUI	Graphic user interface.
HCl	Hydrochloric Acid.
HIF-1 $\alpha$	Hypoxia-inducible Factor-1 $\alpha$ .
HMWMAA	High Molecular Weight Melanoma Associated Antigen.
i.m.	Intra Muscular.
i.p.	Intra Peritoneal.
i.v.	Intra Venously.
i.v.	Intra Venous.
ICC	Immunocytochemistry.
IgG	Immunoglobulin of the class G.
IHC	Immunohystochemistry.
IMS	Industrial Methylated Spirit.
IVM	Intra Vital Microscopy.
LTE	Local threshold entropy.
MFC	Mouse Fibrosarcoma Cell.

Notation	Description
MFC120	Mouse Fibrosarcoma Cells expressing VEGF120 isoform.
MFC188	Mouse Fibrosarcoma Cells expressing VEGF188 isoform.
MPC	2-methacryloxyethyl-phosphorylcholine.
MPM	Multi Photon Microscopy.
MPS	Mononuclear Phagocyte System.
MRI	Magnetic Resonance Imaging.
MSC	Mesenchymal Stem Cells.
MTT	(3 - (4,5 - Dimethylthiazol - 2 - yl) - 2,5 - diphenyltetrazolium bromide.
MVD	Micro Vessel Density.
MW	Molecular weight.
MWP	Micro well plate.
NaOH	Sodium Hydroxide.
NG2	Nerve Glial antigen 2.
PBS	Phosphate Buffer Saline.
PBS <sub>2</sub>	Phosphate Buffer Saline pH 2.
PBS <sub>7.4</sub>	Phosphate Buffer Saline pH 7.4.
PDB	Protein Data Base.
PDGF	Platelet Derived Growth Factor.
PDGF-AA	Platelet Derived Growth Factor-AA.
PDGF-B	Platelet Derived Growth Factor-B.
PDGFR	Platelet Derived Growth Factor Receptor.
PDGFR- $\alpha$	Platelet Derived Growth Factor Receptor- $\alpha$ .
PDGFR- $\beta$	Platelet Derived Growth Factor Receptor- $\beta$ .
PDPA	poly(2-(diisopropylamino)ethyl methacrylate).
PEO	Polyethylene Oxide.
PEO-PDPA	Polyethylen Oxide-poly(2-(diisopropylamino)ethyl methacrylate).
PET	Positron Emission Tomography.
PMPC	Poly(2 - methacryloxyethyl - phosphorylcholine).

Notation	Description
PMPC-PDPA	Poly(2-methacryloxyethyl-phosphorylcholine)-poly(2-(diisopropylamino)ethyl methacrylate).
POEGMA	poly(oligo(ethylene glycol) methacrylate).
POEGMA-PDPA	poly(oligo(ethylene glycol) methacrylate)-poly(2-(diisopropylamino)ethyl methacrylate).
PTA	Phosphtungstenic acid.
PVDF	Polyvinylidene fluoride.
RES	Reticuloendothelial System.
RGS5	Regulator of G-protein Signalling 5.
ROI	Regions of interest.
RP-HPLC	Reverse Phase-High Pressure Liquid Chromatography.
s.c.	Sub Cutaneous.
SEM	Scanning Electron Microscopy.
SMC	Smooth muscle cells.
STED	Stimulated Emission Depletion.
STORM	Stochastic Optical Reconstruction Microscopy.
SVECs	Small Vessel Endothelial Cells.
TAM	Tumour Associated Macrophages.
TE	Tripsin/EDTA.
TEM	Transmission Electron Microscopy.
TFA	Trifluoroacetic Acid.
TGF- $\beta$ 1	Transforming Growth Factor- $\beta$ 1.
THF	Tetrahydrofuran.
TIL	Tumour Infiltrated Lymphocytes.
USPIO	Ultrasmall Superparamagnetic Iron Oxide nanoparticles.
VDA	Vascular Disrupting Agent.
VEGF	Vascular Endothelial Growth Factor.

<b>Notation</b>	<b>Description</b>
VEGF120	Vascular Endothelial Growth Factor isoform 120.
VEGF164	Vascular Endothelial Growth Factor isoform 164.
VEGFR	Vascular Endothelial Growth Factor Receptor.
VPF	Vascular Permeability Factor.
vSMCs	Vascular Smooth Muscle cells.
WB	Western Blot.
WC	Window Chamber.

## 1.1 Cancer. General characteristics

The term tumour describes a group of cells with abnormal and uncontrolled growth. As a tumour grows in size it compresses the surrounding normal tissue, but is localised to a specific area of the body at this stage. Once the tumour induces a vasculature it has the potential to escape the primary site and to induce secondary tumours.

Cancer is a high incidence disease which is characterised by high mortality: cancer was the second highest cause of death in UK in 2011 and it is estimated that one in three people will develop cancer at some time in their life ([Sasieni et al. \[2011\]](#)) (fig. 1.1). Furthermore, cancer accounted for the third highest expenditure by the NHS after mental disorders and cardiovascular diseases, totalling around £5.93bn, and the cost of cancer is estimated to raise to £15.3bn by 2021 (BUPA 2012 report). Thus, providing justification for additional research focusing on molecular, cellular and functional aspects to identify prognostic markers and effective treatment.

There are more than 200 different types of cancer, with names and characteristics reflecting specific localisation (*i.e.* glioblastoma, fibrosarcoma, melanoma, breast cancer etc.). Despite differences in tumour localisation and cell mutations there are morphological features common to almost all of the tumours. A solid tumour is characterised by the initial onset of cancer cells, defined as mutated cells, which grow and divide in an unregulated manner. Normal apoptotic mechanisms are not functional. The tumour microenvironment also consists of *stroma* cells including fibroblasts, immune cells, endothelial cells, and specialised mesenchymal cells, all playing an important role in the development of the primary tumour ([Bremnes et al. \[2011\]](#), [Weinberg \[2013\]](#)). Finally, tumours present a

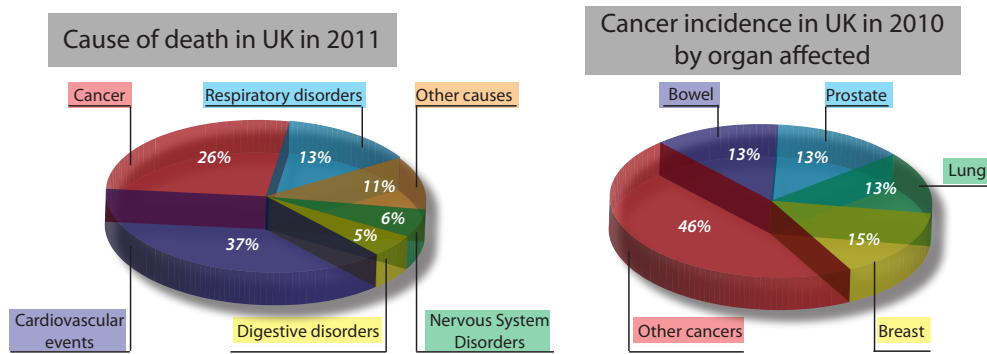


Figure 1.1: Causes of death in 2011 and cancer incidence in 2010. Both data sets are from the UK, from NHS and CRUK respectively. Data set accessed in August 2013.

necrotic, hypoxic central region and are characterised by chaotic and unstable immature vasculature which results in continuous remodelling of the capillary bed in a process called *angiogenesis*.

## 1.2 Angiogenesis

### 1.2.1 Blood vessel anatomy

Blood has an essential role in the homoeostasis of our body as it distributes nutrients, oxygen, hormones and a number of other substances to every cell. Furthermore, blood collects metabolic waste such as carbon dioxide and other small substances and carries them to specialised organs (lungs, liver, kidney) for elimination. The exchange between nutrients and oxygen and waste occurs in the microcirculation, where the arterial system branches into smaller arterioles and finally capillaries ( $\simeq 8\mu\text{m}$  diameter). The capillary bed has a much greater cross-section surface area and the blood flow is much slower when compared to bigger vessels (fig. 1.2). This facilitates the exchange of gases and nutrients between blood and extracellular matrix of the tissue fed by the capillaries.

The driving motor of the circulatory system is the heart. Major arteries and veins leave the heart and branch into smaller vessels and capillaries. Capillaries then rejoin into venules and veins. Main blood vessels and first branches are composed of three layers: *tunica intima*, *tunica media* and *tunica adventitia*, from the lumen to the outside. The *tunica intima* is composed of a layer of endothelial cells, the *tunica media* consists of elastic fibres and **Vascular Smooth Muscle cells (vSMCs)**, especially in arteries. The *tunica adventitia* consists of connective tissue. Progressively smaller vessels have a much thinner wall and they are composed of a layer of endothelial cells surrounded by a basal lamina, supported by

a few perivascular cells. Capillaries in the brain, striated and smooth muscles, lung and connective tissues are known as continuous capillaries as they have no fenestration: endothelial cells form an uninterrupted wall. Other tissues such as kidneys, pancreas and endocrine glands have fenestrated capillaries with gaps of around  $50nm-100nm$ . The gaps are covered with a matrix of unknown molecular composition that regulates substances trafficking (Standring [2008]).

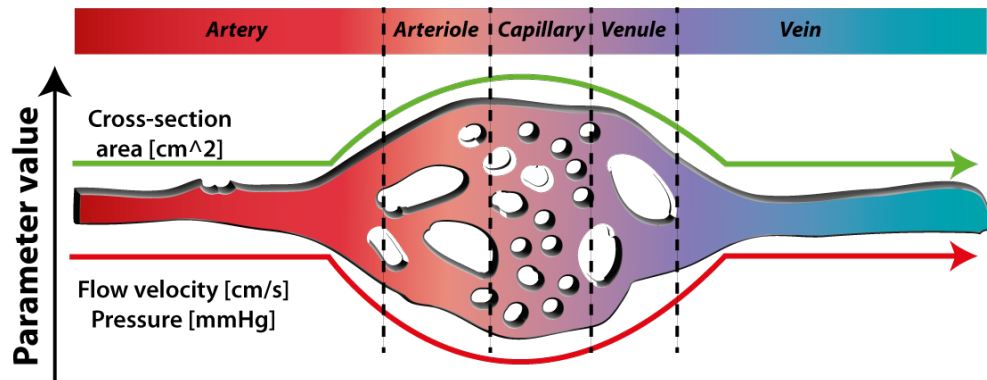


Figure 1.2: *Properties of the vascular system with respect to size. Capillaries have a higher surface area (green line) and lower flow velocity and pressure (red line) than arterioles and venules.*

### 1.2.2 Mechanisms of angiogenesis

The capillary system is mainly formed *de novo* during the embryogenesis by a process known as vasculogenesis. The body has the ability to form specialised capillaries in different organs: capillaries in the liver are fenestrated and form a filtration system, in lungs sacks are formed to facilitate gas exchange. In adult life the formation of new blood vessels is limited to specific physiological situations such as menstrual cycle and wound healing. In addition, new capillaries are formed to meet specific requirements: for example, it has been reported that endurance athletes skeletal muscles have a more developed capillary bed compared to sedentary people (Carrow et al. [1967], Adolfsson et al. [1981], Coggan et al. [1992], Gielen et al. [2010]). In the human adult, new blood vessels are formed from pre-existing ones by a process known as angiogenesis. The ability to control vascular density based on supply/demand and the restoration of damaged vessels is the result of a delicate balance of factors promoting (pro-angiogenic factors) and inhibiting (anti-angiogenic factors) the formation of new blood vessels. Table 1.1 provides an overview of the factors involved in angiogenesis. Angiogenesis must be balanced to maintain homeostasis. A number of pathologies are associated with unbalanced angiogenesis (see figure 1.3), either as the primary cause or as a consequence and hallmark of the disease (fig. 1.3).

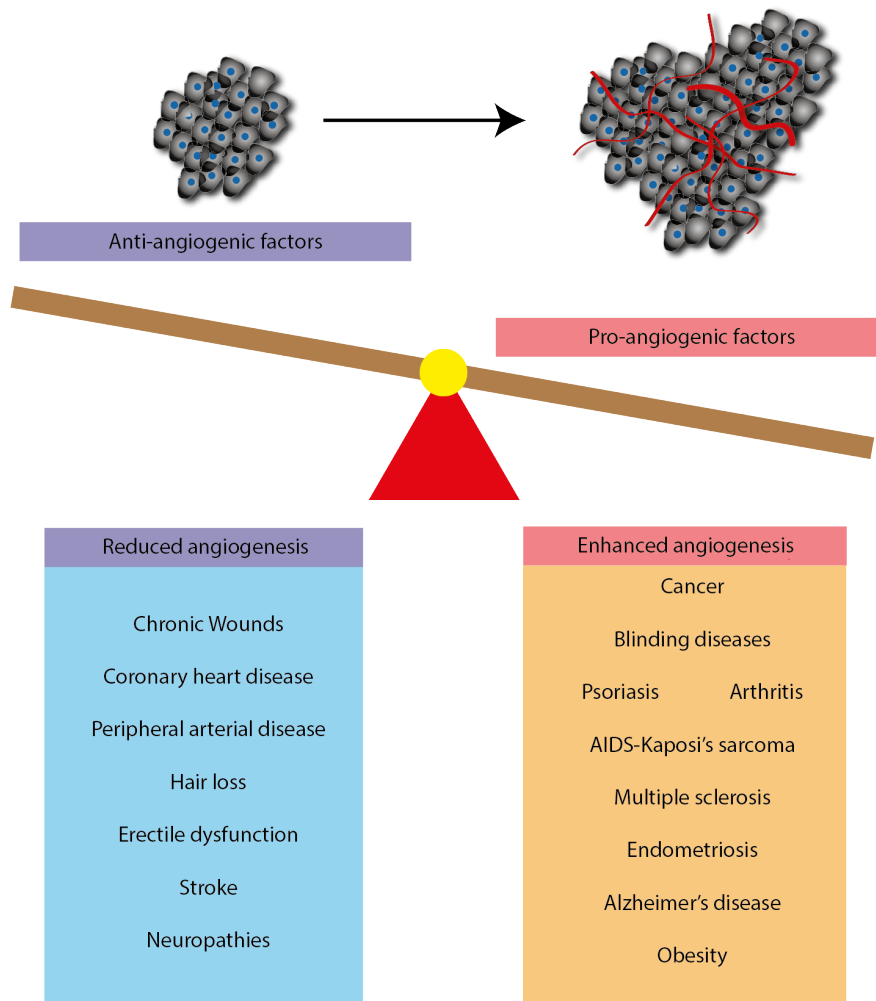


Figure 1.3: Pathologies associated with unbalanced angiogenesis.

Anti-angiogenic factors	Pro-angiogenic factors
TSP-1	VEGF
Angiostatin	PIGF
Endostatin	FGF
Tumstatin	PDGF
Interferon	EGF
Integrins	MMP
TIMP	Low pH and hypoxia
	Angiopoietin
	bFGF

Table 1.1: Pro- and anti-angiogenic factors. Adapted from *Folkman and Kalluri [2004]*.

Angiogenesis normally occurs in wound healing and menstrual cycle in re-

sponse to local damage of the pre-existing vasculature. When a vessel lesion occurs one of the first consequences is decreased oxygenation to the affected area; this is known as hypoxia ( $pO_2$  between 5 and 10 *mmHg*, concentration 0.1-3%) and is one of the initiators of angiogenesis (Moeller et al. [2004]). To form new vessels (a) the pre-existing ones are disrupted, (b) the extracellular matrix is degraded, (c) endothelial and perivascular cells migrate in the direction of the new vessels growth and finally (d) the newly formed vasculature is stabilised (Harris [2002]). Vessel destabilisation results from the loss of cell-cell contact between endothelial cells and also with perivascular cells. In response to hypoxia local NOs concentration increases transcription of Hypoxia-inducible Factor-1 $\alpha$  (HIF-1 $\alpha$ ) and this up-regulates Vascular Endothelial Growth Factor (VEGF) production by tumour (Liby et al. [2012]) and perivascular cells (Pinto et al. [2010]). VEGF is a potent pro-angiogenic factor that was first identified by Senger in 1983 and initially called Vascular Permeability Factor (VPF) (Senger et al. [1983]).

VEGF promotes the secretion of angiopoietin 2 from endothelial cells. Angiopoietin 2 is an inhibitor of angiopoietin 1, which stabilises cell-cell contact (Fagian and Christofori [2013]). Angiopoietin 2 and VEGF, combined with an increased expression of metalloproteases degrading the Extracellular Matrix (ECM), promote vessels instability and increased tissue permeability (Jain [2003]). Once pre-existing vessels are degraded and the extracellular matrix becomes less dense, endothelial cells commence proliferation and migration in the direction of the new vessel sprout. The migration follows a leading endothelial cell called *tip cell* and is stimulated by VEGF, Fibroblast Growth Factor (FGF) and  $\alpha_v\beta_3$  integrins gradients (Cai et al. [2006], Monti et al. [2013], Sato et al. [2012]). Finally the angiogenic process is switched off by the formation of tubular structures (vessels) and cell-cell interactions, particularly endothelial cell-pericyte interactions, promoted by Platelet Derived Growth Factor (PDGF) and angiopoietin 1. Pericytes are recruited by endothelial cells secreting PDGF, angiopoietin 1 and Transforming Growth Factor- $\beta_1$  (TGF- $\beta_1$ ) (Hellstroem et al. [1999]). Vessel stabilisation is regulated by FGF, VE-cadherin, PDGF, TGF- $\beta_1$  and angiopoietin 1 (Ramsauer and D'Amore [2007], Zhang et al. [2009]). Non functional vessels are disrupted and removed in the final remodelling of the new vasculature (Ichioka et al. [1997]).

### 1.2.3 Tumour angiogenesis

When angiogenesis is not initiated, tumours remain vital but do not exceed  $\simeq 1mm^3$ . When angiogenesis is initiated, tumour growth becomes exponential (Folkman [1971]). Small, dormant *in situ* tumours form frequently, but do not

evolve to invasive cancer. This concept was suggested by Folkman in 1989 and is known as *cancer without a disease*. It defined angiogenesis as a hallmark for cancer (Folkman et al. [1989]). When the tumour grows, its centre becomes hypoxic. Hypoxia is a major switch of tumour angiogenesis as it promotes the secretion of angiopoietin 2 and VEGF with exactly the same mechanisms described in physiological angiogenesis. It has been observed that both tumours and normal tissues exhibit similar angiogenic mechanisms, with the crucial difference being that tumours inhibit the *switch off* signal, maintaining the vasculature in an active state of constant remodelling, without final maturation. This allows exponential tumour growth well beyond the limit of  $\simeq 1\text{mm}^3$  reported for non vascular tumours. Finally, cancer cells can escape the primary tumour site, enter the blood system and colonise other tissues to establish secondary tumour. This process is known as metastasis and it is associated with a poor prognosis (Riihimaki et al. [2013]).

## 1.2.4 Tumour vasculature and tumour microenvironment

### Tumour vasculature

Tumour vasculature is immature and unstable. There is no well defined arterioles/capillaries/venules hierarchy. Vessels are tortuous and with a heterogeneous diameter and some are blind ended. Finally, since the vasculature is not mature, large fenestrations (up to micrometers) exist between endothelial cells and there is no or minimal pericytes coverage (Diaz-Flores et al. [1992]). As a result of the large fenestrations the tumour vasculature is more leaky than normal vasculature, a key feature in both the primary and metastatic stages of the disease. In addition, the lymphatic drainage is compromised (Matsumura and Maeda [1986]), resulting in increased hydrostatic pressure within the tumour. The combination of leaky vasculature and reduced lymphatic drainage produces **Enhanced Permeation and Retention (EPR)** and is of great importance in tumour targeting. EPR effect will be discussed in further detail in section 1.4.2.

### Tumour microenvironment

The tumour microenvironment consists of the ECM, chemical factors and a variety of cell sub-types. These include fibroblast, endothelial cells, perivascular cells and immune cells which are normal cells but contribute to tumour growth. The region around the tumour is characterised by inflammation, which supports angiogenesis as it has been observed in wounds. This similarity between tumours and wound resulted in the definition of cancer as a *wound that does not heal* (Dvorak [1986]). Fibroblasts in tumours are more specifically named **Cancer Associated Fibroblast (CAF)** to distinguish them from normal

fibroblasts. CAF are derived from normal fibroblasts, pericytes, Mesenchymal Stem Cells (MSC), endothelial cells or epithelial cell via a transformation process (Endothelial-Mesenchymal Transition (EndT) and Epithelial-Mesenchymal Transition (EMT) respectively) and are often myofibroblast with increased smooth muscle actin (Fuyuhiko et al. [2011]). CAF actively contribute to angiogenesis by secreting VEGF, PDGF and TGF- $\beta$ 1, all pro-angiogenic factors (see section 1.2.2-1.2.3) (Raesanen and Vaheri [2010], Marsh et al. [2013]). Immune cells such as Tumour Associated Macrophages (TAM) and Tumour Infiltrated Lymphocytes (TIL) are also present in the tumour microenvironment, exhibiting reduced cytotoxic activity compared to their normal counterparts. The reduction of cytotoxic activity appears to be mediated by the cancer cells (Qian and Pollard [2010], Valenti et al. [2007]).

### 1.2.5 Angiogenesis as a target in cancer therapy

Angiogenesis is a hallmark of cancer. It has been highlighted how cancer growth and survival is dependant on angiogenesis (section 1.2.3). The combination of these two factors makes tumour angiogenesis an attractive target in cancer therapy. There are several anti-angiogenic compounds already approved by the Food and Drugs Administration (FDA) or in clinical trial, including Bevacizumab, Pegaptanib (Vascular Endothelial Growth Factor Receptor (VEGFR)), Cetuximab (Epidermal Growth Factor Receptor (EGFR)). The aim of vascular targeted therapy is to *starve* tumours by interfering with the disease vascularisation. It has also been proved that traditional chemotherapeutic agents are more effective when combined with anti-vascular agents (Ma and Waxman [2008]). The vasculature can be compromised either by inhibiting the formation of new vessels (anti-angiogenesis therapy) or by disrupting existing vessels (Vascular Disrupting Agent (VDA)-based therapy).

**Anti-angiogenesis.** The concept of anti-angiogenesis was first introduced by Folkman in 1971 (Folkman [1971]). Perhaps the most studied anti-angiogenic target is VEGF. Initially named as VPF by Senger and co-workers in 1983 (Senger et al. [1983]), and later renamed VEGF by Leung who also attributed angiogenic properties to the molecule (Leung et al. [1989]). VEGF is one of the most potent pro-angiogenic factors. Inhibition of VEGF results in reduced new blood vessel formation and tumour stabilisation or regression. Vessel stabilisation has been reported to improve drug biodistribution to the tumour in a synergistic effect of the antiangiogenesis and chemotherapy combination. Another target for anti-angiogenesis are pericytes, a perivascular cell population controlling vessel

stability. The rationale being that tumours having lower pericyte coverage are more sensitive to drugs targeting the endothelial cells, such as anti-VEGF drugs (Benjamin et al. [1998], Erber et al. [2004]). However this approach has failed in clinical studies because of toxicity (Hainsworth et al. [2007]). An alternative pericyte-targeted approach was proposed by Raza and colleagues, using a pro-pericyte strategy which could be beneficial. By stimulating pericyte recruitment blood vessels will be stabilised and new angiogenic sprouting inhibited. This could also limit metastasis by reducing the leakiness of the vasculature (Raza et al. [2010]).

**VDAs** target the differences between the tumour and normal vasculature, such as increased fragility, proliferation and protein up-regulation. Several VDAs are in clinical trials, including for instance combretastatin (Thorpe [2004]). Combretastatin's effect is dependent on tumour type and pericyte coverage, suggesting again the importance of pericytes as an additional potential target in vascular therapy. Pericyte-rich tumour models such as implanted Mouse Fibrosarcoma Cells expressing VEGF188 isoform (MFC188) have a greater response to combretastatin compared to tumours with lower pericyte coverage such as Mouse Fibrosarcoma Cells expressing VEGF120 isoform (MFC120) (Tozer et al. [2008]).

Despite it being more than 80 years since Folkman's anti-angiogenesis hypothesis, more than 25 years since the discovery of VEGF as an anti-angiogenic target and almost 10 years since the approval of the first anti-angiogenic drug there is only a small amount of studies demonstrating clinical efficacy of anti-angiogenesis therapies, even in combination with traditional chemotherapy. Progression free survival is improved but this is not always the case for overall survival. At the time of its approval, overall survival for the VEGF signalling inhibitor Bevacizumab was reported to be increased from 15 to 20 months (Hurwitz et al. [2004]), but later trials failed to reproduce these results (Bellou et al. [2013]). The poor outcome of anti-angiogenic therapy are likely to be due to multiple causes: *a)* Endothelial cells from different tissues have a different phenotype and therefore are likely to have a differentiated response (Hida et al. [2004]); *b)* Resistance to VEGF signalling inhibition has been reported (Bellou et al. [2013]); *c)* The angiogenesis pathway has demonstrated redundancy: the inhibition of one factor or pathway results in the increased secretion of another factor. For instance it has been reported that VEGF inhibition can result in increased Epidermal Growth Factor (EGF) and FGF production (Grothey et al. [2008], Batchelor et al. [2007]); *d)* Vascular disruption can lead to metastatic tumours (Ebos et al. [2009], Paez-Ribes et al. [2009]). Overall, there is no clear understanding of which patients will benefit from anti-angiogenic therapies due to difficulties assessing the correlation

between drugs and their effect (Ribatti [2010]). Pericytes are undoubtedly involved in the response to anti-angiogenic therapies, however their role is not well understood. As pericytes may protect endothelial cells from anti-VEGF therapy a combination of anti-VEGF and Platelet Derived Growth Factor-B (PDGF-B) therapy have been tested with contrasting outcomes. Some studies supported the validity of a combined approach (Bergers et al. [2003], Erber et al. [2004]), while in other models there was no response, or toxic side-effects were reported (Kuhnert et al. [2008]). In another study using a pericyte-deficient mouse no difference in anti-VEGF therapy response was observed when compared to that of normal mouse, suggesting that the therapy may not be specific to the tyrosine-kinase receptors, but may interfere with other pathways (Nisancioglu et al. [2010]).

## 1.3 Imaging techniques

Imaging techniques are an essential tool in research as they provide data from direct observation of biological events. In cancer research, imaging has several applications, including *a)* diagnosis, *b)* understanding of the mechanism of evolution and spreading and *c)* evaluation of treatment outcome. Techniques such as X-ray, Positron Emission Tomography (PET) and Magnetic Resonance Imaging (MRI) are used in clinical practice to localise cancer and evaluate size and eventually metastasis. MRI can also be used to obtain functional information relating to blood flow and permeability of the tumour vasculature (Gaustad et al. [2008]). In pre-clinical research, optical imaging techniques based on fluorescence and bioluminescence can be used to investigate phenomena at the cellular and molecular level. The following sections review imaging techniques, their limitations and strategies to overcome these limitations.

### 1.3.1 Techniques and limitations: an overview

There are a number of different available imaging techniques. Not all of them can be applied to any problem, the appropriate technique should be chosen accordingly to the aim of the study. For example, Transmission Electron Microscopy (TEM) can be used to investigate sub-cellular organelles with nanometre spatial resolution in fixed samples, but cannot visualise the distribution of a radio therapeutic agent in an animal.

The best imaging technique for a specific study should be chosen considering spatial resolution, time resolution, tissue penetration and cost. For a given application, the *ideal* imaging technique should have enough spatial resolution to visualise the structure of interest, enough tissue penetration to visualise such

structure wherever it may be located within the body, and finally it should have good time resolution to image events at the time scale desired. Techniques such as X-ray, MRI, Computed Tomography (CT), PET and ultrasounds are commonly used to detect tumours and assess morphological properties such as size and presence of metastasis (McDonald and Choyke [2003]). Since the original application of the techniques, spatial resolution has been greatly improved. Micro- and nano- bubbles improved spatial resolution of ultrasound from millimetres to micrometers (Lindner [2004], Yin et al. [2012]). Similar improvements have been achieved for MRI, by refining imaging acquisition and processing technique (Brindle [2008]). Thanks to such improvements it is possible to obtain more detailed functional information from MRI. As an example, Brindle and co-workers were able to detect cell death in a tumour by specifically targeting the delivery of the contrast agent gadolinium to apoptotic cancer cells (Krishnan et al. [2008]). Others applications include detection of tumour hypoxia, blood volume and vasculature permeability (Pacheco-Torres et al. [2011], Roberts et al. [2000], Cha et al. [2000], Law et al. [2004]).

Optical imaging such as confocal imaging offers great spatial resolution. In angiogenesis imaging, wide field analysis allows visualisation and quantification of morphological parameters such as tortuosity and Micro Vessel Density (MVD), both important parameters correlated to tumour severity. Improved spatial resolution and 3D mapping are possible with Confocal Laser Scanning Microscopy (CLSM), where the use of a pinhole allows elimination of out of focus light, improving signal to noise ratio. When the focus plane is moved through the specimen a 3D image can be reconstructed (Pawley [2006]). In Multi Photon Microscopy (MPM), fluorescence is generated when two or more photons with total energy equal to the one required by single photon fluorescence excitation are adsorbed by the fluorophore at the same time. This is an unlikely statistical event to occur, therefore the beam of light must be highly focused. As a result, only a restricted plane of focus is generated and no pinhole is required to eliminate out of focus light (Denk et al. [1990]). The main advantages of MPM over CLSM are greater tissue penetration (from  $\simeq 60\mu\text{m}$  of CLSM to a few hundreds of micrometers) and reduced photobleaching and phototoxicity (Lunt et al. [2010]). Despite MPM being achieved with any number of photons, in practical applications MPM is in fact dual-photon. However, recently a tri-photon application has been reported to achieve great spatial resolution and tissue penetration in a mouse brain model (Horton et al. [2013], Howard et al. [2013]). Spatial resolution can be further increased using techniques such as Stochastic Optical Reconstruction Microscopy (STORM) and Stimulated Emission Depletion (STED) (Denk and Webb [1990], Hell and Wichmann [1994], Rust et al. [2006]) in Intra Vital Microscopy (IVM).

Technique	Tissue penetration	Resolution	Acquisition time
Intravital microscopy	400-800 $\mu m$	1 $\mu m$	Seconds
Bioluminescence Imaging	$cm$	$mm$	Minutes
FMT	<10 $cm$	1 $mm$	Minutes
PET	No limit	1 $mm$	Minutes
Ultrasound	$cm$	50 $\mu m$	Seconds
CT	No limit	50 $\mu m$	Minutes
MRI	No limit	10-100 $\mu m$	Minutes

Table 1.2: *Imaging techniques comparison by spatial and time resolution and tissue penetration. Data from Weissleder and Pittet [2008].*

In traditional optical imaging spatial resolution is estimated with the Abbe equation for the diffraction limit  $D = \lambda/2 \cdot NA$  where  $D$  is the diffraction limit,  $\lambda$  is the wavelength used and  $NA$  is the objective numerical aperture. **STORM** and **STED** microscopy bypass the diffraction limit and structures 10 $nm$  apart can be resolved. Despite achieving remarkable progress in tissue penetration, optical imaging *in vivo* without further modification can only be applied to study angiogenesis in the retina, where the eye provides a natural transparent window to access the specimen (Wright et al. [2012]).

## 1.4 Nanocarriers

### 1.4.1 Background

Cancer targeting for therapy or imaging requires specific extravasation which is controlled by the size of the vessel fenestration. Moreover, especially in therapy, some of the most potent drugs are poorly water soluble and have severe side effects. The combination of the these problems (targeting, solubility, side effects) has lead to the development of nanometre sized carriers.

### 1.4.2 Targeting tumour with nanocarriers: basic principles

To take full advantage of any imaging technique or cancer therapy based on nanocarriers, it is critical to maximise the delivery of contrast agents or drugs to the tumour site, while minimising distribution to other organs. This operation is known as targeting. In cancer applications, targeting can be divided into two subsequent mechanisms: *passive targeting* and *active targeting*. *Passive targeting* takes advantage of the irregular anatomy of the tumour micro-vasculature, while

*active targeting* requires specific nanocarrier/cell recognition within the tumour microenvironment.

### Passive targeting

Tumour microvascular anatomy has been described previously (sect. 1.2.4). Tumour blood vessels have fenestrations up to micrometres, while healthy tissue vasculature has no or little fenestration, with the exception of specialised structures such as hepatic sinusoids where fenestration as large as  $150nm$  have been described. Tumour vasculature fenestrations lead to increase vascular leakiness. Moreover lymphatic drainage is compromised. The sum of the two factors is known as the **EPR** effect and it was first described by Maeda ([Matsumura and Maeda \[1986\]](#)). The **EPR** effect represented a revolution in tumour therapy and cancer targeting Delivery agents have been engineered to effectively extravasate into tumours. Using the same mechanisms imaging techniques have been improved too. For instance **MRI** imaging of tumour is enhanced by contrast agent extravasation and accumulation (i.e. gadolinium) and ultrasound imaging can be enhanced by the accumulation of nanobubbles ([Xing et al. \[2010\]](#)). Unfortunately, increased leakiness and reduced lymphatic drainage cause increased hydrostatic pressure. When intra tumour pressure is higher than intra-capillary pressure, gradient driven diffusion of molecules from the vasculature to the tumour is reduced. In this case diffusion is dependent only on the concentration gradient and the diffusion coefficient, which is inversely correlated to the radius according to the Stokes-Einstein equation  $D = \frac{k_b T}{6\pi\eta R}$ , where  $k_b$  is the Boltzmann's constant,  $T$  is the temperature,  $\eta$  is the viscosity and  $R$  is the particle radius. Diffusion is a slower process compared to convection. However, since the first description of **EPR** almost 25 years ago, countless of proofs have been collected in favour of particle accumulation in tumours due to such effect. Delivery systems exploiting the **EPR** effect include a huge heterogeneity of chemistries, ranging from quantum dots to liposomes, bioconjugates, micelles and polymersomes ([Moghimi et al. \[2001\]](#)). In imaging, passive targeting is useful to reveal the presence of tumour mass. For techniques aiming at higher spatial resolution passive targeting is not enough and specific tumour features should be targeted. This second level of targeting is known as active targeting.

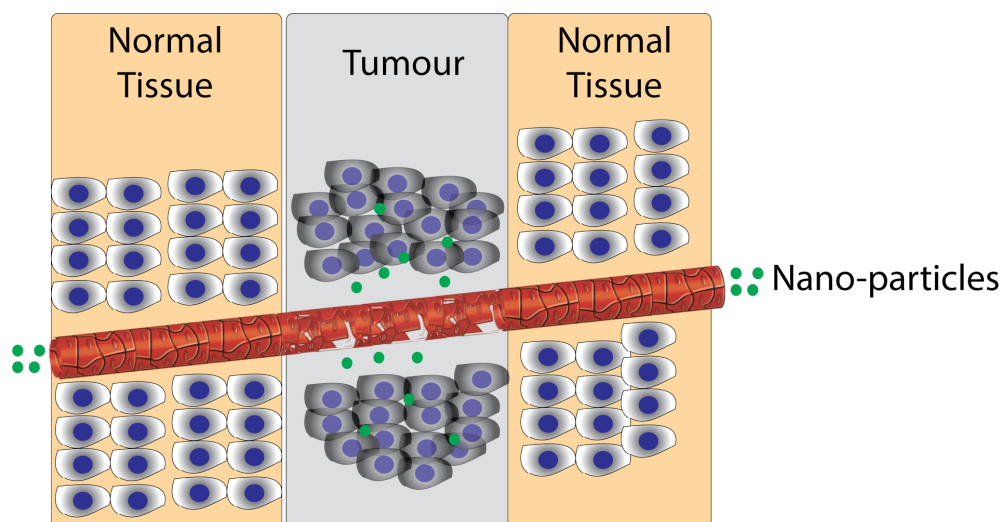


Figure 1.4: *EPR* effect. Tumours blood vessels are characterised by large fenestration that allows nano-particles to extravasate. Furthermore, lymphatic drainage is reduced therefore nano-particles are not rapidly cleared by the interstitial cellular flow. In normal tissues there are no or smaller fenestrations, therefore nano-particles will not extravasate.

### Active Targeting

By the *EPR* effect nano-metre sized particles can passively accumulate within tumours. When a therapeutic or imaging agent is delivered specifically to the cell of interest within the tumour the term *active* targeting is used. Active targeting of nanocarriers is achieved by functionalisation with moieties that can recognise specifically a cell type. Active targeting has been extensively researched in therapy (see Moghimi et al. [2001] for an extensive review). Limiting the subject to imaging, as more relevant to the work presented in this thesis, the most remarkable achievements have been reported when active targeting is coupled to high resolution optical imaging such as *CLSM* or *MPM*. An extensive review of nanocarriers and different targets can be found at (Brannon-Peppas and Blanchette [2012]).

#### 1.4.3 Nanocarriers pharmacokinetics

The body is highly compartmentalised: organs are confined and separated from each others, normally communicating via the circulatory system. Compartmentalisation is found also at the cellular level, where different organelles are separated from each others by lipidic membranes. Nanocarriers *in vivo* will have to travel through a number of different barriers in order to reach the desired site of accumulation. The number and type of barriers depends on both the administration site and the localisation of the target. The fate of any molecule or carrier

in the body is traditionally studied in terms of the **Administration, Distribution, Metabolism, Excretion (ADME)** profile.

**Nanocarriers administration** Typical administration routes are **Intra Muscular (i.m.)**, **Intra Peritoneal (i.p.)**, **Intra Venous (i.v.)** and **Sub Cutaneous (s.c.)**. **i.m.**, **i.p.** or topical administration are useful in local delivery. However, **i.v.** administration is more common and it is referred to as systemic administration, as the injected substances will be spread to the whole body via the circulatory system. Local delivery is useful to maximise the concentration of the delivered agent at the delivered site, and normally release from cargo is slow and sustained, compared for instance to systemic delivery where nanocarriers are challenged by the **Reticuloendothelial System (RES)** which can quickly clear them from the circulation. The term **RES** or the equivalent **Mononuclear Phagocyte System (MPS)** refers to phagocytic cells which are part of the immune system. These include macrophages and monocytes, but also hepatic Kupffer cells. Therefore, the **RES** represents the first barrier that must be overcome to avoid fast blood clearance of nanocarriers.

**Nanocarriers distribution** Nanocarriers delivered systemically will circulate in the blood and distribute to different organs. The profile of distribution is dictated by their size, shape, and charge. Most of the polymeric nanocarriers are cleared by the **RES** (also referred to as **MPS**) after opsonisation. Opsonisation is the recognition by a group of plasma protein known as opsonin which includes specific immunoglobulins and complement proteins. Opsonisation is a fast process: it only takes seconds. Opsonised nanocarriers are recognised by phagocytic cells and accumulate in liver and spleen, but also lung and kidney. The ideal nanocarrier size for tumour accumulation and **MPS** is below  $100\text{nm}$  (**Alexis et al. [2008]**, **Perrault et al. [2009]**, **Petros and DeSimone [2010]**). Nanocarrier shape also affects clearance. It has been reported that tubular micelles exhibit better pharmacokinetic profile than spherical vesicles, probably because elongated shapes are easily up-taken by phagocytic cells (**Geng et al. [2007]**).

Chemical composition of the nanocarrier is important because it affects recognition by **MPS**. For this reason many formulations have a protective brush of **Polyethylene Oxide (PEO)**. Another strategy to prolong particle half life is coating with molecules recognised as *self* by the **MPS**. An example has been reported by Discher and co-workers when they coat microbeads with CD47, a *marker of self* normally found on the surface of red blood cells (**Tsai and Discher [2008]**).

At the tumour site, nanocarriers will need to leave the blood stream to enter the tumour and release their cargo. Size is critical in the extravasation step.

Nanocarriers should have smaller size than the pore size cut-off of vascular fenestration in tumour sites, but bigger than fenestrations in normal tissues. Diffusion from the vessels to the tumour is inversely correlated with particle radius (Dreher et al. [2006]). Charge is also a critical factor in diffusion. Cationic particles diffuse faster and further than neutral or anionic counterparts (Dellian et al. [2000]). Finally, using beads functionalised with quantum dots and targeted to HER2, Tada and co-workers were able to visualise accumulation of the beads in the target cells and by tracking their trajectories they extrapolate extravasation kinetic parameters, including an average travelling speed of  $1\text{-}4\mu\text{m/s}$ , characterised by a stop-and-go movement most likely caused by a *cage* effect of the dense extracellular matrix (Tada et al. [2007]).

At the tumour site, nanocarriers release their cargo either extra-cellularly or intra-cellularly. Extra-cellular release can be achieved by exploiting tumour microenvironment specific features such as low pH ( $\simeq 6$ ) or high temperature (Kratz et al. [2008]). Cellular up-take mechanisms can occur by phagocytosis only in a few specialised cells. The most common mechanisms of up-take include pinocytosis and endocytosis, mediated or not by receptor-ligand interactions. For an extensive review on nanocarriers endocytosis see Canton and Battaglia [2012]. As biodistribution, cellular uptake is controlled by size, shape, chemical properties and topology of the vesicles, however in some cases ideal biodistribution parameters do not match ideal cellular uptake conditions. For instance, cellular uptake is higher for positively charged nanocarriers because of the interactions with the negatively charged proteoglycans expressed at cellular surface. Unfortunately this is also true for the cells of the MPS, therefore positively charged particles have poor biodistribution. Considering nanocarriers size, it is interesting to notice that the same size that in flow escape the MPS (radius  $\leq 100\text{nm}$ ) is also a good size for cellular uptake: smaller particles are up-taken faster in static *in vitro* endocytosis assays which can resemble to a condition of very low flow at the tumour level. In more detail, cellular uptake requires the cellular membrane to bend to engulf around the nanocarriers. This process requires energy and there is a theoretical minimum radius that particles should possess to facilitate the process :  $R_{min} = \sqrt{\frac{2 \cdot k \cdot A}{\mathcal{E} \cdot k_B \cdot T}}$  where  $k$  is the membrane bending modulus,  $A$  is the membrane surface area,  $\mathcal{E}$  is the binding energy (e.g. chemical energy per ligand-receptor pair),  $k_B$  is the Boltzmann constant, and  $T$  is the temperature (Chaudhuri et al. [2011]). Finally, nanocarriers topology affects cellular uptake. In polymeric vesicles it has been found that mixtures of different co-polymers creates domains in the nanocarriers membrane and brush. Such domains affects kinetics uptake (Massignani et al. [2009], LoPresti et al. [2011]).

**Nanocarriers metabolism** Metabolism depends on the nanocarrier chemistry and size. For polymeric vectors, biodegradable polymers can be broken down and the monomer can be recycled in the body's metabolic pathways or eliminated by the kidney or the GI (Mehvar [2000]). Small non biodegradable polymers are secreted by the kidney, provided they are below the glomerular threshold. Glomerular threshold for PEO has been measured to be  $30\text{KDa}$  ( $\simeq 680$  monomers) with elimination rate inversely correlated to molecular weight (Webster et al. [2007]). If the co-polymer is non biodegradable and below the glomerular threshold it may be secreted with the faeces, however accumulation in the body is a concern and more studies are required to elucidate the fate of polymers, especially concerning chronic administration and renal or liver accumulation.

#### 1.4.4 Nanocarriers self-assembly

Nanocarriers can be made by a number of different chemicals, ranging from lipids to polymers to metals. An important classification can be made on the basis of the type of interaction between the components. Systems such as silica beads, quantum-dots, carbon nanotubes and dendrimers are all characterised by strong covalent bonds between the components. Another class of nanocarriers is characterised by weak interaction between the components based on supramolecular forces, such as the hydrophobic effect, hydrogen bonding, coulomb interaction and aromatic forces. Micelles, liposomes and polymersomes belong to this second class. A key difference between the two classes is represented by the synthetic process. Strong bonds are usually generated via chemical synthesis, while weak interactions mimic *self assembly* of natural components in water, such as biological membranes, proteins and nucleic acids.

Self-assembly processes involve the aggregation of molecules to form defined structures. As a general rule, this process is concentration dependant, where at low concentrations, the different building blocks are molecularly dissolved and as the concentration increases, they start to interact and self-assemble. This concentration is known as **Critical Aggregation Concentration (CAC)**. Self-assembly can be triggered by several supramolecular interactions that depend on the chemical structure of the components of the carrier and the solvent. Amphiphilic molecules contain a part that is able to interact with water molecules hence is water soluble and a part that are is water repellent and hence is insoluble. The balance between water attracting and water repelling parts will dictate the final structures formed and it is known as *packing factor*,  $p$ , defined as

$$p = \frac{v}{a_0 \cdot d}$$

where  $v$  is the volume occupied by the packed hydrophobic block,  $a_0$  is the surface area per molecule defined at the hydrophobic chain-water interface, and  $d$  is the length of the hydrophobic block (Nagarajan [2002]). Amphiphilies with packing factor smaller than  $\frac{1}{3}$  will generate spheres (micelles), if  $p$  is between  $\frac{1}{3}$  and  $\frac{1}{2}$  cylindrical micelles will be obtained and finally if the packing factor is between  $\frac{1}{2}$  and 1, bilayers (vesicles) will be formed (fig. 1.5) (Bates and Fredrickson [1990], Matsen and Bates [1996b], Matsen and Bates [1996a], Fredrickson and Bates [1996]).

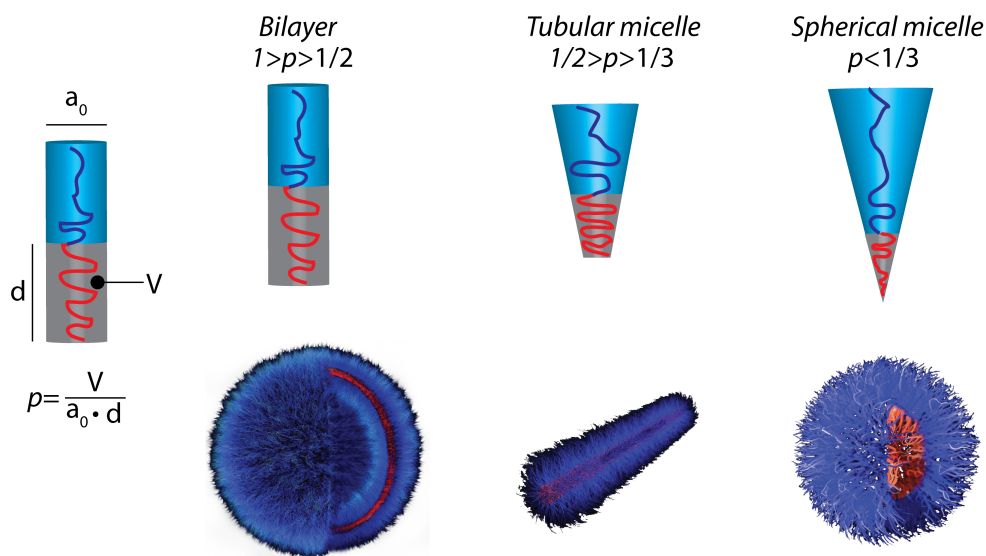


Figure 1.5: *Geometrical parameters governing the self-assembly. If the packing factor  $p$  is higher than  $\frac{1}{2}$  the co-polymers self assemble in bi-layer, if  $p$  is between  $\frac{1}{3}$  and  $\frac{1}{2}$  the resulting geometry will be tubular micelles, if  $p$  is lower than  $\frac{1}{3}$  the favoured shape is spherical micelle.*

A common example of *self-assembled* nanocarriers is the liposome. Such spherical vesicles are made by phospholipids. Phospholipids arrange in water in a way that the hydrophobic *tails* are packed together excluding water, while the polar *heads* are at the interface between the water and the hydrophobic tails. The result is a bilayer membrane. Since the membrane cannot extend indefinitely, it will enclose into a spherical vesicle with an hydrophilic lumen.

Liposomes without any further modification, however, have poor plasma *half life* as they are rapidly cleared by the RES. PEO is a synthetic polymer that has been extensively used in bioconjugation to improve *half life* of drugs and proteins *in vivo*. The application of PEO to liposomes technology gave raise to a class of liposomes known as *stealth* liposomes, in which a percentage of the total phospholipids is conjugated with PEO. The construct showed a prolonged *half life* compared to the previous generation of liposomes, however it had stability issues.

The introduction of a highly hydrophilic chain of PEO of molecular weight typically ranging from 2000-5000Da dramatically altered the packing factor toward values  $< \frac{1}{3}$ , therefore favouring a micellar shape. For this reason only about 5% of the total lipidic composition was conjugated to PEO, and a 100% conjugation was not possible. To be able to use 100% PEO it was necessary to replace the phospholipid with an amphiphilic co-polymer (1.6).

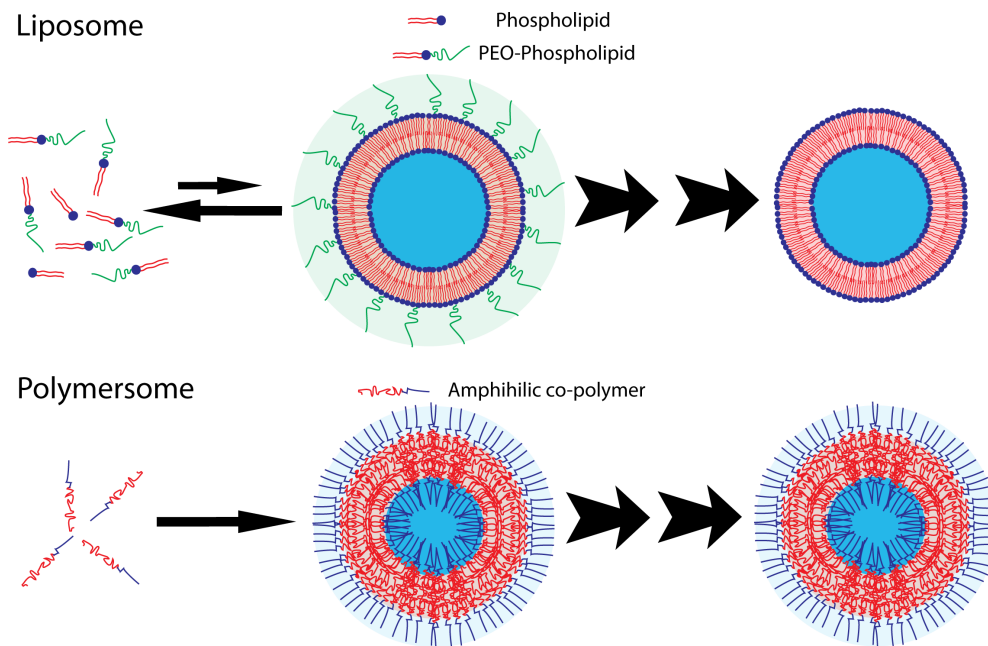


Figure 1.6: *Critical aggregation concentration (CAC)*. In Liposomes, free phospholipids and aggregates exist in equilibrium. Functionalisation with PEO increases the value of CAC of the phospholipids, therefore the equilibrium is shifted towards free PEO-phospholipids. As a result the stealth properties are lost over time. Polymersomes, made of 100% PEO-copolymer, have CAC close to 0, therefore their stealth properties are not lost over time.

### 1.4.5 Polymersomes

Polymersomes are nano/micro-metre sized, spherical vesicles characterised by hydrophilic lumen. Polymersomes can be generated by the self assembling of diblock co-polymers, generally referred to as  $A_m-B_n$ , where A and B are the hydrophilic and hydrophobic blocks,  $m$  and  $n$  represent the number of monomer in A and B respectively, a critical parameter in the determination of the packing factor. Multi-block co-polymers can also be used to form polymersomes, allowing extra-control on the assembly process, surface and membrane topology (see fig 1.7) (LoPresti et al. [2009]).

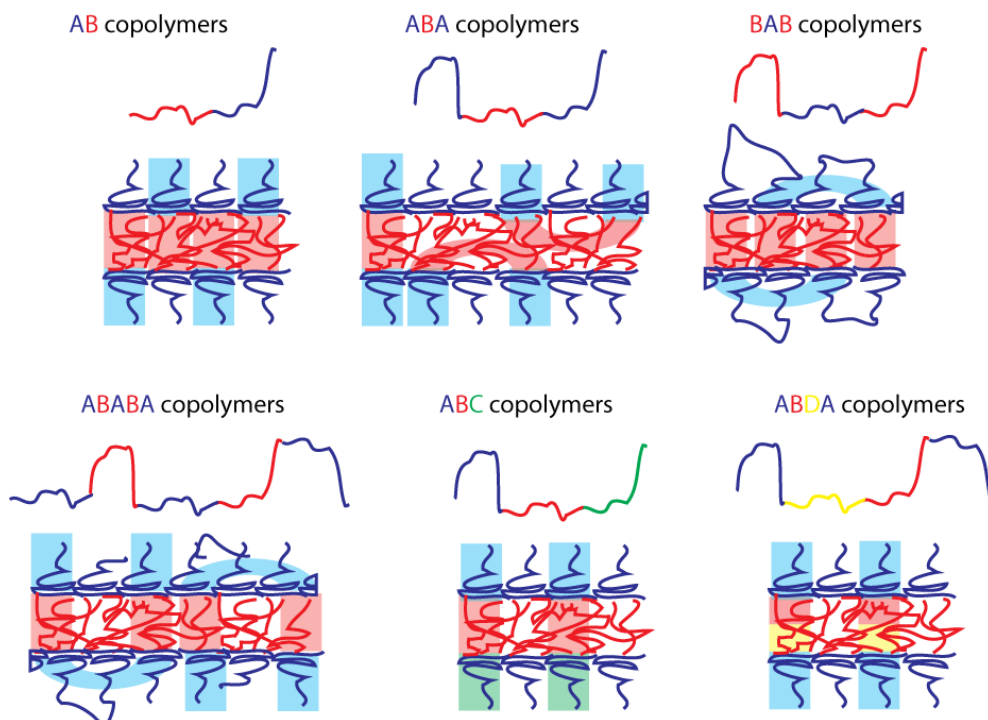


Figure 1.7: Examples of assembly of multi-block co-polymers. Hydrophobic block are always segregated into the membrane, but the co-polymers chain arrangement is dependant on the number and order of the blocks. Adapted from [LoPresti et al. \[2009\]](#).

Polymersomes size, membrane thickness and length of the hydrophilic brush are also dependant of the size of the co-polymers used. Polymersomes in the range 100-200nm made with diblock co-polymers based on PEO have been reported to have a membrane ranging from 8nm to 21nm, with power relation  $d \simeq MW_A^b$  to increasing PEO chain length from 2KDa to 20KDa ([Discher and Ahmed \[2006\]](#)). This increase in membrane thickness was also correlated to membrane permeability and to circulation half life *in vivo*. For PEO-PBO polymersomes permeability was reported to be inversely correlated to membrane thickness, while circulation half life was improved with thickness of at least 16nm ([LoPresti et al. \[2009\]](#)).

### 1.4.6 Polymersomes applications

Polymersomes can be engineered to deliver hydrophilic moieties encapsulated in the hydrophilic lumen and/or hydrophobic molecules intercalated in the membrane. If a contrast agent such as gadolinium or fluorescent dyes are encapsulated or linked to the co-polymers they can be used in imaging applications, both *in vitro* and *in vivo*.

*In vitro* applications include the intracellular delivery of antibodies and lipids

for live cell imaging (Massignani et al. [2010]). pH sensitive polymersomes made of Poly(2 - methacryloxyethyl-phosphorylcholine)-poly( 2 -(diisopropylamino)ethyl methacrylate) (PMPC-PDPA) were reported to escape endosomes and to successfully deliver functional probes intracellularly (Canton et al. [2013]).

*In vivo* applications include therapy and imaging practices. In cancer therapy, tumour regression has been reported after *i.v.* administration of doxorubicin and taxol co-encapsulated in PEO-PLA polymersomes (Ahmed et al. [2006]). Other therapeutic applications include the delivery *in vitro* of the anti-cancer drug gemcitabine to pancreatic tumour cells via PEO-PCL polymersomes (Sood et al. [2013]) and the use of PMPC-PDPA polymersomes in oral squamous cell carcinoma (Murdoch et al. [2010]).

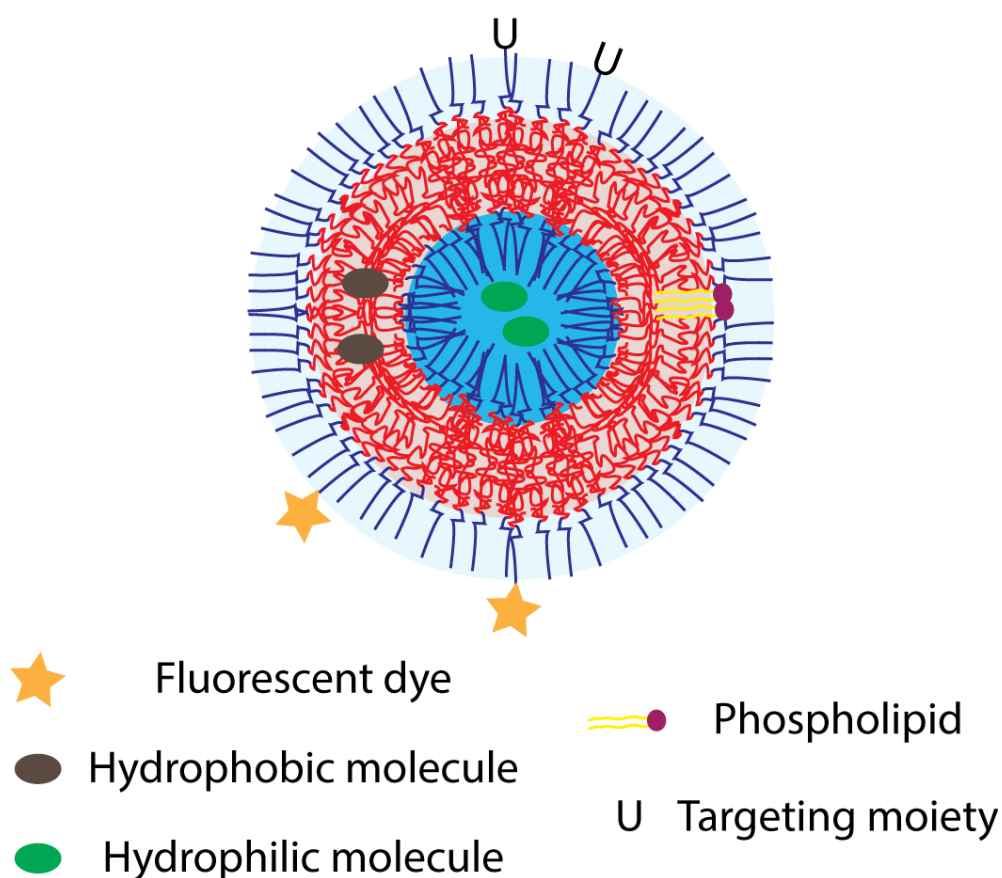


Figure 1.8: *Advantages of the polymersomes. Polymersomes can be loaded with hydrophilic molecules because of the hydrophilic core, they can also incorporate hydrophobic molecules in the membrane, including phospholipids. Finally, they can be functionalise for active targeting or with imaging contrast agent (Christian et al. [2009b], Ahmed et al. [2006], Massignani et al. [2010], Lomas et al. [2010]).*

### 1.4.7 Co-polymers for *in vivo* applications

Blood is a fluid densely packed with cells (eg. erythrocytes, leukocytes and other circulating cells), nanoparticles (i.e. lipoproteins), proteins (albumin, ferritin), immunoglobulin, small molecules (lipids, sugars, salts). As a result, the *free* space available for circulating nanocarriers is limited and interactions between them and blood components occur. When circulating proteins interact and get adsorbed by the nanoparticle the opsonisation process starts, which leads to recognition by phagocytic cells and rapid blood clearance. Alternatively, the nanocarrier might present superficial features directly recognised by the MPS which increase the rate of particle elimination from blood. In both scenarios, short blood half life of nanoparticles is likely to result in insufficient accumulation in the target organs.

The circulation half life of nanoparticles, specifically polymersomes, can be altered by choosing a hydrophilic co-polymer that prevents polymersome interaction with other blood components. Protection from fast clearance from the blood is a combination of chemical and physical protection. Highly hydrophilic polymers are characterised by a large volume of water molecules acting as a *shield*. However, charged polymers cause high disturbance of water structure normally given by weaker hydrogen bonds. Moreover, positively charged polymers strongly interact with proteins, which are mostly negatively charged. As a first general rule, the protective hydrophilic polymer should have no charge and should interact with water without disturbing its structure, for example the polymer PEO. PEO is not charged and the oxygen atoms separated by two methylene groups interact with water via hydrogen bonds. A molecule such as protein or lipid should replace water to interact with the polymer, and this event is energetically not favoured. This chemical protection is however relatively weak and alone is not sufficient to prevent interactions between blood components and the nanocarrier.

In polymersomes, the hydrophilic polymers are packed close to each other, in brush-like conformations and stretch from the hydrophobic membrane towards the exterior (see fig 1.7), generating a physical protective barrier (Vonarbourg et al. [2006]).

In this work, all co-polymers used had the same hydrophobic block (poly(2-(diisopropylamino)ethyl methacrylate) (PDPA)), but different hydrophilic brushes: PEO, poly(oligo(ethylene glycol) methacrylate) (POEGMA) and Poly(2 - methacryloxyethyl - phosphorylcholine) (PMPC).

**PEO** is one of the mostly studied *stealth* polymers. It is non charged, highly hydrophilic, and its molecular geometry allows optimal interaction with water via hydrogen binding. This strong hydrophilicity is one of the bases of the *stealth*

properties of the polymer. It was introduced in bioconjugation to prolong circulation half life of molecules in the late 70s.

**POEGMA** is another hydrophilic and non charged polymer. It is chemically related to **PEO**, however, it is not made by a single long chain of  $-CH_2CH_2O-$ , but of a backbone of poly(methyl ether methacrylate) in which all monomers can be functionalised with short chains of **PEO**. The resulting polymers is still not fouling (Lee et al. [2009], Stetsyshyn et al. [2013]). *Non fouling* is an important property because it means that blood proteins do not accumulate at the surface of the nanocarrier. Protein accumulation is critical as it leads to recognition by the **RES** and rapid blood clearance. Another advantage of **POEGMA** over **PEO** is that it presents more chemical groups available to functionalisation: **PEO** only has two ends, one of which is already linked to the hydrophobic membrane, while the other end is usually methoxylated to reduce fouling.

**PMPC** is hydrophilic and zwitterionic: the monomer has a both a positive and a negative charge, therefore it has no total charge, and it can interact with water to form a chemical barrier to opsonisation. Due to its non fouling properties it is widely used in biological applications such as contact lenses and coronary stents. However, it has been found that polymersomes made of **PMPC** have hydrophilic blocks that are prone to quick internalisation by almost any cell type (Lomas et al. [2010], Massignani et al. [2010], Pegoraro et al. [2014]). Later studies found that **PMPC** is recognised by scavenger receptors class BI (SR-B1), normally receptors for oxidized low density lipoproteins. This class of receptor is expressed by many cells and it is responsible for the rapid internalisation of **PMPC** based polymersomes. It should be noted that this mechanism of internalisation occurs when polymersomes directly interact with the cellular receptor SR-B1, and it does not affect its efficacy as non-fouling material in film coatings (Colley et al. [2014]).

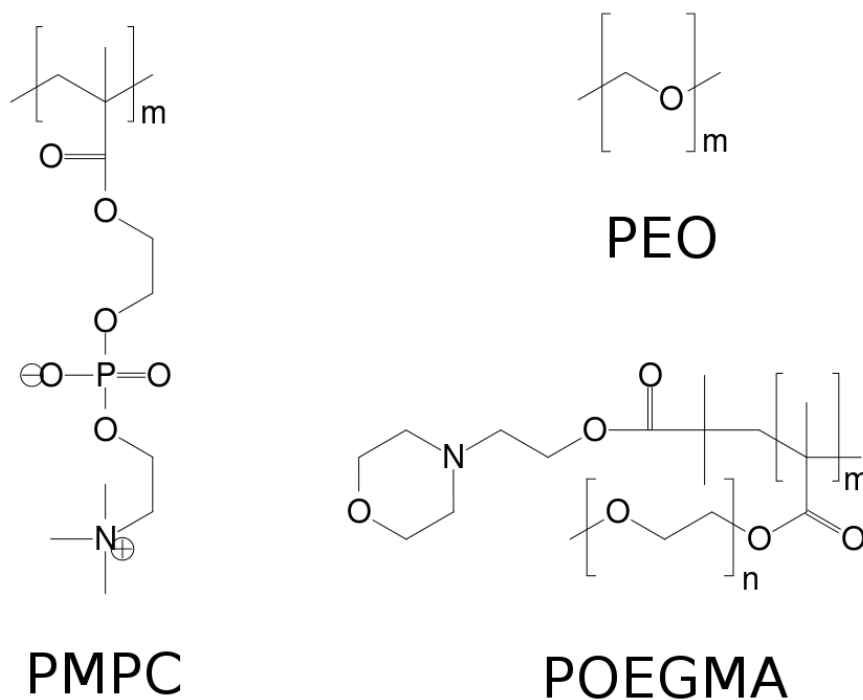


Figure 1.9: The chemical structures of *PEO*, *PMPC* and *POEGMA*. Note how *PEO* and *POEGMA* have no charge, while *PMPC* is zwitterionic. Moreover, *POEGMA* is characterised by chains of *PEO* linked to the backbone of the polymer.

#### 1.4.8 Nanocarriers in *in vivo* imaging

Polymersomes have been used in medical imaging due to their capability to accumulate in tumours. In one study Lecommandoux and co-workers exploited the flexibility of polymeric nanocarriers to functionalised PTMC-b-PGA vesicles with a targeting antibody to HER-2. The same vesicles were labelled with a fluorescent tag for *in vitro* cellular uptake study and **Ultrasmall Superparamagnetic Iron Oxide nanoparticles (USPIO)** were encapsulated in the hydrophobic membrane. This approach allowed them to validate the targeting effect of the functionalisation *in vitro* using **Fluorescence Activated Cell Sorting (FACS)** and to confirm the *in vivo* accumulation within tumour by **MRI** (Pourtau et al. [2013]). In another study Tsourkas and colleagues encapsulated gadolinium conjugated to PAMAM dendrimers into polymersomes of PEO-PBD mixed with the biodegradable PEO-PCL. Polymersomes accumulates into tumour by **EPR** effect and then partial degradation of polymersomes improves water flux trough the membrane. The increased hydration of gadolinium has a positive effect o its relaxation time increasing the signal-to-noise ratio, a common limitation ofencapsulated gadolinium. Because gadolinium was conjugated to PAMAM dendrimers its escape from polymersomes and signal dispersion was prevented (Cheng et al. [2009]). PEO-PBD NIR-polymersomes were imaged *in vivo* using optical imaging , allowing

precise localisation and measuring of the tumour size in 3D *in vivo* (Ghoroghchian et al. [2005]). The same formulation was further developed to target dendritic cells *in vivo* by conjugation with the Tat peptide. Dendritic cells were exposed to the polymersomes and then injected in mouse and tracked with an optical imaging set up ( eXplore Optix MX2 system) (Christian et al. [2009b]). Another possibility was explored by Battaglia and co-workers by labelling PMPC-PDPA and PEO-PDPA polymersomes with rhodamine, a fluorescent dye that was later tracked *in vivo* with a macroimaging system (Murdoch et al. [2010]).

Polymersomes have also been used in theranostic systems. In this field of research a drug and an imaging reporter are co-encapsulated. For example, PTMC-PGA polymersomes loaded with both the drug doxorubicin and maghemite  $\gamma$ - $\text{Fe}_2\text{O}_3$  which provides contrast for magnetic resonance. The magnetic properties were also used to *drive* the polymersomes to the tumour site using an external magnetic field (Sanson et al. [2011]). The anticancer drug paclitaxel and MRI contrast agent super paramagnetic iron nanoparticles have been co-encapsulated into polymersomes to simultaneously deliver the anticancer drug and visualise the tumour response *in vivo* (Muthiah et al. [2013]).

## 1.5 Aims

Polymersomes are nano-sized carriers successfully developed for *in vitro* and *in vivo* applications, including low resolution optical imaging *in vivo*. However, information on pathological disease at the sub-tissue level requires higher spatial resolution. This can be achieved using confocal microscopy. Because of poor tissue penetration of light, confocal microscopy *in vivo* is not possible at depths greater than a few micrometers. To overcome this limitation, it is possible to use a surgical procedure known as **Window Chamber (WC)**, in which part of the tissues obstructing the light pathway are replaced with optically transparent glass.

An interesting application of high resolution optical imaging *in vivo* is in tumour microvasculature imaging. Tumour microvasculature development (tumour angiogenesis) is a key step in tumour and metastasis progression. Imaging of the vasculature at high resolution using polymersomes can provide useful insight into the mechanisms governing the diffusion the nanoparticles in the tumour environment, which in turn could be used to increase the fundamental body of knowledge required to design formulations specifically targeted to the tumour microenvironment or specific cell types present.

The aim of this work is to investigate the use of polymersomes in *in vivo* optical imaging coupled with a **WC** set up. To do so, it will be necessary to

develop a number of screening techniques to test polymersome interactions with cells *in vitro*, and analyse their distribution *in vivo* in the tumour microenvironment. During the *in vivo* screening, efforts will be made to improve the analysis throughput.

Specifically, the *in vitro* development will include quantification of uptake of two different rhodamine labelled polymersome formulations (poly(oligo(ethylene glycol) methacrylate)-poly(2-(diisopropylamino)ethyl methacrylate) (POEGMA-PDPA) and PMPC-PDPA) by three cell types representative of the tumour microenvironment: tumour cells Mouse Fibrosarcoma Cell (MFC), endothelial cells Small Vessel Endothelial Cells (SVECs) and pericytes *in vitro* precursor 10T1/2. The quantification will be conducted both in cells growing in static conditions and in cells growing under flow. Polymersome uptake in flow will be assessed using a specifically developed flow bio-incubator.

*In vivo* applications will focus on the analysis of distribution of polymersomes in the vasculature via image analysis. The analysis aims to highlight the differences between the two polymersome formulations PMPC-PDPA and POEGMA-PDPA in terms of circulation half life and tumour accumulation. These are useful parameters in the rationale design of polymersomes for imaging and therapeutic applications in cancer research.

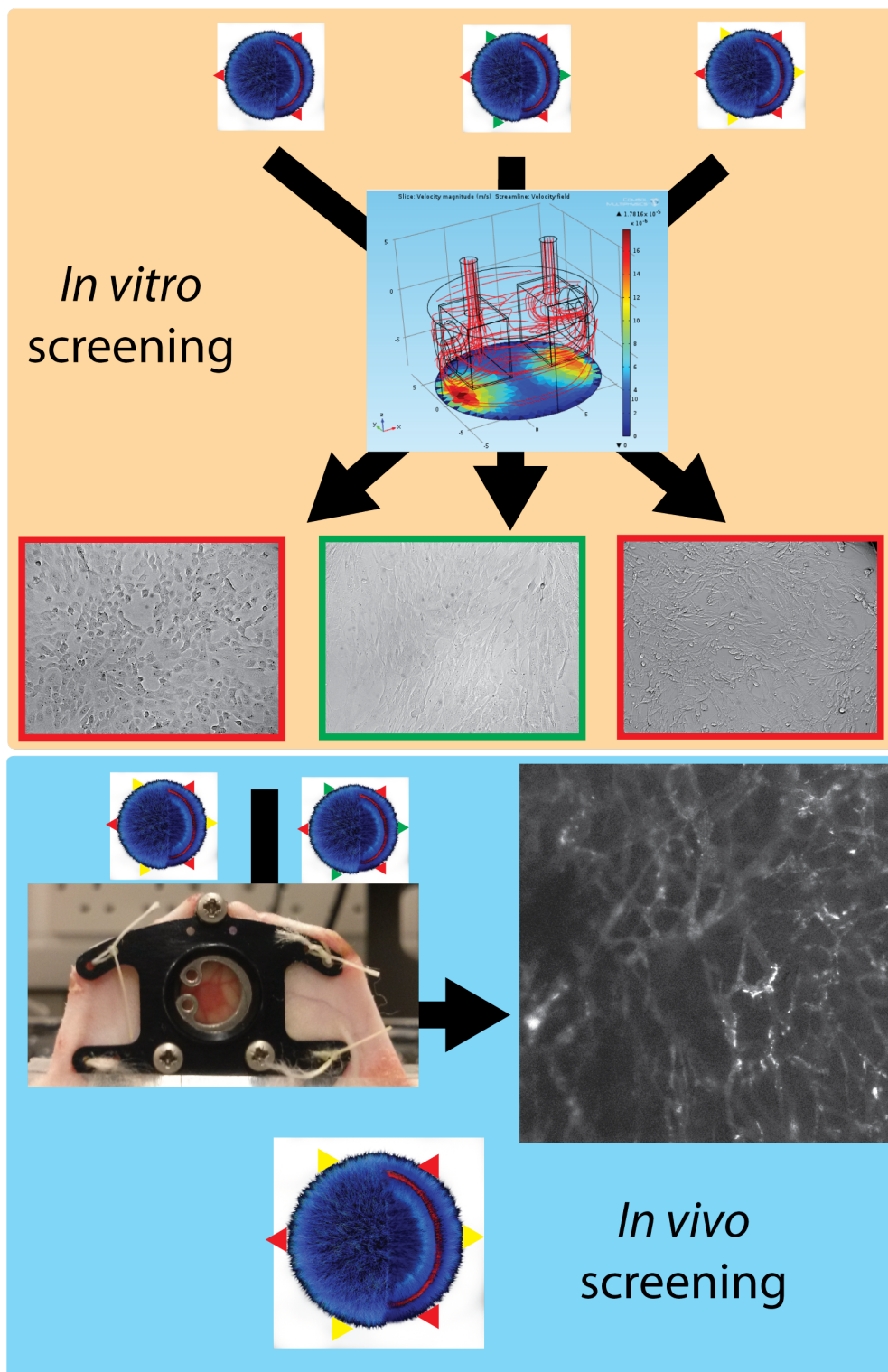


Figure 1.10: *Aim of the work. Different polymersome formulations will be screened in vitro for uptake by different cell lines (10T1/2, MFC188, SVECs. In vitro screening will be performed under flow conditions. Following the in vitro screening, formulations will be tested in vivo using Dorsal Skinfold Chamber (DSC).*

## 2.1 Polymersomes

### 2.1.1 Copolymers synthesis

All co-polymers were synthesized by Prof. Steve Armes' group, Chemistry Department, University of Sheffield, UK.

#### PMPC<sub>25</sub>-PDPA<sub>70</sub> Copolymer synthesis

PMPC-PDPA copolymer was synthesized by [Atom Transfer Radical Polymerisation \(ATRP\)](#) as previously reported ([Du et al. \[2005\]](#)). ATRP is a polymerisation technique characterised by synthesis of copolymers with low polydispersity.

Briefly, [2-methacryloxyethyl-phosphorylcholine \(MPC\)](#) (1.32g, 4.46mmol) and CuBr (25.6mg, 0.178mmol) were added with 2ml of a deoxygenated (30min with bubbling N<sub>2</sub>) methanol solution of [bpy](#) (55.8mg, 0.358mmol) and ME-Br (50.0mg, 0.178mmol). The reaction was conducted for 65min at 20°C in N<sub>2</sub> saturated environment. A 3ml solution of [2-\(diisopropylamino\)ethyl methacrylate \(DPA\)](#) (2.67g, 12.5mmol) was injected into the flask and allowed to react for 48h. The final reaction mixture was diluted with 200ml isopropanol and purified from the catalyst using a silica column.

#### Rhodamine-PMPC<sub>25</sub>-PDPA<sub>70</sub> Copolymer synthesis

Rhodamine labelled (Rhd)-PMPC-PDPA copolymer was synthesized by [ATRP](#) as previously reported ([Madsen \[2009\]](#)). Briefly, [MPC](#) (1.20 g, 4.05mmol) was solubilised in 0.75ml of anhydrous methanol inside a round bottom flask. An in-house prepared rhodamine 6G-based initiator (83.8mg, 0.135mmol) was added to the solution and the flask was washed with 0.75ml anhydrous methanol. [bpy](#)

(42.17mg, 0.171mmol) and CuBr (19.37mg, 0.135mmol) were added to the reaction after degassing with N<sub>2</sub> for 30min. The reaction was conducted for 40min at 20°C in N<sub>2</sub> saturated environment. DPA (1.73g, 8.10mmol) dissolved in deoxygenated methanol (2ml) was injected into the flask. After 48h, the reaction solution was diluted by addition of methanol (about 70ml) and opened to the flask. The reaction considered complete when turned green. It was then added of chloroform (200ml) and purified from the catalyst using a silica column. *bpy* was removed by 3days dialysis against a solution 3:1 chloroform:methanol. The solution was changed daily. After dialysis, the product of the reaction was desiccated, dispersed in water, freeze-dried. Traces of organic solvents were removed by desiccation in a vacuum oven at 80°C for 48h.

### PEO<sub>113</sub>-PDPA<sub>70</sub>

PEO<sub>113</sub> conjugated with the polymerisation macro-initiator Br was dissolved in methanol degassed with N<sub>2</sub> for 30min. *bpy* and DPA were added to the solution and the mixture was heated to 50°C before adding the catalyst CuCl. After 16h an aliquot was analysed by <sup>1</sup>H-NMR and the reaction was considered concluded when less than 0.1% of monomer was detected. The reaction was stopped by exposing it to air. The reaction mixture was then dissolved in Tetrahydrofuran (THF) and purified from the catalyst using a silica column. The product was then purified from unreacted *bpy* by dialysis against water for 7days followed by dialysis against methanol for 2days. After purification, the product of the reaction was desiccated and characterised by <sup>1</sup>H-NMR.

## 2.1.2 Polymersomes synthesis

Polymersomes formulations were prepared by *pH switch* or *film hydration*. Both methods can be used to obtain polymersomes, however they differ in preparation time and condition. pH switch is faster, as it can produce milliliters of samples in few hours, while film hydration requires at two weeks of constant stirring. However, because of the faster kinetic pH switch method is characterised by a lower polymersomes yield as micelles formation is favoured. Furthermore, pH switch method requires solubilisation of co-polymers at pH=2, which is not compatible with protein stability and could compromise chemical the binding between co-polymers and functionalising moieties, such as biotin. For this reason the pH switch method was employed in routine preparation of rhodamine labelled formulations, while *film hydration* was choose in the preparation of biotin labelled polymersomes to prevent hydrolysis of the biotin/co-polymer link. The composition of all the polymersomes formulations used is reported in table 8.9.

## Film hydration

Co-polymers were dissolved in chloroform:methanol (2:1 solution) in a sterile glass vial at the concentration of  $2\text{mg/ml}$ . The organic solvent was evaporated under vacuum in a desiccator for at least  $24\text{h}$  in order to obtain a thin film of co-polymer on the vial wall. The co-polymer film was rehydrated with  $2\text{ml}$  of Phosphate Buffer Saline pH 7.4 (PBS<sub>7.4</sub>) and the vial was left under constant magnetic stirring for 2 weeks.

## pH switch

$20\text{mg}$  of co-polymers were dissolved in a  $7\text{ml}$  bijoux with  $2\text{ml}$  of Phosphate Buffer Saline (PBS) acidified to  $\text{pH}=2$  with Hydrochloric Acid (HCl)  $1\text{N}$ . The solution was filtered into a new  $7\text{ml}$  plastic bijoux through a  $220\mu\text{m}$  filter. The solution was kept under constant agitation using a magnetic stirrer and a pH meter was used to continuously monitor the pH.  $220\mu\text{m}$  filtered Sodium Hydroxide (NaOH)  $0.5\text{N}$  was added to the solution through a programmable pump to ensure slow and constant delivery ( $18\mu\text{l}/\text{min}$ ). The pump was stopped at  $\text{pH}=7.4$ . All steps were performed at room temperature. Sterile polymersomes were prepared inside a class II cabinet.

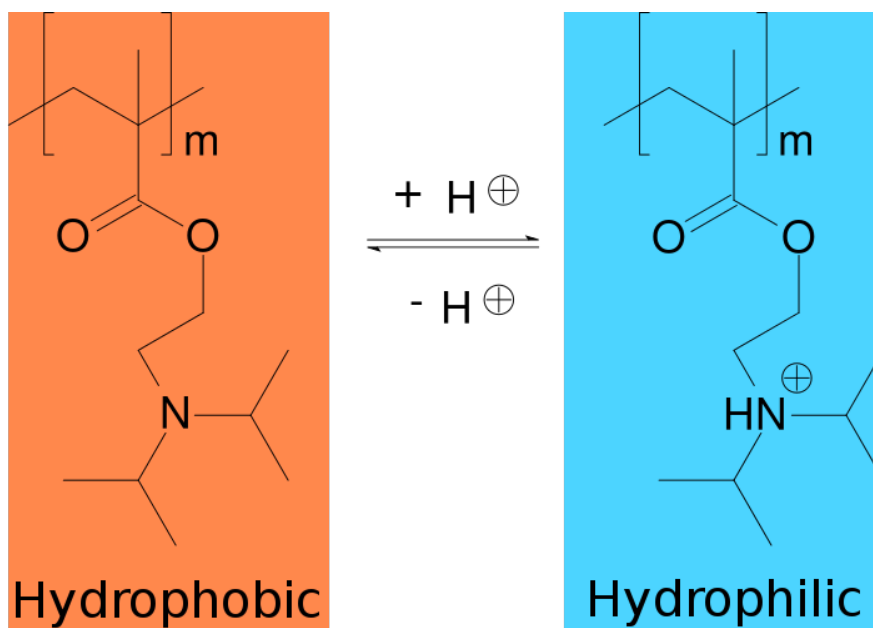


Figure 2.1: *PDPA pH sensitivity. At  $\text{pH} < \text{pK}_a$  the tertiary amino group is protonated. The polymer is charged and hydrophilic. At  $\text{pH} > \text{pK}_a$  the aminogroups are deprotonated: the polymer becomes hydrophobic.*

### 2.1.3 Polymersomes purification

Polymersomes were purified by [Gel Permeation Chromatography \(GPC\)](#) using 4B Sepharose resin.  $500\mu L$  of samples were loaded to the head of a  $15cm$  column. Samples were collected in fractions and fractions were characterised by [Dynamic Light Scattering \(DLS\)](#). Fractions containing polymersomes of  $100-200nm$  were joined together. Samples were then concentrated by centrifugation.  $1ml$  was transferred into a  $2.0ml$  eppendorf and centrifuged for  $20min$  at  $2000rcf$  for  $20min$ . The supernatant was transferred to a new  $2.0ml$  eppendorf and centrifuged at  $20000rcf$  for  $20min$ . The supernatant was then discarded and  $500\mu l$  of sterile [PBS<sub>7.4</sub>](#) was used to re-suspend the pellet.

The suspension was sonicated for  $20min$  to ensure complete re-suspension of the polymersomes. Polymersomes concentration was measured by fluorometer or [Reverse Phase-High Pressure Liquid Chromatography \(RP-HPLC\)](#) for functionalised polymersomes and the final concentration was adjusted to  $10mg/ml$  with sterile [PBS<sub>7.4</sub>](#)

### 2.1.4 Polymersomes characterisation

#### Dynamic Light Scattering (DLS)

Size distribution was determined by [DLS](#) analysis. Small particles in solution scatters light in all directions. The scattered light at a specific angle can be measured and its fluctuations correlated with time. The intensity of scattered light fluctuates because particles undergo Brownian motion, and smaller particles have higher diffusion coefficients compared to big particles, according to the Stokes-Einstein equation:

$$D = \frac{k_b T}{6 \pi \eta R}$$

where  $k_b$  is the Boltzmann's constant,  $T$  is the temperature,  $\eta$  is the viscosity and  $R$  is the radius of the particle.

[DLS](#) analysis assumes that particles are spherical. The [DLS](#) used was equipped with a He-Ne laser  $633nm$  and was measuring scattered light at an angle of  $173^\circ$ . Briefly, a small aliquot ( $\simeq 50\mu l$ ) of polymersome was diluted 1:20 with  $220\mu m$  filtered [PBS<sub>7.4</sub>](#), placed into a clean small volume plastic vial and analysed using a Malvern Zetasizer Nano set to  $20^\circ C$ , [PBS](#) dispersant and latex beads as particle type. Results are expressed as intensity number against size distribution (fig. [2.2](#)).

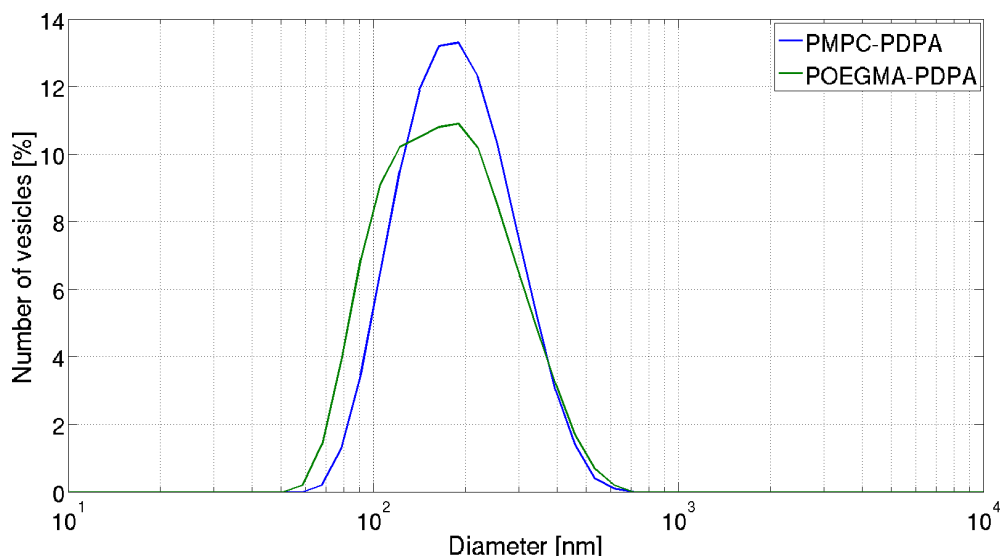


Figure 2.2: Typical *DLS* results for *PMPC-PDPA* and *POEGMA-PDPA* synthesised by pH switch. Both formulations have average hydrodynamic diameter of  $\simeq 150\text{nm}$ .

### Transmission Electron Microscopy (TEM)

Size distribution and morphology of polymersomes were characterised by *TEM*. *TEM* is a microscopy technique in which a beam of electron is focused through a thin specimen. In order to achieve optical contrast it is necessary to have electron-dense specimens. In our experiments contrast is achieved with *Phosphotungstic acid (PTA)* positive staining. *PTA* stains the ester bonds present in *PDPA* and *PMPC* polymersomes membrane (*Gedde [1996]*). Polymersomes suspension were diluted to  $0.5\text{mg/ml}$  with  $220\mu\text{m}$  filtered *PBS<sub>7.4</sub>*. 400 meshed copper carbon coated grids were charged using a glow charger to allow hydrophilic polymersomes to attach to the grid.  $5\mu\text{l}$  of polymersomes were allowed to settle on the grid for  $1\text{min}$  and the excess of liquid was removed using filter paper.  $5\mu\text{l}$  of  $0.75\%w/v$  *PTA* were added to the grid and allowed to stain for  $5\text{s}$ . Excess of liquid was removed using filter paper and compressed air. Grids were imaged using a *FEI Tecnica Spirit* microscope with maximal working voltage of  $120\text{KV}$  and equipped with *Gatan1K MS600CW* CCD camera (fig. 2.3).

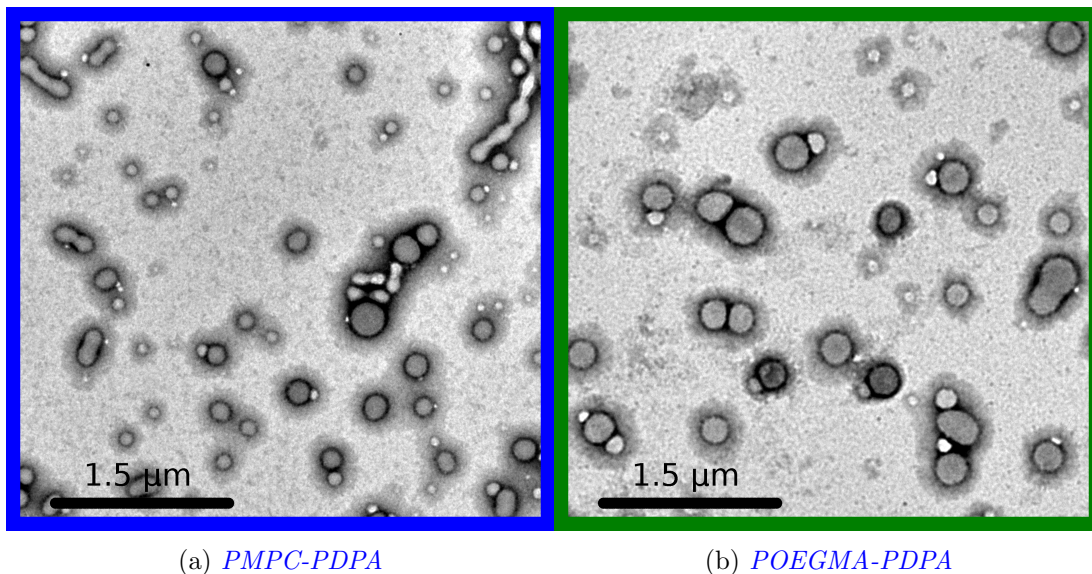


Figure 2.3: Typical *TEM* results for *PMPC-PDPA* and *POEGMA-PDPA* synthesised by pH switch. *Polymersomes* are visible as rounded features of  $\simeq 150\text{nm}$  of diameter.

### 2.1.5 Polymersomes concentration

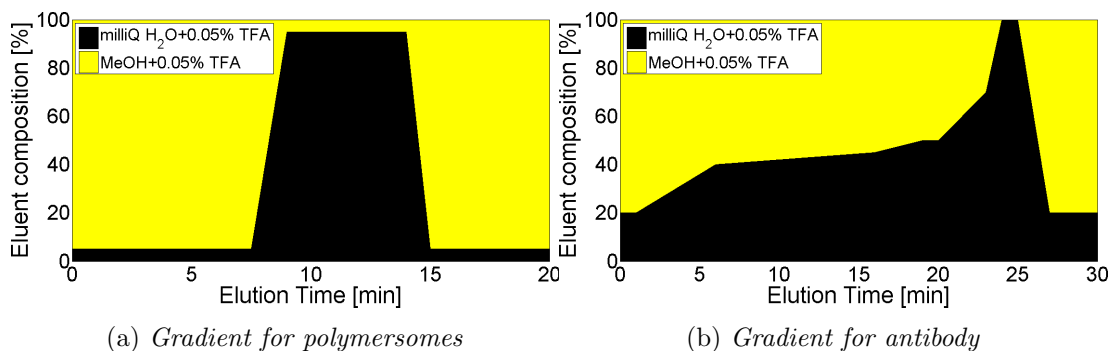
#### Fluorometer

Rhodamine labelled polymersomes were prepared including in the formulation 10% w/w of rhodamine labelled copolymer prepared as described in section 2.1.1. The concentration of the rhodamine labelled copolymer was quantified using a fluorometer equipped with a 96 well plate reader. An aliquot ( $\simeq 20\mu\text{l}$ ) of polymersomes were diluted 20 times with Phosphate Buffer Saline pH 2 ( $\text{PBS}_2$ ). The solution was transferred to a 96 well plate and the concentration of rhodamine labelled copolymer was determined against a calibration curve. Because the polymersomes were prepared starting with 10% molar ratio of rhodamine labelled copolymer the final concentration of polymersomes was calculated by multiplying the fluorometer result by 10.

#### RP-HPLC

In this work a C18, 150X4.60mm, 5μm, 300Å column was used. The flow ratio was always 1ml/min, the eluents milliQ water and methanol, both acidified with 0.05% of Trifluoroacetic Acid (TFA). The different gradients used are reported in table 2.1 and figure 2.4. An aliquot of 100μl of sample was placed into a RP-HPLC vial and acidified with 2μl of TFA. 80μl of sample were injected and the concentration was determined against a calibration curve.

Gradient	Analyte	Wavelength [nm]	Retention time [min]
POLY	Rhodamine labelled copolymers	UV 220 EX/EM 540/565	11.3
AB	Rhodamine labelled copolymers	UV 220 EX/EM 540/565	7.8
	Antibody	UV 280 EX/EM 270/300	28.0

Table 2.1: *RP-HPLC settings used.*Figure 2.4: *Gradients used in RP-HPLC analysis. a) Gradient POLY, b) gradient AB. Eluent A was milliQ water acidified with 0.05% of TFA, eluent B was methanol acidified with 0.05% of TFA.*

## 2.1.6 Polymersomes functionalisation

### Biotin/streptavidin

Biotinylated polymersomes were prepared by film hydration. Composition is available in table 8.9. Polymersomes were then added with streptavidin (1:1 molar ratio with biotinylated copolymer) and kept stirring for 2h at room temperature. Reaction mixture was purified by GPC. The purified reaction was added with biotinylated antibody to Platelet Derived Growth Factor Receptor- $\beta$  (PDGFR- $\beta$ ) or biotin-TexasRed (1:2 molar ration with streptavidin). The reaction was left stirring for 2h at room temperature. Reaction mixture was purified by GPC and the product was characterised by DLS, TEM and RP-HPLC.

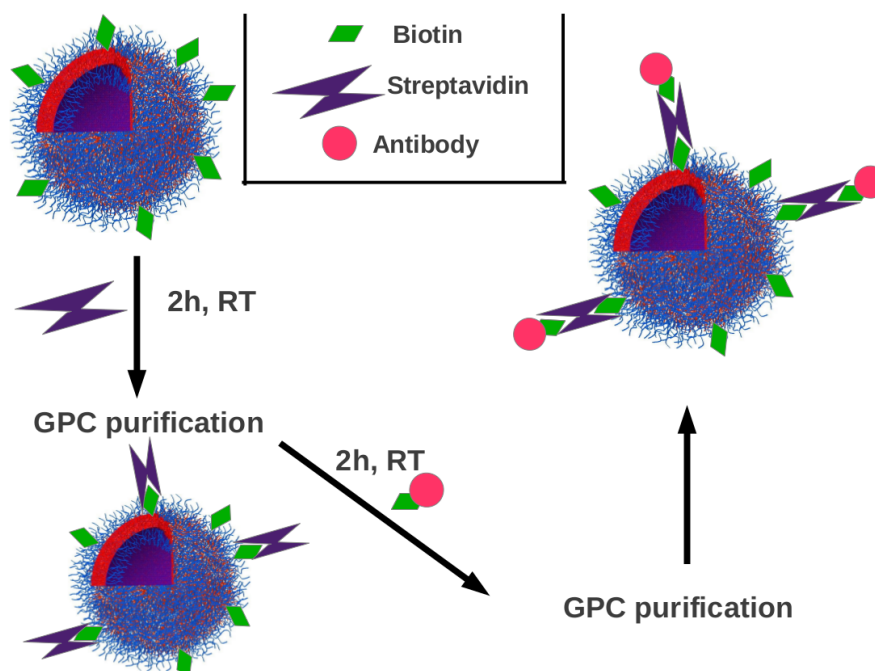


Figure 2.5: *Biotin Streptavidin functionalisation.* Biotinylated polymersomes were added of streptavidin. The excess of streptavidin was removed by GPC. Biotinylated antibody was added. The excess of antibody was removed by GPC.

### Maleimide reaction

The reaction was carried out to functionalise polymersomes with [Immunoglobulin of the class G \(IgG\)](#), acting as a model for targeting antibody. A generic rabbit IgG was used instead of a specific antibody to contain costs during the optimisation of the reaction. Composition is available in table 8.9. All liquid reagents were purged with bubbling  $N_2$  for 15min for every millilitre of solution. Weighted copolymers were dissolved in  $PBS_2$  to a final concentration of 10mg/ml. pH was slowly increased to 7.4 as previously described (2.1.2), but in this case the reaction mixture was kept under bubbling  $N_2$  to avoid maleimide inactivation by atmospheric oxygen. IgGs were added 1:2 molar ratio with PMPC-PDPA-Mal and the reaction was performed 2h room temperature. Excess of IgG was removed by GPC. Reaction mixture was purified by GPC and the product was characterised by DLS, TEM and RP-HPLC.

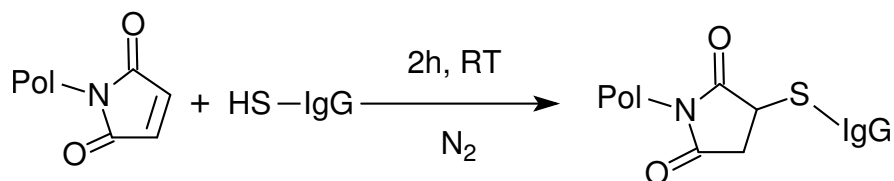


Figure 2.6: *Maleimide reaction.* Maleimide reacts with thiol groups in IgG.

## 2.2 Tissue culture

### 2.2.1 Routine subculture of Murine Fibrosarcoma cells

MFC cells expressing single iso-form of VEGF were kindly provided by Prof. Tozer Group, Oncology Department, University of Sheffield. The development of the cell lines is described elsewhere (Shima et al. [1996], Greco and Dachs [2005]). Briefly, primary fibroblast were isolated from 13.5 days post-coitum Swiss mouse embryo. The cultured fibroblast cultures were genotyped for VEGF-A isoform expression. Finally, retrovirus SV40 was used as vector to immortalise the fibroblasts and oncogenically transform them via H-Ras activation. MFC were maintained in Dulbecco's Modified Eagle's Medium (DMEM) supplemented with 10% Fetal calf serum (FCS), G-418 600 $\mu$ g/ml and puromycin 2 $\mu$ g/ml. Sub-confluent cells were washed with 10ml PBS, treated with 5ml trypsin and incubated 5min 5% CO<sub>2</sub> at 37°C. Detached cells were counted using a Neubauer improved hemocytometer and subdivided into cell culture flasks and 10ml of fresh media was added. Cells were sub-cultured every 3-4 days at a ratio of 1:15

### 2.2.2 Routine subculture of SVECs

SVECs were maintained in DMEM supplemented with 10% FCS, 1% penicillin/streptomycin and 1% fungizone. Sub-confluent cells were washed with 10ml PBS, treated with 5ml trypsin for 5min and centrifuged. The pellet was resuspended in DMEM and incubated 5min 5% CO<sub>2</sub> at 37°C. Detached cells were counted using a Neubauer improved hemocytometer and subdivided into cell culture flasks and 10ml of fresh media was added. Cells were sub-cultured every 3-4 days at a ratio of 1:10

### 2.2.3 Routine subculture of C3H/10T1/2

C3H/10T1/2 were purchased from American Type Culture Collection (ATCC). Cells were maintained in Basal medium eagle (BME) supplemented with 10% FCS, G-418 600 $\mu$ g/ml and puromycin 2 $\mu$ g/ml. Sub-confluent (below 70% confluency) were washed with 10ml PBS, treated with 5ml trypsin and incubated 5min 5% CO<sub>2</sub> at 37°C. Detached cells were counted using a Neubauer improved hemocytometer and subdivided into cell culture flasks and 10ml of fresh media was added. Cells were sub-cultured every 3-4 days at a ratio of 1:10.

## 2.2.4 Differentiation of 10T1/2

10T1/2 differentiation into pericytes was stimulated using **TGF- $\beta$ 1**. In this work the effect of different concentration and time exposure to **TGF- $\beta$ 1** was assessed. In every experiment the desired concentration of **TGF- $\beta$ 1** was obtained by diluting the stock solution (R&D system) in fresh 10T1/2 media, and then incubating the cells with the **TGF- $\beta$ 1** enriched media for the 24h, 48h or 72h at 37°C, 5% CO<sub>2</sub>. The effect of conditioned media was assessed as well. In these studies 10T1/2 were incubated with media obtained from a flask of **MFC188** or **SVECs** cultured for 72h. **TGF- $\beta$ 1** was diluted into the conditioned media before incubation with 10T1/2 cells.

## 2.2.5 Fibronectin coating

Fibronectin coating of wells was used to assess the effect of different growing substrates in 10T1/2 differentiation and in flow studies to guarantee adhesion of cells under flow. Wells were coated with 5 $\mu$ g/cm<sup>2</sup> of fibronectin dissolved in **PBS<sub>7.4</sub>**. 200 $\mu$ l of fibronectin solution were deposited in a well (24 well plate) and allow to dry at room temperature for 60min. Coated plates were stored at 4°C until use and for no longer than 72h. Wells were rinsed with media before cell seeding.

## 2.3 Pericyte markers expression quantification

### 2.3.1 Immunocytochemistry (ICC)

10T1/2, **MFC188** or **SVECs** were seeded at 5000cell/well in dark 96 well plate and incubated 24h at 37°C,5% CO<sub>2</sub>. **TGF- $\beta$ 1** was added to 10T1/2 by replacing the growth media with fresh media added with the desired concentration of **TGF- $\beta$ 1**. Cells were placed back in the incubator for the desired exposure time.

Conditioned media was obtained from sub-confluent T75 flasks of **MFC188** or **SVECs** cultured for 96h.

At the end of the experiment cells were washed 3 times with **PBS<sub>7.4</sub>** and fixed with 3.6% formaldehyde for 10min. Cells were washed 3 times for 5min with **PBS<sub>7.4</sub>**. To assess  **$\alpha$ -Smooth Muscle Actin ( $\alpha$ -SMA)** expression cells were permeabilised with 0.1% triton X-100 for 10min and then washed with **PBS<sub>7.4</sub>** for 5min This step facilitate the penetration of the primary and secondary antibody inside the cell, where  **$\alpha$ -SMA** is located. Non specific reactions between primary antibody and cells component other than  **$\alpha$ -SMA** were prevented by incubating cells at room temperature for 1h with blocking solution (5% **Bovine serum albu-**

mine (BSA) in PBS<sub>7.4</sub>). Primary antibody was dissolved in blocking solution and incubated with cells overnight at 4°C. Cells were washed 3 times for 5min with PBS<sub>7.4</sub>. Secondary antibody was diluted in blocking solution and incubated with cells for 2h at room temperature. Cells were washed 3 times for 5min with PBS<sub>7.4</sub>. DAPI diluted 1:100 in PBS<sub>7.4</sub> was added to the cells and the plate was stored at 4 °C until imaged. A list of the primary and secondary antibodies used is given in table 8.4. Nerve Glial antigen 2 (NG2) and PDGFR- $\beta$  were detected using the same protocol, but without the permeabilisation step as they are located on the external cell surface, therefore there is no need to facilitate the penetration of the primary and secondary antibodies inside the cell.

### 2.3.2 Western blot

For Western Blot (WB) analysis cells were cultured in T75 flasks. Cells were washed carefully with PBS<sub>7.4</sub>, excess of liquid was removed and the proteins were extracted by lysis with 500 $\mu$ l of RIPA buffer for 10min at 4°C. The lysate was transferred to a 2.0ml eppendorf and aggregates were mechanically broken using a syringe equipped with a 30G needle by 10 cycle of aspiration/injection. The lysate was then centrifuged at 4°C for 20min at 10000g and the precipitate was discarded. Protein concentration in the samples was measured using the Bicinchoninic acid assay (BCA) assay, samples were stored in 50 $\mu$ l aliquot at -80°C for further analysis.

BCA is a colorimetric assay used to quantify the protein concentration. It is based on a two steps reaction. In the first step cupric acid is added to the sample, and Cu<sup>2+</sup> is reduced to Cu<sup>+</sup> at a rate proportional to the protein concentration. In the second step each newly formed Cu<sup>+</sup> ion chelate with with two molecules of bicinchoninic acid. The product of the reaction can be detected by quantifying its optical density at 562nm.

In this work, the BCA assay was used to normalise the loading of all the samples analysed in western blot experiments. Cell lysate were added with the BCA reagents as indicated by the kit supplier for a 96 well plate assay. Samples were incubated 40min at 37°C and optical density was measured at 562nm. Protein concentration was calculated from a calibration curve obtained with a BSA standard.

**Samples preparation** Protein loading was normalised by total protein concentration and loading volume. 20 $\mu$ g of total proteins were loaded in a volume of 40 $\mu$ l. The volume of diluent (RIPA buffer) was calculated as  $V_X = 26 - V_S$  where  $V_S$  is the volume of stock sample containing 20 $\mu$ g of proteins and  $V_X$  is the volume

of RIPA buffer to add. All volumes in  $\mu\text{l}$ . The solution obtained was added of  $4\mu\text{l}$  of sample reducing buffer 10X and  $10\mu\text{l}$  of sample buffer 4X. Samples were then denatured at  $95^\circ\text{C}$  for  $5\text{min}$  and  $35\mu\text{l}$ , and  $30\mu\text{l}$  were loaded into the gel. One channel was reserved for molecular weight ladder.

**Western blot gel preparation** The composition of all gels and buffers is reported in table 8.8. Running gel was poured into a  $0.75\text{mm}$  9 lines template, the template was filled with 2-butanol and the gel was allowed to settle at room temperature for  $60\text{min}$ . Excess of 2-butanol was removed and the stacking gel was added on top of the running gel. The system was closed with a template to allow the formation of 9 loading channels. Stacking gel was allowed to settle for  $60\text{min}$  at room temperature. The gel was then placed into the running support and loaded into the running tank filled with running buffer.

**Western blot run** Samples were run for  $15\text{-}20\text{min}$  at  $100\text{V}$  to allow uniform sample loading at the top of the running gel. Once samples entered the running gel, voltage was increased to  $180\text{V}$  and samples were run until the ladder corresponding to the molecular weight of the protein analysed run for about  $2/3$  of the high of the gel. This usually took  $120\text{min}$  for PDGFR- $\beta$  and  $150\text{min}$  for NG2. When the separation was over, the gel was placed into a semi-dry membrane transfer cassette to transfer the proteins from the gel to a Polyvinylidene fluoride (PVDF) membrane suitable for chemoluminescence staining. Transfer was performed at  $100\text{V}$  for  $60\text{min}$ .

**Membrane blotting** After transfer the membrane was blocked for  $1\text{h}$  at room temperature with blocking solution (5% non-fat milk in milliQ water). The primary antibody diluted 1:500 in blocking solution was left on the membrane over night at  $4^\circ\text{C}$ . After washing 5 times for  $4\text{min}$  with PBS<sub>7.4</sub> the secondary antibody diluted 1:10000 in blocking solution was added for  $1\text{h}$  at room temperature. The membrane was then washed 5 times for  $4\text{min}$  with PBS<sub>7.4</sub>. The Enhanced chemiluminescence (ECL) solution was added ( $1\text{ml}/\text{membrane}$ ) and allow to react for  $5\text{min}$  at room temperature. Excess of ECL was removed and the membrane was developed using photographic film.

**Membrane development** Photographic film development was carried out in a dark room. The PVDF membrane was placed into a development cassette. A photographic film was cut to size and placed on top of the PVDF membrane. Exposure time was optimise every time, but it was usually between  $30\text{sec}$  and  $5\text{min}$ . The photographic film was then placed for a few seconds in developing

solution, washed with tap water and the development was then fixed with fixing solution for  $\simeq 30\text{sec}$ . The film was washed with tap water and dried at room temperature. The film was scanned and the digital image was used to quantify bands intensity using the *Gel Analyser Tool* available in ImageJ-64bit v1.47. Results are expressed as ratio of band intensity between the sample and the control (10T1/2 cells not treated with [TGF- \$\beta\$ 1](#)).

### 2.3.3 Quantitative size-based protein assay

Quantitative size-based protein assay was performed using a *Protein simple* equipment commercially known as *Simon*. This machine automates the process of protein separation and quantification aiming to remove user-dependant variables, to make the quantification faster compared to western blot and to reduce costs by reducing the volume of reagents required. This is achieved by a full automation of the process. The user is required to prepare the protein samples and to load them into the machine together with all the other required materials: running and stacking gels, primary and secondary antibodies. When the run starts, the machine automates the process of preparing the gels and to load the samples. Furthermore, reaction with primary and secondary antibody, gel imaging and quantification of protein is also automated by the machine. A schematic of the working principle of *Simon* is given in figure 2.7. Samples are prepared as described for traditional western blot (section 2.3.2), but only  $5\mu\text{l}$  are required for the final analysis. A 384 well plate is prepared by loading a maximum of 12 samples, separation matrix, primary and secondary antibodies and internal standard. The machine automatically loads running capillaries with the reagents and runs the samples according to the specified parameters. In this work samples were run at  $300\text{V}$  for  $46\text{min}$ , matrix was diluted  $80\% v/v$  with antibody diluent. All the other parameters are used as default. All reagents are provided by the equipment producer, except RIPA buffer and primary antibodies. Data were normalised with the internal standard and antibody signal peak was integrated using *Simon* dedicated software. Results were expressed as ratio of signal integration between the sample and the control (10T1/2 cells not treated with [TGF- \$\beta\$ 1](#)).

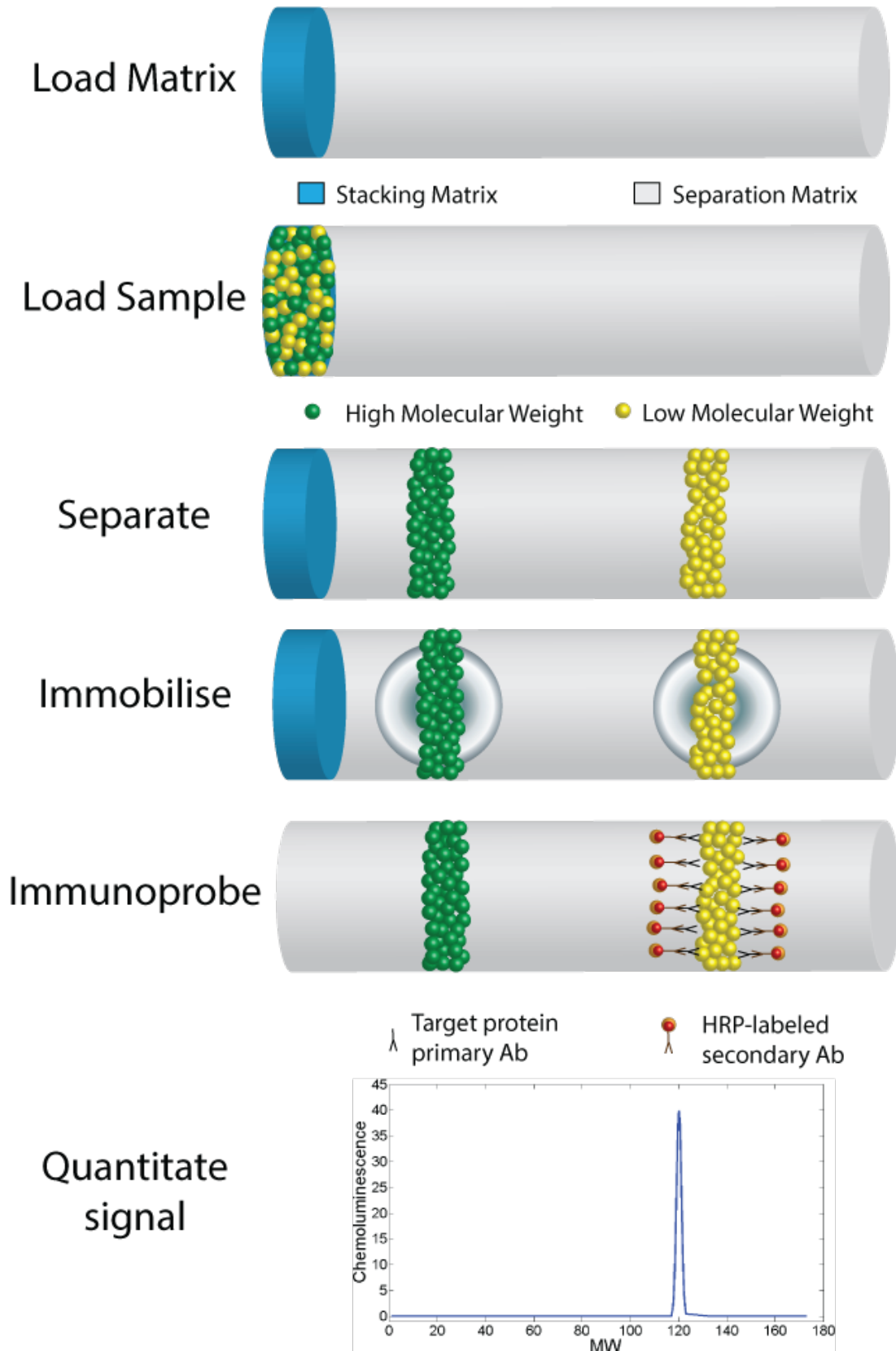


Figure 2.7: Automated western blot work-flow. Samples are loaded into a capillary containing a separation gel. Separation occurs because of proteins different molecular weights and charge as in traditional *WB* (a voltage is applied to the capillary). At the end of the run the proteins are cross-linked with UV and immunoprobed using a primary antibody and a HRP-labelled secondary antibody. Signal coming from the HRP probe is finally quantified.

## 2.4 Polymersomes *in vitro*

### 2.4.1 Static culture cells treatment

For a typical uptake study, MFC and SVECs cells were seeded on a 24 well plate at a density of  $50 \cdot 10^3$  cells density. 10T1/2 cells were seeded at  $25 \cdot 10^3$  cell/well and treated for 48h with 2ng/ml of TGF- $\beta$ 1 prior exposure to polymersomes. This different seeding density is required to avoid confluency of 10T1/2, which can inhibit further differentiation and proliferation (Reznikoff et al. [1973b], Reznikoff et al. [1973a]). 500 $\mu$ l of media containing 1mg/ml of polymersomes were then added, cells were incubated at 37°C and 5%CO<sub>2</sub> and uptake was quantified at defined time-points for up to 24h.

### 2.4.2 Cytotoxicity

Cytotoxicity was assessed by (3 - (4,5 - Dimethylthiazol - 2 - yl) - 2,5 - diphenyltetrazolium bromide (MTT) assay, a colorimetric method that exploits the ability of living cells to metabolize MTT into a purple formazan salt (see figure 2.8). MFC and SVECs cells were seeded on a 24 well plate at a density of  $50 \cdot 10^3$  cells density. 10T1/2 cells were seeded at  $25 \cdot 10^3$  cell/well and treated for 48h with 2ng/ml of TGF- $\beta$ 1. 1mg/ml polymersomes dispersed in cell media were incubated with cells at 37°C, 5% CO<sub>2</sub> for 24h cells were washed with 3 times with PBS<sub>7.4</sub>. 500 $\mu$ l of MTT 0.5mg/ml were added to each well in a 24 well plate. Cells were incubated 40min at 37°C and 5% CO<sub>2</sub>. MTT solution was removed and 300 $\mu$ l of isopropanol acidified with HCl (25 $\mu$ l of concentrated HCl for 20ml of isopropanol). This will solubilise the formazane salts. 150 $\mu$ l of the solution were transferred to a 96 wells plate and the optical density was measured at 540nm (referenced at 630nm). The optical density measure correlates linearly with the cell viability and results are expressed as percentage of viability with respect of a control (cells treated with PBS<sub>7.4</sub>, the polymersomes diluent). In *in flow* studies the 100% viability control was defined as the viability of the same cell line cultured *in static* conditions.

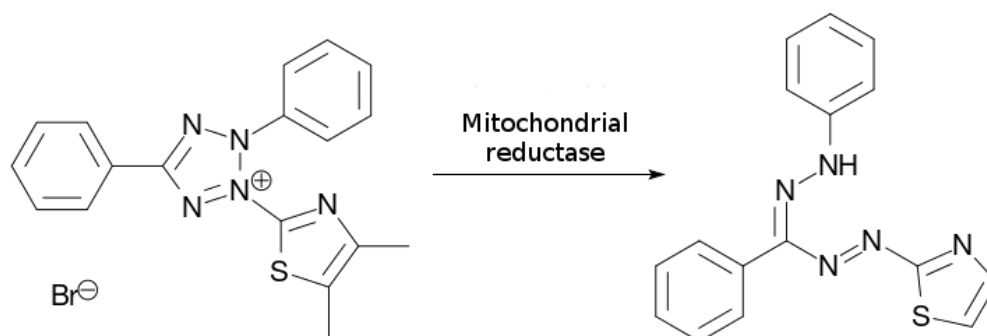


Figure 2.8: *MTT* reaction. Yellow water soluble *MTT* is converted by cell mitochondria in non water soluble purple formazane salts.

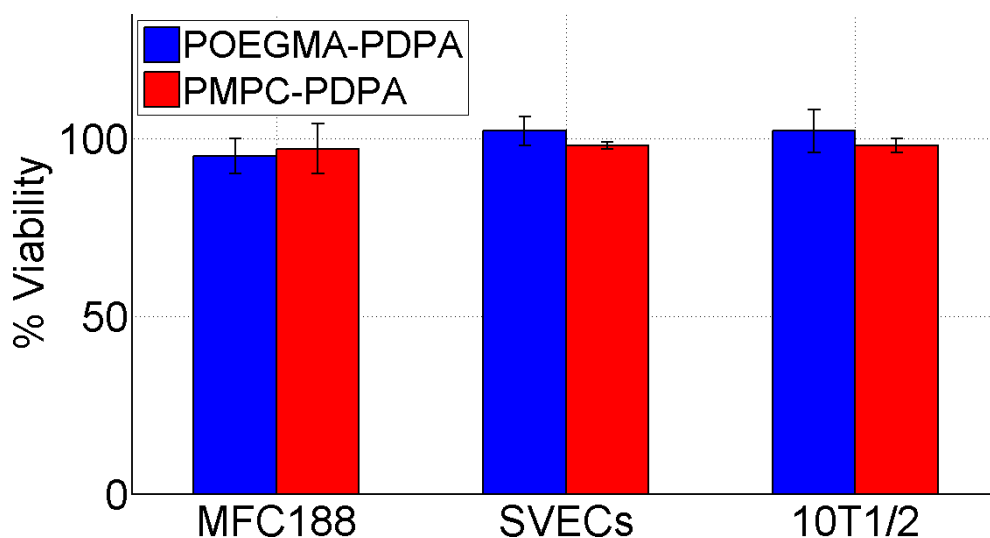


Figure 2.9: *MFC188*, *SVECs* and *10T1/2* viability after 24h exposure to 1mg/ml of polymersomes. Viability express as percentage with respect to the same cell type treated with an equal volume of only *PBS*.

### 2.4.3 FACS

Cells were detached using a *Trypsin/EDTA* (TE) cell scraper, transferred to a eppendorf tube and centrifuged at 1000*rcf* for 5*min*. From now on every step was performed keeping the cells at 4°C. The pellet was washed with 1ml of ice cold 220μm filtered *PBS*<sub>7.4</sub> and cells were centrifuged again. This step was repeated 3 times. The pellet was then re-suspended with 200μl of ice cold *PBS*<sub>7.4</sub> and analysed using a BD FACSArray equipment. Cells were gated for size and granularity and for fluorescence intensity using untreated cells as a negative control.

#### 2.4.4 RP-HPLC

RP-HPLC was used to quantify the amount of polymersomes internalised by cells. Because the polymersomes used were 10% rhodamine labelled it is possible to use this chromatography technique coupled with a fluorescent detector to accurately quantify the amount of copolymer present in the sample. To use this technique, it is essential to extract the internalised polymeric material from the cells and solubilise it in a solvent compatible with the RP-HPLC equipment used. This section presents the method optimised to extract the co-polymer from the cells and to quantify it by RP-HPLC. The RP-HPLC gradient used is reported in figure 2.11. After polymersomes treatment cells were washed 3 times with PBS<sub>7.4</sub> and excess of liquid was carefully removed. Cells were then left at -20°C for 24h. This step cause cell lysis because of the formation of water ice crystals. 200µl of PBS<sub>2</sub> were added to the well and using a 200µl tip as a scraper cells were mechanically broken and the suspension was transferred to a 2.0ml eppendorf. The liquid was centrifuged for 30s at 20000rpm. 150µl of supernatant were transferred into a RP-HPLC vial and 80µl were injected for quantification. RP-HPLC settings are reported in figure 2.11. The work-flow of the method is illustrated in figure 2.10. The recovery efficiency, critical to accurate quantification, was assessed to be > 95% with respect of maximal theoretical recovery when a known amount was incubated for 24h at 37°C with cell lysate (see fig. 2.12).

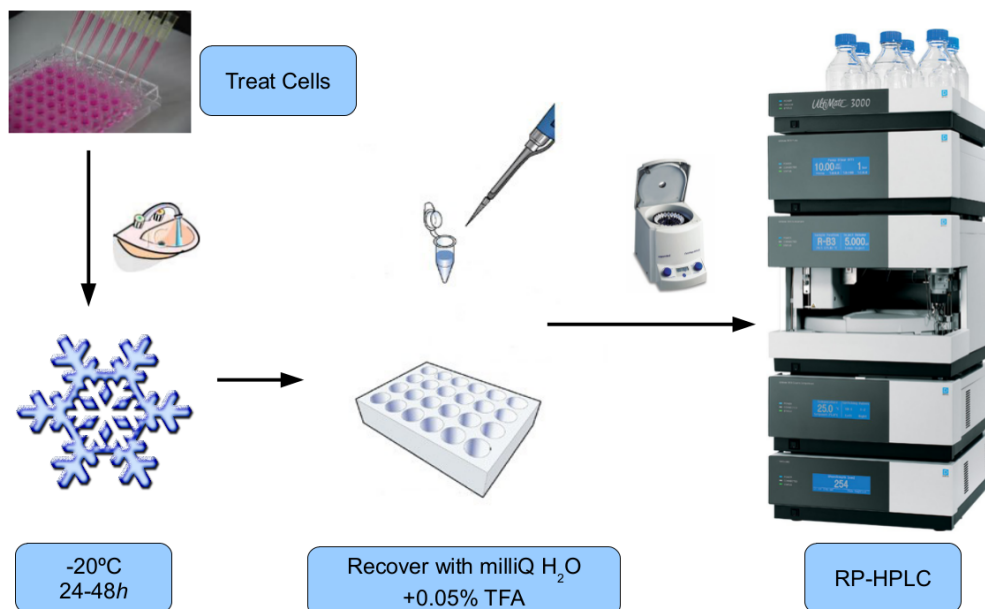


Figure 2.10: Work-flow of polymersomes extraction from cells for RP-HPLC analysis. Cells are lysate by incubation at -20°C for 48h. The co-polymer is recovered by solubilisation in PBS<sub>2</sub>.

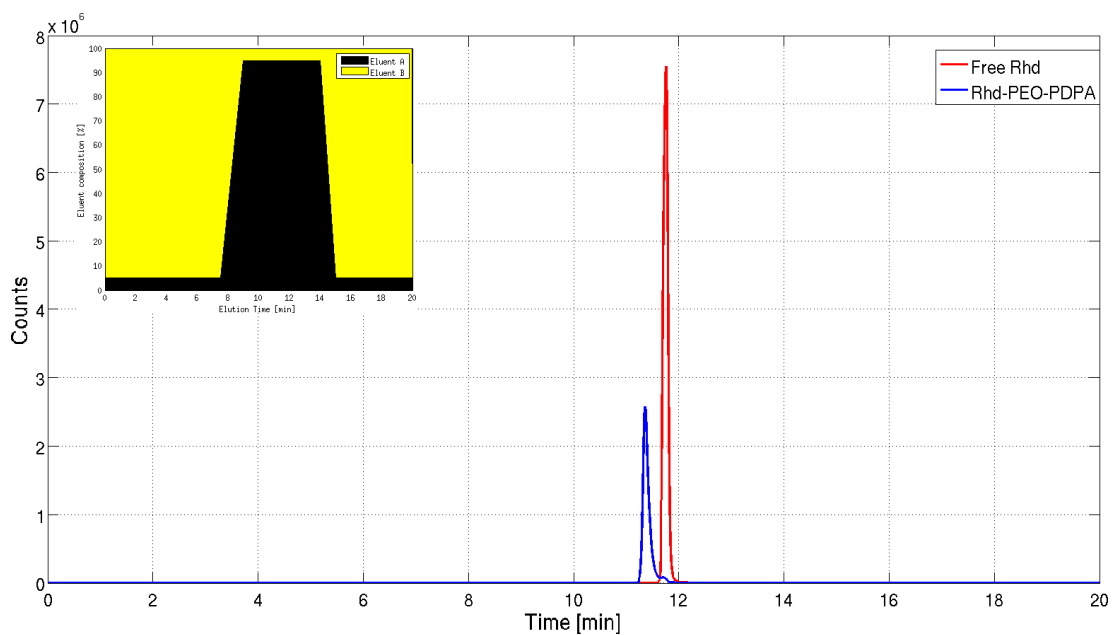


Figure 2.11: *RP-HPLC* gradient and chromatogram for rhodamine labelled polymersomes. The insert represents the gradient. Free rhodamine and rhodamine labelled co-polymer were resolved in sharp peaks.

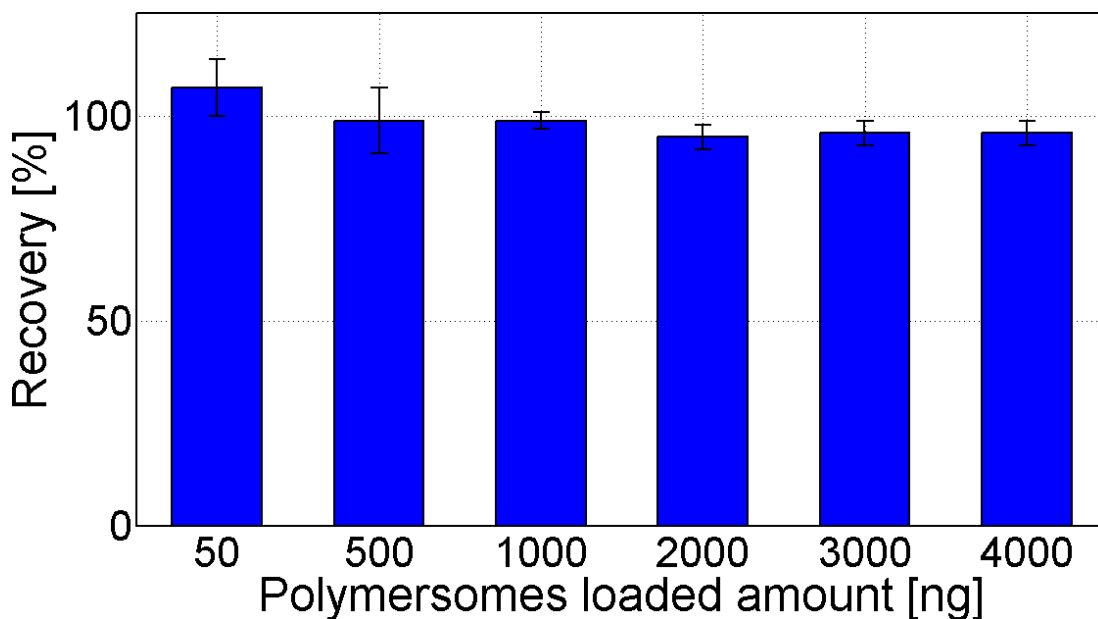


Figure 2.12: Recovery of RhdPMPC-PDPA from cells. Rhd-PMPC-PDPA was efficiently recovered (yield > 95%) from cells incubated with the co-polymer (treatment) compared to the theoretical 100% total recovery derived from the calibration curve.

## 2.5 In flow uptake studies

### 2.5.1 Flow modelling

The flow chamber was developed based on the geometry of a 24 well plate. The flow was delivered using a peristaltic pump Watson Marlow 205S connected to the well with a marprene tube, 0.8mm bore. The rotation speed of the rotor of the pump can be tuned to obtain different flow rates. The rotation speed and flow rate were calibrated by collecting different volumes of liquid from the outlet at different time points. The flow inside the chamber was simulated using a finite element approach and COMSOL Multiphysics, [Computational fluid dynamic \(CFD\)](#) module. Different design parameters such as depth of inlet and outlet and the use of a shield to protect cells from direct perpendicular flow were tested *in silico* using such approach. General simulation settings are reported in table 2.2.

General boundary condition	No slip, $u = 0$
Density $\rho$	$1000kg * m^{-3}$
Pressure $p$	$101325Pa$
Temperature $T$	$310.15K$
	Laminar flow
Inlet conditions	$L_{entr} = 0m$ $L_{entr} \nabla_t \cdot [-p_{entr}I + u(\nabla_t u + (\nabla_t u)^T)], \nabla_t \cdot u = 0$ Laminar flow
Outlet conditions	$L_{exit} = 0m$ $L_{exit} \nabla_t \cdot [-p_{exit}I + u(\nabla_t u + (\nabla_t u)^T)], \nabla_t \cdot u = 0$
Initial flow	Flow inlet=Flow outlet, $2 \cdot 10^{-8}m^3 * s^{-1}$
Fluid	Newtonian fluid, non compressible

Table 2.2: *In silico* parameters.

COMSOL shear rate  $\phi$  output was converted to shear stress  $\tau$  assuming the media as a newtonian fluid:  $\tau = \mu \cdot \phi$ . The shear stress and velocity magnitude were analysed at the level of cellular growth (bottom of the well).

### 2.5.2 Device sterilisation and preparation

The well plate was replaced with a new one for every experiment. The outer part of the tubing and the lid were routinely sterilised using azo-wipe. The inside of the tubing and the lid were sterilised by submersion in 70% [Industrial Methylated Spirit \(IMS\)](#) over-night, followed by 2h of slow flow when submerged in

trigene. Finally, the trigene was substituted with 70% IMS for 1h and eventually with sterile PBS<sub>7.4</sub> for 1h. The PBS<sub>7.4</sub> was changed every 15min. At this point the device, already kept inside a class II cabinet, was ready to be used. Prior inserting the tubing in the wells the system was equilibrated with cell media for 30min.

### 2.5.3 Cell seeding

MFC188 and SVECs were seeded in 24 well plate at a density of  $50 \cdot 10^3$  cell/well 24h before incubation in flow. 10T1/2 were seeded at a density of  $35 \cdot 10^3$  cell/well and 24h after media was replaced with fresh media added with 2ng/ml of TGF- $\beta$ 1 and incubated for 48h before applying flow. Flow was increased to the analysis flow rate at a rate of increased of  $\simeq 3.5 \mu\text{l/s}$  every 60min. The two cell lines were seeded at different densities because 10T1/2 are sensitive to confluency, which should be avoided. Therefore they were seeded at a lower density compared to SVECs.

## 2.6 Polymersomes *in vivo*

### 2.6.1 DSC

#### Animals

Experiments were performed on male SCID mice weighing  $30 \pm 3\text{g}$  obtained from the University of Sheffield Field Laboratories and held in the animal facility for at least 1 week before experimentation. Prior to surgery, animals were housed in pairs on sawdust, in Perspex cages in a holding facility maintained at  $21.5 \pm 1.5^\circ\text{C}$ , 40-65% relative humidity, with a 12/12 hour light/dark cycle. Food in the form of standard pelleted commercial diet and tap water were available *ad libitum*. All procedures were performed under the Animal Scientific Procedures Act (1986).

**Spheroids preparation** A tumour was implanted in the window of the dorsal skinfold chamber in the form of a spheroid obtained from MFC188. Sub-confluent cells were detached from a flask and counted using a Neubauer counting chamber. Cells were re-suspended to a concentration of  $150 \cdot 10^3$  cells/20 $\mu\text{l}$  and 20 $\mu\text{l}$  drops were deposited on the lid of a 3cm Petri dish. Cells were then incubated 48h at 37°C 5% CO<sub>2</sub> to allow spheroids to form in the drops. Humidity was assured by putting 2ml of media at the bottom of the Petri dish.

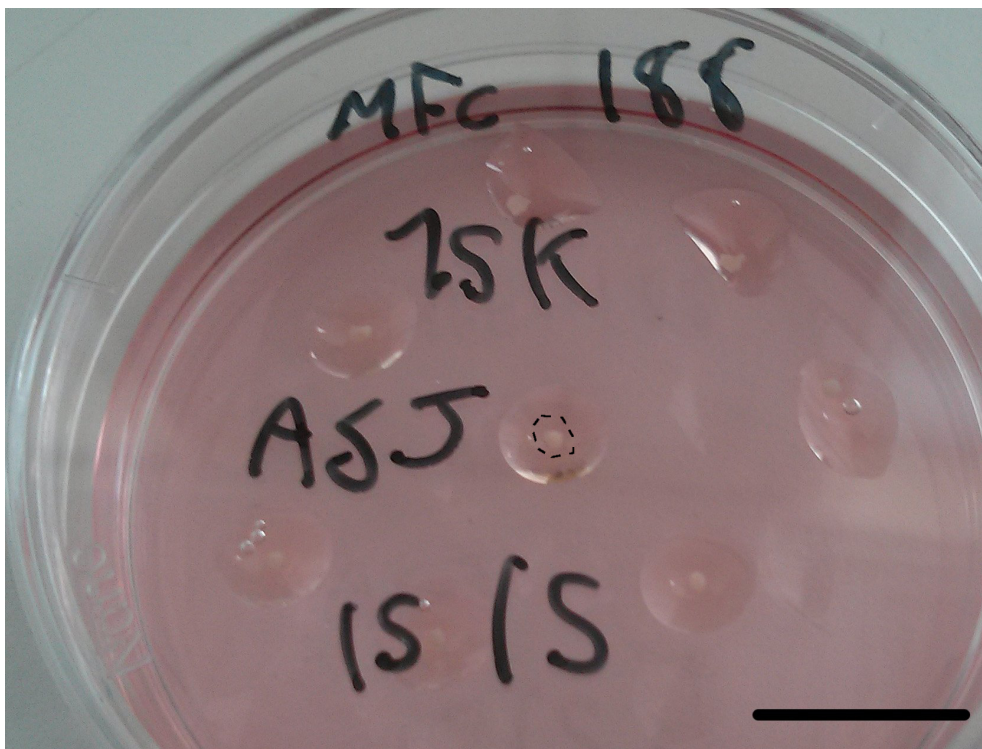


Figure 2.13: Spheroid of [MFC188](#) cells growing in drops placed on the lid of a Petri dish. 2ml of media at the bottom of the dish assured humidity and avoid that drops drained out. One spheroid is highlighted by a black dotted circle. Bar 7.5mm.

### DSC Surgery

Immediately prior to surgery the warming pad and the site of the surgical preparation were sprayed with Trigene. The chambers, nuts, screws and spacers were sterilised by autoclave. The window chamber was custom made by the University Workshop, University of Sheffield. The parts of the chambers are pictured in figure [2.14](#). The frame is made of titanium and weights  $\simeq 2g$ .

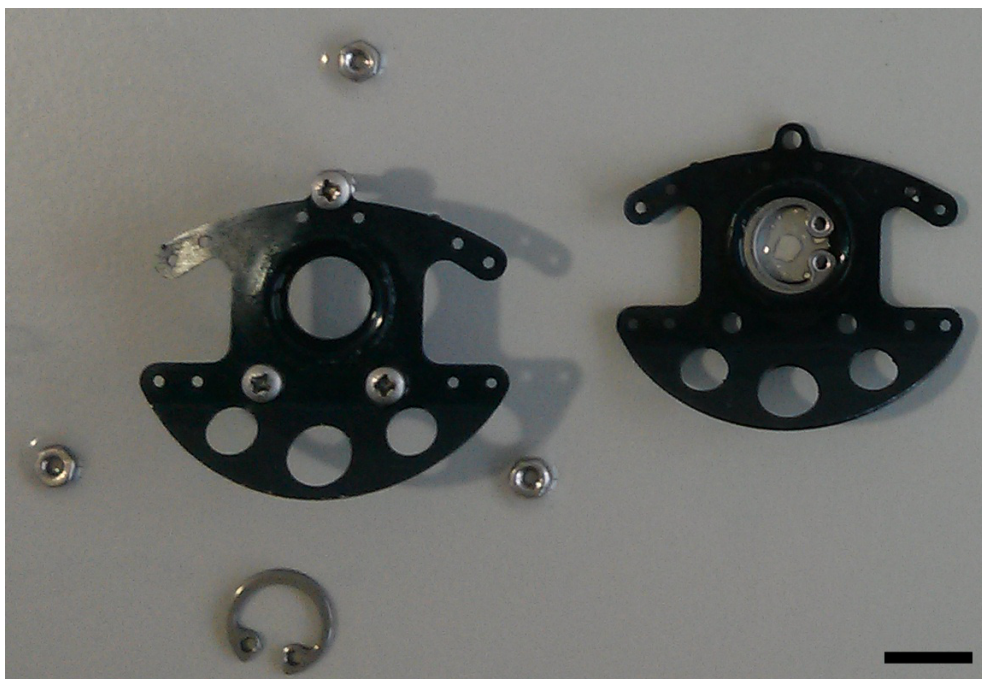


Figure 2.14: Parts of the custom made window chamber. The two black frames holding the flap of skin are visible, together with the bolts and the clip holding the optical glass. Bar 7mm.

**Anaesthesia** Animals were anaesthetised with a *i.p.* injection of a mixture of Hyponorm, 1 part of Hypnovel and 2 parts of injectable water. 100 $\mu$ l per 30g animal were used.

**Shaving** All the steps of the surgery were performed with the animal lying on a hotplate heated at 37°C. The animals dorsal area was shaved from hip to shoulder and around the edge of the ventral area using shaving clippers. Remaining fur was removed with Veet shaving cream applied for 5min and removed with dH<sub>2</sub>O and gauze swabs. Skin was sterilised with hibi-scrub and alcohol gauze pad. The area where the chamber sits was marked using a sterile marker pen.

**Placement of the chamber** A flap of skin was sutured with 4/0 Ethilon suture to a C-clamp to keep the skin evenly tensioned before applying the chamber. 6 evenly spaced suture points were used. Using a template, the position of the 3 screws and the glass window was marked with a sterile marker pen. A 0.5cm circle of tissue (epidermis, dermis, subcutis, muscle and subcutaneous fat) corresponding to the area of the glass window was removed, leaving blood vessels exposed. Tissue drying was prevented using saline. Finally, the two frames of the chamber were sutured on the two sides of the flap of skin using ethibond suture. Tumours were implanted by placing one spheroid in the middle of the

exposed vasculature of the window. A glass coverslip was placed in the chamber and secured with a spring grip.

**Post operative care and husbandry** Aureomycin ointment was applied to the chambers frames edges,  $100\mu\text{l}$  of Vetergesic (buprenorphine  $30\mu\text{g}/\text{ml}$ ) were administered i.p. and  $1\text{ml}$  of dextrose/saline was given subcutaneous to aid recovery. Animals were kept in individual cages in a  $30^\circ\text{C}$  cabinet. Animals were monitored daily for signs of infections or distress.

**Intra vital microscopy (IVM)** Imaging sessions started when tumour grow to cover around 80% of the chamber and developed a visible vasculature, typically 7 days post surgery.  $80\mu\text{l}$  of  $10\text{mg}/\text{ml}$  rhodamine labelled polymerosomes were injected i.v. into the tail vein. Animals were restrained but not anaesthetised during imaging sessions. One imaging session lasted  $\simeq 15\text{min}$ . Imaging sessions were performed routinely for up to  $24\text{h}$  after injection. Images were acquired using a Zeiss confocal microscope equipped with a 10X objective and a Nikon epi-fluorescence microscope equipped with a 2.5X and a 20X objective.

## 2.7 Statistical analysis

All *in vitro* experiments were performed at least in triplicate ( $N=3$ ). Statistical analysis and comparisons of groups were performed in MATLAB using the *Statistical Analysis Toolbox*. Experimental error is expressed as standard deviation. Statistical comparisons between groups was performed with a Mann-Whitney  $U$  test. This non-parametric test is a strong test for difference in mean between two independent set of data non-normally distributed. For normally distributed data, it is comparable to the parametric Student  $t$ -test. Therefore, as data were not assessed for normality, the Mann-Whitney  $U$ -test was preferred to the Student  $t$ -test. Significance level was set to  $p < 0.05$ .

*In vivo* experiments were performed in  $N=1$  for **PMPC-PDPA** imaged at the confocal,  $N=2$  for **POEGMA-PDPA** imaged at the confocal and  $N=2$  for **POEGMA-PDPA** imaged with the epifluorescence microscope. Error was calculated as  $error = \frac{|animal_1 - animal_2|}{2}$  when  $N=2$ . Because of the small sample size, animal experiments should be considered as pilot experiments, and no statistical significant conclusion can be inferred from the results.

### *Abstract*

Quantification of polymersomes uptake *in vitro* and intra-tumour distribution *in vivo* relies on dedicated fluorescence image analysis tools capable of high throughput. Such methods are based on image segmentation to identify [Regions of interest \(ROI\)](#)s such as cell cytoplasm or nucleus, regions of a well corresponding to flow parameter, blood vessel or tumour stroma. The spatial information relative to a specific [ROI](#) must finally be correlated with the relative fluorescence signal intensity. The following chapter will focus on the development of such analytical tools.

## 3.1 Introduction

The large amount of images to analyse requires automation of the method to make the analysis faster and more reliable. Of the many possible alternatives in image analysis, such as ImageJ, R or other commercially available software, MATLAB was chosen as the developing platform. This because MATLAB has a strong *Image Analysis* toolbox and it is highly customisable through the integration of a number of scripts and functions.

All the software developed are based on segmentation: the extraction of particular [ROI](#) from the rest of the image. The segmentation process can be implemented with a number of algorithms, all of which are targeted for enhancing the contrast between the [ROI](#) and the background. The algorithms applied and the order they are applied in is highly dependent on the original image. A good confocal image can be segmented using a simple threshold approach: only regions with pixel intensity higher than the threshold are considered. Other images,

such as vasculature images here analysed, do not have enough contrast to use a thresholding masking. In this case, other filters should be applied to facilitate segmentation. Such filters usually operate in multi-step, first blurring the image to eliminate noise, then enhancing the contrast at the edges of the ROI and finally restoring the original sharpness.

In this work, several different pictures (Immunocytochemistry (ICC), up-take, vasculature *in vivo*) have been acquired using different microscope set-ups (epi-fluorescence, confocal, different magnification). As a result, the analysis tool should perform the same task (segmentation and intensity-based analysis) using a flexible approach, to allow satisfactory results in different conditions. This result was obtained by implementing different segmentation tools into a software with Graphic user interface (GUI) that allows flexible interaction of the user with the masking algorithms.

## 3.2 Image segmentation

### 3.2.1 Thresholding masking

The thresholding masking is the simplest approach in segmentation problems. In good confocal or epi-fluorescence images, the background has signal intensity close to 0, while the feature of interest is characterised by brighter regions. When a thresholding masking is applied, the ROI is identified by all the areas having intensity value higher than the threshold. In the software GUI, this was implemented by a slide bar that the user can move to adjust the threshold. A limitation of this approach is that the background should be highly homogeneous and there should be enough contrast between background and ROI, otherwise it is impossible to discriminate the two area. In the analysis here performed, this was achieved only in nuclear DAPI staining, where nucleus are homogeneously stained and the contrast DAPI/background is relatively high (see fig. 3.1). Images characterised by weaker signal and lower contrast, such as low polymersomes uptake or blood vessels, were segmented using different algorithms.

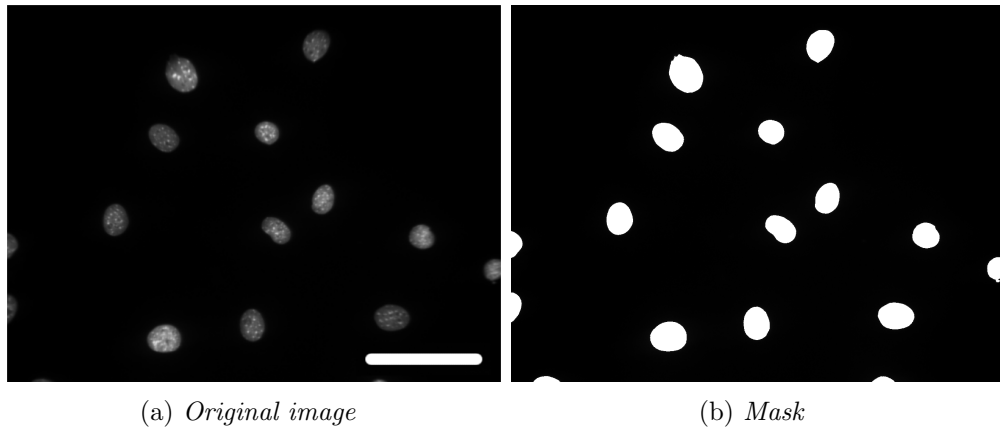


Figure 3.1: *Example of intensity thresholding masking on epi-fluorescence image of nucleus stained with DAPI. Pixel values with intensity higher than the threshold are considered as ROI and highlighted in white on the right image. Bar 13 $\mu$ m.*

### 3.2.2 Difference of gaussians (DoG)

DoG algorithm is a form of band-pass filter (Marr and Hildreth [1980]) commonly used to detect edges. Its operating principle is that Gaussian blurring of an image only excludes high frequency spatial information: noise. By applying to the original image two different Gaussian blurring with different standard deviation and subtracting the two blurred images from each other, it is possible to remove noise, and identifying the area of the images corresponding to the lower difference of Gaussian (minimum of the function) allows to accurately identify the edges of the ROI. In MATLAB, a Gaussian convolution kernel is generated with

```
gaussian = fspecial('Gaussian', hsiz, sig);
```

Where *hsiz* define lowpass filter size, and *sig* define the standard deviation of the Gaussian. The difference between two kernel is obtained using

```
dog = gaussian1 - gaussian2;
```

Finally, the original image is convoluted with the DoG filter using

```
d = conv2(double(I), dog, 'same');
```

The minimum in the resulting *d* matrix represents the regions of the image to be analysed. The DoG algorithm is implemented in MATLAB using two slide bars that allow the user to define the standard deviation of each of the two Gaussian, and a third slide bar to define the *hsiz* parameter, common between the two gaussians. Note that the DoG is not an absolute value: inverting the values of *sig1* and *sig2* generates the negative of the mask, i.e. identifies the background rather than the ROI. Figure 3.2 report an example of the application

of the **DoG** algorithm. Note that the image refers to a micrograph acquired with a 20X objective, which was the most difficult to segment because of the poor background. However, the segmentation analysis did allow to correctly identify the blood vessels. A limited amount of wrongly assigned pixels can be seen around the micrograph edges, but those areas can be excluded by the analysis applying one the filters provided with the developed software.

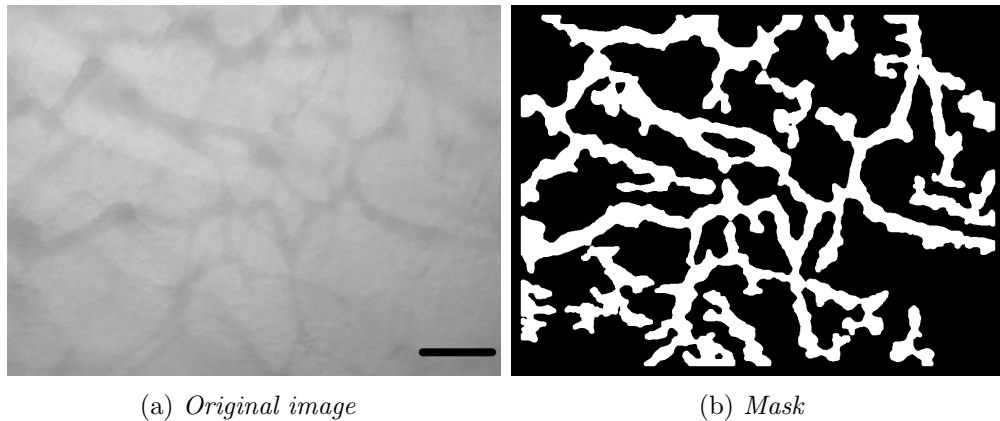


Figure 3.2: *Example of **DoG** application on a vessel image acquired in bright field using a 20X objective. The original image on the left has poor contrast and cannot be segmented by simple intensity thresholding. **DoG** algorithm was capable of correctly identifying vessels (right image, in white). Bar 70 $\mu$ m.*

### 3.2.3 Local threshold entropy (LTE)

The **LTE** algorithm was used to segment some of the *in vivo* images. It was proposed by Fan and co-workers (**Thitiporn and Guoliang [2003]**), and it was here slightly modified to meet the specific requirements of the analysis. **LTE** is a two steps algorithm. The first step is a *matched filtering*, followed by *local entropy thresholding*. Matched filtering is an enhance filter that enhances contrast of blood vessels by detecting linear segments in the image (vessels) and assuming Gaussian distribution of intensity at the edges. Once the contrast has been enhanced at the edges of the **ROI** using the matching filtering, the **LTE** automatically detects the optimal thresholding for vessel extraction. This is done locally on small regions of the image by assuming that the intensity values are spatially correlated and not pixel-position independent: the **ROI** is a contiguous region of space characterised by a local homogeneous distribution of intensity values. This is different to the intensity thresholding approach as two different images with the same overall signal intensity but different spatial pixel distribution will have different threshold. A critical parameter is the size of the matching filter, which is correlated to the size of blood vessels. In early versions of the segmentation

software the user was given the possibility to tweak the parameter, however it was later found that results were not better or faster than DoG filtering. The only exception was in segmentation of vessels images acquired with the 2.5X objective. Those images were effectively masked by the algorithm proposed by Fan using the same size of the match filter, most likely because of the resemblance with the images analysed in the cited work, at least regarding blood vessels pixels size.

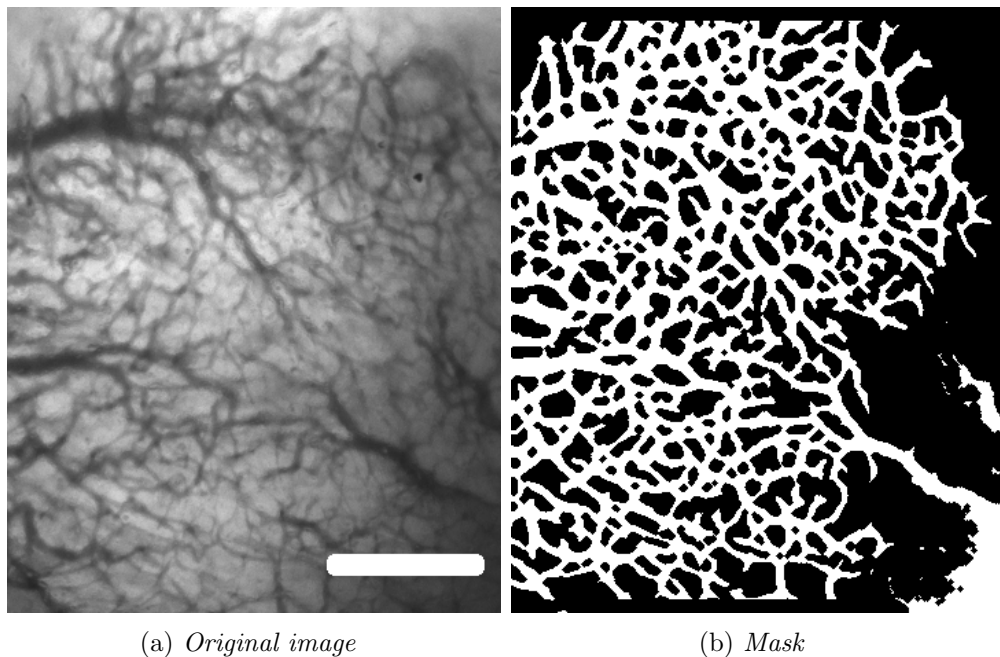


Figure 3.3: *Example of LTE. An image of blood vessels acquired with a 2.5X magnification was effectively segmented using the LTE algorithm. Extracted vasculature on the right, in white. Bar 800 $\mu$ m.*

### 3.2.4 Mask post-processing

**Post-processing intensity thresholding** Regardless of the segmentation process used, the mask generated was not perfect. It could contain some noise given by isolated bright pixels or in some pixels the signal intensity was out of scale (saturated pixels, intensity=255 in an 8bit image). All those values can negatively interfere therefore they should be removed. Saturated pixels were removed by applying a thresholding filter on the mask, and the threshold level was set by the user as previously described. There was also the possibility to remove very dark pixels, an option useful in the *clean up* process of *in vivo* images, where some dark pixels occasionally generated unwanted ROI.

**Size-filtering post-processing** Isolated pixels or small groups of isolated pixels (noise) can be removed by applying a size filter to exclude regions smaller (or

bigger) than a defined size limit. This feature is based on the internal MATLAB function *regionprops* and its optional argument *Size*. The *regionprops* command accepts as input a binary image (mask), where white represents the ROI and black the background. The function identifies separate ROIs defined as continuous, uninterrupted regions of white, and store their size values separately. The size filter then check for the size values and excludes ROI outside the size boundaries. T size filter is implemented in the GUI with the use of two side bars that allow to interactively fix the size threshold (upper and lower limit).

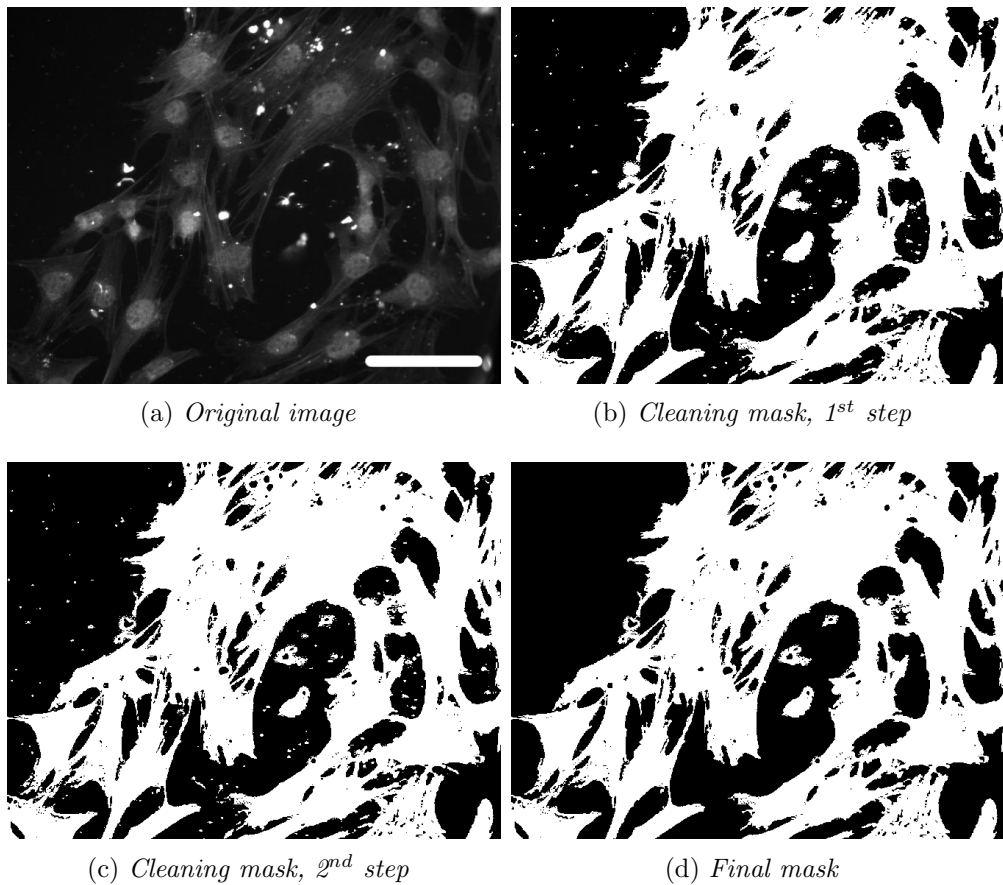


Figure 3.4: Original picture (a) was segmented. The mask obtained (b) was cleaned by eliminating high intensity values (c) and small, isolated pixels (d). Bar  $22\mu\text{m}$ .

### 3.3 Pericyte markers image analysis

Images were segmented using the specifically developed software. The workflow of the analysis and a segmentation example is reported in figure (3.5). Nuclear mask was subtract from the cell mask to exclude any cross-talk between the channel by excluding the nuclear ROI from the cell mask. To be able to compare different sets of experiments, the ratio of the average intensity in samples over

the control was used rather than the absolute intensity value. An example of such operation for 10T1/2 treated with 0, 2 or 5ng/ml of **Transforming Growth Factor- $\beta$ 1 (TGF- $\beta$ 1)** is reported in figure 3.5-3.6.

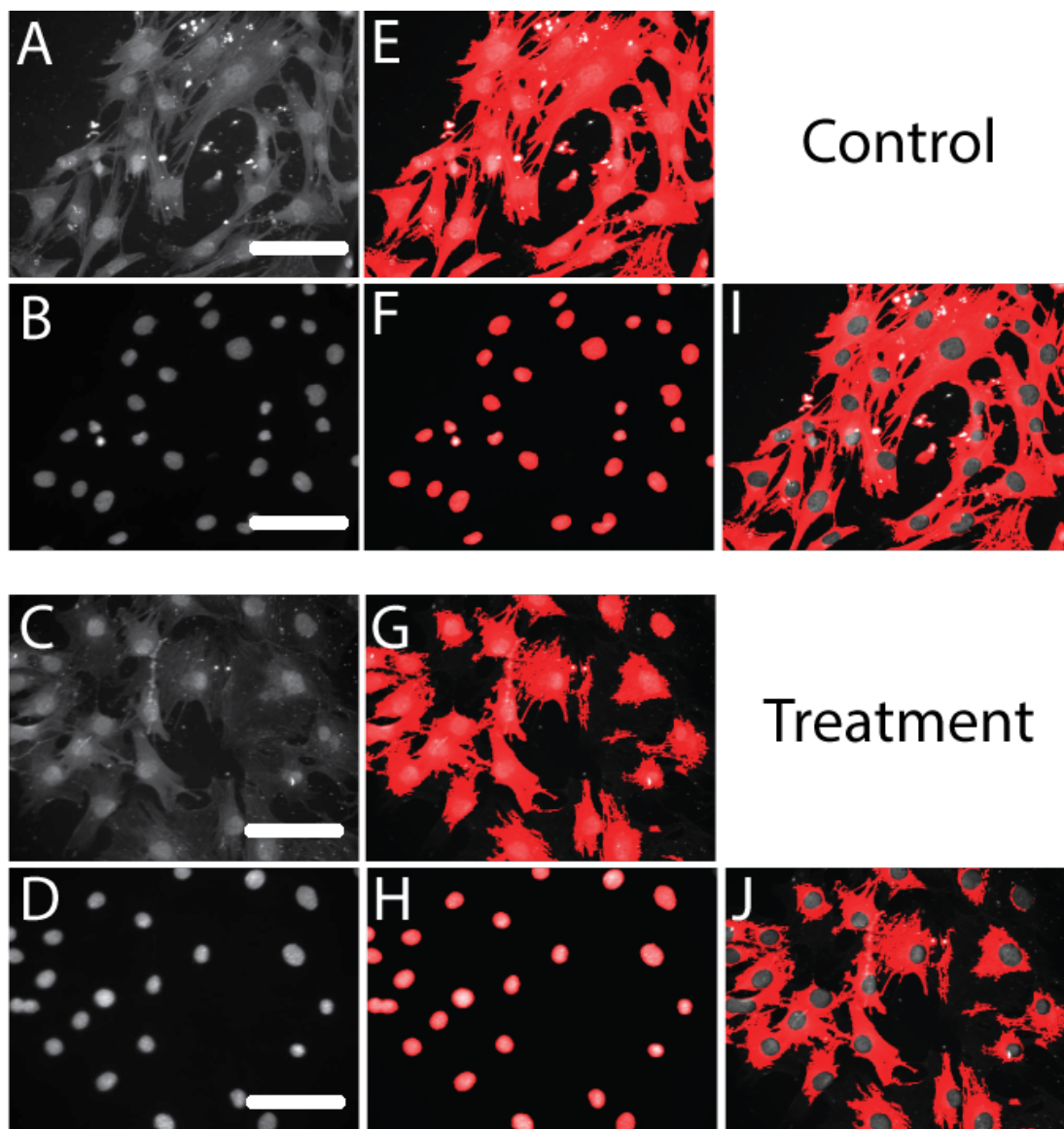


Figure 3.5: *Work-flow of image analysis for ICC experiments. Cells were segmented using the antibody channel (A, C) to identify the cells and the DAPI channel (B, D) to identify the nucleus. The nucleus masks (F, H) were subtracted to the respective cell masks (E, G) and the average intensity was measured in the resulting ROI (I, J). Bar 22 $\mu$ m.*

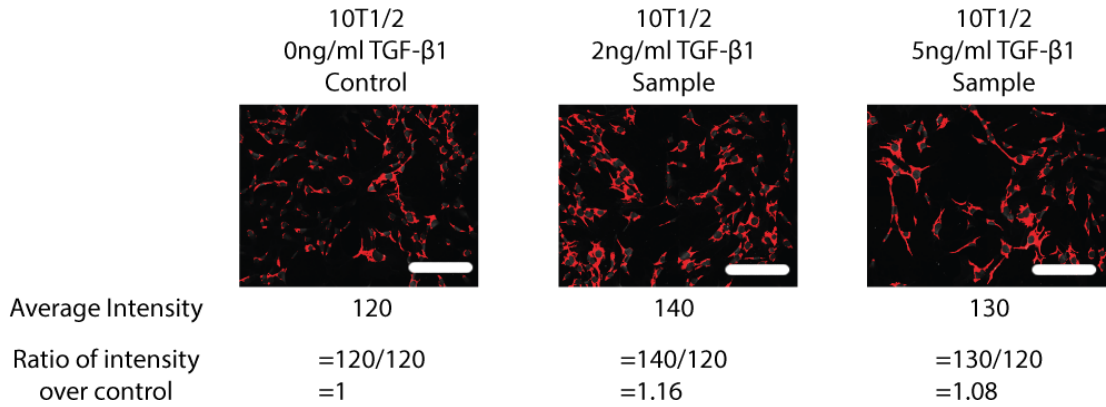


Figure 3.6: Average intensity in selected *ROI* was measured for control and samples. The average intensity of the sample over the control gave the ratio used to compare expression between different concentrations and samples. Bar  $30\mu\text{m}$ .

### 3.4 Image analysis for uptake *in static conditions*

Uptake quantification was performed by quantifying the average intensity of cells detected by the segmentation software and plotting the result as a variation of the average intensity over time. To be able to easily compare results between different cell lines, data were expressed with respect of the maximal uptake, fixed as a 100%. The maximal uptake is here defined as the maximal value of intensity recorded for the analysis, which correspond to the uptake of rhodamine labelled Poly(2 - methacryloxyethyl-phosphorylcholine)-poly( 2 -(diisopropylamino)ethyl methacrylate) (PMPC-PDPA) polymersomes from the tumour cell type Mouse Fibrosarcoma Cells expressing VEGF188 isoform (MFC188) at  $t=24h$ . An example of this application using modified pictures used in the testing phase is reported in figure 3.7.

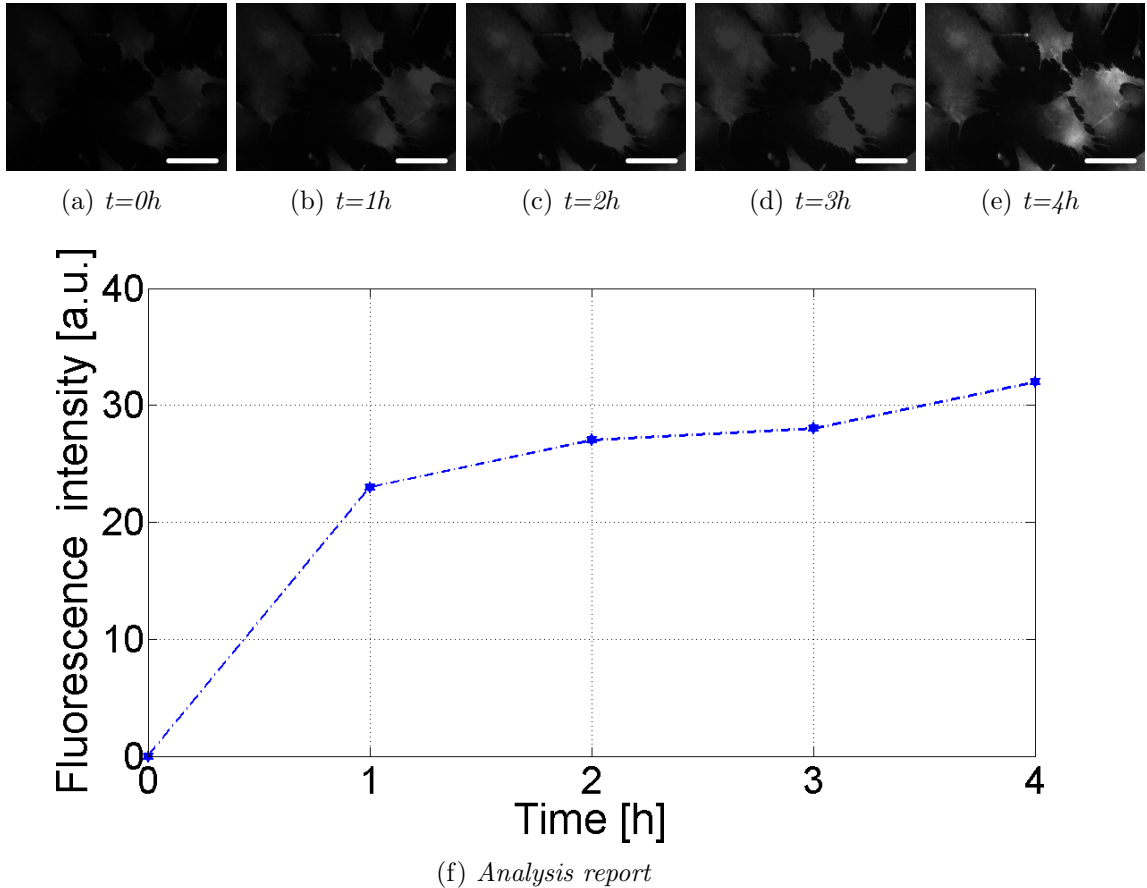


Figure 3.7: *Example of time analysis. The top row represents an ideal set of five pictures of increasing intensity, such as the ones that could be obtained in an uptake study from  $t=0$  to  $t=end$ . The bottom plot shows the variation on average intensity recorded in the *ROI* identified in the segmentation analysis versus time. As expected, the software report an increase of intensity over time, reflecting what can be seen in the pictures. Bar  $30\mu m$ .*

### 3.5 Image analysis for uptake *in flow* conditions

This analysis aimed to correlate physical flow parameters in specific area of cell in the imaged plate with polymersomes uptake. Images of different areas of a 24 well plate were imaged and the measured uptake was correlated to shear stress or velocity magnitude in the same area.

#### 3.5.1 BD Pathway 855 microscope set-up

The analysis depends on accurately mapping the imaging area of the 24 well plate. Because the BD Pathway 855 does not natively support 24 well plate the well was manually mapped and the imaging positions were saved into the microscope settings as *xy* offsets from defined positions. The mapping was performed

by accurately drawing a grid on the bottom of the well and using the intersection of the grid as guideline for setting the offset. The grid also allowed us to accurately identify the position of the inlet and the outlet (see fig 3.8).

Imaging a full 24 well plate and all the well used in one analysis required a long amount of time, which was not compatible with cell viability in the microscope. Cell fixation also proved to not be an option, as the fixation severely compromised rhodamine signal (see fig. 3.9) To overcome this limitation, a lower resolution objective was used (10X) three representative areas were imaged instead of the whole well.

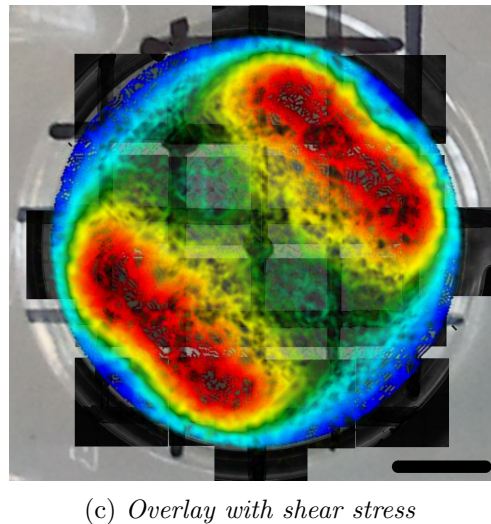
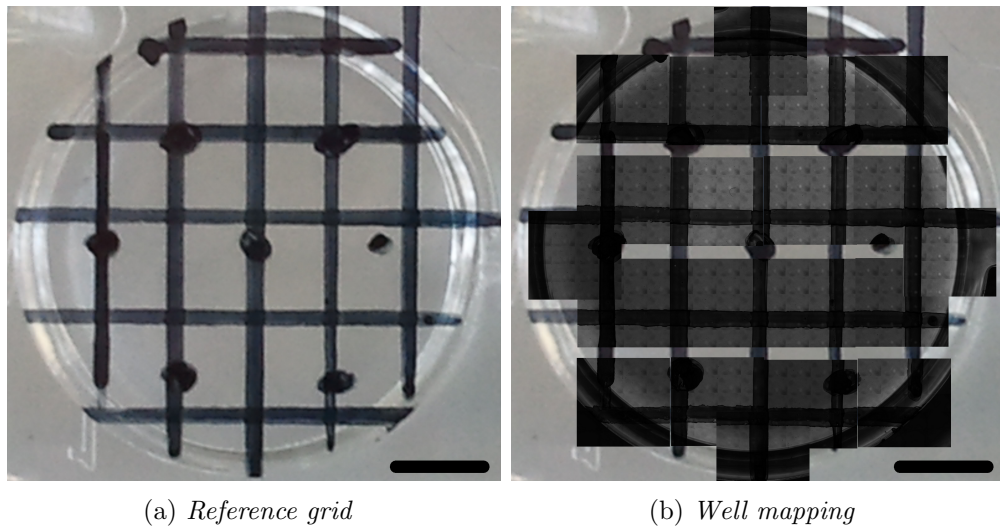


Figure 3.8: Mapping a well. Using a well with marked position as a reference (a) images were taken and then a well was reconstructed saving on the microscope software the xy offset (b). Finally, the shear stress mapping obtained from Comsol MultiPhysics simulation was overlaid (c). Bar 3mm.

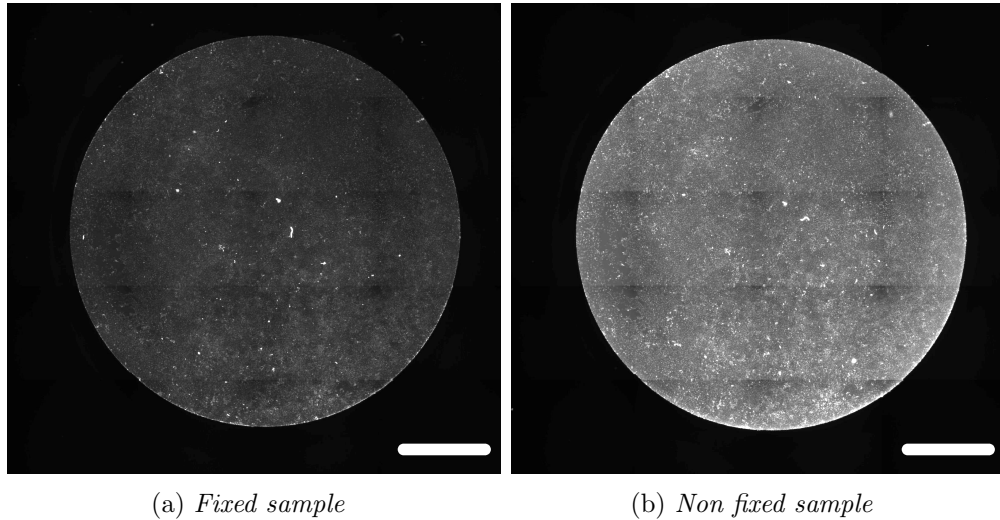


Figure 3.9: *Effect of fixation on rhodamine labelled polymersomes signal in cell imaging. After fixation (left) the intensity signal from rhodamine labelled polymersomes up-taken is severely compromised compared to live cell imaging (no fixation, right picture). Bar 2mm.*

### 3.5.2 *In silico* well mapping segmentation

*In silico* simulations was used to quantify shear stress and velocity magnitude at the cell level. Because COMSOL is based on finite element analysis, it divides the volume to be analysed (the well) into a finite mash, and when asked for the value of shear stress or velocity magnitude at the cell level it only gives the values at the intercept between the mesh and the plane of cell growth. Depending on the size of the meshing this can be a rather sparse matrix. To obtain a detail reconstruction of the well mapping the data were passed to MATLAB and the function *meshgrid* was called to interpolate missing data to the tenth of micrometer resolution, significantly higher than the resolution achievable with the 10X objective used in later imaging. The resulting map was stored as grey scale image and used for segmentation. The range 0-255 was then divided into 8 ROI each one of step 32, so that the first area had intensity 0-31, the second 32-63 etc. Because it is a grey scale 8bit image, the intensity values will range from 0 to 255, corresponding to low and high values of shear stress and velocity magnitude. Knowing the corresponding values it is possible to directly correlate the intensity value to the actual shear stress or velocity magnitude. For instance, if the range 0-255 corresponds to a range of velocity 0-80 $\mu\text{m}/\text{s}$ , then it can be derived that intensity value of 32 will correspond to velocity  $\frac{80 \cdot 32}{255} \simeq 10\mu\text{m}/\text{s}$  (fig. 3.10)

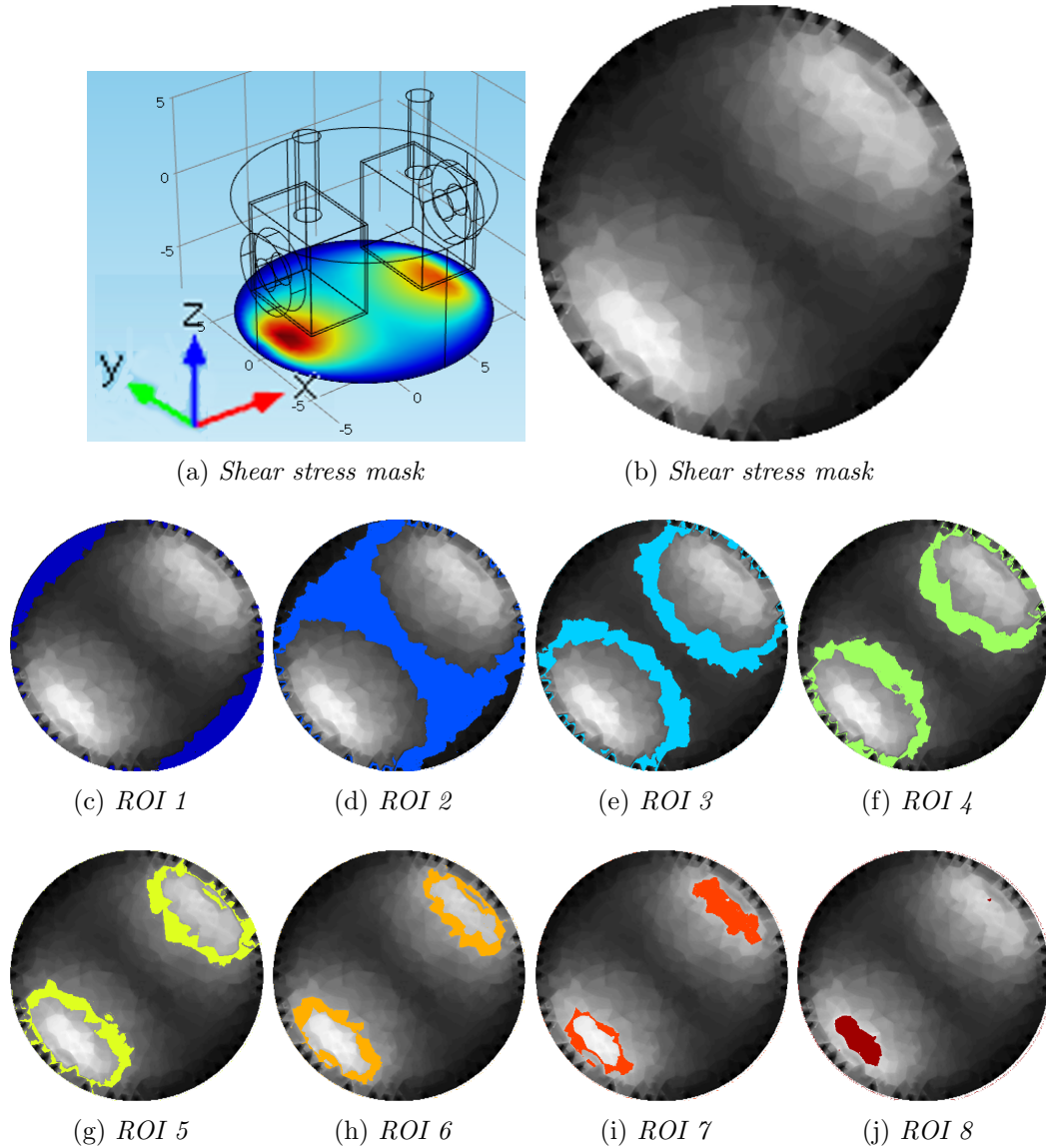


Figure 3.10: *Segmentation of the flow parameter. The reference well with the analysed z-plan is displayed in (a). In this example the shear stress is considered. The original range of grey intensity 0-255 (b) was divided into 8 ROIs, showed in different colours in picture (c-j). Every ROI has intensity range of  $\frac{256}{8} = 32$ . The corresponding full range of shear stress was 0-12dyn \* cm<sup>-2</sup>, therefore every ROI correspond to a range of shear stress of  $\frac{12}{8} = 1.5\text{dyn} * \text{cm}^{-2}$ .*

### 3.5.3 Image analysis

After image acquisition, the images were carefully overlaid with the well mapping of a defined flow parameter (shear stress or velocity magnitude). Average signal intensity of cells growing in area with a specific flow parameter was finally correlated with the flow parameter itself, to identify a correlation between up-take and shear stress or velocity magnitude (see fig 3.11).

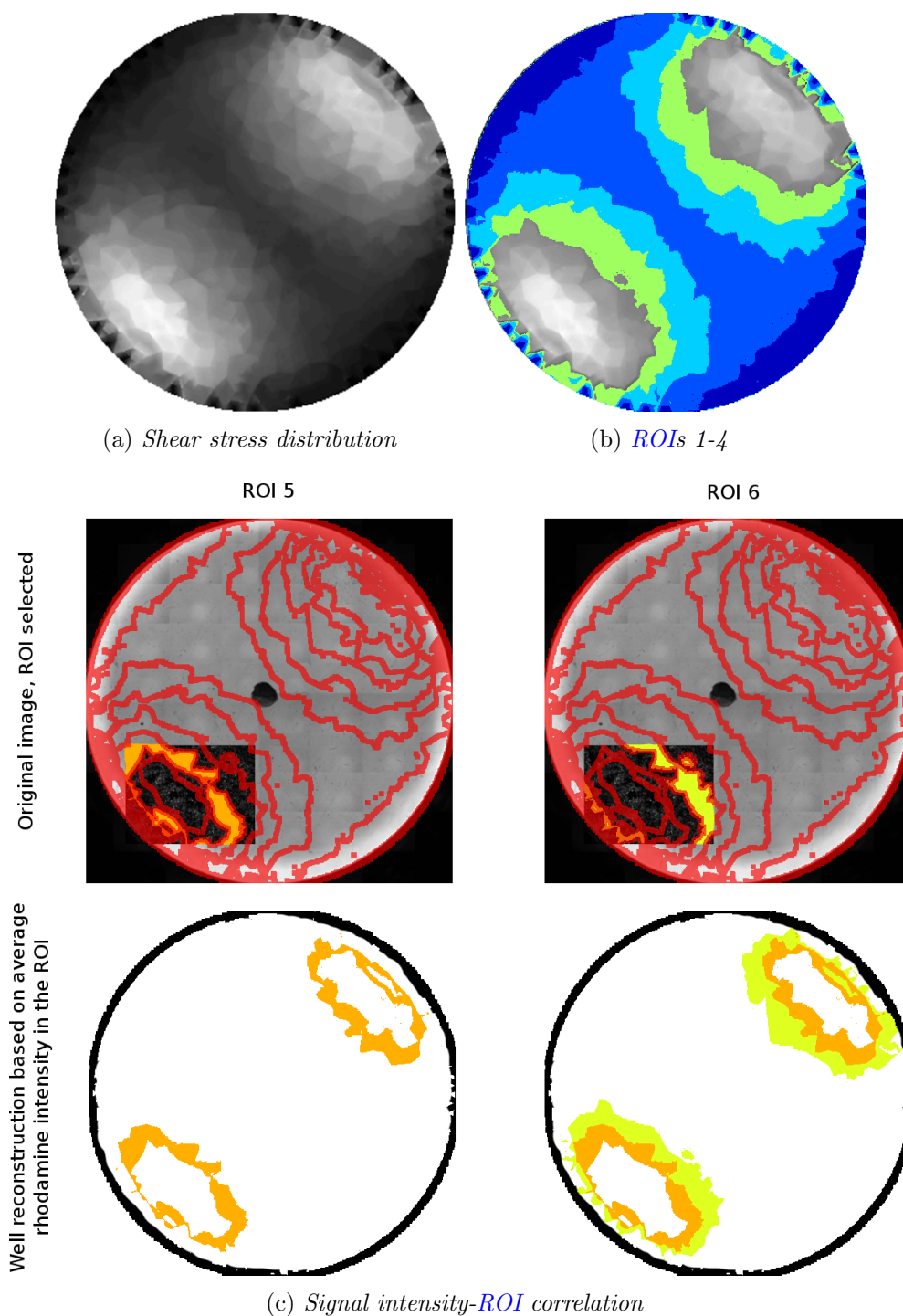


Figure 3.11: *Image analysis method. The first four of the total eight ROIs corresponding to the lower values of shear stress are highlighted in the figure (top right), from dark blue to pale green. A micrograph is placed on the appropriate xy position of an entire well and the 8 ROIs are overlaid to the micrograph (the red lines represents the edges of the single ROI. Intensities of the areas belonging to a ROI are averaged and a new well-uptake image is reconstructed based on the average value).*

## 3.6 Image Analysis for *in vivo* experiments

### 3.6.1 Masking

*In vivo image* analysis had the aim to quantify and localise signal intensity of rhodamine labelled images of tumour vasculature. This is a segmentation problem as it requires identification of at least two ROIs in every image: vasculature and stroma. The identification of these two ROIs in confocal pictures is not an easy task, mostly because of the very variable and weak signal, especially at later time points. However, the confocal microscope used can acquire simultaneously a transmitted light image of the vasculature, where the vessels are always clearly visible in black over brighter tumour stroma. The simultaneous acquisition together with imaging in different areas of the tumour over-time eliminates the need for registration. Tumour images were segmented using a software specifically developed. First of all, the tumour area to analyse was manually chosen (this option included the possibility to analyse the whole as well), finally intensity threshold, LTE and DoG algorithms were implemented to allow vessel segmentation. Different images were segmented better with different algorithms, depending on the image characteristics (see fig 3.12).

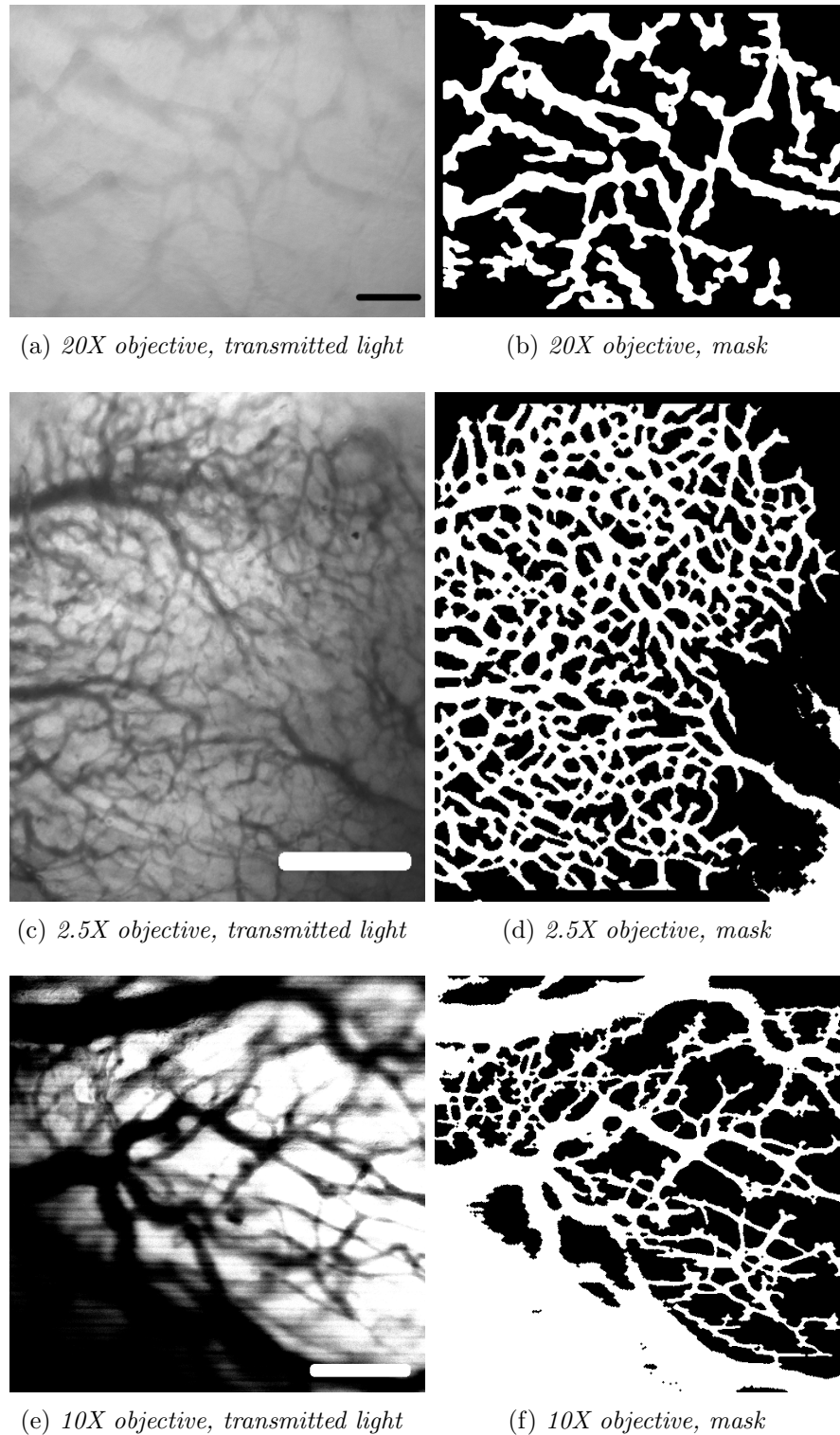


Figure 3.12: Mask generation in different pictures. Images of vasculature acquired using transmitted light in an epi-fluorescence microscope (20X (a), 2.5X (c)), and in a confocal (10X (e)). Images (a) and (b) were both segmented using *DoG* algorithm. Image (c) was segmented using *LTE* algorithm. For all images, vessels were correctly identified. Bar (a)  $70\mu\text{m}$ ; (c)  $800\mu\text{m}$ ; (e)  $200\mu\text{m}$ .

As in *ICC* and uptake image analysis, masks were further processed to reduce

noise by *size filtering*. A crucial difference between the ICC and uptake image analysis software and the *in vivo* image analysis software is the introduction of a third ROI in the latter. This third ROI correspond to the perivascular region and it is therefore located between the vessel mask and the stroma mask. There are two main reasons to justify the introduction of this third mask. First of all, in low resolution images such as 2.5X images, it can be used as a *safe zone*, to exclude pixels which cannot be assigned to the vessel or the stroma mask because of the low resolution. The second reason is that, in higher resolution images, it can be used to assess the distribution of polymersomes in perivascular region, where pericytes are normally located, and also to evaluate the diffusion of polymersomes into the tumour by measuring the average intensity in this region, which can be dynamically expanded (fig. 3.13).

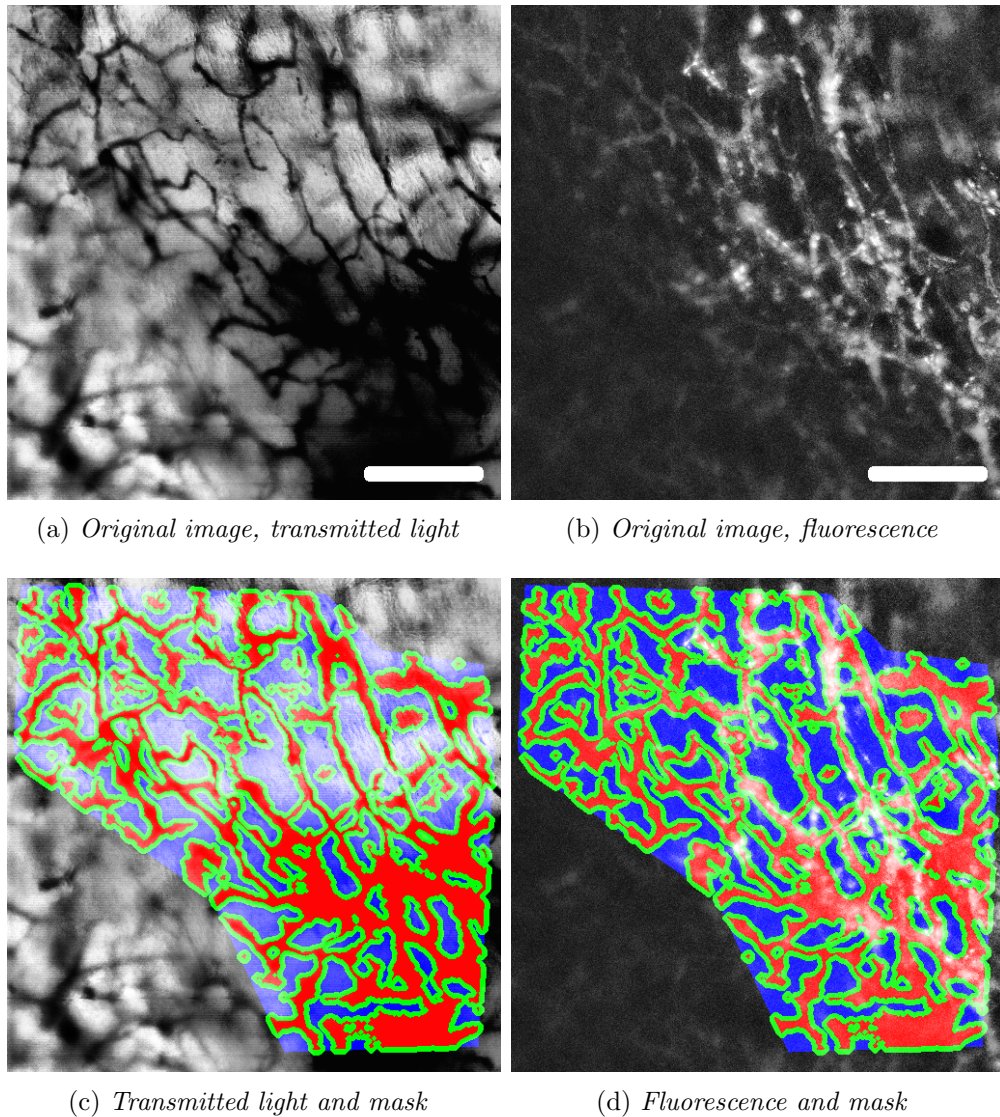


Figure 3.13: *Masking blood vessels. Original images on top(a-b), masks overlay at the bottom (c-d). Masks were created on transmitted light images (a-c) and then transferred to rhodamine images (b-d) The tumour area was identified manually and is shown as coloured RGB overlay. Vessels were identified automatically by the proposed segmentation algorithm. Vessels in red, stroma in blue and perivascular region in green. Bar 210 $\mu$ m.*

### 3.6.2 Vessel mask segmentation: Isolating vessels to determine vascular diameter and diffusion profile

To correlate diffusion of nanoparticles with vessel diameter and travelled distance it is necessary to separate all the vessels identified with the vascular mask. This was achieved by reducing the vasculature mask to its skeleton using the MATLAB built in function *bwmorph*

```
skeleton-ves = bwmorph(ves, 'skel', inf);
```

The skeleton mask is a binary mask where the vessel has value 1, the non-vessel has value 0. Considering the vessel a linear sequence of 1s, vessels ends and branching points can be easily identified as the only one surrounded by 1 or 3 1s respectively (see fig 3.15). By subtracting the branching points from the skeleton mask a new mask will be created where the continuity of 1s sequence is interrupted at the branching level. The *regionprops* function can be called at this point as it will identify every different ROI, where ROI is defined as a continuous region of space completely surrounded by 0s.

```
list_vessels=regionprops(skeleton-ves-new , ...
                        'PixelIdxList ', 'Area ', 'PixelList ');
```

Note that since it is a skeleton mask running from vascular node to vascular node, the *Area* corresponds to the vessel length. Finally, the function *bwdist* can be called on the negative of the vessels mask to calculate the Euclidean distance between every pixel of the vessel and the closest pixel belonging to the tumour stroma:

```
edtImage = 2 * bwdist(~ves);
```

Note that the multiplicative factor of 2 will directly give the diameter of the vessel. For every vessel, the diameter calculated in the middle of the vessel was stored.

Finally, the Euclidean distance of every pixel of the tumour stroma from the closest vessel is calculated in a similar way:

```
[distances , label] = 2 * bwdist(~stroma);
```

For every pixel belonging to the tumour stroma, its coordinates were used to store simultaneously the distance from the closest vessels and its rhodamine signal intensity. The *label* option of the *bwdist* command allows to correlate the distance measured to the corresponding vessels, and therefore to retrieve its diameter. All data are stored in a matrix correlating pixel by pixel the rhodamine intensity, the distance from the closest vessel and the vessel diameter. The function *griddata* was used to produce a meshed grid of data useful to produce a surface plot of vessel diameter against distance, with the pixel intensity represented in a colour map (3.14-3.15):

```
xlin=linspace(0,max_diam,max_diam*10);
ylin=linspace(0,max_dist,max_dist*10)';
zg=griddata(vess_diam,distance,intensity,xlin,ylin,'linear');
surf(zg,'Edgecolor','none')
```

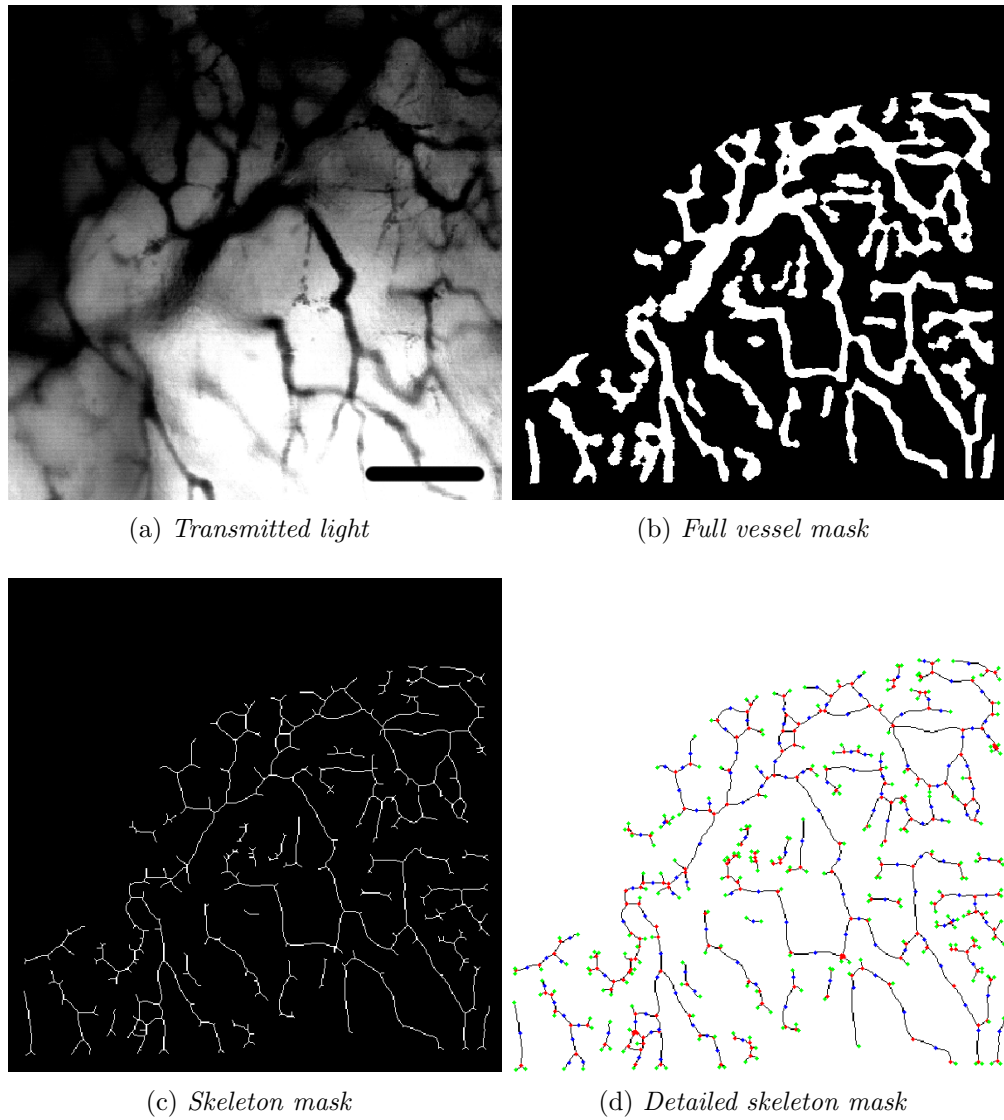


Figure 3.14: *Identification of vessels and branching points. From the transmitted light image (a) the full mask vessel was obtained (b). The skeleton mask (c) showing only the vessels central line was computed from the vessels mask. Finally, vessel ends (green), vessel branching points (red) and vessel centre (blue) were identified as reported in fig. 3.15. Bar 210 $\mu$ m.*

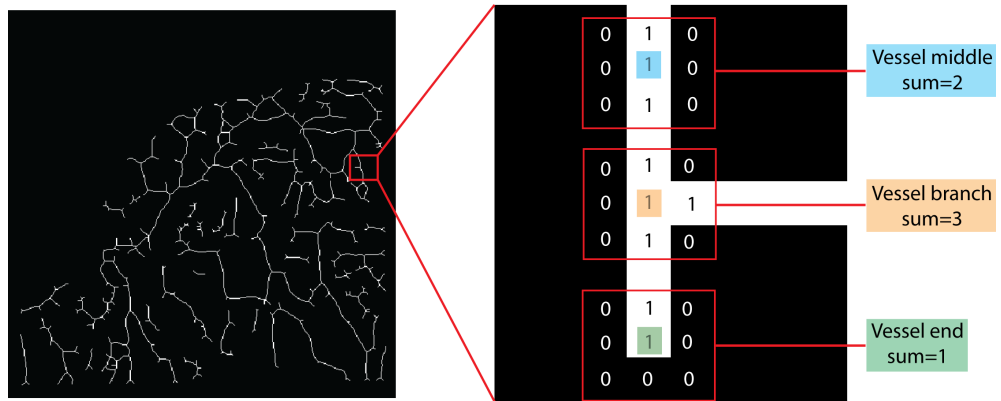


Figure 3.15: *Identifying vessels, ends and branching points in a binary mask. Pixels belonging to the middle of the vessel have sum of surrounding pixels of 2. Branching points have sum of 3 and ends have sum of 1.*

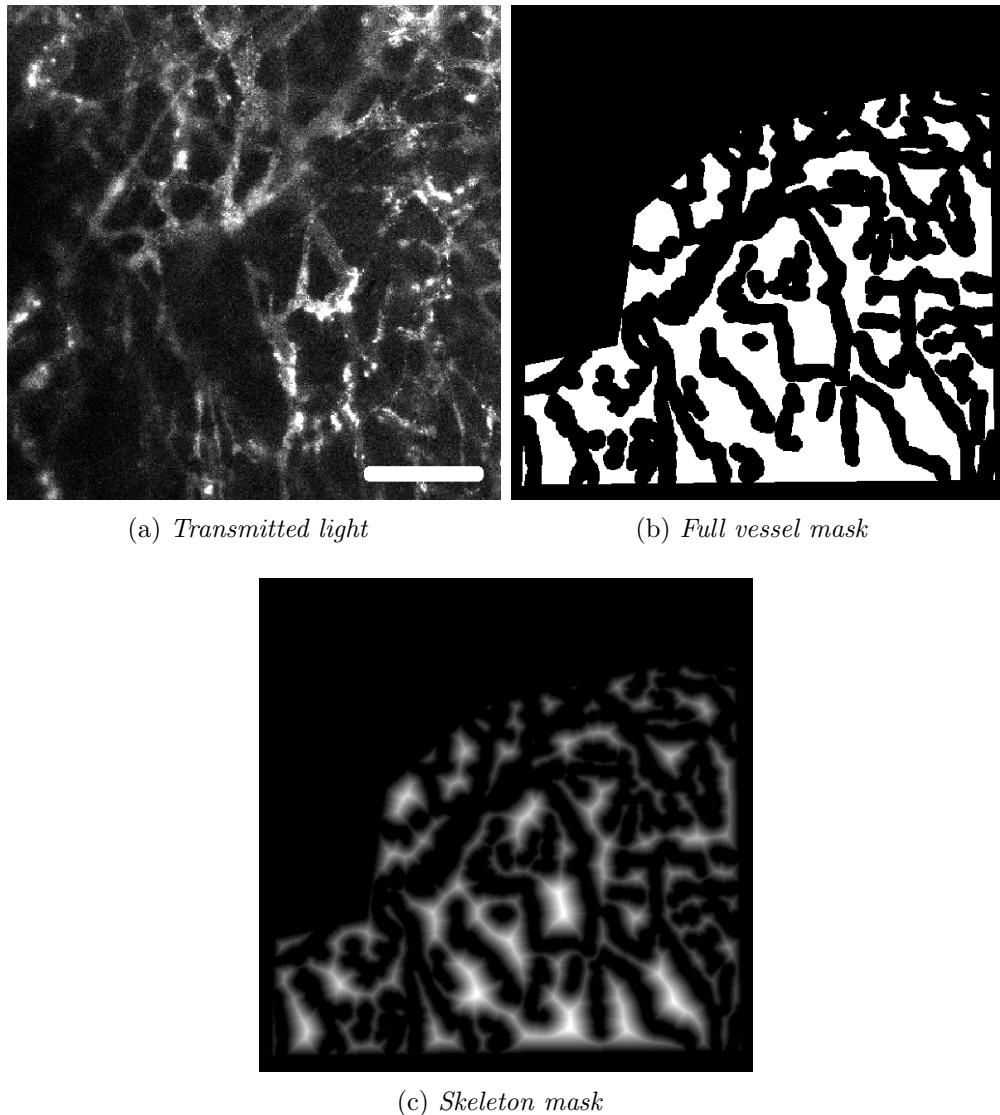


Figure 3.16: *Computation of vessel diameter. The tumour stroma mask was used to compute Euclidean distances from the vessels (shown in (c) as grey scale image, with brighter points representing points far from vessels). By correlating the pixel position in the distance map and in the original image it is possible to correlate signal strength with distance from vessel. 300 $\mu$ m.*

### 3.7 Automatisation of image analysis

Automatisation of image analysis allows faster image processing and higher throughput. Image analysis automatisation was implemented with the development of two GUI softwares using MATLAB *GUIDE toolbox*. One software is dedicated to *in vitro* image analysis (3.17), the second one to *in vivo* image analysis (3.18). Both softwares store images in a database for batch processing and allow the user to categorise images using a tag system. The tag system is used to recall images from the database and to perform analysis on data sub-sets, i.e. pro-

cess only images acquired with a specific microscope or from cell treated with a specific polymersomes formulation. A panel allows to test different algorithm and post-processing mask settings in order to identify the ideal conditions for segmentations. The settings can be then applied to the entire database or to a sub-set specified by the tag system. Segmentation results can reviewed individually for further refinement. *In vitro* GUI was optimised to perform intensity based studies such as calculation of average intensity on specific ROIs, either in relation to specific growing condition (i.e. TGF- $\beta$ 1 concentration) or over time (i.e uptake studies). The software can also perform co-localisation (Pearson and Manders coefficient). *In vivo* GUI was optimised to identify the three ROIs blood vessel, vessel edges and tumour stroma and to measure the relative average intensity.

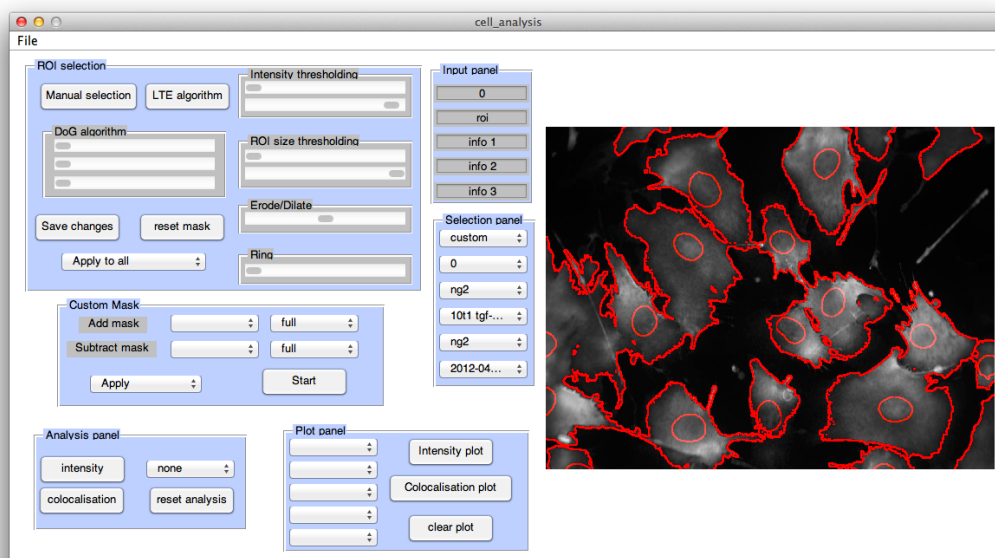


Figure 3.17: *GUI of the software used to analyse ICC and Immunohistochemistry (IHC) images. The interface is divided in panels to group different stages of the analysis: data input, data retrieval, mask creation, combination of masks, analysis and plotting. On the right, the chosen picture is always displayed. During batch analysis, the right picture box provides feedbacks on the analysis status (i.e. on-going, finished, errors).*

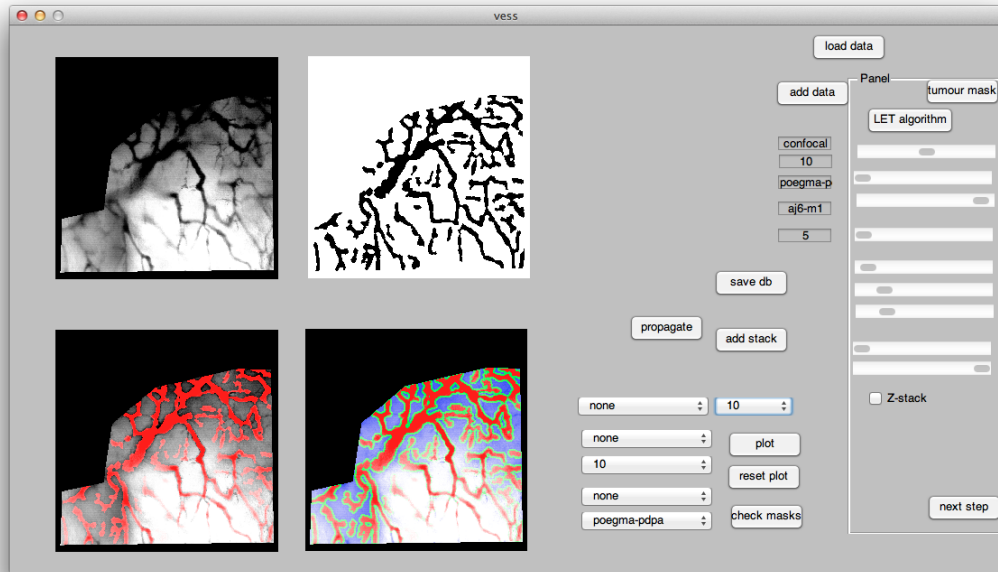


Figure 3.18: *GUI* of the software used to analyse tumour vasculature images. The interface is divided in panels to group different stages of the analysis: data input, data retrieval, mask creation, analysis and plotting. On the left, the chosen picture is always displayed along with the different masks obtained.

### *Abstract*

Fluorescently labelled polymersomes can be detected in cells using a variety of techniques, including [Reverse Phase-High Pressure Liquid Chromatography \(RP-HPLC\)](#), [Fluorescence Activated Cell Sorting \(FACS\)](#) and microscopy. Of these, the latter is the most sensitive, being capable of resolving uptake at the single cell level. It is also the quickest one to perform routinely in a high throughput screening context, as it does not involve extraction or preparation steps: cells can be imaged live. In this part of the work, the use of fluorescence microscopy to quantify cellular uptake was validated through comparison with consolidated quantitative ([RP-HPLC](#)) and semi-quantitative ([FACS](#)) techniques. Furthermore, the analytical system was complicated by the introduction of an *in house* developed flow bio-incubator to assess the effect of shear stress and fluid velocity on cellular uptake.

The polymersomes used had hydrophilic brush composed of [Poly\(2 - methacryloxyethyl - phosphorylcholine\) \(PMPC\)](#) or [poly\(oligo\(ethylene glycol\) methacrylate\) \(POEGMA\)](#), known to interact with cells in different ways: [PMPC](#) based polymersomes were expected to be internalised quickly, while [POEGMA](#) based polymersomes were expected to have a significant slower uptake kinetic. The tumour microenvironment was replicated *in vitro* by studying the uptake in three cell type characteristic of the disease: tumour cells ([Mouse Fibrosarcoma Cells expressing VEGF188 isoform \(MFC188\)](#)), blood vessel endothelial cells ([Small Vessel Endothelial Cells \(SVECs\)](#)), and perivascular cells (10T1/2). [MFC188](#) cells can originate a more vascularised and pericytes rich tumour when used *in vivo* in [Dorsal Skinfold Chamber \(DSC\)](#) preparation ([Tozer et al. \[2008\]](#)). This will facilitate vascular imaging *in vivo* in later experiment presented in this thesis.

For this reason **MFC188** cells were chosen as a model of tumour cell for both *in vitro* and *in vivo* studies.

## 4.1 Introduction

### 4.1.1 Uptake and *in vitro* screening

A comprehensive understanding of the mechanism and parameters regulating uptake of polymersomes by cells is at the basis of a clever design of nanoparticles for a specific application.

Direct quantification of the vector up-taken *in vitro* is strongly dependent on the properties of the vector itself. Delivery of radioactive marked nanocarriers can be quantified by measuring the radioactivity signal (**Penate Medina et al. [2010]**). This is a very sensitive technique and it is also useful to determine the metabolic fate of the carrier, however it is a costly technique and it requires specific equipment and working spaces. Fluorescently labelled carriers represent a valid alternative (**McDonald and Choyke [2003]**, **Beerling et al. [2011]**) both *in vitro* (**Massignani et al. [2010]**) and *in vivo* (**Christian et al. [2009a]**), a routine step of pre-clinical development. Fluorescently labelled particles can be detected in a number of way. *In vitro*, the most commonly used techniques for detection of fluorescently labelled vectors in cells are **RP-HPLC**, **FACS** and cell imaging.

**RP-HPLC** is a quantitative technique capable of separate solute according to their charge and molecular weight, and to quantify their concentration when coupled with a detector, typically a UV-VIS spectrophotometer or a fluorometer (**Horvath et al. [1967]**, **Gerber et al. [2004]**). In drug development and discovery it has been used to detect a number of different molecules, from peptides to anti-cancer drug (**Carr [2002]**, **Tekade et al. [2013]**). In this study, **RP-HPLC** was used to quantify the amount of polymersomes, specifically of rhodamine labelled copolymer, up-taken by the cell.

**FACS** is a technique capable of sorting every cell in the cell individually on the basis of its size and granularity/complexity. As a result, **FACS** allows to separate (sort) different cell type in a sample as they will have different size and granularity (**Dittrich and Gohde [1973]**, **Kiziltepe et al. [2012]**, **Lee and Tung [2011]**). Furthermore, every cell is analysed for fluorescence intensity at a given wavelength. This aspect is of importance for this work as it allows to obtain information regarding the amount of rhodamine labelled polymersomes internalised by cells (**Massignani et al. [2009]**).

**Live cell imaging** , specifically coupled with fluorescence detectors, is a commonly used technique to assess cellular uptake of fluorescent labelled moieties. Traditionally capable of micrometer spatial resolution, it is now possible to break the diffraction limit and to resolve at the nanometer scale (Hell and Wichmann [1994]). Fluorescence microscopy can record intensity of emission from fluorescent material uptaken by cells, and the signal strength is proportional to the amount of material uptaken (Canton and Battaglia [2013], Kim et al. [2009], Discher et al. [2008]).

### 4.1.2 Static and flow *in vitro* cell growth

*In vitro* study of cells in every day laboratory practice is mostly performed on a plastic **Micro well plate (MWP)**. MWPs are a confined environment fully controlled by the researcher, making them ideal to increase reproducibility of the analysis and to study impact of single variables on cellular phenomena. However, cells in the body are subjected to a much more complex environment given by interactions with other cells types, different chemicals and mechanical stimuli. One of the determinants of the local concentration of chemicals is blood flow, as it is responsible for mass transfer. Blood flow affects cells also because of direct mechanical stimuli, to the point that some cells have specifically evolved to sense flow and to adapt phenotype in response to variation of flow. An example of such cells include endothelial cells, the cells that constitute the wall of blood vessels. An interesting study on the effect of shear stress on endothelial cells (HUVEC) was performed by Khan and Sefton. Using a specifically designed microchip that recreates a number of obstructions and channels of different sizes they were able to recreate several different shear stress and flow streamlines within the same chip. They then investigated the changes in expression of VE-cadherin and other adhesion molecules to show a clear effect of the flow on the expression of such molecules and the phenotype of the cells (Khan and Sefton [2011]).

### 4.1.3 Effect of flow on cellular uptake

It is easy to speculate that flow can affect cellular uptake, especially by cells specialised to sense flow such as the endothelial cells. Despite this there is a surprisingly lack of literature supporting this statement, most uptake studies being still conducted in static conditions in **MWP**. A recent study performed by Volkov and co-workers correlates uptake of positively and negatively charged quantum dots and SiO<sub>2</sub>-NPs by endothelial cells (HUVEC) under different shear stress stimulation. Surprisingly, they reported no uptake in static in 20min despite one of the formulation being significantly toxic at the same exposure time. Fur-

thermore, they showed maximum uptake at low shear stress ( $0.05Pa$ ) for all the formulations tested, and then a decrease of up-take that reflects the increase in shear stress, even if the trend was not statistically relevant (Samuel et al. [2012]). In another study Discher and co-workers investigated the effect of flow on up-take of filomicelles of different lengths. They reported how immobilised macrophages under flow rates similar to the ones measured in spleen *in vivo* can recognise and uptake small spherical vesicles, but the flow forces the filomicelles in a streamlined conformation, and as a result a small fragment of the tip can be detached and up-taken, but the majority of the mass of the filaments is rapidly taken away from the cell by the flow therefore prolonging its circulation time in the device. This *in vitro* data was confirmed in *in vivo* results showing circulation half time proportional to filament length (Geng et al. [2007]). To date, no studies have been published providing a comprehensive correlation of uptake for a given polymersomes formulation and cell line with shear stress.

#### 4.1.4 Flow devices

Several devices have been designed to overcome static tissue culture limitations. Such devices tend to be application specific and custom made, not commercially available. Examples include reproduction of blood vessels (Miyakawa et al. [2008], Leong et al. [2013], Samuel et al. [2013]), heart valves (Dumont et al. [2002]), liver (Powers et al. [2002]) and bones (Kim and Ma [2012]). An interesting exception is represented by the flow bio-incubator developed by Mazzei and collaborator, (Mazzei et al. [2010]), and commercialised with the name *Quasi-Vivo*® by Kirkstall, a company based in Sheffield. The system resembles a 24 well plate and has a modular nature which allows interconnecting of chambers to recreate cross-talking between organs, an approach they describe as *organomics*.

An important classification of flow bio-incubator is based on size. Most of the devices cited above have chambers at least millimetre-sized. Another popular type of device is known as micro-fluidic devices. These have the great advantages of being highly reproducible because of the precise manufacturing process and to minimise the requirements of cells, media and other reagents. However, their small size is also their main limitation. Because of the limited number of cells used they cannot be representative of big and complex tissues (Tingley [2006]). Furthermore, because of their geometry they have a big edge/surface ratio (Lundholt et al. [2003]).

### 4.1.5 Aim

RP-HPLC, FACS and live cell imaging are all techniques suitable for quantifying polymersomes uptake. In routine screening for uptake the technique giving the most accurate results should be used, and that technique should ideally be fast and easy to set-up. Here the three techniques were compared and integrated in the study of uptake of different formulations by different cell type. The aim was to validate the use of live cell microscopy as a semi-quantitative technique to screen polymersomes uptake by tumour-relevant cell types: tumour cells (Mouse Fibrosarcoma Cell (MFC)), endothelial cells (SVECs) and perivascular cell (10T1/2). Furthermore, the analysis protocols will be applied to *in flow* uptake studies, to elucidate the role of shear stress and fluid velocity on cellular uptake. This is critical as polymersomes will be administered *in vivo* Intra Venous (i.v.), therefore they will be subjected to flow dynamics.

## 4.2 Results

### 4.2.1 Static conditions

#### Quantification of uptake with RP-HPLC, FACS and live cell imaging

The technique of choice in this work is imaging, therefore almost all uptake data collected will be based on image analysis. Comparison with established analytical techniques RP-HPLC and FACS was used to validate the method. MFC188 cells were treated with  $1\text{mg/ml}$  of rhodamine labelled Poly(2 - methacryloxyethyl-phosphorylcholine)-poly( 2 -(diisopropylamino)ethyl methacrylate) (PMPC-PDPA) polymersomes and the uptake was quantified with RP-HPLC, FACS and live cell image analysis. All three methods showed very similar uptake profile (fig. 4.1).

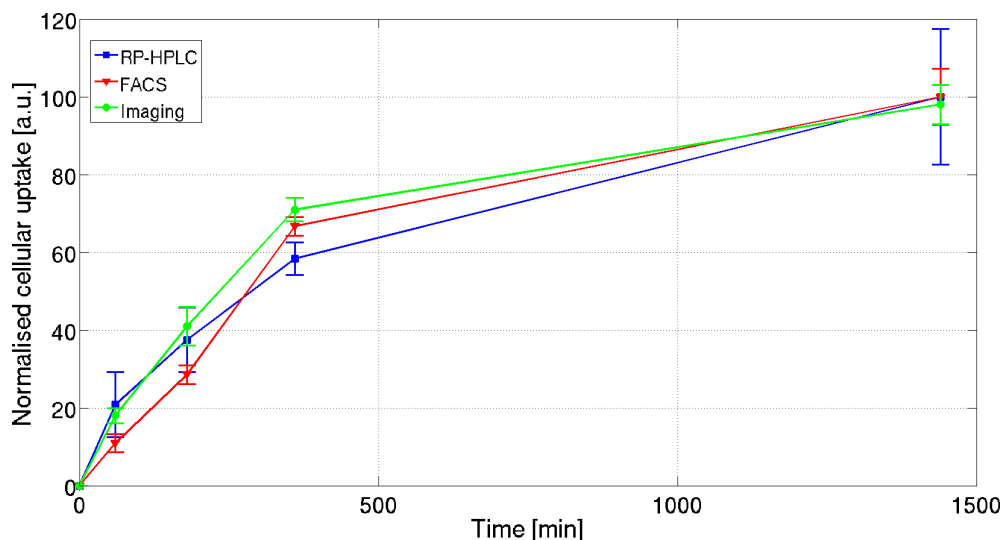


Figure 4.1: *RP-HPLC*, *FACS* and live cell imaging comparison. All uptake refer to 10% rhodamine labelled *PMPC-PDPA* polymersomes, 1mg/ml, *MFC188* cells. All data were normalised with respect to the maximal uptake for the relative quantitative technique, corresponding to the uptake at  $t=24h$ . All techniques have similar uptake profile.  $N=3$ ,  $\pm SD$ .

Once confirmed the validity of the method, live cell imaging analysis was used to compare uptake of rhodamine labelled *PMPC-PDPA* and poly(oligo(ethylene glycol) methacrylate)-poly(2-(diisopropylamino)ethyl methacrylate) (*POEGMA-PDPA*) polymersomes from *MFC188*, *SVECs* and *10T1/2*. All cells were treated for up to 24h with 1mg/ml of rhodamine labelled polymersomes. For any of the three cell types, uptake of *PMPC-PDPA* polymersomes was higher compared to *POEGMA-PDPA* ( $p < 0.05$ ) (fig. 4.2). This was observed both in *FACS* and image analysis. *MFC188* had higher uptake compared to *SVECs* or *10T1/2*, especially for *PMPC-PDPA* polymersomes.

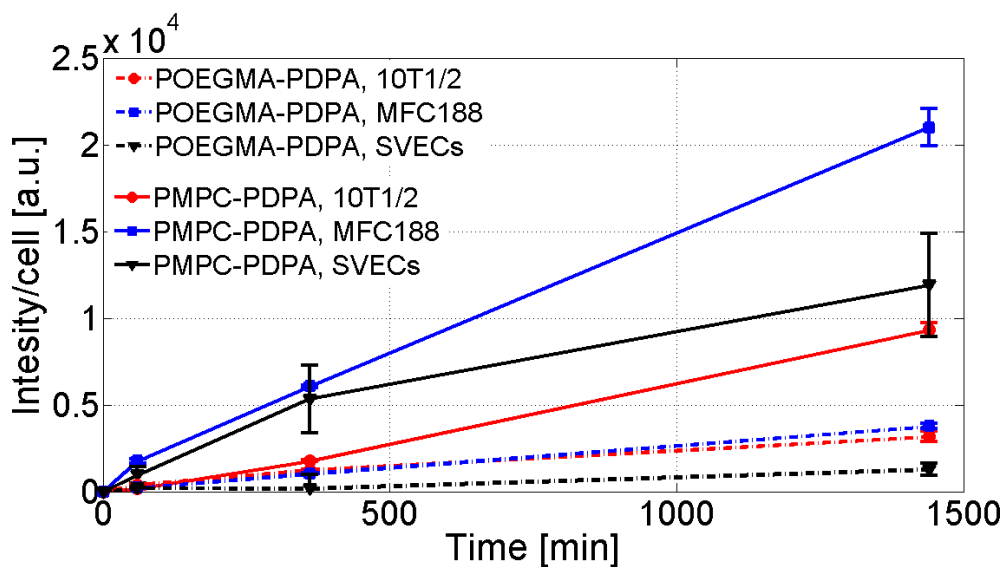
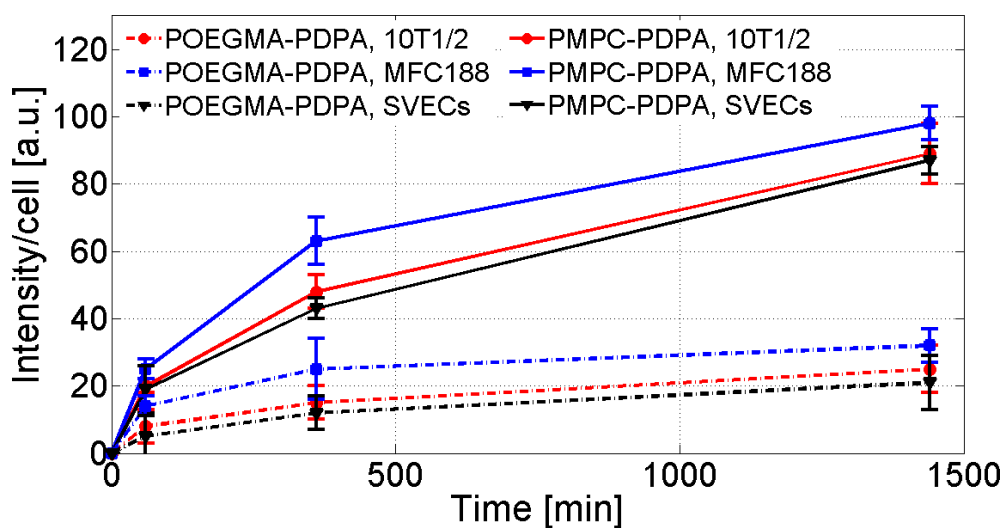
(a) *FACS*(b) *Image analysis*

Figure 4.2: Quantification of uptake of rhodamine labelled *PMPC-PDPA* and *POEGMA-PDPA* polymersome by *10T1/2*, *MFC188* and *SVECs*. Uptake was quantified by *FACS* (a) and image analysis (b). *PMPC-PDPA* uptake was greater than *POEGMA-PDPA*, and *MFC188* had greater uptake compared to *SVECs* or *10T1/2*, with the only exception of uptake of *POEGMA-PDPA* measured by *FACS*.  $N=3$ ,  $\pm SD$ .

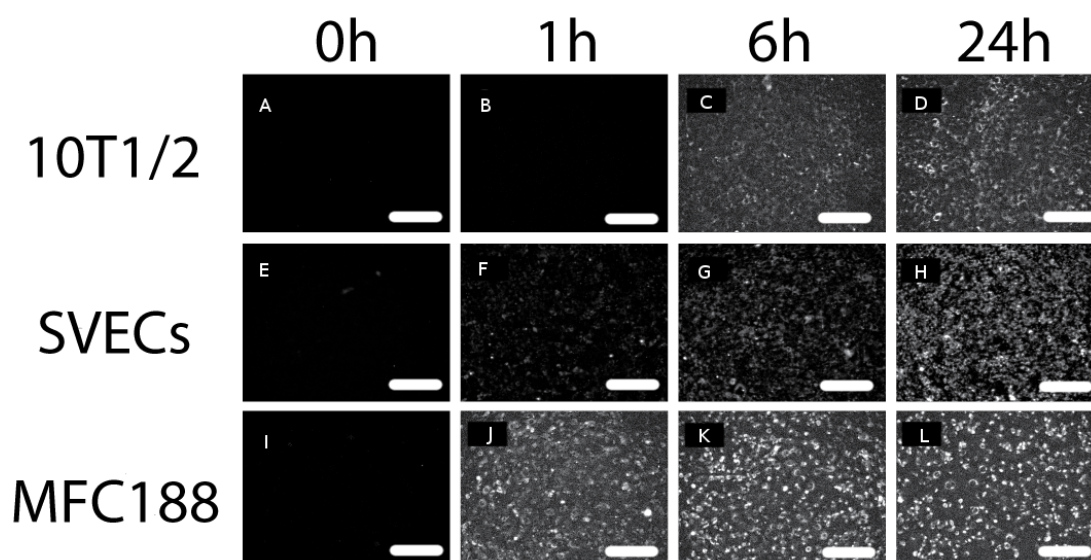


Figure 4.3: Representative images of *PMPC-PDPA* uptake in live cells imaging from 10T1/2 (A, B, C, D), *MFC188* (E, F, G, H) and *SVECs* (I, J, K, L). Images were acquired at 0h, 1h, 6h and 24h. Cells cultured in static conditions. Uptake in *MFC188* is greater than uptake in 10T1/2 or *SVECs*. Bar 70 $\mu$ m.

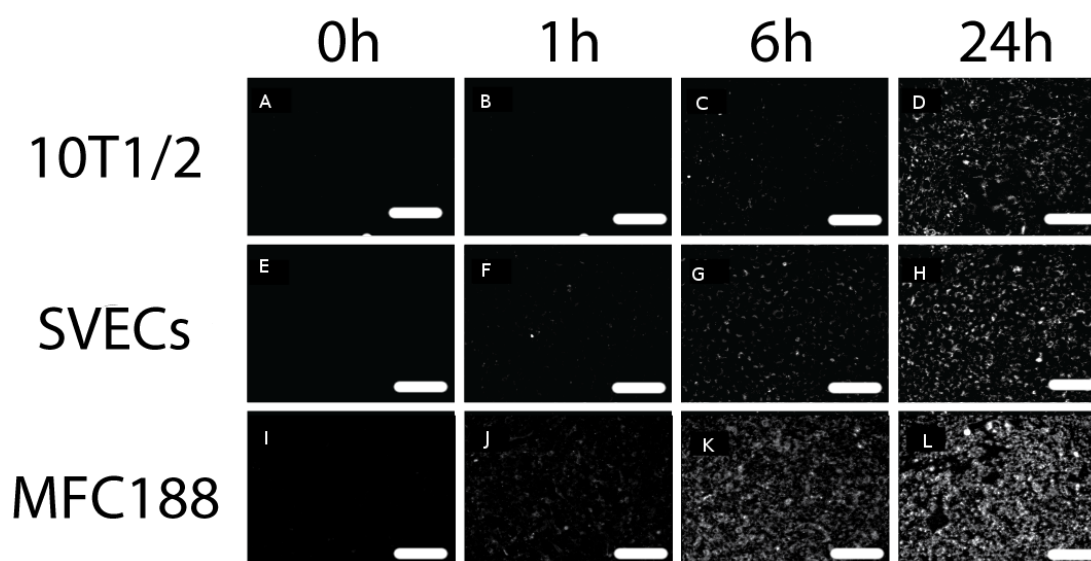


Figure 4.4: Representative images of *POEGMA-PDPA* uptake in live cells imaging from 10T1/2 (A, B, C, D), *MFC188* (E, F, G, H) and *SVECs* (I, J, K, L). Images were acquired at 0h, 1h, 6h and 24h. Cells cultured in static conditions. Uptake in *MFC188* is greater than uptake in 10T1/2 or *SVECs*. Bar 70 $\mu$ m.

#### 4.2.2 Flow bio-incubator

##### Flow bio-incubator optimisation

The flow bio-incubator developed here was based on the 24 well plate geometry for easy translation of existing experimental protocols to the new device.

COMSOL Mutliphysics was employed to assess shear stress at the cellular level and to optimise the design to deliver a homogeneous flow. From the first simulations run a clear problem emerged: the inlet and outlet positioned perpendicular to the cell plane generated a high local peak of shear stress. Furthermore, this design was difficult to assemble in a reproducible manner: the tubes were subjected to movement that deviated from the simulated perpendicular angle (see fig. 4.5).

To protect the cells from perpendicular flow a *shield* was introduced, so that the liquid was entering the well parallel to the cell surface. This was achieved using L-shaped elbow connectors attached to the tubing. The elbow connectors had several advantages. Their bulk volume substituted liquid volume in the well, reducing the amount of media needed. Furthermore, the inlet and the outlet shield provided stability to the tubing reducing movement. As with the previous design, the position of the tubing was optimised using *in silico* modelling. Results from the simulations are reported in figure 4.6-4.7. When inlet and outlet are too close to the cells ( $H=1mm$ ) there is almost no flow at the cell level (velocity and shear stress close to 0). At medium high ( $H=4mm$ ) the situation improved, and finally at  $H=7mm$  the flow was higher, but less parallel to the horizontal plane. Regarding the relative position of inlet and outlet it was found that if they are located close to the edge the flow profile was irregular with localised peaks of shear stress and velocity close to the wall edges. If the tubes are located close to the centre the profile was more homogeneous. Considering the *in silico* results, the model chosen was with inlet and outlet located at the edges of the well and at  $4mm$  from the cell level. This model was the easiest to assemble in a controlled way, and it gave a good balance between homogeneous flow at the cellular level and shear stress-velocity magnitude range in relation to the peristaltic pump set-up. Positioning the tubing further away from the cells would have caused loss of accuracy at lower *rpm* and flow rate, which are the critical parameter to use when simulating low flow rates such as those characteristic of the tumour microenvironment.

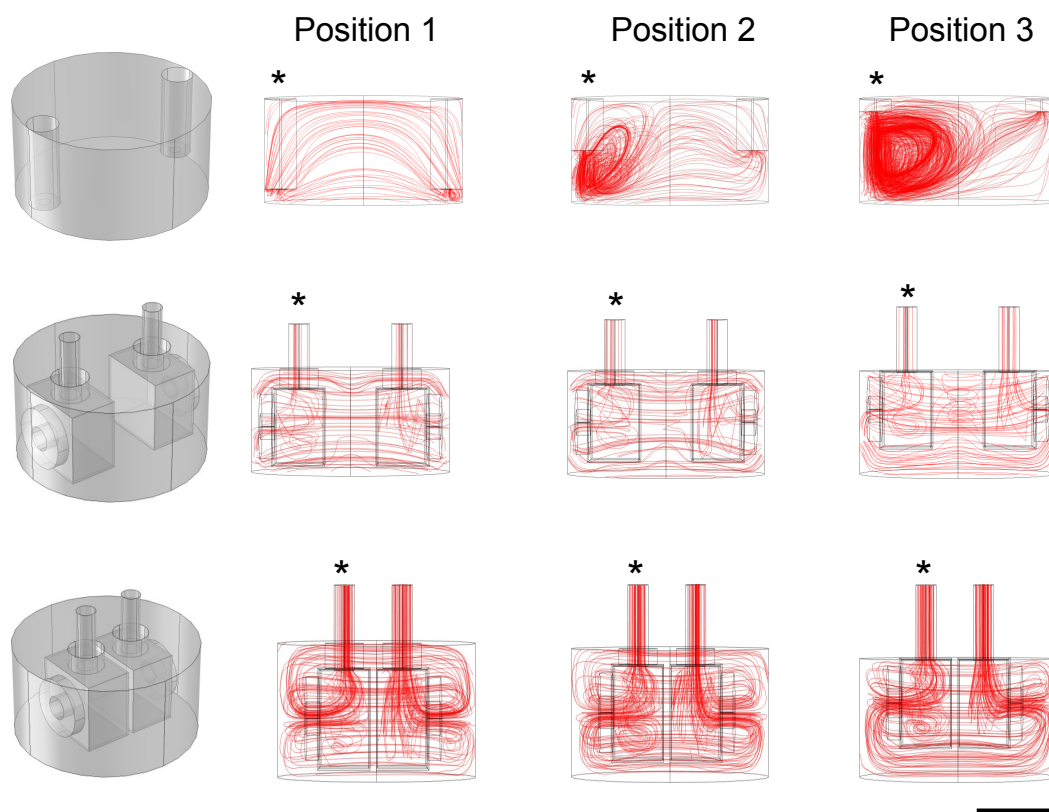


Figure 4.5: *Flow device models. The three proposed flow device models. The first model (top row) had no shield. The second and third models (second and bottom rows) had a shield orientating the flow parallel to the cell plane. The difference between the two models is in the relative position of the inlet and the outlet. In the second model they are close to the well wall, in the third model they are located close to each other. In silico simulations were run positioning the tubing at close to the bottom of the well (left column, Position 1), in the middle of the well (middle column, Position 2) or far from the cell level (right column, Position 3). Flow =  $20\mu\text{L/s}$ . \* Identifies the inlet. Scale bar 7mm.*

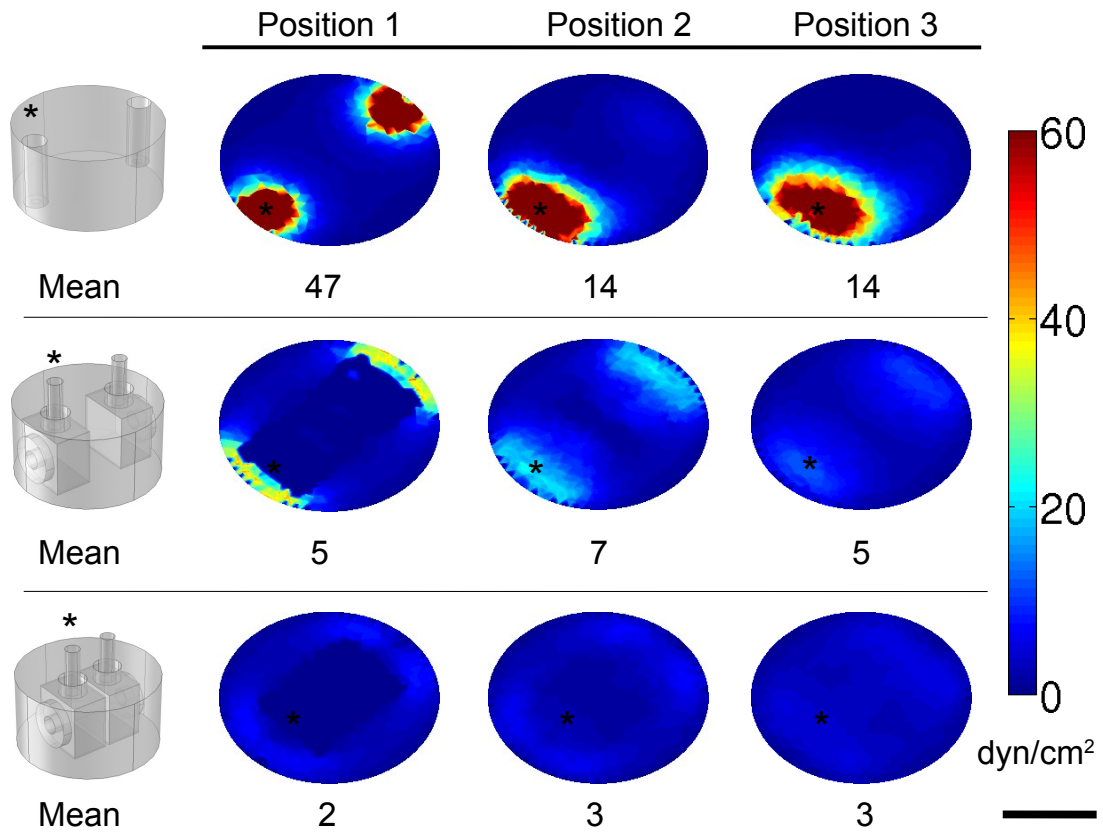


Figure 4.6: Shear stress distribution across the three models. The coloured disc represent the plane of cell growth (bottom of the well). When no shield is present (top row) there is high heterogeneity between different areas of the well depending on their location with respect to the inlet or the outlet. When a shield was used (second and third rows) the shear stress distribution was more homogeneous. However, when the shield was too close to the bottom of the well (Position 1) there was almost no flow (shear stress  $\simeq 0 \text{ dyn} \cdot \text{cm}^{-2}$  under the shield itself). Mean refers to the mean shear stress generated  $5 \mu\text{m}$  from the bottom of the well. Flow =  $20 \mu\text{L/s}$ . \* Identifies the inlet. Scale bar 7mm.

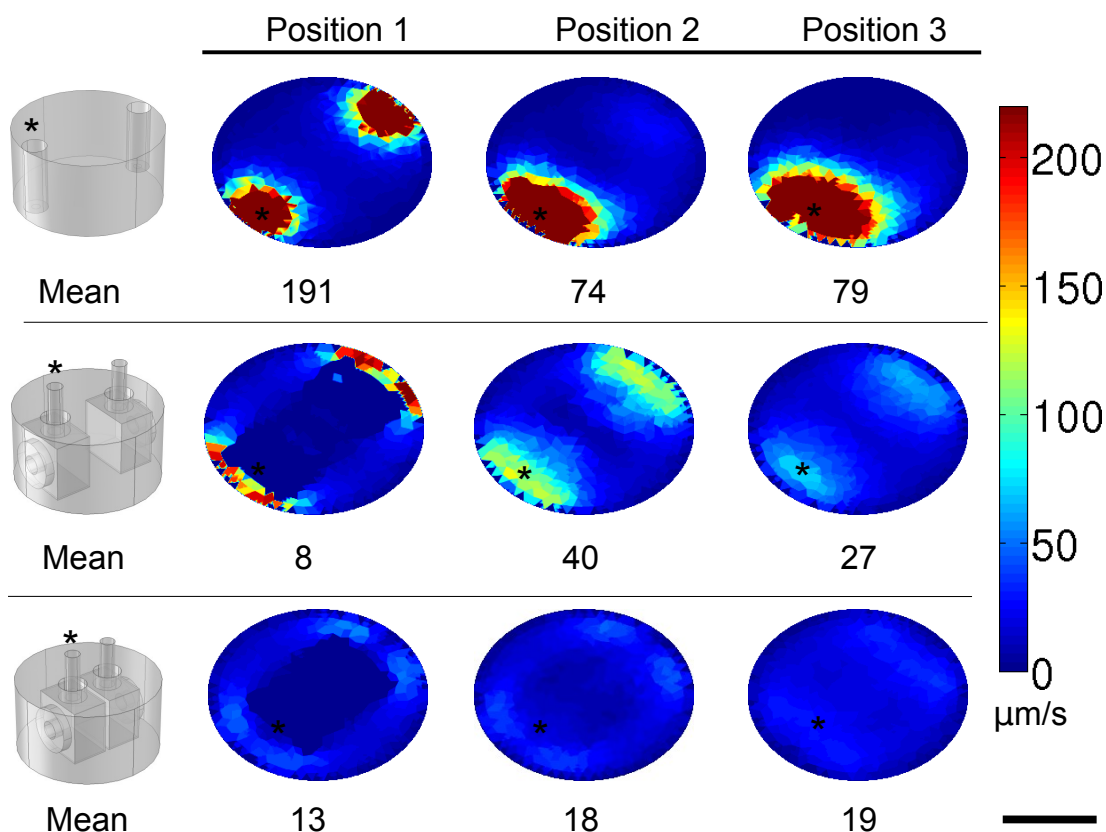


Figure 4.7: Velocity distribution across the three models. The velocity considered here is the total absolute velocity parallel to the cell plane. The coloured disc represent the plane of cell growth (bottom of the well). The general observations reported for shear stress in figure 4.6 are confirmed for the velocity profiles here presented. Mean refers to the mean velocity generated  $5\mu\text{m}$  from the bottom of the well. Flow =  $20\mu\text{L/s}$ . \* Identifies the inlet. Scale bar  $7\text{mm}$ .

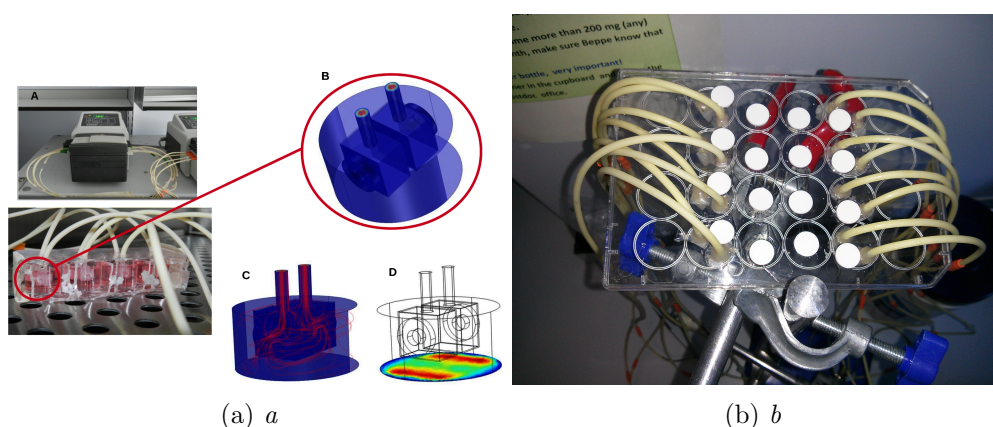


Figure 4.8: Flow device overview. The wells are connected with  $0.8\text{mm}$  bore tubing to a peristaltic pump. In (a) the elbow connectors are made visible by sectioning the well plate. In (b) the lid used is visible. The white circles are self-sealing membrane pierced with a  $30\text{G}$  needle when injecting polymersomes into the system.

## Cell viability

Cell viability was measured as described previously (sec. 2.4.2), and cell viability of cells growing in static was compared to cell viability of cells growing under flow. The flow rate chosen for this analysis was  $30\mu\text{l}/\text{s}$  because this value is 50% higher than the maximum value planned to be used in the uptake experiment, and it was assumed that if cells have no significant decrease in viability at this flow rate, then any lower flow rate could have been used without compromising cell viability. Cell viability was assessed for MFC188, SVECs and 10T1/2 treated with Transforming Growth Factor- $\beta$ 1 (TGF- $\beta$ 1). Results are reported in figure 4.9. No significant decrease in viability was observed for any of the cell lines ( $p>0.05$ ).

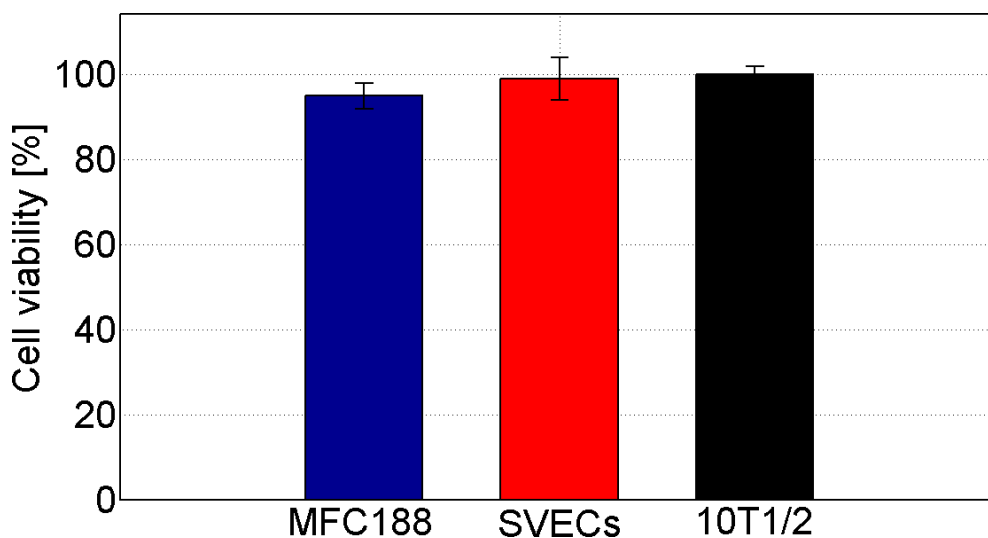


Figure 4.9: Cell viability in flow, (3 - (4,5 - Dimethylthiazol - 2 - yl) - 2,5 - diphenyltetrazolium bromide (MTT) assay. Cell viability was assessed for 10T1/2, MFC188 and SVECs. No significant decrease in cell viability was observed for any of the cell type used with respect of the same cell type cultured in static condition: 100% viability (U-test,  $p>0.05$ ). Flow rate was  $30\mu\text{L}/\text{s}$ .  $N=3$ ,  $\pm\text{SD}$ .

## Cellular uptake

In this study we compared uptake at  $20\mu\text{l}/\text{s}$  with uptake in no flow conditions. We compared PMPC-PDPA and POEGMA-PDPA, MFC188, SVECs and 10T1/2. Uptake was quantified by FACS and live cell image analysis. Results from both analysis showed higher uptake of polymersomes in static compared to in flow conditions. Furthermore, uptake of PMPC-PDPA polymersomes is higher than uptake of POEGMA-PDPA. Cell imaging allowed for better resolution, probably due to a better sensitivity. Analysis of cell imaging data revealed that in flow conditions the difference in uptake kinetics between the two formu-

lations is minimal compared to the difference of uptake in static conditions. For example, uptake of PMPC-PDPA at 24h from SVECs is double compared to the uptake of POEGMA-PDPA, while in flow there was no significant difference. It is also interesting to notice that the difference between different cell types is minimal in flow compared to static, where *mfc188* showed the greater uptake and 10T1/2 the lowest. Image analysis and FACS results are reported in fig. 4.11. FACS data expressed as percentage of cells positive for rhodamine over time are reported in section 9.2, figure 9.5-9.7.

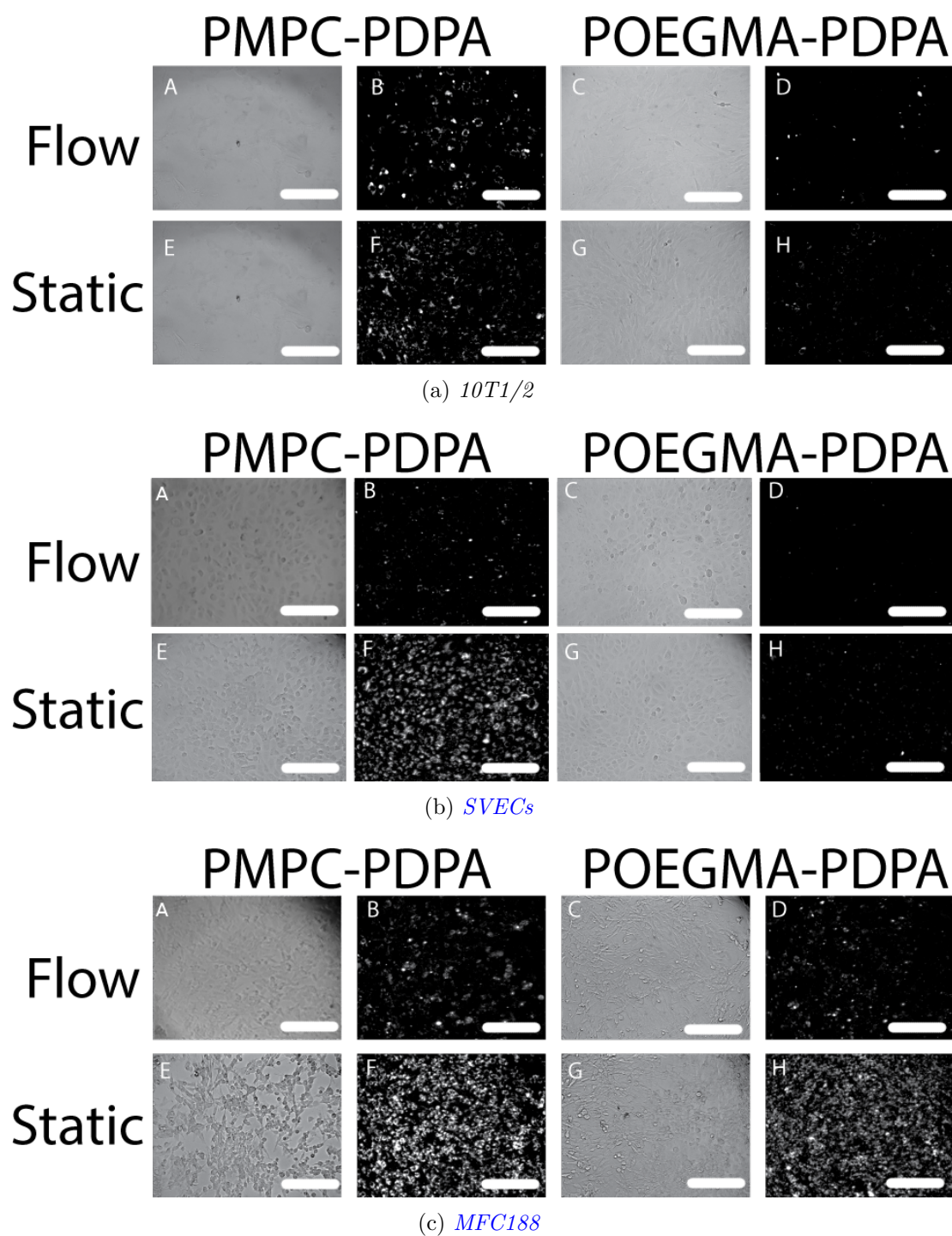


Figure 4.10: Uptake of *PMPC-PDPA* (b, f) and *POEGMA-PDPA* (d, h) from *10T1/2*, *MFC188* and *SVECs* in static and in flow ( $20\mu\text{l/s}$ ). Images a, c, e, g are bright field images showing cells distributions in the well. Uptake in static conditions is greater than uptake in flow, and uptake of *PMPC-PDPA* is greater than uptake of *POEGMA-PDPA*. In static condition uptake from *MFC188* is greater than uptake from *SVECs* or *10T1/2*, while in flow conditions there is little difference between the three cell types. Bar  $170\mu\text{m}$ .

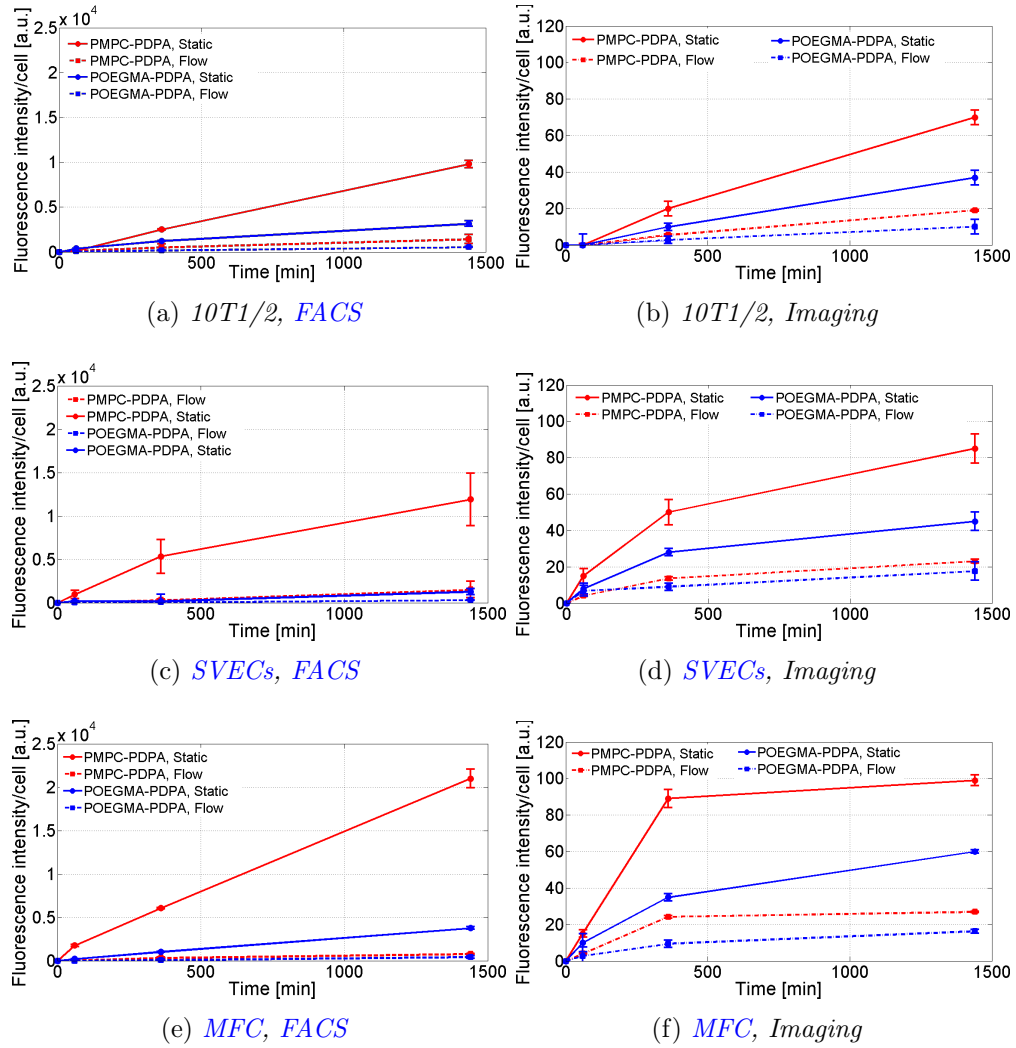


Figure 4.11: Quantification of uptake in static (solid lines) and in flow (dotted lines) conditions with *FACS* (a, c, e) and *imaging* (b, d, f). Uptake was quantified for *PMPC-PDPA* (red lines) and *POEGMA-PDPA* (blue lines) polymersomes. *10T1/2* (a, b), *SVECs* (c, d) and *MFC188* (e, f) cells were compared. Uptake in static conditions is greater than uptake in flow, and uptake of *PMPC-PDPA* is greater than uptake of *POEGMA-PDPA*. In static condition uptake from *MFC188* is greater than uptake from *SVECs* or *10T1/2*, while in flow conditions there is little difference between the three cell types.  $N=3$ ,  $\pm SD$ .

### Image analysis and well mapping

In the developed device, shear stress and velocity magnitude at the cell growth level is not perfectly homogeneous (see fig. 4.6-4.7). This is generally regarded as a disadvantage, especially compared to commercially available flow macro-chamber (i.e Ibidi IV<sup>0.4</sup> chamber slides) or microfluidic devices. In those bio-incubators the flow delivered is perfectly homogeneous across the whole observation chamber. However, in this study this can be used as an advantage. First of all, it can reproduce heterogeneous flow in tumour microenvironment, but it can

also be used to obtain uptake data in different flow conditions from the same well. In this situation the only variable is the flow rate at the cell level, as the rest of the well is exactly the same (same cells, same formulation, same pH and temperature). In order to correlate uptake with different areas of the well characterised by different shear stress, parallel (horizontal) or perpendicular (vertical) velocity the microscope was programmed to acquire images in different areas of the well, and the well was divided into eight regions having different flow properties. This was of interest because it was hypothesised that cells exposed to different flow rate, therefore to different shear stress and flow velocity, could not only exhibit altered phenotype, such as elongated shape as already reported for endothelial cells (Khan and Sefton [2011]), but also different uptake. The analytical method here reported will allow quantify uptake in relation to flow parameter in the same well, therefore in cells otherwise identical. This approach will also increase the throughput of the analysis by allowing multiple data collection (i.e uptake *vs* flow) in the same well. The process of dividing the well into different areas characterised by different flow properties is described in section 3.5.2-3.5.3. Details of the different Regions of interest (ROI)s with corresponding physical properties are reported in table 4.1-4.3. This analysis was performed for PMPC-PDPA polymersomes up-taken by MFC188.

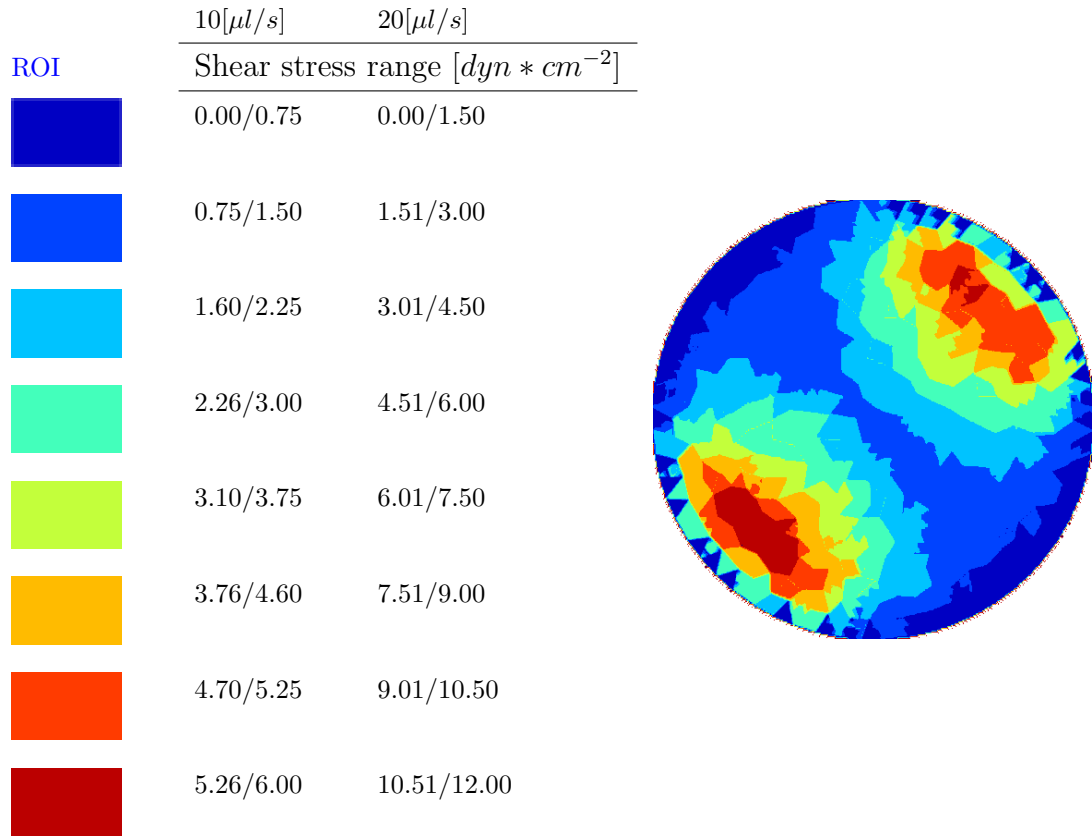


Table 4.1: *ROI segmentation for shear stress. Shear stress in  $\text{dyn} * \text{cm}^{-2}$ . Data for flow rate of  $10\mu\text{l} * \text{s}^{-1}$  and  $20\mu\text{l} * \text{s}^{-1}$ . Data refers to division of ROI from Position 2, shield located near walls, reported in figure 4.6. The resulting well segmentation with all eight different ROI is reported.*

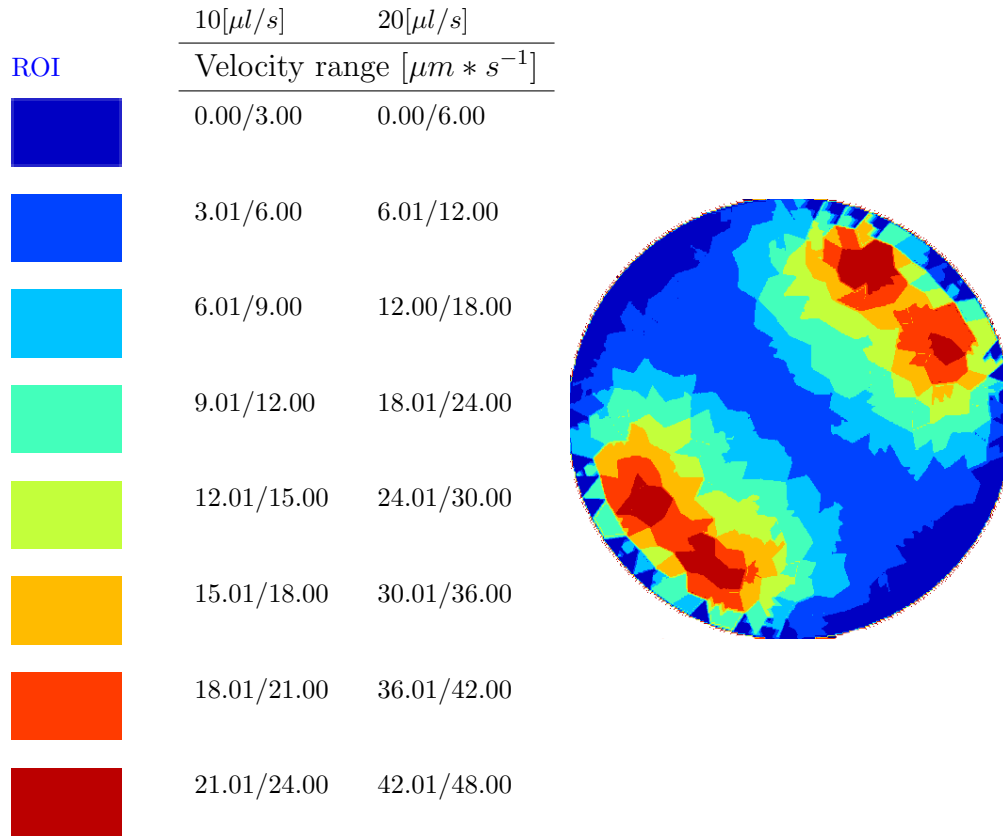


Table 4.2: *ROI segmentation for horizontal velocity magnitude. Velocity in  $\mu\text{m} * \text{s}^{-1}$ . Data for flow rate of  $10\mu\text{l} * \text{s}^{-1}$  and  $20\mu\text{l} * \text{s}^{-1}$ . Data refers to division of ROI from Position 2, shield located near walls, reported in figure 4.7. The resulting well segmentation with all eight different ROI is reported.*

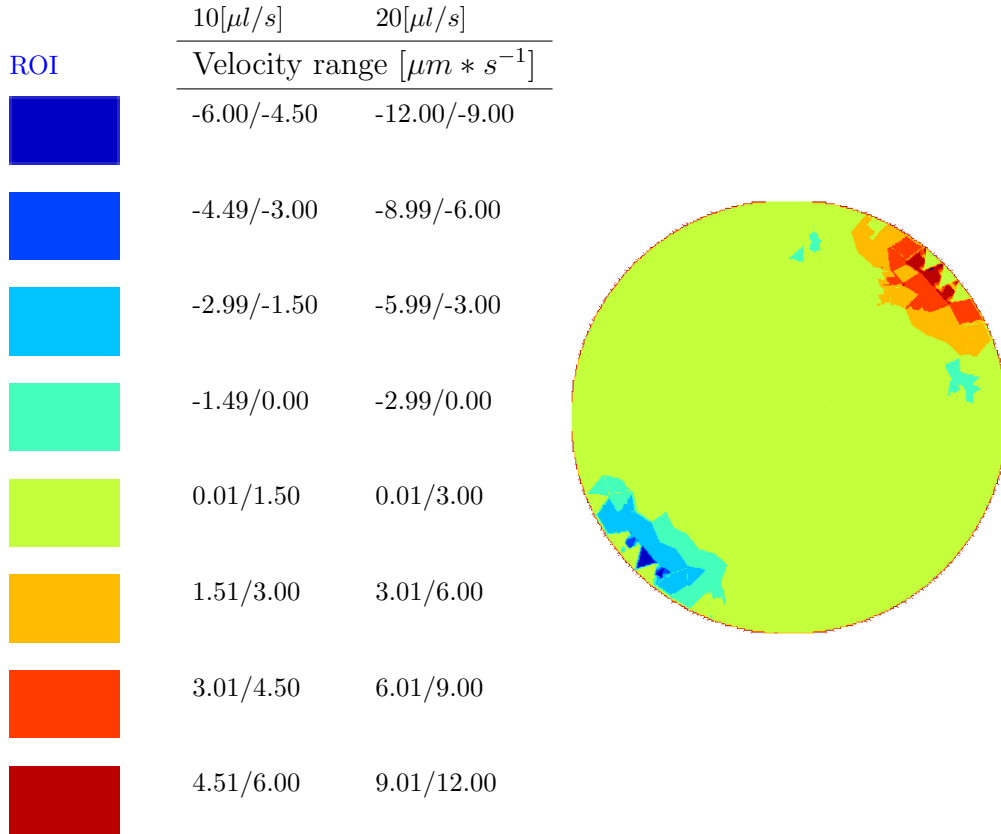


Table 4.3: *ROI segmentation for vertical velocity magnitude. Velocity in  $\mu\text{m} * \text{s}^{-1}$ . Data for flow rate of  $10\mu\text{l} * \text{s}^{-1}$  and  $20\mu\text{l} * \text{s}^{-1}$ . Data refers to division of ROI from Position 2, shield located near walls, reported in figure 4.7. The resulting well segmentation with all eight different ROI is reported.*

Images recorded by the epifluorescence BD-Pathway 855 microscope equipped with a 4X objective were analysed as described previously (sections 3.5.2-3.5.3) to correlate average fluorescence intensity with any specific flow parameter. Results are reported in figure 4.12-4.14. Analysis revealed higher uptake ( $p < 0.05$ ) in static compared than in flow, as already seen in FACS and single image analysis (section 4.11). Furthermore, it can be observed that uptake at  $10\mu\text{l} * \text{s}^{-1}$  is higher than uptake at  $20\mu\text{l} * \text{s}^{-1}$ , particularly at the  $t=24\text{h}$  time point. However, the relative small difference seems to indicate that in the range of flow rates studied there is no significant difference of uptake ( $p > 0.05$ ): there is a significant difference compared to static conditions, but once flow is applied the difference is minimal across the range  $10\text{-}20\mu\text{l} * \text{s}^{-1}$ . Shear stress and horizontal velocity magnitude had a peak of uptake generally located in the middle of the well, corresponding to average values and more horizontal fluid streamline (see fig. 4.5). Vertical velocity showed a higher correlation of increased uptake with increased velocity magnitude, with higher uptake in areas with higher velocity.

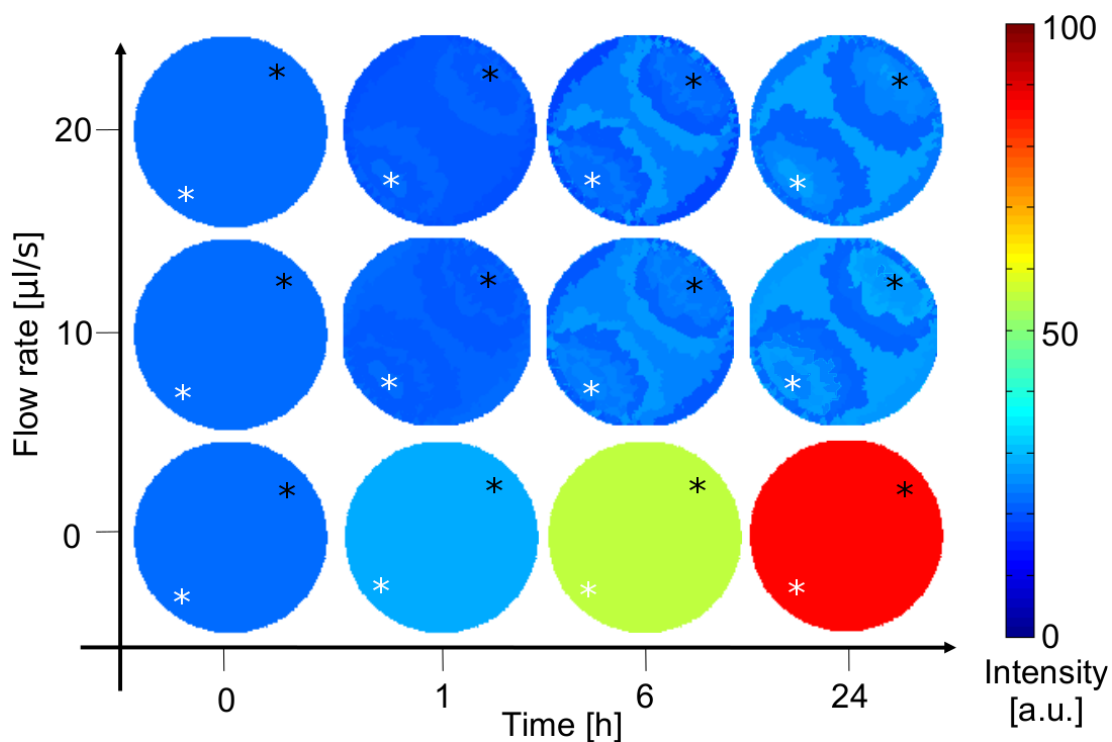


Figure 4.12: Mapping of rhodamine intensity in the eight different ROI for shear stress. The average intensity measured in the area of a given ROI, identified as described in figure 3.10 is represented in colour code from blue (low intensity) to red (high intensity). Intensity is proportional to polymersomes uptake. Analysis refers to PMPC-PDPA polymersomes uptake by MFC188. In static condition (bottom row) uptake was homogeneous across the well. Uptake in flow at  $20\mu\text{l/s}$  and  $10\mu\text{l/s}$  was similar and uptake in the center of the well was greater than on the ROI corresponding to the inlet (white asterisk) and the outlet (black asterisk) region.

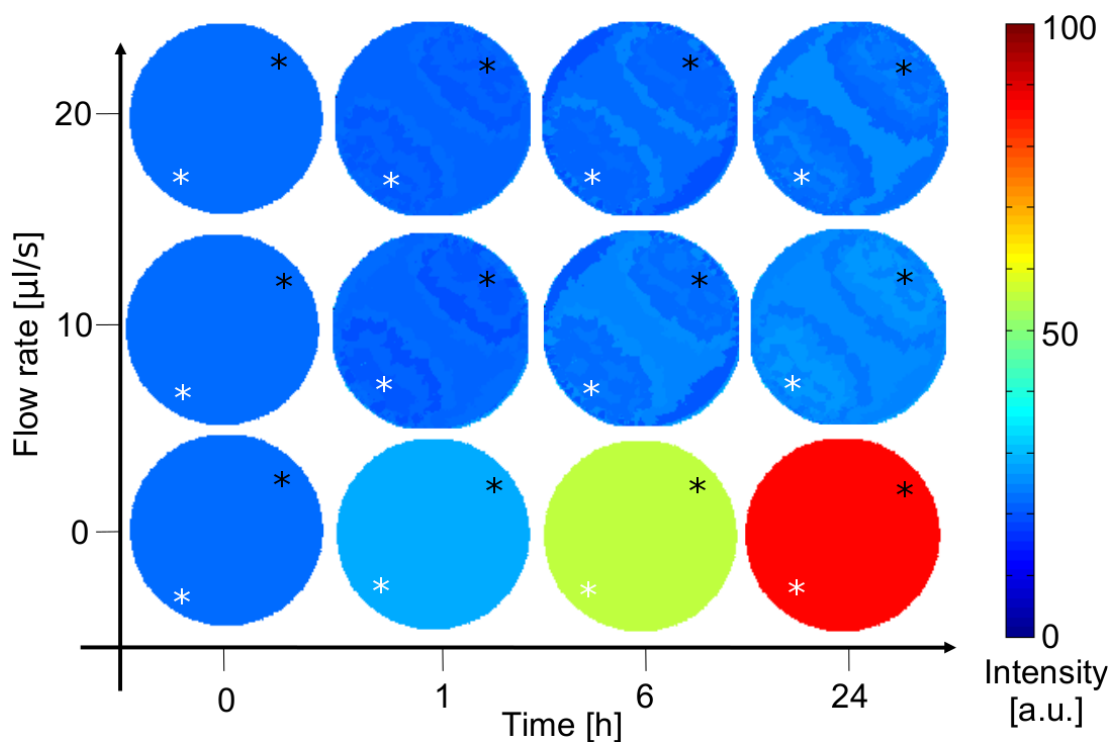


Figure 4.13: Mapping of rhodamine intensity in the eight different ROI for shear stress. The average intensity measured in the area of a given ROI, identified as described in figure 3.10 is represented in colour code from blue (low intensity) to red (high intensity). Intensity is proportional to polymersomes uptake. Analysis refers to PMPC-PDPA polymersomes uptake by MFC188. In static condition (bottom row) uptake was homogeneous across the well. Uptake in flow at  $20\mu\text{l/s}$  and  $10\mu\text{l/s}$  was similar and uptake in the center of the well was greater than on the ROI corresponding to the inlet (white asterisk) and the outlet (black asterisk) region.

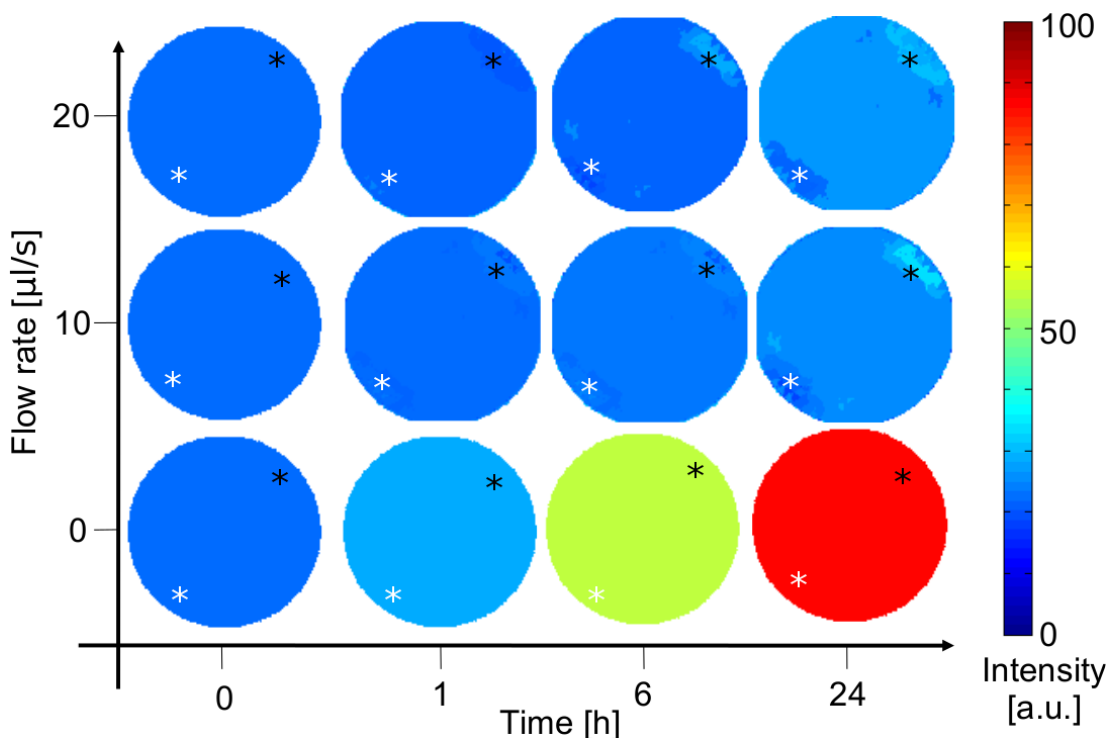


Figure 4.14: Mapping of rhodamine intensity in the eight different ROI for shear stress. The average intensity measured in the area of a given ROI, identified as described in figure 3.10 is represented in colour code from blue (low intensity) to red (high intensity). Intensity is proportional to polymersomes uptake. Analysis refers to PMPC-PDPA polymersomes uptake by MFC188. In static condition (bottom row) uptake was homogeneous across the well. Uptake in flow at  $20\mu\text{l/s}$  and  $10\mu\text{l/s}$  was similar and uptake in the center of the well was greater than on the ROI corresponding to the inlet (white asterisk) and the outlet (black asterisk) region.

## 4.3 Discussion

In this work, polymersomes will be engineered to image the tumour microenvironment. Before screening different formulations *in vivo*, polymersomes were tested *in vitro* for uptake kinetics in three tumour relevant cell types: tumour cells (MFC188), endothelial cells (SVECs) and perivascular cells (10T1/2). These three cell types were specifically chosen as they represents an *in vitro* model of the tumour that was implanted in *in vivo* experiments, obtained from MFC188 spheroid. This specific cell type is known to form tumours well vascularised and rich on perivascular cells (Akerman et al. [2013]). 10T1/2 are *in vitro* precursors of perivascular cells.

Two different polymersome formulations were tested: PMPC-PDPA and POEGMA-PDPA. The two formulations chosen were expected to have different uptake kinetics, with PMPC-PDPA having faster uptake compared to POEGMA-PDPA.

The kinetic of uptake of fluorescent labelled polymersomes can be monitored using RP-HPLC, FACS and cell imaging. RP-HPLC and FACS are commonly used quantitative techniques, however they are less suitable to fast and sensitive screening than live cell imaging because of longer sample preparation. RP-HPLC is useful to quantify the exact amount of fluorescent labelled polymersomes delivered to the whole cell population. FACS analysis can sort cells in co-culture systems and analyse intensity at the single cell level. FACS cannot exactly quantify the amount of polymersomes delivered to the cells. Live cell imaging is the most sensitive technique as it allows to monitor uptake at the subcellular level. Like FACS, image analysis cannot quantify the exact amount of polymersomes up-taken, however it is a faster technique and it allows continuous monitoring of the same group of cells for the entire analysis, limiting the amount of materials required to perform the analysis. These characteristics make live cell imaging the ideal candidate for high throughput screening.

The image analysis method reported in section 3.4 was validated through comparison with RP-HPLC and FACS. The validation was performed studying uptake of 10% rhodamine labelled PMPC-PDPA polymersomes from MFC188. This formulation was chosen as it is known to have fast and high uptake from many cell type, especially cancer cells (Massignani et al. [2010], Pegoraro et al. [2014], Colley et al. [2014]). Results showed a very similar uptake profile in the time of analysis considered (up to 24h, fig. 4.1). Following experiments were therefore performed analysing uptake preferentially with optical imaging, and using FACS for confirmation. RP-HPLC was abandoned as it was considerably more time consuming and not suitable for high throughput set-up.

Uptake kinetics analysis showed a faster uptake for PMPC-PDPA compared to poly(2-(diisopropylamino)ethyl methacrylate) (PDPA), and a greater uptake from MFC188 compared to SVECs or 10T1/2. These findings are consistent with the reported mechanism of uptake of PMPC-PDPA, which is mediated by scavenger receptor SR-B1 (Colley et al. [2014]). POEGMA-PDPA uptake is not receptor mediated, therefore it was expected to have slower uptake. Furthermore, it has already been reported that PMPC-PDPA polymersomes have faster uptake compared to Polyethylen Oxide-poly(2-(diisopropylamino)ethyl methacrylate) (PEO-PDPA) polymersomes (Murdoch et al. [2010]). The hydrophilic block POEGMA used here is a chemically related to Polyethylene Oxide (PEO), as it is essentially made by short PEO chains linked to a polymeric backbone. Finally, the cited work of Colley and co-workers (Colley et al. [2014]) reported how tumour cells have greater expression of scavenger receptors compared to normal cells. Further experiments confirming the validity of the statement for MFC188 could explain the greater polymersomes uptake observed in this cell type com-

pared to SVECs and 10T1/2.

Uptake studies performed in static tissue culture conditions are a laboratory standard. However, cells in the natural environment are growing in completely different conditions, caused by different surrounding (i.e. other cell lines present in proximity), extracellular matrix and shear stress. This latter one can be mimicked *in vitro* by using a flow bio-incubator. There are several flow chambers commercially available, however most of them are developed to mimic specific environments, such as coronary vessels, or to be used in conjunction with specific techniques, usually live cell imaging.

Considering that a number of protocols for RP-HPLC, FACS and live cell imaging analysis of uptake have been developed in the first part of the work, it was decided to develop a flow bio-incubator that allowed easy transfer of pre-existing protocols. The device was based on the geometry of 24 well plate. *In silico* modelling was used to optimise the design of the device so that the flow delivered was as uniform as possible and to make sure that the shear stress and flow rate delivered were comparable to the physiological ones at the capillary level:  $\tau = 100 \text{ dyn} \cdot \text{cm}^{-2}$ ,  $U = 10 - 100 \mu\text{m} \cdot \text{s}^{-1}$  (Decuzzi and Ferrari [2006]). It should be noted that for the flow rates used in the final experiments (10-20  $\mu\text{l}/\text{s}$ ) the corresponding fluid velocity was well within the indicated range, while the shear stress was  $\simeq 8$  times lower. However, tumour microvasculature is characterised by irregular flow compared to healthy capillaries, therefore it could be that the stated value of  $100 \text{ dyn} \cdot \text{cm}^{-2}$  is lower in tumours. Furthermore, the experimental set-up used media, a Newtonian fluid with viscosity significantly lower than blood. Further development of the device will be focused on the use of more viscous media, for instance by adding dextran to the media.

Whole-well analysis of uptake kinetics were performed by FACS and cell imaging. The two analysis methods showed significant decrease of uptake for all cell lines under flow compared to static uptake. Furthermore, the difference of uptake between the two polymersome formulations PMPC-PDPA and POEGMA-PDPA was significantly reduced. This could be explained considering that uptake is a dynamic event requiring interactions of polymersomes with specific cellular structures, such as scavenger receptors SR-B1 for PMPC-PDPA. When polymersomes are administered under flow, they are carried away from the cell surface by the flow. This is likely to reduce the interaction time between polymersomes and the receptors, and therefore to decrease the uptake rate. Furthermore, by limiting the receptor mediated uptake, the difference between PMPC-PDPA and POEGMA-PDPA observed in static are likely to be reduced consequently.

A close observation of the shear stress and velocity magnitude profile at the cell level (fig. 4.5-4.7) revealed areas characterised by different flow parameters.

This could be seen as a disadvantage of the device developed, which is unable to deliver perfectly homogeneous flow. However, live cell imaging unique capability to focus on different areas of the plate can be used to obtain uptake data of cells growing in slightly different conditions, but still on the same well. Potentially, this can considerably decrease the amount of materials and experiments needed to characterise uptake and flow correlation, with a positive impact on analysis throughput.

Cell growth area was divided in 8 different ROIs corresponding to 8 areas characterised by different horizontal or vertical velocity magnitude or shear stress. Fluorescence intensity of cells growing in one of the 8 ROI was use to map the uptake intensity in the area *vs* the corresponding physical parameter. For this analysis uptake in static (control) was compared to uptake at  $10\mu/l$  and  $20\mu/l$ . For the development and testing of the method the same combination of cell type and polymersome formulation used to validate imaging was chosen: MFC188 and 10% rhodamine labelled PMPC-PDPA.

Data showed a small but not significant ( $p>0.05$ ) difference between uptake at  $10\mu l \cdot s^{-1}$  and  $20\mu l \cdot s^{-1}$ . However, there is a clear decrease of uptake between no flow and  $10\mu l \cdot s^{-1}$ . A comprehensive study on the effect of flow on nanoparticle uptake has not been reported yet. In 2012, Samuel and co-workers (Samuel et al. [2012]) reported a decrease in uptake of negatively charged quantum dots with increasing shear stress from  $0.1Pa$  to  $5dyn/cm^{-2}$ , a behaviour similar to the findings here reported. However the two studies cannot be directly compared because of different experimental set-up. Samuel and coworkers used negatively charged quantum dots of  $50nm$  of diameter, while we used  $120nm$  neutral polymersomes. The uptake was studied for up to  $20min$  after exposure in the cited work; in our experiment the uptake was analysed for  $24h$ , with the first time point recorded after  $30min$ . Finally, the average shear stress used in our system is up to 10 fold higher.

It should be noiced The inverse correlation between uptake rate and shear stress was confirmed in this work, however the two systems cannot be directly compared because of the different nanoparticles used: negatively charged  $50nm$  quantum dots and non-charged  $120nm$  polymersomes. Furthermore, in the cited work the uptake was monitored for  $20min$ , in our experiment it was monitored up to  $24h$ , with the earliest time point recorded after  $30min$ .

Considering the segmentation of flow parameters, it was observed that for both shear stress and horizontal velocity magnitude there is an higher uptake in the region corresponding to the middle of the well, characterised by an intermediate parameter magnitude. This suggested a relatively low impact of shear stress or velocity on uptake in the range considered. Perhaps a wider range

would reveal a correlation between the physical parameter and uptake, but this correlation cannot be confirmed by the data reported. A correlation was observed between vertical velocity and uptake, with uptake higher at the higher vertical velocity (near the outlet) and lower at lower vertical velocity (near the inlet). A low uptake with low (negative, inlet) vertical velocity was expected, as it was the region where polymersomes were moving *faster* pushed away from the inlet. However, a high uptake at the outlet was not anticipated, as it is a region characterised by particles moving away from the cells towards the outlet of the chamber. Further investigation on polymersomes distribution in the well will clarify the role of vertical velocity and uptake, particularly with respect of local particles concentrations. Such results can be obtained by integrating the *in silico* simulation performed with the COMSOL Multiphysics *CFD module* with the module *particle tracking*.

In conclusion, different methods have been developed to assess polymersomes uptake under static and flow conditions. Protocols can be used to quickly screen several different formulations in combination with different cell types. Results obtained will be useful in the optimisation of polymersomes for imaging the tumour microenvironment, as it was found that **PMPC-PDPA** polymersomes are up-taken preferentially by tumour cells, while **POEGMA-PDPA** polymersomes have generally lower uptake, but less affected by flow dynamics in perivascular-like cells (10T1/2). Furthermore, **PMPC-PDPA** polymersomes fast uptake will likely correlate with fast clearance *in vivo*, while the other two formulations are expected to have longer circulation time in blood. This could result in an improved accumulation within the tumour via **Enhanced Permeation and Retention (EPR)** effect. Finally, uptake under flow conditions analysis revealed a strong effect of capillary-like flow rates on uptake, with significant reduction of uptake kinetic, especially for **PMPC-PDPA**. Further studies will better elucidate the correlation between uptake and different flow parameters, however preliminary results suggested that uptake by cells at the vascular and perivascular level will not be significantly shifted towards a specific cell line, as flow minimised the differences between cell types and polymersomes formulations.

### *Abstract*

[Dorsal Skinfold Chamber \(DSC\)](#) allows detailed visualisation of tumour physiology in real time *in vivo*. Fluorescent labelled polymersomes have been successfully used in *in vitro* and *in vivo* imaging, however their use in a [DSC](#) chamber set-up has not been reported yet. The aim of this work is to assess the suitability of fluorescent labelled polymersomes for *in vivo* optical imaging using [DSC](#). [Poly\(2 - methacryloxyethyl-phosphorylcholine\)-poly\( 2 -\(diisopropylamino\)ethyl methacrylate\)](#) (PMPC-PDPA) and [poly\(oligo\(ethylene glycol\) methacrylate\)-poly\( 2 -\(diisopropylamino\)ethyl methacrylate\)](#) (POEGMA-PDPA) rhodamine labelled were injected [Intra Venously \(i.v.\)](#) into a mouse tail bearing a [DSC](#). Preliminary results showed intravascular distribution of polymersomes at the early time point (1h) for both formulations, but at the later time point (15h) [PMPC-PDPA](#) was not detected in tumour vasculature or stroma, while [POEGMA-PDPA](#) was seen to extravasate and accumulate within the tumour. These finding will set the basis for future further development of polymersomes aimed at imaging the tumour microenvironment *in vivo*.

## 5.1 Introduction

### 5.1.1 Window chamber

*In vivo* optical imaging, and particularly high resolution [Intra Vital Microscopy \(IVM\)](#), is affected by poor tissue penetration of light. To negate this limitation the layers of tissues between the objective and the plans of focus can be removed and replaced with an optically transparent material. This approach

is adopted in the preparation known as the **Window Chamber (WC)**. WC was first introduced in a rabbit model in 1924 ([Sandison \[1924\]](#)), adapted for mice in 1943 ([Algire \[1943\]](#)) and developed for application to the hamster cheek pouch in 1947 ([Fulton et al. \[1947\]](#)) before being optimised for angiogenesis studies in the mouse **DSC** in 1993 ([Lehr et al. \[1993\]](#)).

When applied to the back of the animal (**DSC**) a skin layer and associated connective tissue and fat are surgically removed from the dorsum to provide optical clarity. A chamber holds the skin away from the mouse body exposing the vascularised layer of muscle and skin on the opposite side of window. The preparation is then closed with a thin optical glass coverslip. Before closing the chamber, a tumour fragment or tumour cells are implanted ([Koehl et al. \[2009\]](#)). In a few days, the tumour starts to vascularise and angiogenesis can be imaged. Applications of **IVM**, an umbrella term including **WC**, have been extensively reviewed by Fukumura and co-workers ([Jain et al. \[2002\]](#)). Some of the most significant ones are reported in the next paragraph. The **WC** can be used to monitor molecular, cellular, anatomical and functional parameters. As Laschke defined, it is a '*window into the dynamic interaction of biomaterials with their surrounding host tissue*' ([Laschke et al. \[2011\]](#)).

The **WC** preparation may be used to study a number of different parameters *in vivo*, at different levels of spatial resolution. Such parameters can be classified into molecular, cellular, anatomical and functional parameters.

**Molecular parameters** Molecular parameters include monitoring pH and pO<sub>2</sub>, expression of receptors and molecular pathways ([Helmlinger et al. \[1997\]](#)). Monitoring such parameters require the use of probes that change optical properties according to the concentration of the molecule to test. An example of such probe that may be useful in measuring pH *in vivo* has been recently reported by Madsen and co-workers. They synthesised a copolymer linked to a dye that changes emission spectra at different pH values. This copolymer was used in the self-assembling of a class of nanocarriers known as polymersomes ([Madsen et al. \[2013\]](#)). Imaging in the **WC** also allows determination of the molecular mechanisms of angiogenesis. Fukumura and co-workers, using this technique observed that tumour cells induce production of **Vascular Endothelial Growth Factor (VEGF)** in stromal cells, which can represent up to 50% of the total **VEGF** present ([Fukumura et al. \[1998\]](#)).

**Cellular parameters** The **WC** can be used to observe the establishment and development of a tumour. A common strategy is to use genetically modified tumour cells expressing fluorescent proteins, mostly **Green Fluorescent Protein**

(GFP). This allows the visualisation of tumour growth, to establish the minimal number of cells required for tumour growth and the visualisation of the tumour metastasis cascade: cells leave the primary site, extravasate into the blood vessels, reach a secondary site, extravasate into such location and finally establish as a secondary tumour (Chambers et al. [1995], Reeves et al. [2009]).

**Anatomical parameters** Anatomical parameters include vascular density, length, diameter and architecture. Such parameters are useful to describe the tumour microenvironment and to establish readouts for therapy. For instance, a decreased **Micro Vessel Density (MVD)** indicates the efficacy of an anti angiogenic agent, however **MVD** may not change if a reduction in vessel number is followed by a reduction in tumour size. Another anatomical feature derived from **WC** is pore-size cut-off, a critical aspect in nanocarrier therapy and imaging (Hobbs et al. [1998]). Nanocarriers extravasate to the tumour site through gaps between endothelial cells in the compromised vascular bed. To allow extravasation, it is therefore essential that nanoparticles have smaller radius than the inter-cellular gap. In the cited work, Jain and co-worker demonstrated the mechanism of extravasation, and they showed that extravasation of small molecules such as ( $\simeq 7nm$ ) is not affected in different tumours characterised by different gap (pore-size cut off) size, but in the range  $200nm-1.2\mu m$ . Opposite to albumin, extravasation of nanocarriers (liposomes or latex microsphere with diameter ranging from  $250nm$  to  $2.5\mu m$ ) was highly dependent on tumour type and localisation, with greater extravasation occurring in tumours with bigger gaps.

**Functional parameters** Functional parameters include hemodynamic variables such as red blood cell velocity, flow velocity and blood volume, vascular permeability and interstitial diffusion (Samuel et al. [2013], Øye et al. [2008], Dreher et al. [2006], Endrich et al. [1979], Reyes-Aldasoro et al. [2008]). Such studies are conducted using size-specific macromolecules, useful to evaluate extravasation and diffusion, or plasma markers such as the ones used in the study conducted by Reeves and co-workers (Reeves et al. [2012]) These studies elucidated not only the specific features of tumour vasculature compared to normal vasculature but also provided information related to the tumour heterogeneous blood supply and nanoparticle design to achieve better intra-tumour distribution.

**DSC** is also used in multi-modal imaging, normally combined with **Magnetic Resonance Imaging (MRI)**. This approach is useful to validate vascular parameters extrapolated from **MRI** by using **IVM**, even if errors are possible due to different time acquisition points, a problem that could be overcome by simultaneous multi-modal data acquisition (Gaustad et al. [2008], Neeman et al. [2001],

Lin et al. [2008]). Validation of MRI functional information is critical because MRI is not quantitative, a correlation is required between contrast agent concentration and signal strength. Furthermore MRI is widely used in clinical practice, while WC cannot be used in this context. Multi-modal imaging can also provide information which are complementary such as whole body drug biodistribution (MRI) and cellular effect (DSC).

WC preparations can be analysed longitudinally, spatially and temporally and multiple parameters can be extrapolated from the same animal. As a result, the molecular, cellular, anatomical and functional parameters described above can be obtained simultaneously. Perhaps the most cited example is the study conducted by Fukumura and co-worker, in which they monitored gene expression, angiogenesis and physiological function of the tumour (Brown et al. [2001]). In another study Tozer and co-workers investigated tumour response to Vascular Disrupting Agent (VDA) combretastatin after implantation of fibrosarcoma cell-lines over-expressing different iso-form of VEGF. They correlated response to treatment with vessel length and density (anatomical parameter) and vasculature leakiness (functional parameter) (Tozer et al. [2008]). Quantification of response to treatment is another key application of WC. Classical therapy response is evaluated in terms of tumour size. However tumour shrinkage is not the only possible outcome of a therapy and in animal models is not always indicative of tumour response. In response to treatment tumours may become quiescent, therefore there is no change in size and no apparent response to the treatment. In both cases, changes in tumour size are slow, and there is the need to understand if a therapy is effective in a certain time frame. WC can help to identify molecular markers that respond rapidly to therapy which may help in predicting the outcome, or even more interesting, they could help in designing a personalised therapy based on prediction of outcome generated by the presence of such markers.

WC in mouse has many advantages: the multiple imaging of a single animal limits the number of animals required to achieve statistical significance at any given time-point. There is fast recovery from surgery and imaging analysis can commence 48h after surgery. However its execution requires dedicated training and skills. Furthermore the chamber is not always an orthoptic site for the tumour of interest and this explains why chambers have been created to be implanted in different parts of the body (e.g. cranial chamber and abdominal chamber (Coisne et al. [2013], Ritsma et al. [2013])). Furthermore, tumour growth is visualised in a time-frame of days/weeks, while human tumour development can take months or even years. Finally, the 3D growth of the tumour is restricted by the coverslip on at least one of the two sides of the frame, and this can cause artificially increased intra-tumour pressure which affects vasculature permeability (Staton

et al. [2009], Gaustad et al. [2008]). Despite this limitations, WC is a valuable tool in angiogenesis and tumour biology research, being used to unravel tumour angiogenic mechanisms at different levels.

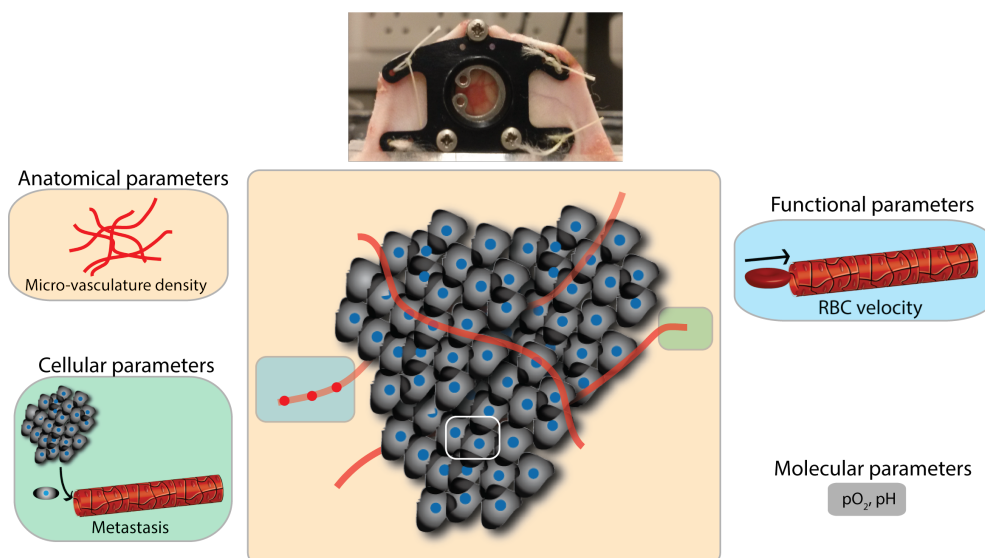


Figure 5.1: Using a *DSC* it is possible to observe angiogenesis at different levels, such as the anatomical level (i.e. micro-vascular density), the cellular level (i.e. primary tumour growth and tumour metastasis), the functional level (i.e. quantification of the red blood cell velocity) and the molecular level (i.e. feedback on  $pO_2$  and  $pH$  of the tumour).

### 5.1.2 Vascular Endothelial Growth Factor

**VEGF** is a family of cytokines including four main members in humans: **VEGF-A**, **VEGF-B**, **VEGF-C** and **VEGF-D**. The most important in cancer angiogenesis and the first one discovered was **VEGF-A**, which is a potent pro-angiogenic factor and stimulates vasodilation and vessel permeability. **VEGF-A** is also a mitogen and a chemoattractant (Shibuya [2013]). **VEGF-A** binds to two receptors: **VEGFR-1** and **VEGFR-2**. There is evidence that the binding affinity to **VEGFR-1** is higher than to **VEGFR-2**. In early angiogenesis binding to **VEGFR-2** is pro-angiogenic, whilst binding to **VEGFR-1** suppress the angiogenic response (Sawano et al. [1996], Fong et al. [1995]).

**VEGF-A** mRNA is transcribed from 8 exons alternatively sliced resulting in different isoforms, the most common ones being **VEGF120**, **VEGF164**, **VEGF188** in mouse, 1 amino acid longer in human. **VEGF120** does not have a heparin binding site and is readily diffusible, **VEGF188** has a heparin binding site, and binds strongly to proteoglycans in the **Extracellular Matrix (ECM)** and cell membrane. **VEGF164** has intermediate properties (Ferrara [2004]). During development in the mouse model, it has been shown that the presence of **VEGF164** is sufficient

to establish a functional vasculature, VEGF<sub>120</sub> supports endothelial cell proliferation, but the vessels formed are haemorrhagic. VEGF<sub>188</sub> is essential for the formation of a normal vasculature in 50% of animals (Stalmans et al. [2002]).

### 5.1.3 Single VEGF-A isoform producing tumours

Mouse fibrosarcoma cells expressing single isoforms of VEGF have been developed and tumours obtained from such cells have been analysed in a DSC. Tumour growth rate is independent of the isoform used but dependent on VEGF concentration (Yu et al. [2002]). Tumours expressing different specific isoforms of VEGF have specific characteristics. VEGF<sub>120</sub> tumours are less well-vascularised (CD31 staining) than VEGF<sub>188</sub> or VEGF<sub>164</sub> tumours, and VEGF<sub>188</sub> tumours have higher pericyte coverage ( $\alpha$ -Smooth Muscle Actin ( $\alpha$ -SMA) staining). VEGF<sub>120</sub> tumours are more permeable to injected FITC-dextran 40KDa, and this is consistent with lower pericyte coverage. In terms of tumour growth, VEGF<sub>120</sub> tumours shows dilation of pre-existing vessels which become highly haemorrhagic. VEGF<sub>188</sub> tumour growth have narrower non haemorrhagic vessels. VEGF<sub>120</sub> established tumours are characterised by a vasculature limited to the periphery while VEGF<sub>188</sub> tumours are completely vascularised. Wild type (all isoform expression) and VEGF<sub>164</sub> tumours had intermediate properties (Akerman et al. [2013]).

### 5.1.4 Nanoparticles extravasation in tumour

Nanoparticles can extravasate and accumulate within tumours via the Enhanced Permeation and Retention (EPR) effect (see 1.4.2). Once blood-borne nanoparticles reach the tumour, extravasation and tissue penetration is a function of nanoparticles size, shape, charge, vascular morphology and physical properties. The effect of particle size and shape has been discussed in section 1.4.3. Here, the role of vascular characteristics will be discussed.

The tumour vasculature is highly heterogeneous, characterised by vessels of different diameter and anatomy, including capillaries, venules, arterioles, vascular *shunts*, anastomosis and blood channels without endothelial cells (Jain [1988]). Furthermore, the organisation of the vessels is not constant in space or time, with heterogeneous flow rates (Dudley [2012]). In addition, tumours are often characterised by a central necrotic area surrounded by a vascularised, growing area. The first challenge is the homogeneous delivery of nanoparticles to tumour via heterogeneous vasculature.

Once nanoparticles reach the tumour and distribute in the vasculature, the intra-tumour penetration is a function of two main parameters: diffusion and

convection. Diffusion  $D$  is a slow process and is dependent on surface area of the vessel ( $S$ ) and on the difference in concentration of the nanoparticles between the plasma and the tumour stroma ( $C_P - C_S$ ). Finally, convection is proportional to blood leakage (and therefore to vessel surface area  $S$ ), to the difference in osmotic pressure between plasma and tumour ( $\pi_P - \pi_S$ ) and the difference in hydrostatic pressure ( $p_P - p_S$ ) (Jain [2001]).

To be able to predict the intra-tumour distribution of nanoparticles is of great interest as it would help to optimise the design of the nanoparticle to achieve specific delivery via the EPR effect and higher tumour accumulation, which in turn lead to an improved therapeutic outcome or improved signal-to-noise ratio for an imaging application. In the last decade a great effort has been made to model tumour vasculature and nanoparticle extravasation *in silico* (Frieboes et al. [2013], Stylianopoulos et al. [2012], Chou et al. [2013], Sinek et al. [2004]).

Unfortunately, tumour *in silico* models are still far from perfect, due to the difficulties relating to accurate modelling of events occurring simultaneously at the vascular level ( $\mu m$ ) and at the nanoparticle level ( $nm$ ) and for the computational demand of running the simulation for biologically relevant time periods. For this reasons a number of simplifications have been introduced in every model, limiting their broader applicability to different scenarios (i.e. different tumour, with different vasculature characteristics). Experimental data will assist in developing the critical parameters regulating extravasation and accumulation and to perfect existing models.

### 5.1.5 Aim

DSC allows highly detailed visualisation of tumour pathophysiology in real time *in vivo*. Fluorescent labelled polymersomes have been successfully used in *in vitro* and *in vivo* imaging, however their use in a DSC chamber set-up has not yet been reported. The aim of this work is to assess the suitability of fluorescently labelled polymersomes for *in vivo* optical imaging using DSC. To do so, PMPC-PDPA and POEGMA-PDPA rhodamine labelled polymersomes were injected and their distribution in the tumour microenvironment was monitored using fluorescence microscopy.

## 5.2 Results

Tumour growth after Mouse Fibrosarcoma Cells expressing VEGF188 isoform (MFC188) spheroid implantation was monitored regularly to assess the extension of vascularisation and animal well-being. A typical time-frame of tumour develop-

ment for **MFC188** is reported in figure 5.2. Tumour vasculature can be observed starting at day 4 after surgery (4% of total chamber area), and it is fully established around day 7 (70%). After this time the vasculature and tumour will start to overgrow the chamber. Imaging sessions were performed when the tumour was covering between 70% and 90% of the chamber, 8 days after surgery.

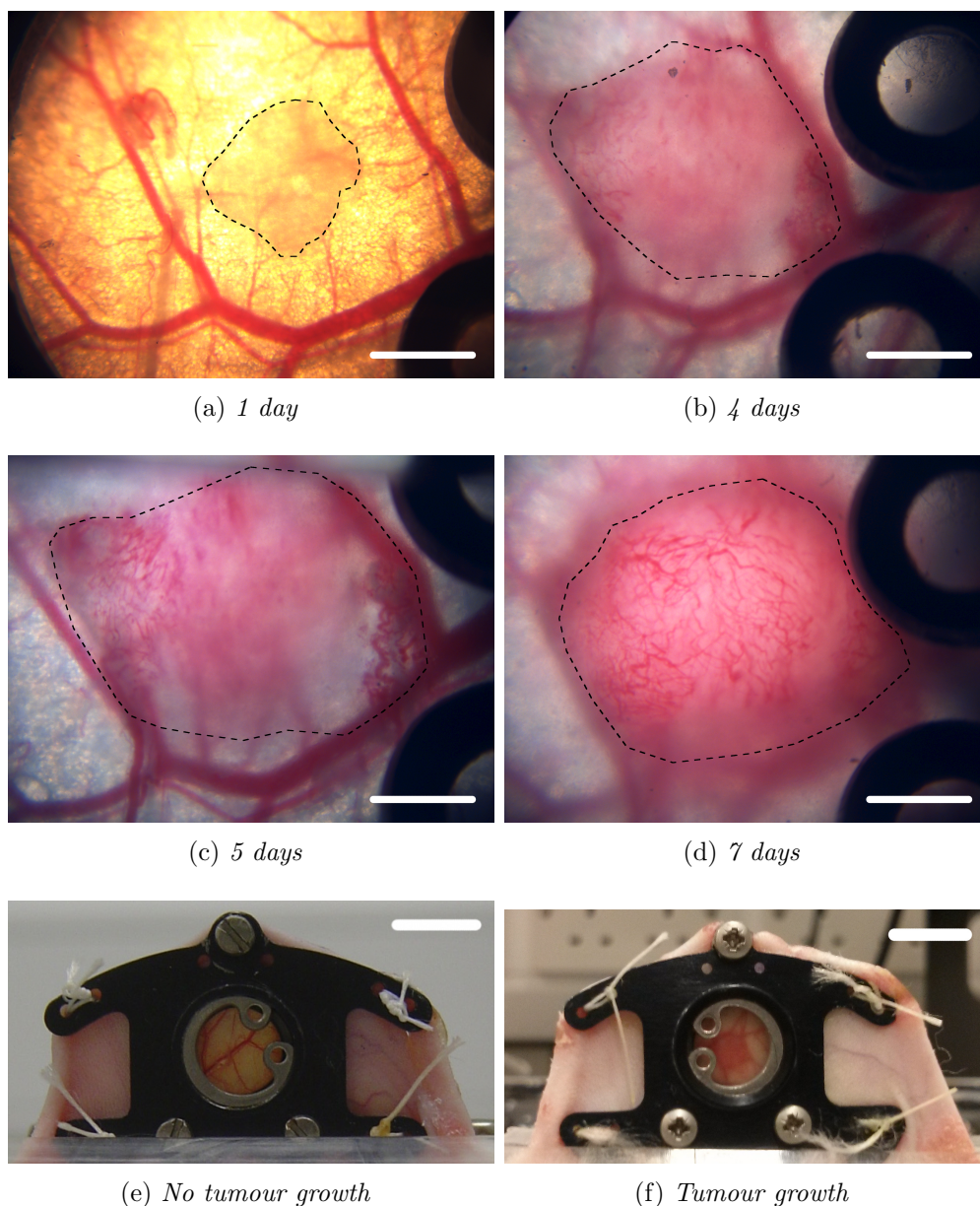


Figure 5.2: **MFC188** tumour development from 24h after surgery to 7 days after surgery (d). Tumours are highlighted by the black dotted line. Picture (e) shows a chamber with no tumour growing, picture (f) shows a chamber with tumour established. Bar (a, b, c, d) 1.5mm; (e,f) 7mm.

Rhodamine labelled polymersomes were injected via the tail vein (**Intra Venous (i.v.)**) and a number of imaging sessions were conducted regularly from immediately after injection up to 18h after injection. Imaging settings such as

fluorescence intensity were defined before injection so that no background noise was detected. Images were acquired using a confocal microscope equipped with a 10X objective. Under transmitted light, vessels are visible in black over a bright tumour stroma. In the rhodamine channel, vessels are highlighted by polymer-somes and are seen in bright over dark tumour stroma (fig. 5.3).

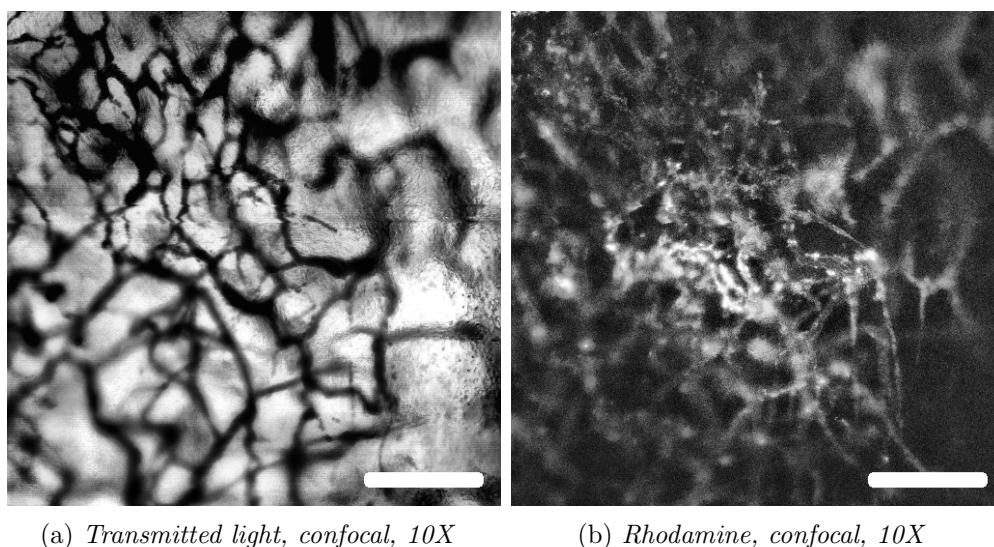


Figure 5.3: *DSC* images, 10X confocal microscopy. Image acquired 5min after *i.v.* injection of rhodamine labelled *POEGMA-PDPA* polymersomes. On the left (a) transmitted light picture, on the right (b) fluorescence pictures. Rhodamine labelled *POEGMA-PDPA* can be seen localised inside the blood vessels. Bar 230 $\mu$ m.

Representative images for rhodamine labelled *POEGMA-PDPA* polymersomes can be seen in figure 5.3. The images were acquired 5min after injection. A time-lapse for the same polymersomes formulation is reported in figure 5.4. Transmitted light images always show vessels as dark structures, acting as a reference image. In the rhodamine channel it is visible that initially vessels are highlighted as bright over dark stroma (2min, fig. 5.4-b), but at a later time point vessels appeared in dark over brighter stroma (15h, fig. 5.4-f). This suggests polymersome extravasation and accumulation within tumour.

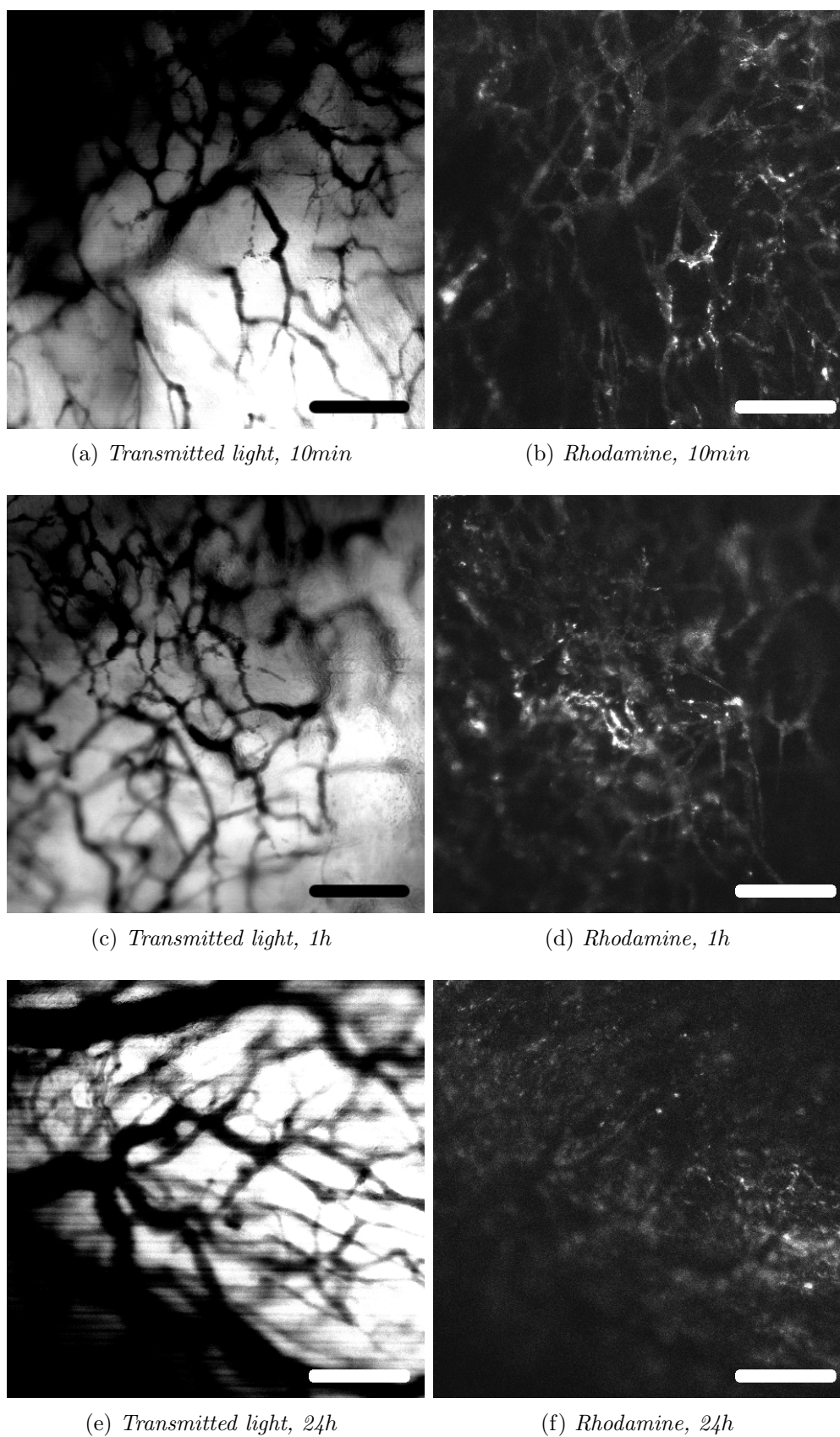


Figure 5.4: *MFC188* tumour microvasculature confocal images, 10X objective. At earlier time point (a-d) the tumour stroma is darker than vessels in the rhodamine channel (b, d), indicating circulating polymersomes. 24h after injection the tumour stroma is brighter than the vessels (f), suggesting intra-tumour accumulation. Bar 230 $\mu$ m.

Rhodamine labelled **POEGMA-PDPA** and **PMPC-PDPA** polymersome localisation were compared. At earlier time points, both **PMPC-PDPA** and **POEGMA-PDPA** were localised in vessels. Interestingly, at later time points the **PMPC-PDPA** signal was significantly weaker in the vasculature and the tumour stroma, suggesting that the formulation was rapidly cleared from the circulatory system (see fig. 5.5).

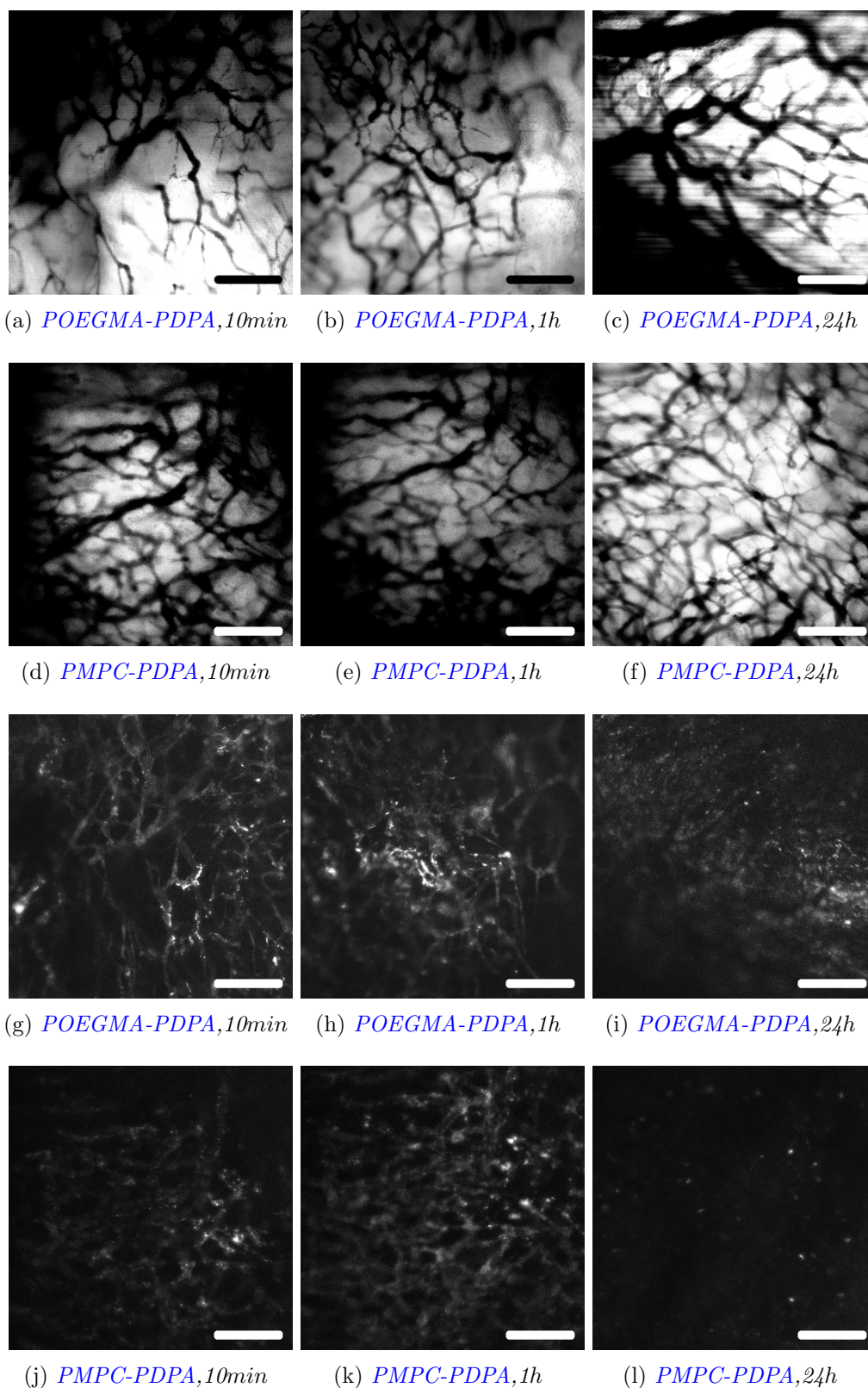


Figure 5.5: Confocal imaging comparison of *POEGMA-PDPA* and *PMPC-PDPA*, transmitted light (a-f) and rhodamine channels (g-l). 10min and 1h after injection both *PMPC-PDPA* and *POEGMA-PDPA* are localised in vessels (g, j, h, k). At 24h, *PMPC-PDPA* (l) is almost not detectable, while *POEGMA-PDPA* is clearly localised in tumour stroma (i). Bar 200 $\mu$ m.

All images were analysed as described in section 3.6 and results are reported in figure 5.6-5.7. Confocal image analysis confirmed the qualitative observation of increased accumulation of **POEGMA-PDPA** compared to **PMPC-PDPA** poly-mersomes (higher average intensity). Furthermore, for both formulations it was observed that at early time points, blood vessels contribute to the overall image intensity at a higher percentage than the tumour stroma, while at later time points the contribution is reversed. Edges have intermediate contribution between stroma and vessels. Thus, this analysis confirmed the qualitative observation of extravasation (decreasing vessel contribution) and accumulation within tumour (increasing stromal contribution).

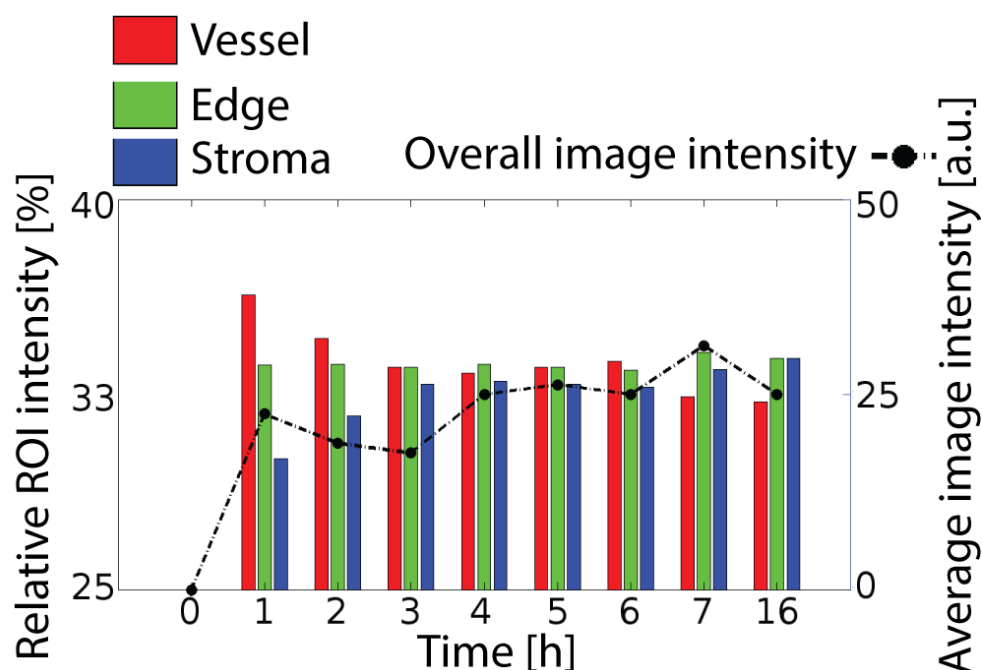


Figure 5.6: **PMPC-PDPA** *in vivo* image analysis. Data are represented as overall mean intensity of rhodamine signal in the tumour area (right axis) overlaid with a break down of the relative contribution of vessels, edges and tumour stroma to the signal intensity (left axis, coloured bars). The overall image intensity showed a slight increase over time. Moving from  $t=1h$  to  $t=16h$  it was observed that poly-mersomes relative distribution in the vessels *Regions of interest (ROI)* decreased, while the intensity of the stroma *ROI* increased.

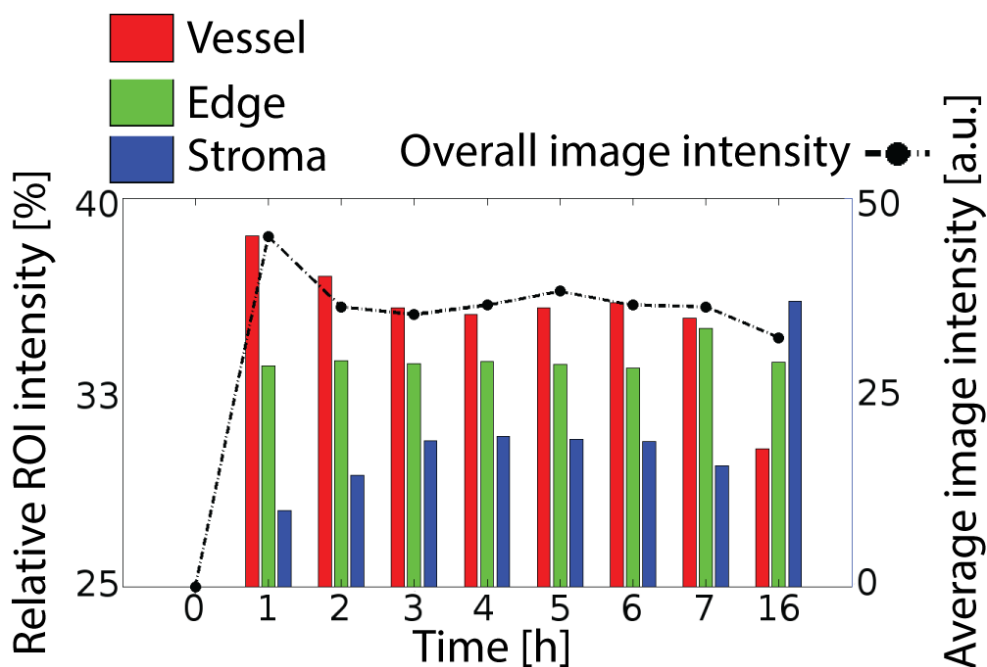


Figure 5.7: *POEGMA-PDPA* in vivo image analysis. Data are represented as overall mean intensity of rhodamine signal in the tumour area (right axis) overlaid with a break down of the relative contribution of vessels, edges and tumour stroma to the signal intensity (left axis, coloured bars). The overall image intensity showed a slight increase over time. Moving from  $t=1h$  to  $t=16h$  it was observed that polymersomes relative distribution in the vessels ROI decreased, while the intensity of the stroma ROI increased. At  $t=16h$  there was a clear inversion between the two intensity distributions, evidence of the extravasation observed in fig. 5.5.

Qualitative and quantitative confocal image analysis suggested polymersomes extravasation and accumulation in tumours. Further image analysis was carried out to gain insight into the dynamics of tumour extravasation. Confocal images were segmented to correlate the amount of extravasation against the distance travelled by the polymersomes and the diameter of the nearest vessel, here assumed to be the origin of travel of polymersomes. The analysis is discussed in section 3.6.2. The analysis revealed less extravasation of *PMPC-PDPA* compared to *POEGMA-PDPA*, as was already anticipated by the previous analysis (fig. 5.6-5.7). The analysis was performed also in pictures acquired with epifluorescence microscope equipped with a 2.5X or a 20X magnification lenses, however only confocal images analysis is reported here. This is due to the lack of spatial resolution in epifluorescence microscopy compared to confocal microscopy: masks identifying different ROI can potentially be less accurate. Furthermore, in epifluorescence the transmitted light channel and the rhodamine channel were not acquired simultaneously, therefore the translation of the mask created on the transmitted light micrograph to the rhodamine one is less accurated as it

is affected by mouse movements. Image analysis for epifluorescence pictures is reported in annex section 9.3. Analysis of **POEGMA-PDPA** extravasation profile interestingly reveals how extravasation is more intense at the level of bigger vessels ( $\approx 12\mu\text{m}$ ), however higher distances are travelled from lower calibre vessels ( $\approx 6\mu\text{m}$ ) (see fig. 5.8-5.9).

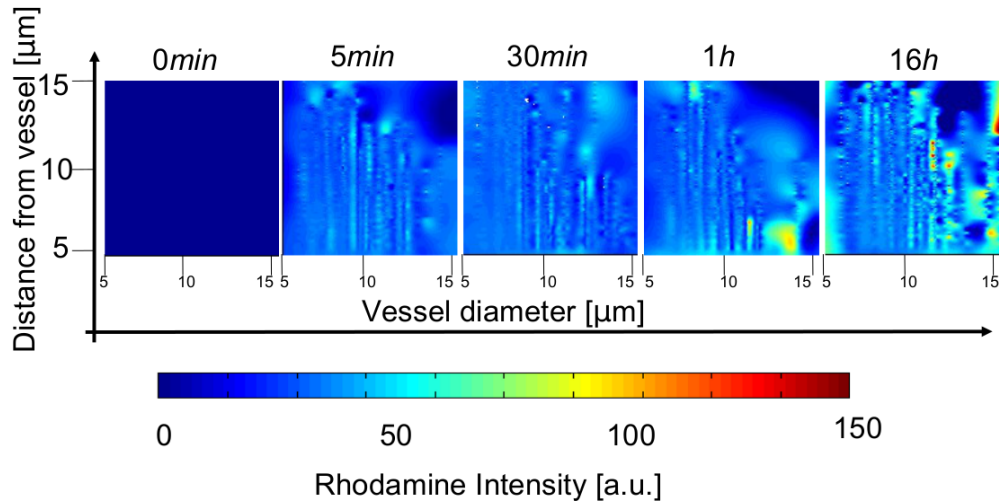


Figure 5.8: *Extravasation analysis of POEGMA-PDPA polymersomes. Over-time (0min-16h) mapping of extravasation. For every pixel belonging to tumour stroma, the distance to the closest vessel and the diameter of the closest vessels were measured together with the rhodamine intensity. Data were then mashed to obtain a heatmap where rhodamine intensity is colour coded from blue (low intensity) to red (high intensity). Polymersomes extravasating from smaller vessels (5-10 $\mu\text{m}$ ) travelled the greatest distance ( $\approx 15\mu\text{m}$ ). Polymersomes extravasating from larger vessels (10-15 $\mu\text{m}$ ) travelled a shorter distance, however their accumulation is greater (greater intensity).*

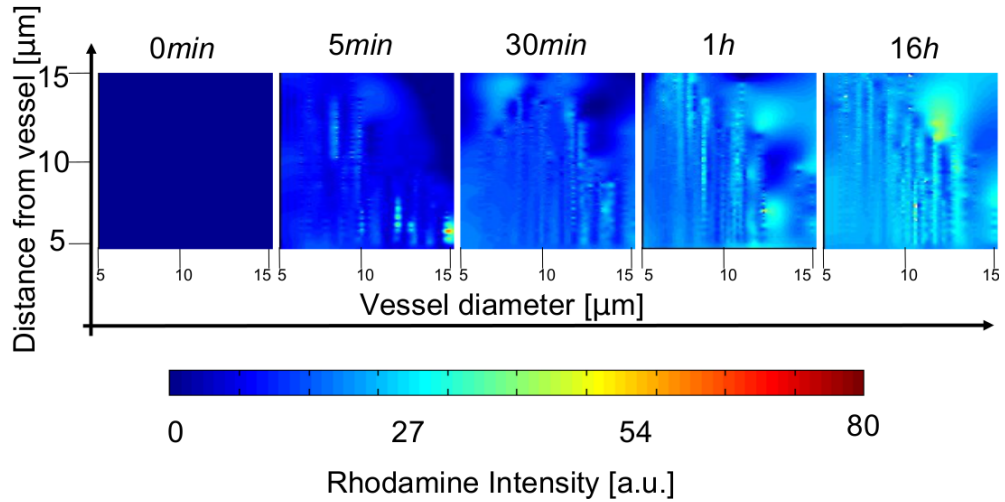


Figure 5.9: *Extravasation analysis of PMPC-PDPA polymersomes. For every pixel belonging to tumour stroma, the distance to the closest vessel and the diameter of the closest vessels were measured together with the rhodamine intensity. Data were then mashed to obtain a heatmap where rhodamine intensity is colour coded from blue (low intensity) to red (high intensity). Polymersomes extravasating from smaller vessels (5-10 $\mu\text{m}$ ) travelled the greatest distance ( $\approx 15\mu\text{m}$ ). Polymersomes extravasating from larger vessels (10-15 $\mu\text{m}$ ) travelled a shorter distance, however their accumulation is greater (greater intensity).*

### 5.3 Discussion

High resolution *IVM* of the tumour microenvironment has been made possible by the use of a *DSC*. The *DSC* had the advantage of reducing the limitation of poor tissue penetration of light characteristic of optical imaging techniques. *DSC* models have the disadvantage of being usually non orthotopic and results can be hindered by increased intra-tumour pressure, due to growth constraints by the two glass cover slips of the chamber, however it is still a widely used model to study angiogenesis and vascular response to therapy.

The tumour implanted within the chamber was a fibrosarcoma, derived from *Mouse Fibrosarcoma Cell (MFC)* cell expressing *VEGF188*. This particular cell type was chosen over the *MFC* wild type or cell-lines expressing *VEGF120* or *VEGF164* because studies from our group reported that they are characterised by a more vascularised tumour with higher pericyte coverage (*Akerman et al. [2013]*). This is a more appropriate tumour to start developing polymersomes for *IVM* imaging, compared to the *MFC* expressing *VEGF120*, where there is a poor vasculature.

The results here discussed represent the outcome of a very limited number of animals, not sufficient to draw conclusions based on solid statistic. Overall, this part of the work should be considered a pilot experiment aimed to test the

analysis methodology described in chapter 3 and to investigate possible correlation between *in vitro* uptake discussed in chapter 4 and *in vivo* intra-tumour distribution.

It was of interest to test both formulations *in vivo* to visualise any differential distributions within the tumour microenvironment. Because of the greater uptake of PMPC-PDPA compared to POEGMA-PDPA polymersomes observed from the *in vitro*, we expected to observe a shorter plasma half-life of PMPC-PDPA compared to POEGMA-PDPA polymersomes. It was also hypothesised that circulation time affects accumulation within the tumour and that the two formulations may have different intra-tumour distribution due to the interactions with different cell types in the tumour microenvironment.

Confocal microscopy allowed simultaneous acquisition from the rhodamine and transmitted light channel. Simultaneous acquisition is critical to transfer segmentation result from the transmitted light image to the rhodamine channel avoiding offsets generated by mouse movement. Qualitative image observation revealed gradual polymersomes extravasation and accumulation within tumour. Qualitative comparison between POEGMA-PDPA and PMPC-PDPA polymersomes images revealed that accumulation of POEGMA-PDPA was higher than PMPC-PDPA. This was confirmed by image analysis, performed using a specifically developed segmentation and analysis algorithm (section 3.6). POEGMA-PDPA distribution profile could be explained when considering the chemical similarity between poly(oligo(ethylene glycol) methacrylate) (POEGMA) and Polyethylene Oxide (PEO). PEGylated systems are known to have prolonged plasma half-life (Pasut and Veronese [2012]) because of their ability to avoid interaction with protein (*non-fouling*) and to escape the Reticuloendothelial System (RES) (*stealth* properties). POEGMA is likely to exhibit similar properties to PEO.

Finally, we investigated polymersome extravasation, specifically the relationship between distance travelled by the polymersomes over time with respect to the diameter of the closest blood vessel, here assumed to be the origin of diffusion. Despite having an overall different magnitude of accumulation, PMPC-PDPA and POEGMA-PDPA polymersomes showed similar diffusion profiles. A peak of extravasation can be observed at the level of largest vessels ( $>10\mu\text{m}$ ), however the longest distance is travelled when extravasation occurs at the level of smaller vessels ( $<10\mu\text{m}$ ) (fig. 5.5). A similar irregular accumulation has been reported by Yuan and co-workers for liposomes. Liposomes accumulated close to larger vessels, and normally at the bifurcation points (Yuan et al. [1994]). Higher accumulation around bigger vessels could be explained by the increased superficial area of larger diameter vessels (therefore increasing both diffusion and

convection), and perhaps increased hydrostatic pressure between larger vessels and tumour stroma, compared to smaller vessels and tumour stroma. This could be due to increased blood flow which in turn increases convection, which is a faster phenomena compared to simple diffusion. Furthermore, local rheological properties of flow at bifurcation (i.e. increased turbulence) could affect extravasation. Further development of the method should implement functional and cellular parameters. Functional parameters include hydrostatic and osmotic pressure and flow velocity, cellular parameters include macrophage distribution, which could be responsible for polymersomes uptake and local accumulation.

Overall, the findings suggest that **PMPC-PDPA** polymersomes rapidly interact with other cells and organs, including the **RES** which is the usual body defence mechanism against circulating *non-self*, such as the polymersomes. **POEGMA-PDPA** polymersomes have reduced interactions with the **RES** and therefore have prolonged half-life, resulting in the increased potential to extravasate into the tumour via the **EPR** effect. These hypotheses are supported by unpublished data from Prof. Battaglia, showing significantly shorter half-life of **PMPC-PDPA** compared to **POEGMA-PDPA** in mouse model. The reduced plasma half-life of **PMPC-PDPA** affects intra-tumour accumulation, which resulted in significantly lower accumulation compared to **POEGMA-PDPA** polymersomes. Distribution in other organs was not investigated in this work, however preliminary data obtained from analysis of biodistribution of **PMPC-PDPA** and **POEGMA-PDPA** in healthy SCID mouse were conducted previously by Prof. Battaglia group. For both polymersome formulations it was found a profile of biodistribution typical for nanoparticles, with significant accumulation in liver, spleen, lung and kidney. Further work with tumour bearing animals should be performed to investigate the overall intra-tumour accumulation compared to accumulation in other, off-target organs.

A final remark should be made on the surgical procedure. The rate of success proved to be poor, with major complications due to the tumour not vascularising in the chamber or the chamber itself falling on the flank of the mouse a few hours after surgery instead of staying on the top of the back. Some of these complications are currently being addressed by standardising the cell spheroid preparation or by changing some of the components of the chambers, such as the spacers between the two frames. However, more work is required to improve the outcome of the surgery, which has not only ethical implications, but is also vital to obtain reliable information from *in vivo* experimentation.

## CHAPTER 6

# PERIVASCULAR CELLS TARGETING

### *Abstract*

In the previous chapters, methodologies for quantification of cellular uptake of polymersomes have been developed. In this chapter the methodologies developed will be integrated in the context of further development of functionalised polymersomes to target a specific cell type: perivascular cells. Perivascular cells is a collective name identifying a group of cells, namely pericytes and [Vascular Smooth Muscle cells \(vSMCs\)](#), in direct contact with endothelial cells on the outer side of the blood vessel, hence the name *perivascular*. In tumour angiogenesis the perivascular cells coverage is reduced and vasculature becomes unstable. The ability to image perivascular cells *in vivo* and to monitor their response to anti-angiogenic therapies may lead to an improved understanding of their role in angiogenesis. Active targeting of perivascular cells with polymersomes requires the identification of a suitable specific marker. The first part of this chapter will focus on the identification of such a marker in a *in vitro* cell model: 10T1/2 cells. The expression of such markers in 10T1/2 and other tumour microenvironmental cells will be compared: endothelial cells ([Small Vessel Endothelial Cells \(SVECs\)](#)) and cancer cells ([Mouse Fibrosarcoma Cells expressing VEGF188 isoform \(MFC188\)](#)). Finally, different synthetic strategies to functionalise polymersomes with a targeting antibody will be investigated and the functionalised formulation will be tested *in vitro*.

## 6.1 Introduction

### 6.1.1 Perivascular cells

Blood vessels are formed by the endothelial cells and a number of supporting cells collectively referred to as *perivascular cells* or *mural cells*. As the name implies, perivascular cells are located outside the blood vessels and in contact with the endothelial cells. The first report of perivascular cells was made by Rouget in 1873 (Rouget [1873]). He described contractile cells located outside and around small blood vessels (Rouget [1873]). Pericytes were initially called Rouget cells. A few years later Zimmermann renamed the cells as pericytes due to their perivascular location (Zimmermann [1923]). Since the discover of pericytes and the improvement in phenotyping and microscopy techniques, other perivascular cells have been reported, namely vSMCs. The main difference between the cell type is in markers expression and location with respect of the vasculature bed., i.e in contact with capillaries, pre- or post- capillaries or larger vessels. However, there is no clear differentiation between the cell types, to the point that the name *pericytes* is often used as synonym for perivascular cells.

Perivascular cells are rounded cells with long primary cellular protrusions running parallel to the blood vessel, from which small secondary processes perpendicular to the blood vessel are observed. Where the secondary processes are in contact with the endothelial cell, a discontinuity of the basal membrane is observed, suggesting direct contact between the two cell types through peg-socket junctions and tight junctions. The ratio between the number of perivascular cells and endothelial cells is known as pericyte coverage, the term reflecting the lack of clear distinction between pericytes and other perivascular cells. Pericyte coverage varies in different organs with specific tissue characteristics. Tissues with high endothelial cell turnover have lower pericyte coverage and tissues subjected to high orthostatic blood pressure have high pericyte coverage (Armulik et al. [2011], Díaz-Flores et al. [2009]).

Pericytes are traditionally restricted to a capillary and post-capillary location, however other mural cells are found in the same area. Furthermore, it has been reported that the pericyte embryological origin differs between organs. Pericytes in the Central Nervous System (CNS) and cardiac tract vessels originate from the neural crest (Creazzo et al. [1998], Ema et al. [2003]) while in the rest of the body pericytes are mesenchymal in origin, with Transforming Growth Factor- $\beta$ 1 (TGF- $\beta$ 1) responsible for their differentiation (Creazzo et al. [1998]). In adult tissues, pericyte development is not well characterised. They have been reported to derive from tissue derived stem cells including pericytes themselves and myofibroblasts (Diaz-Flores et al. [1992]) but also from peripheral blood pluripotent stem cells

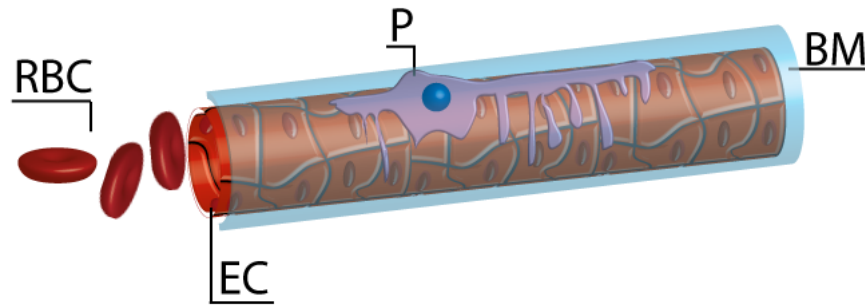


Figure 6.1: A perivascular cell ( $P$ ) in a capillary. Endothelial cells ( $EC$ ) constitute the capillary tube, one perivascular cell is directly in contact with many endothelial cells and embedded within the basal membrane ( $MB$ ). Red blood cells are pictured as well ( $RBC$ ).

(Rajantie et al. [2004], Ozerdem et al. [2005]). In fact pericytes are both descendant and precursor cells and they have mesenchymal potential (Crisan et al. [2008], Crisan et al. [2009]). Pericyte identification is made difficult by the lack of a specific marker. Commonly pericytes are described as  $\alpha$ -Smooth Muscle Actin ( $\alpha$ -SMA), Platelet Derived Growth Factor-B (PDGF-B) and Nerve Glial antigen 2 (NG2) positive (Bergers and Song [2005]). Furthermore, they can be identified by assessing their position with respect of blood vessel using techniques such as Transmission Electron Microscopy (TEM) or Scanning Electron Microscopy (SEM) imaging (Wagner and Hossler [1992], Hayden et al. [2007]).

### Perivascular cells functions

Due to their important position and structural role in the vasculature, perivascular cells contribute to the regulation of several homeostatic functions; including regulation of blood flow, stabilisation of blood vessels, vascular permeability, production of extracellular matrix and immune defence (Díaz-Flores et al. [2009], Bergers and Song [2005]).

**Contractility** Contractile properties of perivascular cells have been described since the early original publications (Rouget [1873], Zimmermann [1923]) and are now well documented (Kutcher et al. [2007], Peppiatt et al. [2006]). Endothelin 1 secreted by endothelial cells stimulates pericyte contraction (Rucker et al. [2000]), whilst relaxation is induced by nitric oxide, atrial natriuretic peptide, adenosine, lipopolysaccharide and reactive oxygen metabolites (Edelman et al. [2006a], Edelman et al. [2006b]). The contraction mechanism is supported by the expression of the contractile protein  $\alpha$ -SMA, a marker for both pericyte and vSMCs, which can also be transferred to endothelial cells through adherent junctions (Hirschi

and D'Amore [1996]). Contraction of perivascular cells in response to different stimuli results in hemodynamic regulation at the microvascular level, with the greatest impact observed in arterioles.

**Capillary permeability regulation** Perivascular cells regulate capillary permeability by two mechanisms: one physical and one chemical. Physical regulation is a consequence of the pericyte coverage. The amount of pericyte coverage on the albuminal side of endothelial cells correlates with capillary permeability (Hellstroem et al. [2001], Wang et al. [2012]). Perivascular cells are also sensitive to chemical signalling. In angiogenesis perivascular cells produce **Vascular Endothelial Growth Factor (VEGF)**, known to increase blood vessel permeability (Reinmuth et al. [2001]). Although the mechanisms that regulate capillary permeability are not fully characterised it is generally accepted that perivascular modulate vascular permeability by modulating **Endothelial cell (EC)** signalling pathways.

**Vessel stabilisation** Vessel stability is the result of functional endothelial cell/endothelial cell, endothelial cell/perivascular cell and cell/**Extracellular Matrix (ECM)** contacts. This is achieved by a balanced secretion of factors such as **TGF- $\beta$ 1**, **Platelet Derived Growth Factor (PDGF)** and **angiopoietin 1/angiopoietin 2** from both endothelial cells and perivascular cells (Armulik et al. [2005]).

**TGF- $\beta$ 1** is a cytokine regulating cell proliferation and apoptosis modifying angiogenesis in different ways (Mehta and Dhalla [2013]). It is a potent activator of endothelial cell proliferation and induces mural cell recruitment with subsequent differentiation into pericytes. Mouse models with abnormal **TGF- $\beta$ 1** signalling are embryonic lethal, demonstrating an unformed and non-functional vasculature phenotype (Larsson et al. [2001], Dickson et al. [1995]). **TGF- $\beta$ 1** recruits and induces **vSMCs** differentiation which in turn promotes vessel stability. In wound healing **TGF- $\beta$ 1** interacts with endoglin, a part of the **TGF- $\beta$ 1** receptor complex expressed many proliferating and stem cells, in addition to promote **vSMCs/pericytes** differentiation (Valluru et al. [2011]). **TGF- $\beta$ 1** is secreted in a latent form by both endothelial cells and perivascular cells, with contact between the two cell types being reported to be essential for **TGF- $\beta$ 1** activation (Hirschi et al. [1997], Hirschi et al. [1998], Hirschi et al. [1999]). In the presence of **TGF- $\beta$ 1**, perivascular cells increase the production of  **$\alpha$ -SMA**, whereas absence results in increased **NG2** and **desmin** (Song et al. [2005]). Furthermore, **TGF- $\beta$ 1** in conjunction with **angiopoietin 1** decreases the production of **PDGF-B** by endothelial cells (Betsholtz [2004]).

The **angiopoietin-Tie2** balance is another key regulator of vessel stability. An

increase in angiopoietin 2 expression is a marker of tumour angiogenesis (Zhang et al. [2003]), although neither the angiopoietin ligand or receptor expression is correlated as a prognostic indicator (Staton et al. [2011]). Angiopoietin 1 is secreted by perivascular cells, with the receptor Tie2 expressed by endothelial cells (Sundberg et al. [2002], Sato et al. [1995]). Angiopoietin 1 stabilises blood vessels by inhibiting endothelial cell proliferation. Angiopoietin 1 or Tie2 negative mice do not survive due to vascular abnormalities. It has also been hypothesised that endothelial cell deficiency induced by the absence of angiopoietin 1 also negatively affects TGF- $\beta$ 1 expression (Suri et al. [1996]). Angiopoietin 2 is an antagonist of angiopoietin 1 secreted by perivascular cells. Angiopoietin 2 over-expression has been reported to mimic angiopoietin 1 deficiency (Gale et al. [2002]). Angiopoietins require TGF- $\beta$ 1 to function. Angiopoietin 1 or angiopoietin 2 have no effect on endothelial cell proliferation and tube formation *in vitro* but angiopoietin 1 antagonises TGF- $\beta$ 1-induced tube disruption and angiopoietin 2 antagonises angiopoietin 1 (Ramsauer and D'Amore [2007]).

The PDGF-B/Platelet Derived Growth Factor Receptor- $\beta$  (PDGFR- $\beta$ ) system is also required for vessel stabilisation. In angiogenesis PDGF-B is secreted by endothelial cells, particularly by the tip cell in a vessel sprout. The tip cell is the endothelial cell leading the growth of the forming vessel in angiogenesis. It is followed by other endothelial cells that will constitute the wall of the vessel and by perivascular cells that stabilise the forming tubular structure. PDGF-B is a chemotactic factor for perivascular cells (Bjarnegard et al. [2004]). Lack of PDGF-B or PDGFR- $\beta$  is lethal in knock-out mouse models. The phenotype is characterised by reduced perivascular cells coverage which leads to a non-functional vasculature (Levéen et al. [1994], Soriano [1994]).

VEGF is probably the most potent pro-angiogenic factor modulating both perivascular cells and endothelial function. It is responsible for direct stimulation of perivascular cells proliferation and migration and also to indirect stimulation of recruitment, by increasing NO production in endothelial cells. VEGF inhibition has proven anti-angiogenic effects by increasing pericyte coverage (Tozer et al. [2008]).

### Perivascular cells in angiogenesis

Perivascular cells in the quiescent vasculature have different morphology, location and protein expression when compared to those during active angiogenesis. In the early stages of angiogenesis, perivascular cells bulge and the cytoplasmatic processes become shorter (Baluk et al. [2003], Ozawa et al. [2005]). The basal membrane is degraded, perivascular cells detach from endothelial cells and coverage is decreased, a process mediated by VEGF (Díaz-Flores et al. [2009]). In

the sprouting phase of angiogenesis, endothelial cells migrate in the direction of growth of the new vessels without perivascular cells recruitment (Reynolds et al. [2000], Bjarnegard et al. [2004]). Perivascular cells are normally recruited soon after and are among the first cells to colonise the new vascularised area. Other studies have shown that perivascular cells can lead endothelial cells in the vessel sprouting and have the ability to form functional tubes without endothelial cell recruitment (Ozerdem and Stallcup [2003]). If angiogenesis resolves, endothelial PDGF-B recruits perivascular cells thus increasing pericyte coverage. This is a stabilising event, but pericyte coverage alone is not sufficient to protect vessels from VEGF-induced degradation: endothelial cell/perivascular cell functional contact must be established to ensure full vascular stability through the mechanism previously described (see paragraph 6.1.1) (Hoffmann et al. [2005]). Finally, perivascular cells have been reported to influence metastasis, with perivascular cells function directly correlating to increased metastatic potential in a fibrosarcoma model, which may be mediated by increasing vasculature permeability (Xian et al. [2006]).

### 6.1.2 Perivascular cells *in vitro* models

Perivascular cells are an elusive cell population characterised by highly heterogeneous marker expression. Identification of perivascular cells in *ex vivo* studies relies mostly on the description of their location with respect to blood vessels, coupled with the expression of a panel of markers, none of which are expressed only or by all perivascular cells. *In vitro* studies have shown similar limitations, therefore there is not a unique model for perivascular cells *in vitro*. In some studies perivascular cells have been extracted from *in vivo* tissues (Bryan and D'Amore [2008]). Typically this is achieved in larger animals and examples include extraction from corpus luteum and the bovine retina (Beckman et al. [2006], Dore-Duffy [2003]). Extraction from smaller animals has been reported, including hamster skeletal muscle and stria vascularis of the mouse ear (Mogensen et al. [2011], Neng et al. [2013]). There is a commercially available source of perivascular cells extracted from normal fetal brain (Bagley et al. [2005]). Primary perivascular cells present the advantage of demonstrating similar characteristics to *in vivo* perivascular cells. However, extraction procedures are time consuming, costly and require specific equipment and training, although improvements with semi-automated systems and protocols are now available (i.e. *gentleMACS* from Miltenyi Biotec). Alternatively, perivascular cells can be derived *in vitro* using a stem cell precursor. Perhaps the most studied is C3H/10T1/2, Clone 8, commonly referred to as 10T1/2. These cells were isolated in 1973 from C3H mouse embryos

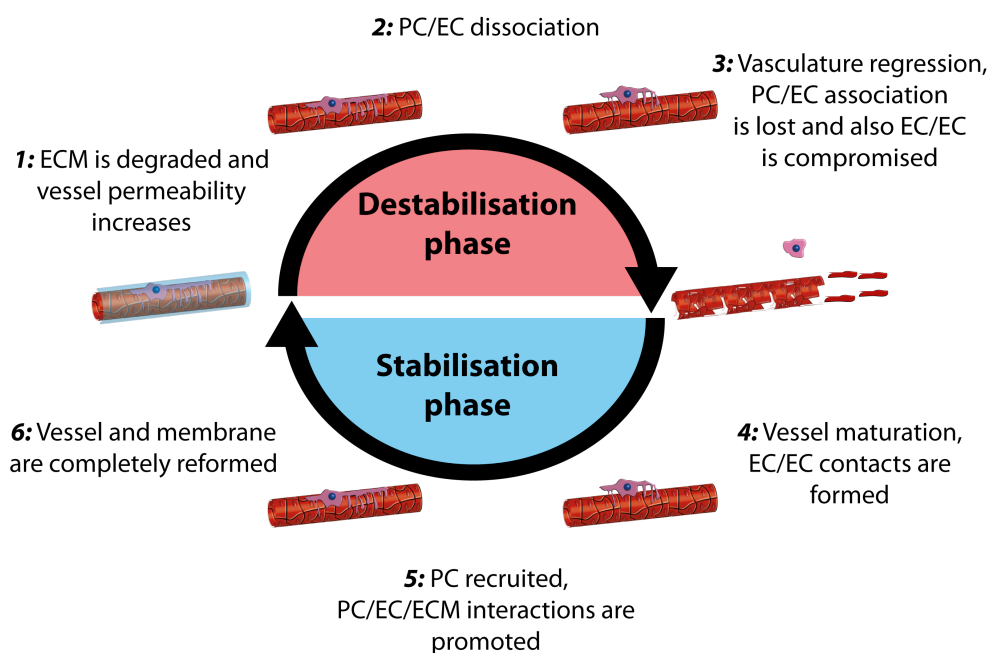


Figure 6.2: *Pericytes in angiogenesis.* A stable vessel is characterised by endothelial cells (EC, red constituents of the tubes) associated with pericytes (PC, pink perivascular cell) and the structure is enclosed in the basal membrane (ECM, light blue layer). In response to pro-angiogenic signalling such as NO and VEGF the membrane is degraded and vessels become more permeable. Angiotensin 2 then causes the dissociation of pericytes from the endothelial cells and vascular regression. PDGF-B signalling recruits pericytes which follow the tip endothelial cell. If angiogenesis resolve pericytes are recruited and make contact with the endothelial cell. Angiotensin 1 stabilises the formed vessels. The deposition of a new ECM is promoted by TGF- $\beta$ 1.

(Reznikoff et al. [1973b]). In 1997 D'Amore and co-workers hypothesised the use of 10T1/2 as perivascular cells precursors (Hirschi et al. [1997]) and in 1998 they reported a more detailed characterisation of such a system (Hirschi et al. [1998]). Cells responded in co-culture with endothelial cells, by directional migration following PDGF-B signalling, with co-culture increasing expression of the marker  $\alpha$ -SMA. In cell culture, TGF- $\beta$ 1 affected the phenotype of 10T1/2 and increased the expression of  $\alpha$ -SMA while decreasing the expression of NG2 (Darland and D'Amore [2001]). Recently, 10T1/2 cells have been used to recreate the vasculature not only *in vitro*, but also *in vivo*. A gel containing both endothelial cells and 10T1/2 as supporting cells has been implanted into the mouse cranial window chamber and a functional vasculature was developed (Samuel et al. [2013]). The panel of markers identified by D'Amore and co-workers does not describe specifically pericytes or vSMCs cells. In fact, the authors referred to 10T1/2 as both pericytes and vSMCs precursor. This is due in part to the fact that there is no clear distinction between the two cell lines, at least regarding cellular marker expression. If the only differentiation possible is based on location (capillaries for pericytes, larger vessels for vSMCs), then of course an *in vitro* model as the one described above cannot distinguish between the two. In the work here presented, 10T1/2 were chosen as model for perivascular cells to investigate any selective targeting against tumour cells or endothelial cells, without the specific need to distinguish between pericyte or vSMCs.

### 6.1.3 TGF- $\beta$ 1 and perivascular cells

TGF- $\beta$ 1 has been reported to act as both a pro- and anti-angiogenic factor *in vivo* (Pepper et al. [1993]). This dual role can be explained in terms of the local concentration of TGF- $\beta$ 1. For example, specific concentrations (0.1ng/ml) appear more efficient in stimulating Smooth muscle cells (SMC) proliferation *in vitro* than lower (0.02ng/ml) or higher concentrations (1-5ng/ml) (Battegay et al. [1990]). TGF- $\beta$ 1 response is dependent on the expression of the Activin receptor-like kinase 1 (ALK-1), a receptor phosphorylated by TGF- $\beta$ 1 (Tallquist et al. [2003]). TGF- $\beta$ 1 is secreted by both endothelial cells and perivascular cells in an inactive form and the association between the two cell types is required for TGF- $\beta$ 1 activation, mediated by a mechanism involving gap junctions (Antonelli-Orlidge et al. [1989], Hirschi et al. [2003]). TGF- $\beta$ 1 also has the ability to modify specific perivascular markers expression.  $\alpha$ -SMA expression has been detected in perivascular cells treated with TGF- $\beta$ 1 but not in untreated cells, which in turn expressed NG2 and desmin.

The TGF- $\beta$ 1 response by 10T1/2 has mainly been studied in co-culture sys-

tems with endothelial cells, with tubular structures characterised. Selective blocking of **TGF- $\beta$ 1** receptor resulted in reduced formation of tubular structures, suggesting a key role for **TGF- $\beta$ 1** in recruitment and differentiation of 10T1/2 into perivascular-like cells (Darland and D'Amore [2001]). In single cell culture it has been reported that **TGF- $\beta$ 1** increases the expression of  **$\alpha$ -SMA** (Lien et al. [2006]).

### Perivascular cells markers

A number of markers have been used to identify perivascular cells. However, none has been reported to be consistently expressed. Commonly used perivascular cells markers include **PDGFR- $\beta$** , **NG2**, **Regulator of G-protein Signalling 5 (RGS5)**,  **$\alpha$ -SMA**, desmin, aminopeptidase A and N and the reporter *XlacZ4*. Unfortunately the expression of such markers is highly heterogeneous. Variations have been reported not only between species, but also within organs in the same species. Furthermore, perivascular cells markers can be modified in pathological states (Armulik et al. [2005], Armulik et al. [2011]). As an example,  **$\alpha$ -SMA** expression is not detected in normal skin and the **CNS**, but it is highly expressed in tumours implanted in these organs (Abramsson et al. [2002]). **RGS5** expression follows a similar pattern in a mouse model of pancreatic islet cell carcinogenesis (Berger et al. [2005]).

**$\alpha$ -SMA** is part of the contractile apparatus of perivascular cells and is organised into cytoplasm microfilaments.  **$\alpha$ -SMA** is expressed by perivascular cells in pre and post capillary vessels, but not in mid-capillary vessels (Nehls and Drenckhahn [1991]).  **$\alpha$ -SMA** is not perivascular cells specific being expressed by other cells, such as fibroblasts and keratinocytes (Hinz et al. [2001], Szentmáry et al. [2013]). In 10T1/2  **$\alpha$ -SMA** expression has been reported to be up-regulated by exposure to **TGF- $\beta$ 1** (Hirschi et al. [1998]).  **$\alpha$ -SMA** expression is correlated to contractile properties of perivascular cells and is the basis for the molecular mechanisms regulating microvasculature flow and vessel diameter.

**PDGFR- $\beta$**  is one isoform of the receptor for **PDGF-B**, secreted by endothelial cells and some tumour cells and responsible for perivascular cells recruitment. **PDGFR- $\beta$**  is a tyrosine kinase transmembrane receptor and one of the members of the **Platelet Derived Growth Factor Receptor (PDGFR)** family. **PDGF** exists in 4 isoforms: A, B, C and D, which dimerise to **PDGF-AA**, **PDGF-BB**, **PDGF-CC** and **PDGF-DD**. **PDGFR** exists in two isoforms: **Platelet Derived Growth Factor Receptor- $\alpha$  (PDGFR- $\alpha$ )** and **PDGFR- $\beta$** , which dimerise after binding to **PDGFR- $\alpha\alpha$** , **PDGFR- $\beta\beta$**  and **PDGFR- $\alpha\beta$** . The receptor is characterised by two

intracellular domains responsible for the signal transduction of the signal and the five extracellular domains (Shim et al. [2010]). Affinity of the different receptor isoforms is reported in figure 6.3. PDGFR- $\beta$  has been often reported to be expressed by 10T1/2 (Hirschi et al. [1997], Hirschi et al. [1998], Díaz-Flores et al. [2009]).

**NG2** or High Molecular Weight Melanoma Associated Antigen (HMWMAA) is a chondroitin sulfate proteoglycan membrane receptor. NG2 was initially found to be expressed by immature cells in the CNS that demonstrated the ability to differentiate either into neurons or glial cells, thus the name nerve/glial antigen. NG2 is expressed by several cell-types including mesenchymal stem cells and perivascular cells, both in physiological and pathological angiogenesis (Ozerdem et al. [2002], Ozerdem and Stallcup [2004]). NG2 has also been identified in some cancer cells, such as melanomas and glioblastomas (Stallcup [2002]). NG2 contributes to cell proliferation and motility. NG2 is an auxiliary receptor for growth factors such as Fibroblast Growth Factor (FGF), Platelet Derived Growth Factor-AA (PDGF-AA) and integrins (You et al. [2013]). As with other proteoglycans, NG2 sequesters the factors presenting them to their receptors. NG2 also binds metalloprotease, which appears important in ECM degradation caused by tumour cells. Cell motility is probably enhanced by binding with collagen VI (Stallcup [2002]). NG2 has not been reported to be expressed by 10T1/2 cells.

#### 6.1.4 Immunoglobulin of the class G (IgG) structure

The antibodies that will be used to functionalise the polymersomes are IgG. An IgG is a protein with a molecular weight of  $\simeq 150\text{KDa}$ , and is the most prevalent isoform of antibody. It is composed of two identical long (*heavy*) chains (Molecular weight (MW)  $\simeq 50\text{KDa}$ ) and two identical shorter (*light*) chains (MW  $\simeq 25\text{KDa}$ ). Disulfide bonds link together the heavy chains and the light chains in the typical quaternary Y-shaped structure (see fig 6.4). There are also functional distinctions. The non-binding region (*Fc* fragment) is a highly conserved and glycosylated portion of the IgG. Ideally, any chemical modification should occur in this area as it is not involved in the antigen recognition. The two arms of the Y-shape (*Fab* fragment) includes the binding site. Knowing the exact amino acid composition and 3D structure of an IgG is important to identify the most probable binding site and the best binding strategy, to avoid compromising the antigen recognition efficiency.

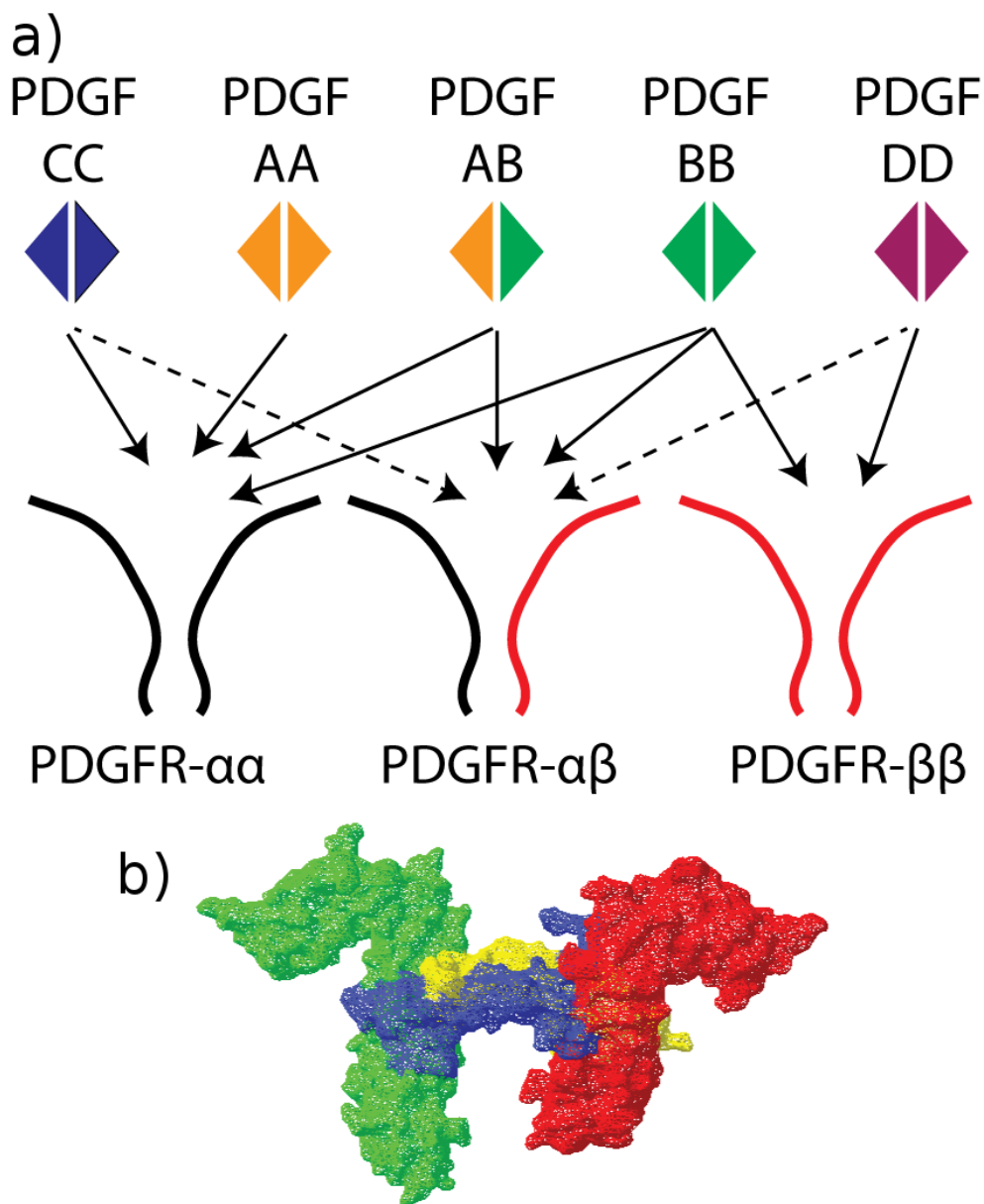


Figure 6.3: (a) Affinity of the iso-form of *PDGF* for the *PDGFR*. Solid lines indicate high affinity, dotted lines indicate low affinity. (b) Reconstruction of the interaction of *PDGF-BB* dimer with the dimerised *PDGFR- $\beta\beta$* . The two receptor monomers are represented in red and green and the two *PDGF* monomers are represented in blue and yellow. *Protein Data Base (PDB)* file obtained from Shim et al. [2010].

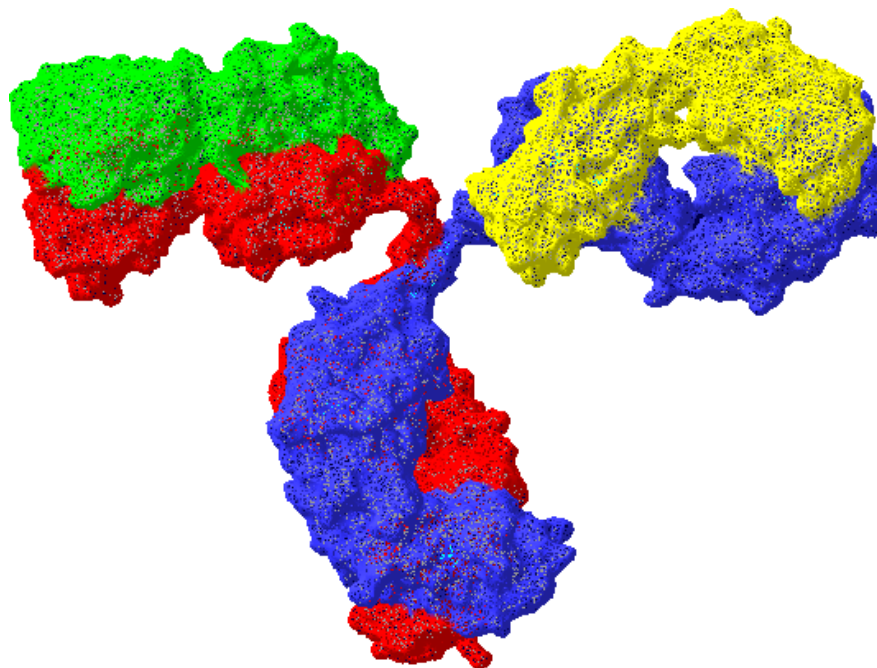


Figure 6.4: *IgG Structure*. The two heavy chains are visible in red and blue, while the two light chains are coloured in green and yellow. Image obtained by visualisation of *PDB* file 1IGT (Harris et al. [1997]).

### 6.1.5 Conjugation methods

Nanoparticles can accumulate in tumours by taking advantage of increased leakiness and reduced lymphatic drainage ([Enhanced Permeation and Retention \(EPR\)](#), sec. 1.4.2). Side effects are limited by delivering the cargo preferentially to the tumour site, therefore increasing distribution volume and local concentration. Passive targeting can be coupled with active targeting to a specific cell population. Active targeting can be achieved by decorating the nanoparticle surface with specific antibodies to recognise cell markers.

There is a vast literature available on conjugation of molecules with differential composition (peptides, antibodies, nucleic acid, small molecules, dyes and more) to polymers. The process is called bio-conjugation and it has been developed mostly for polymer therapeutics. In 1975 Ringsdorf proposed a polymer-drug model characterised by a polymeric backbone conjugated to a drug and a targeting moiety (Ringsdorf [1975]). Over the years this model proved to efficiently improve the pharmacokinetics and pharmacodynamic profile of the drug by limiting side effects and improving drug efficacy due to the targeting moiety. Bio-conjugation has resulted in a number of [Food and Drugs Administration \(FDA\)](#) approved therapeutic agents, although mostly non actively targeted (Duncan et al. [2006]).

One of the simplest approaches is complexation. This has been widely used

Amino acid	Conjugation strategy
N-terminal	N-terminal
Glutamine	TGase mediated
Cysteine	Thiolation
Cysteine (2)	Oxidation, bridging (2 cysteine required)
Threonine	O-glycosilation
Lysine	Amino-functionalisation
Asparagine	N-glycosilation
Serine	O-glycosialtion
C-terminal	C-terminal functionalisation

Table 6.1: *Sites of bioconjugation of proteins. Amino acid residuals offer a number of sites available for bioconjugation using different chemical strategies. Adapted from Pasut and Veronese [2012]).*

to decorate polymers and liposomes with nucleic acids (Felnerova et al. [2004], Grinstaff et al. [1997], Li and Szoka Jr [2007], Kataoka et al. [2013]). It is not a direct chemical link and requires the interaction between anionic nucleic acids and cationic lipids or polymers. The use of cationic polymers is a major drawback of the system, due to rapid clearance and higher toxicity when compared to neutral polymers. Another popular strategy for non-covalent binding involves the use of biotin/streptavidin. Covalent binding offers a wide range of chemical strategies depending on the structure of the two molecules. When considering proteins, such as the IgG used in the present work, the main possibilities are listed in table 6.1. Once a conjugation strategy has been chosen, for instance targeting of primary amino groups with N-hydroxysuccinimide, it is helpful to assess the availability of leucin in the protein and the location with respect to the active site (see fig.6.5). Ideally the targeted amino group should be highly represented, but not easily available for reaction near the functional site of the protein, to avoid a potential reduction in target-recognition efficiency.

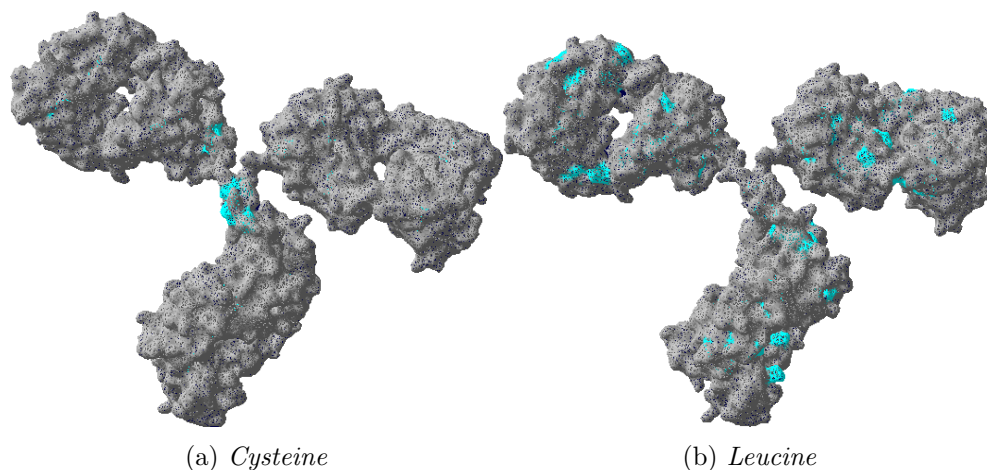


Figure 6.5: *Distribution of cysteine (left) and leucine (right) in IgG. Amino acids are highlighted in light blue. Note how leucine is more frequent and at more accessible sites compared to cysteine.*

During polymersome functionalisation for targeting purposes, the targeting moiety is linked to the hydrophilic block of the co-polymer to direct it towards the exterior of the polymersome, where the target will be located. Functionalisation of nanoparticles can be performed before or self-assembly, as described for liposomes in the review published by Marques-Gallego (Marqués-Gallego and de Kroon [2014]). The considerations made for liposomes can be here extended to polymersomes. Pre self-assembly functionalisation involves the synthesis of the co-polymer-protein construct as a first step, followed by solubilisation of the reaction product with pristine co-polymer and polymersome self-assembly. In post self-assembly functionalisation, the pristine co-polymer is mixed with reactive co-polymer, polymersomes are prepared and finally the polymersomes are functionalised. Both techniques have advantages and disadvantages. In pre self-assembly functionalisation, a percentage of the functionalised co-polymer will be oriented towards the internal hydrophilic core, therefore it will not be useful for targeting purposes. However, post self-assembly functionalisation can be difficult due to the steric hindrance generated by the packed hydrophilic brush. Furthermore, the non-fouling formulation will tend to repel proteins. Pre self-assembly functionalisation is not affected by these limitations, however the solvent and the reaction condition must not compromise protein stability (6.6).

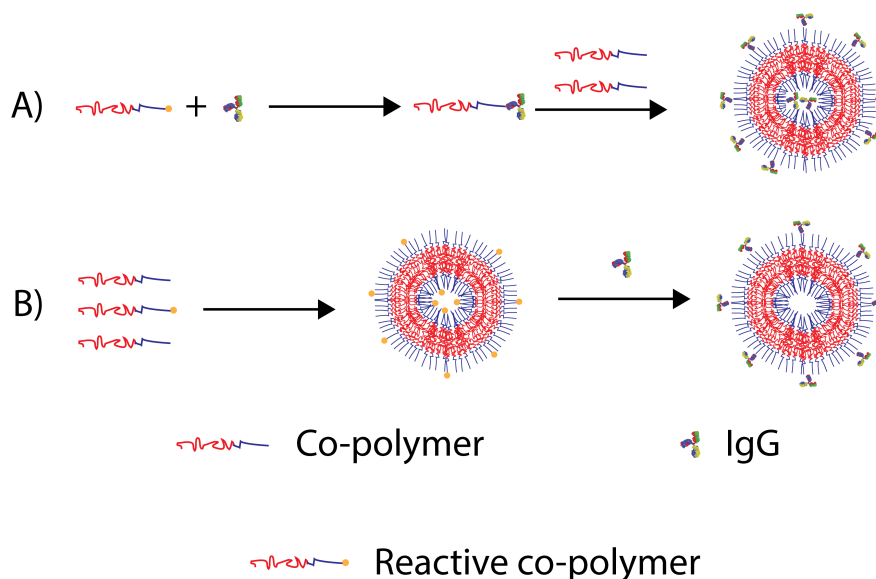


Figure 6.6: *Polymersomes can be functionalised (A) before self-assembly or (B) after self-assembly. The choice of best strategy depends on the self-assembly conditions and ligand (IgG) stability.*

**Biotin/streptavidin conjugation** Biotin is a small ( $244.31\text{g} \cdot \text{mol}^{-1}$ ) water soluble molecule. In bio-conjugation, more specifically biotinylation, the small size is one of the advantages since it does not affect the properties of the molecule to which it is linked. Biotinylated compounds bind strongly to avidin and streptavidin ( $K_d \simeq 10^{-14}\text{mol} \cdot \text{l}^{-1}$ ). Streptavidin and avidin have a similar secondary structure despite sharing only  $\simeq 30\%$  of the amino acid sequence. They are large tetramers ( $\simeq 53\text{kg} \cdot \text{mol}^{-1}$ ) binding up to four biotin moieties. Affinity for biotin decreases at higher rate in avidin than in streptavidin after the first binding event. Furthermore, avidin is glycosylated and positively charged. Streptavidin/biotin functionalisation is used daily in laboratories, for instance in [Immunohistochemistry \(IHC\)](#) and [Immunocytochemistry \(ICC\)](#) to link biotinylated primary antibodies to dyes conjugated with avidin or streptavidin. Using this non-covalent binding strategy polymersomes have been functionalised to map their surface via [Atomic Force Microscopy \(AFM\)](#) ([Battaglia et al. \[2011\]](#)), to mimic leukocyte binding strategy through integrins or selectins ([Hammer et al. \[2008\]](#)) or to target macrophages *in vitro* ([Brož et al. \[2005\]](#)).

**Maleimide conjugation** Maleimide is traditionally used to functionalise thiol groups via oxidation of the sulphur atom ([Pasut and Veronese \[2012\]](#)), typically cysteine. At low pH (6.5-7.5) it is a specific reaction, however at  $\text{pH} > 8$  it can undergo nucleophilic attack from primary amines (i.e. lysine), and this reaction is favoured over thiol functionalisation (6.7)([Brewer and Riehm \[1967\]](#)).

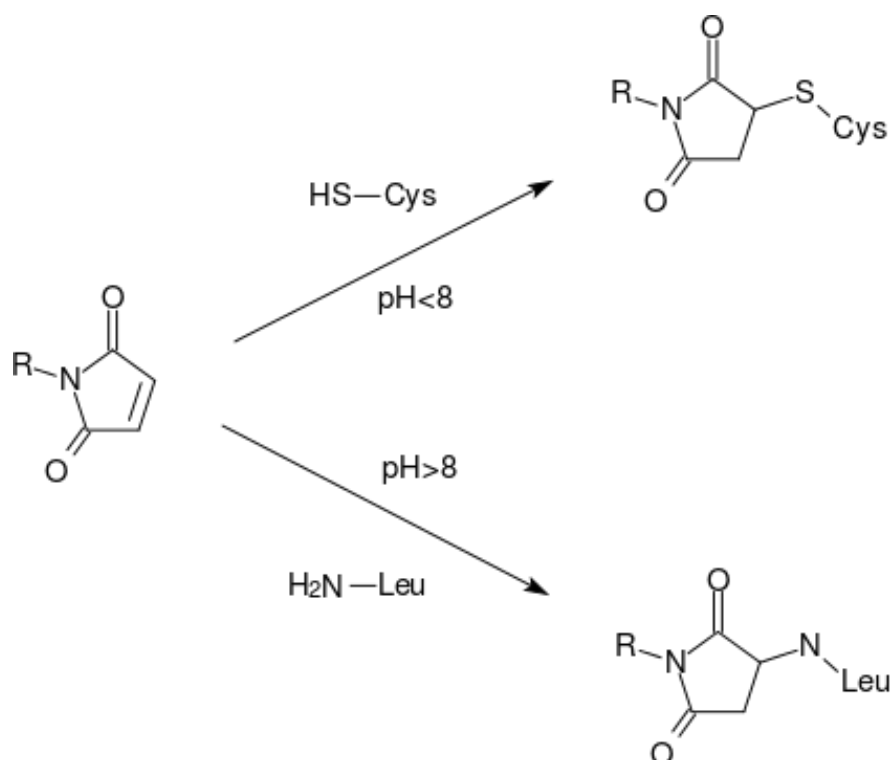


Figure 6.7: *Maleimide reactivity.* At  $\text{pH} < 8$  maleimide oxidates thiol groups (cysteine), but at  $\text{pH} > 8$  it undergoes nucleophilic attack from primary amino groups (leucine).

### 6.1.6 Aim

An interest application of the methodologies developed in the chapter 4 is the active targeting of perivascular cells with rhodamine labelled polymersomes for optical imaging *in vivo*. Targeting of perivascular cells is of interest because of their role in vessel stabilisation, particularly in the context of tumour angiogenesis. However, pericyte targeting is challenging because of the lack of specific extracellular markers. In this chapter the expression of two of the most commonly reported perivascular cells markers *ex vivo* (PDGFR- $\beta$  and NG2) will be tested in an *in vitro* perivascular cells model embryonic cells 10T1/2. The expression in 10T1/2 will be compared to the expression in SVECs and MFC188, with the aim of identifying a marker expressed preferentially by the perivascular cells model, therefore suitable for active targeting. Once the marker is identified, two different conjugation strategies will be investigated in order to functionalise polymersomes to target the perivascular cells. Finally, the targeting efficiency of the conjugate will be tested *in vitro*.

## 6.2 Results

### 6.2.1 ICC

ICC was used to assess the expression level of NG2, PDGFR- $\beta$  and  $\alpha$ -SMA in 10T1/2, MFC188 and SVECs. The aim of this analysis was to confirm expression of perivascular cell markers on 10T1/2 cells and to identify a marker expressed by 10T1/2 and not SVECs or MFC188. This is critical for the purpose of functionalise polymersomes to selectively target perivascular cells. Transformation of 10T1/2 into perivascular cells was induced by exposure to TGF- $\beta$ 1, initially used at 1ng/ml. The expression levels of NG2, PDGFR- $\beta$  and  $\alpha$ -SMA were assessed after 24h, 48h and 72h of treatment (fig. 6.8). Image analysis showed a small increase in expression of  $\alpha$ -SMA after 48h compared to the 24h treatment. At the 72h time point there was no further increase ( $p > 0.05$ ). PDGFR- $\beta$  expression was also increased after 48h compared to 24h, while at 72h the expression decreased compared to the control. NG2 ratio of expression at 24h was unchanged with respect to the control, similar to  $\alpha$ -SMA and PDGFR- $\beta$ . However, NG2 expression decreased further at 48h and 72h compared to the control, while the expression of PDGFR- $\beta$  and  $\alpha$ -SMA was increased ( $p > 0.05$ ). The expression of the markers was affected by exposure time to TGF- $\beta$ 1, and this first result suggested an ideal treatment of 10T1/2 with 1ng/ml for 48h in order to maximise expression of PDGFR- $\beta$  and  $\alpha$ -SMA without losing the expression of NG2.

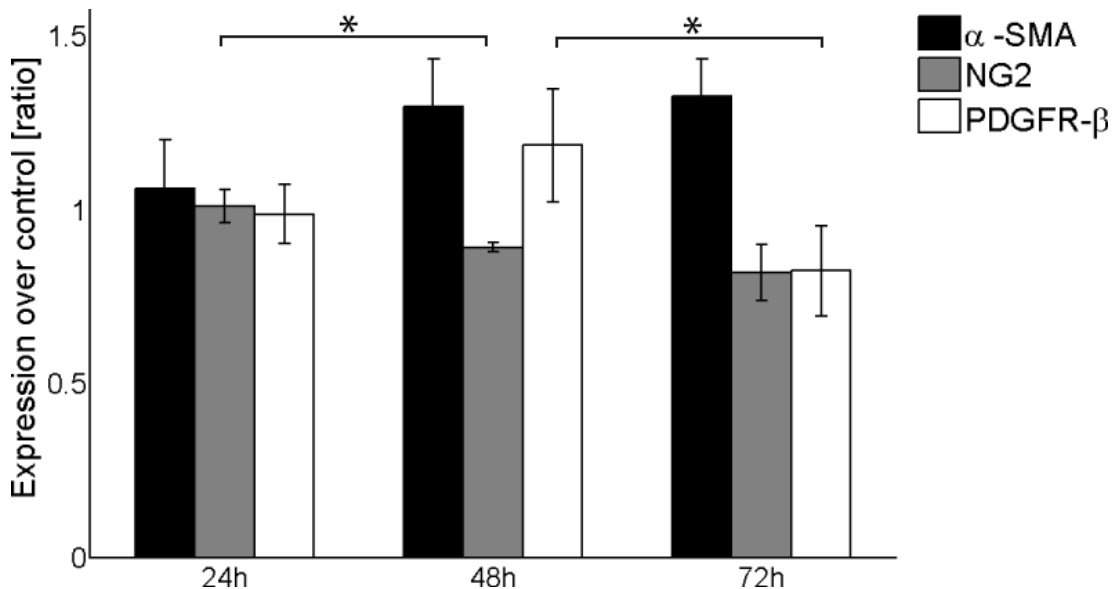


Figure 6.8: Quantification of expression of  $\alpha$ -SMA, NG2 and PDGFR- $\beta$  in 10T1/2 cells treated with 1ng/ml of TGF- $\beta$ 1 for 24h, 48h or 72h. ICC micrographs were analysed as reported in 3.3. Expression is compared to 10T1/2 cells not treated with TGF- $\beta$ 1 (\*=statistical difference from untreated 10T1/2, U-test,  $p < 0.05$ ).

In a subsequent experiment the exposure to **TGF- $\beta$ 1** was further optimised by assessing the expression of the same markers in 10T1/2 after treatment with a range of **TGF- $\beta$ 1** concentration (1-10ng/ml). The exposure time was limited to 24h and 48h as it was observed previously that 72h had no significant positive effect on the expression of any of the markers ( $p > 0.05$ ). Results are reported in figures 6.12-6.14.  **$\alpha$ -SMA** expression was higher after 48h treatment at every concentration used except 10ng/ml. At 24h exposure the highest expression was measured when 10ng/ml were used, although the increase was not statistically significant ( $p > 0.05$ ). At 48h a trend can be observed where the ratio of expression is on average decreasing with increasing **TGF- $\beta$ 1** concentration, however there is no statistical significant difference between the different concentrations ( $p > 0.05$ ). **PDGFR- $\beta$**  expression after 48h showed a remarked increase compared to the 24h treatment ( $p < 0.05$ ), with the only exception of 10ng/ml treatment as was observed for  **$\alpha$ -SMA**. Another similarity to  **$\alpha$ -SMA** expression is that at 24h the ratio is proportional with concentration, but in this case there was a decrease at 2ng/ml. At 48h the maximal expression was measured at 2ng/ml. **NG2** expression showed a different pattern compared to  **$\alpha$ -SMA** and **PDGFR- $\beta$** . Expression ratio was  $\leq 1$ , with the exception of 2ng/ml and 5ng/ml at 24h treatment. At 1ng/ml for 48h showed a significant decrease in expression ( $p < 0.05$ ). Increased concentrations of **TGF- $\beta$ 1** restored the ratio to  $\simeq 1$  (no significance between treatment and control,  $p > 0.05$ ).

These results suggested that expression of perivascular markers in 10T1/2 is better induced by treatment with 2ng/ml of **TGF- $\beta$ 1** for 48h. At this concentration and time the expression of both  **$\alpha$ -SMA** and **PDGFR- $\beta$**  was at the maximum observed, although the increase was not always significant, while the expression of **NG2** was retained at a similar level compared to the control.

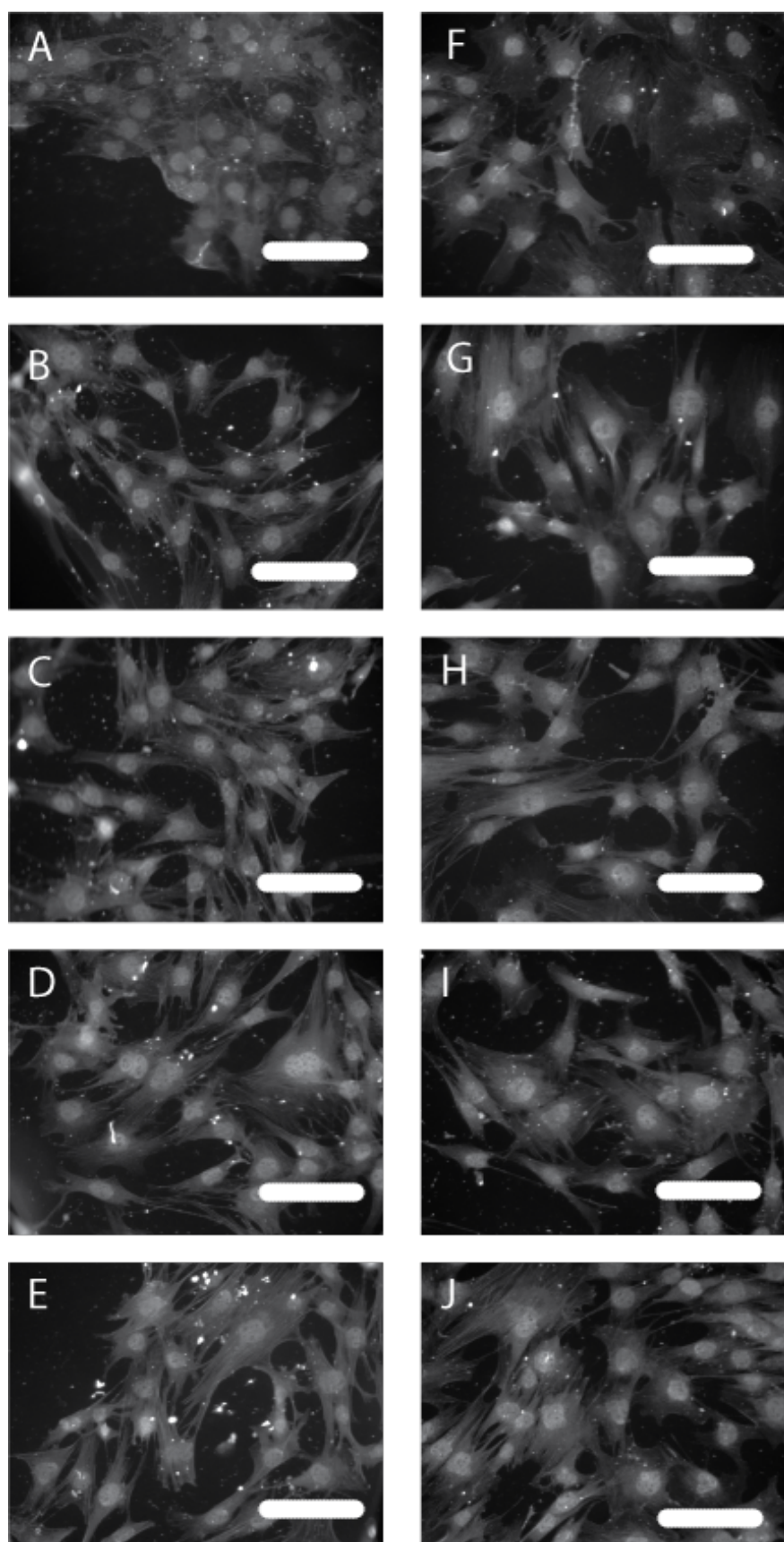


Figure 6.9: Representative images for staining of  $\alpha$ -SMA for 10T1/2. (A, B) 10T1/2 cells. 10T1/2 cells were added with (B, G) 1ng/ml, (C, H) 2ng/ml, D, I) 5ng/ml or (E, J) 10ng/ml of TGF- $\beta$ 1. Cells were grown for (B,C,D,E) 24h or (F, G, H, I) 48h before imaging. Bar 18 $\mu$ m.

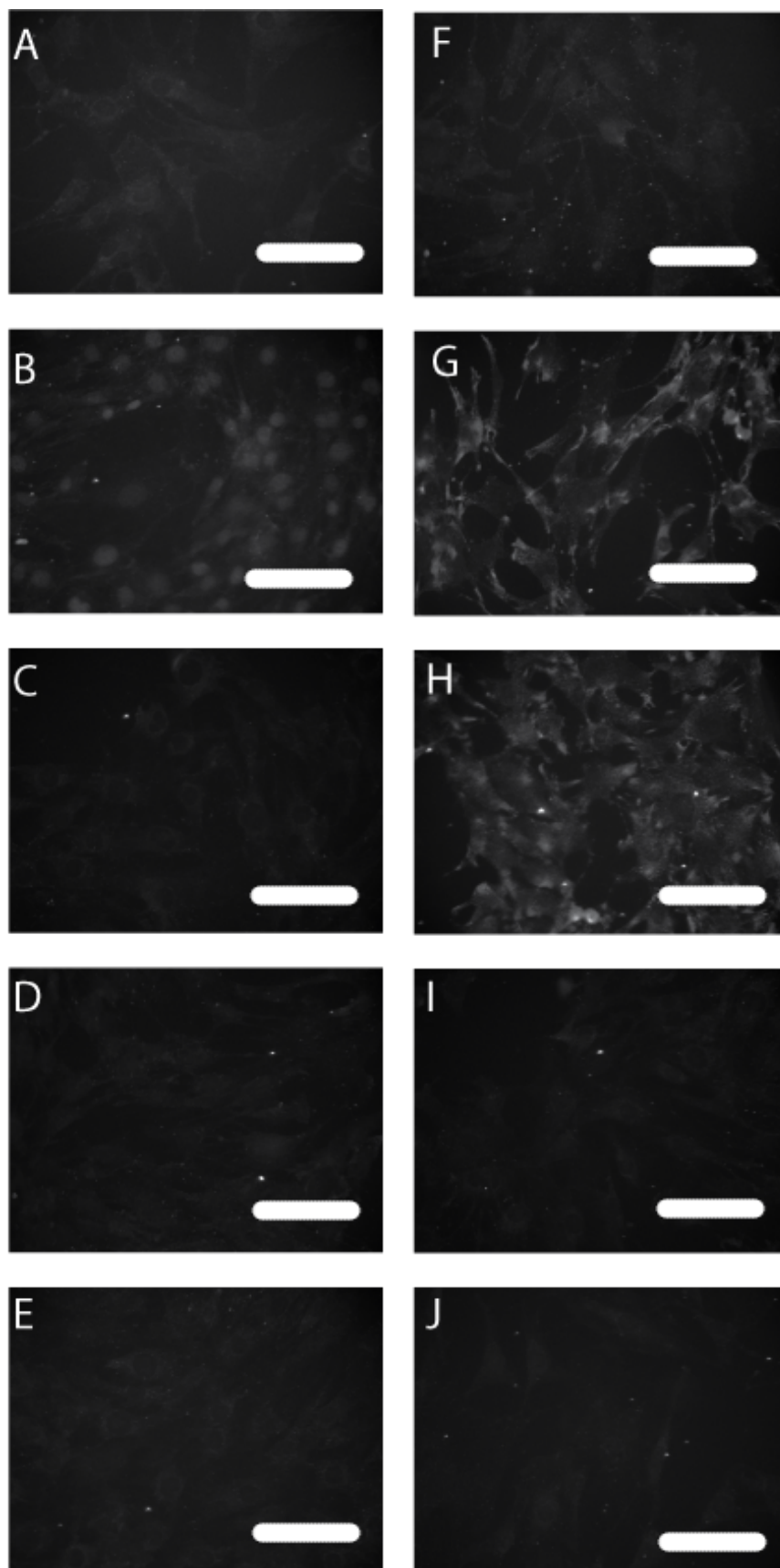


Figure 6.10: Representative images for staining of *PDGFR-β* for 10T1/2. (A, B) 10T1/2 cells. 10T1/2 cells were added with (B, G) 1ng/ml, (C, H) 2ng/ml, (D, I) 5ng/ml or (E, J) 10ng/ml of *TGF-β1*. Cells were grown for (B,C,D,E) 24h or (F, G, H, I) 48h before imaging. Bar 18μm.

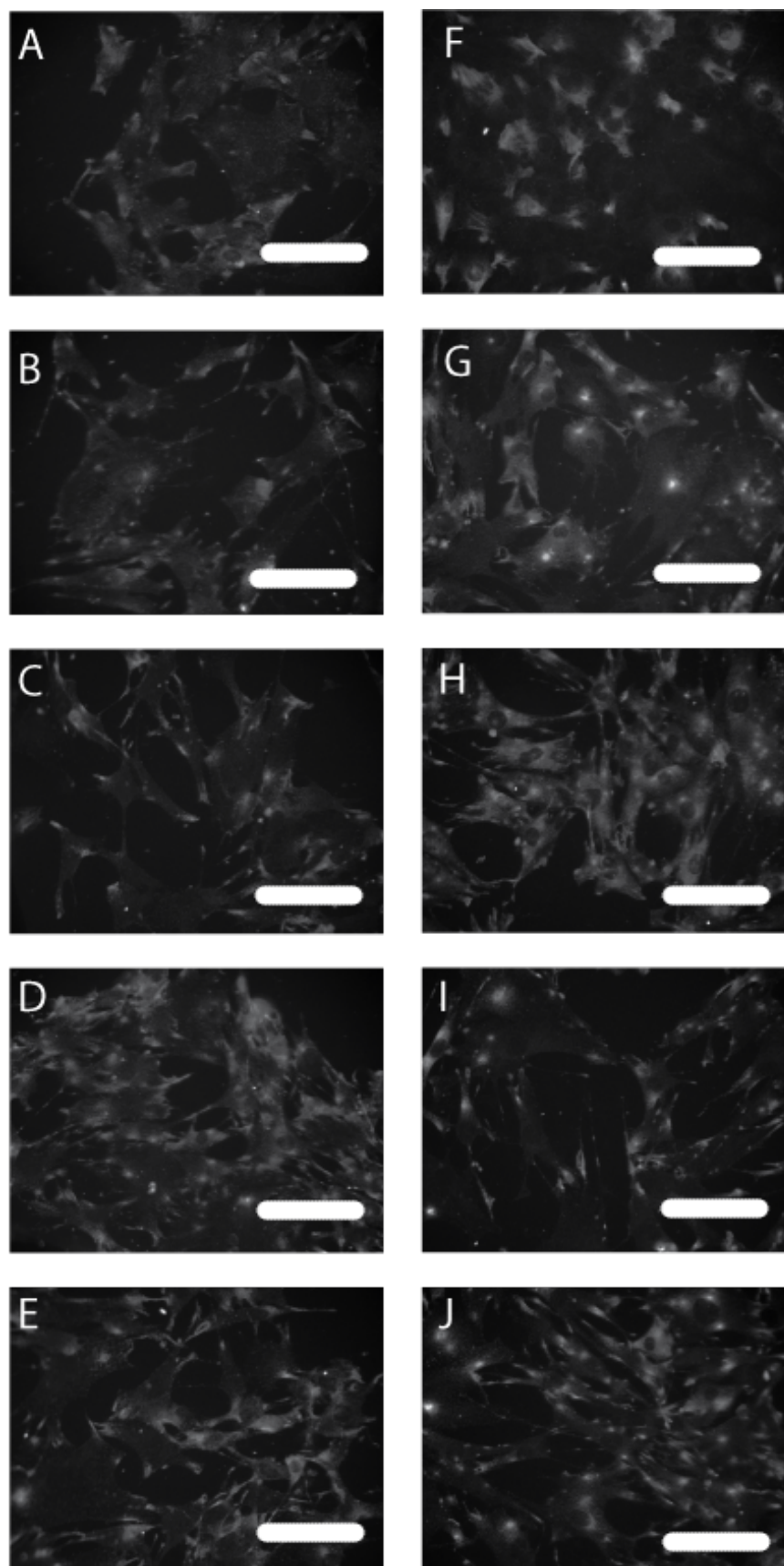


Figure 6.11: Representative images for staining of *NG2* for 10T1/2. (A, B) 10T1/2 cells. 10T1/2 cells were added with (B, G) 1ng/ml, (C, H) 2ng/ml, (D, I) 5ng/ml or (E, J) 10ng/ml of *TGF- $\beta$ 1*. Cells were grown for (B,C,D,E) 24h or (F, G, H, I) 48h before imaging. Bar 18 $\mu$ m.

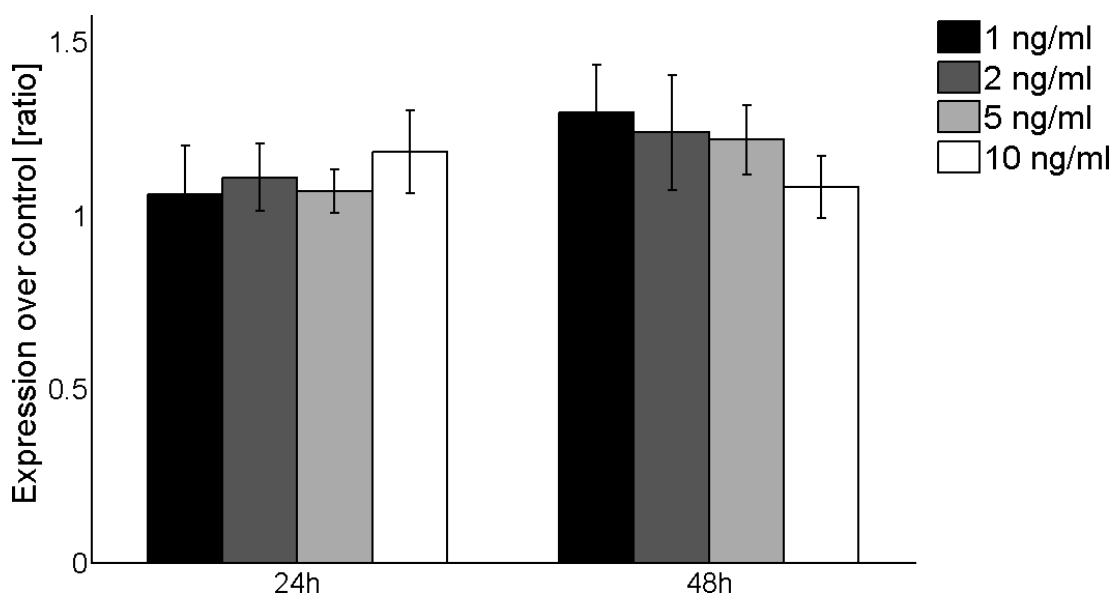


Figure 6.12: Quantification of expression of  $\alpha$ -SMA in 10T1/2 cells treated with 1-10ng/ml of TGF- $\beta$ 1 for 24h or 48h. ICC micrographs were analysed as reported in 3.3. Expression is compared to 10T1/2 cells not treated with TGF- $\beta$ 1 (\*=statistical difference from untreated 10T1/2, U-test,  $p < 0.05$ .  $N=3$ ,  $\pm SD$ ).

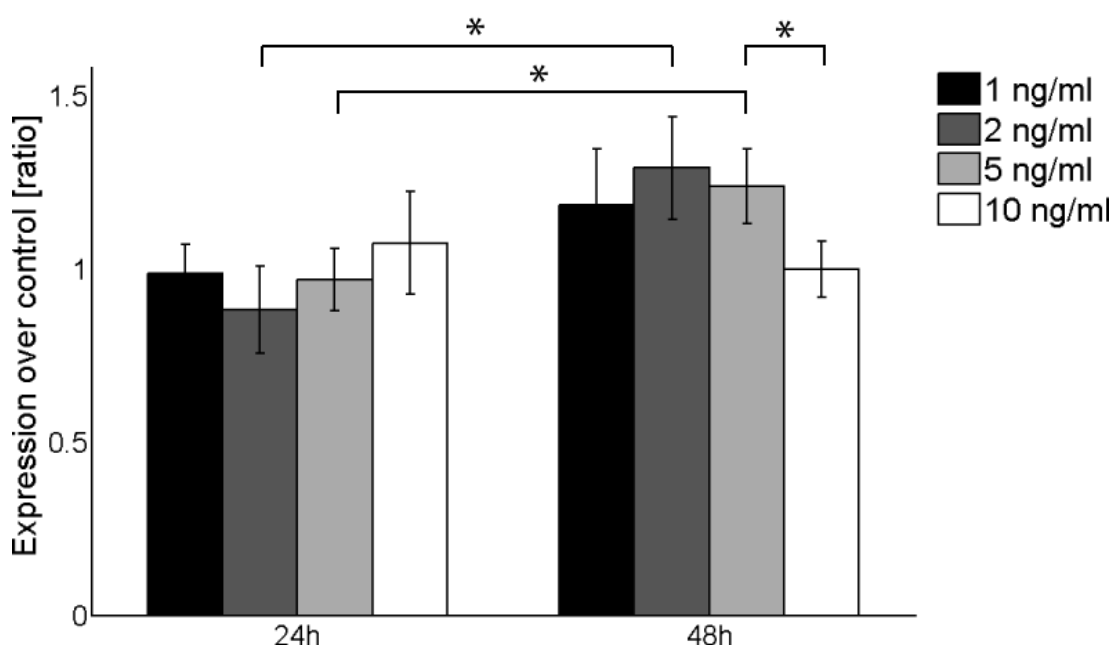


Figure 6.13: Quantification of expression of PDGFR- $\beta$  in 10T1/2 cells treated with 1-10ng/ml of TGF- $\beta$ 1 for 24h or 48h. ICC micrographs were analysed as reported in 3.3. Expression is compared to 10T1/2 cells not treated with TGF- $\beta$ 1 (\*=statistical difference from untreated 10T1/2 U-test,  $p < 0.05$ .  $N=3$ ,  $\pm SD$ ).

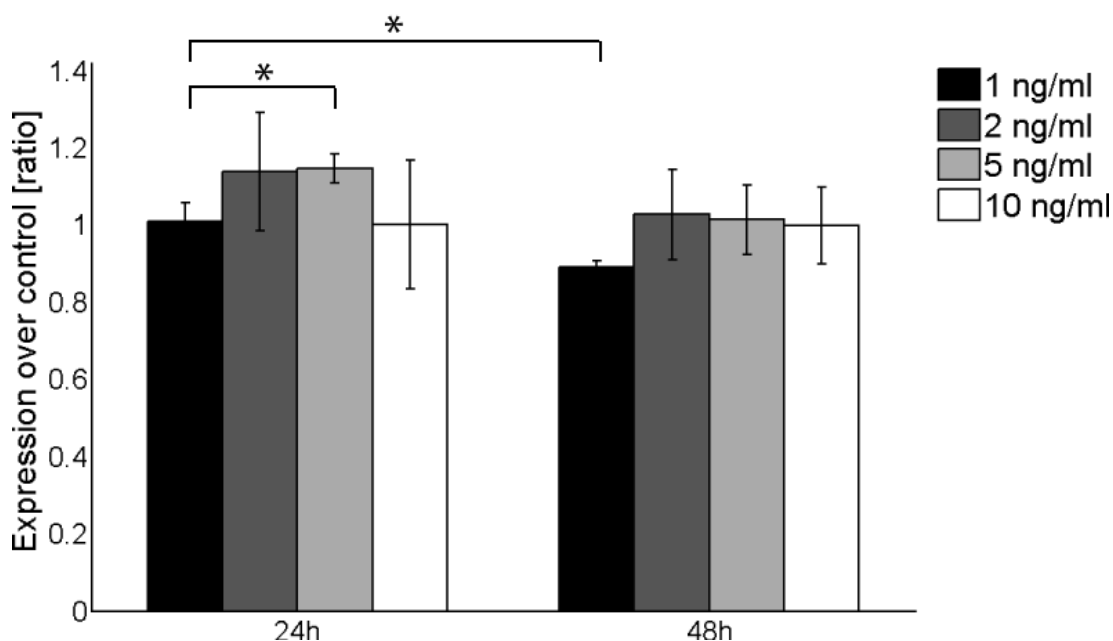


Figure 6.14: Quantification of expression of *NG2* in 10T1/2 cells treated with 1-10ng/ml of *TGF-β1* for 24h or 48h. ICC micrographs were analysed as reported in 3.3. Expression is compared to 10T1/2 cells not treated with *TGF-β1* (\*=statistical difference from untreated 10T1/2, U-test,  $p < 0.05$ .  $N=3$ ,  $\pm SD$ ).

Additional experiments investigated the effect of growing condition on markers expression. The expression of  $\alpha$ -SMA because, despite being useful to confirm the perivascular nature of 10T1/2 cells, it cannot be used for targeting purposes as it is located inside the cell, therefore not accessible to polymersomes. In these experiments *TGF-β1* was added at 2ng/ml for 48h. The effects of culturing 10T1/2 in conditioned media from MFC188 or SVECs and fibronectin coating of the well were assessed (fig. 6.17-6.16). In parallel to marker detection on 10T1/2, MFC188 and SVECs were probed for the same markers (fig. 6.18-6.16). Data quantification is reported in figure 6.19.

*NG2* expression was significantly decreased in 10T1/2 cultured in MFC188 conditioned media (ratio 0.9,  $p < 0.05$ ) compared to untreated 10T1/2 cells, but there was no significant difference in any other culturing condition or in expression on MFC188 cells, when compared to 10T1/2 cultured in standard conditions (Basal medium eagle (BME), no *TGF-β1* added). No expression of *NG2* was detected in SVECs cells. *PDGFR-β* expression did not showed any statistical difference ( $p > 0.05$ ) between 10T1/2 cultured in conditioned media and MFC188 or SVECs compared to 10T1/2 cultured in standard condition. High levels of expression of *PDGFR-β* was detected in NIH-3T3 cells, a positive control for the antibody used (Santa Cruz SC-432).

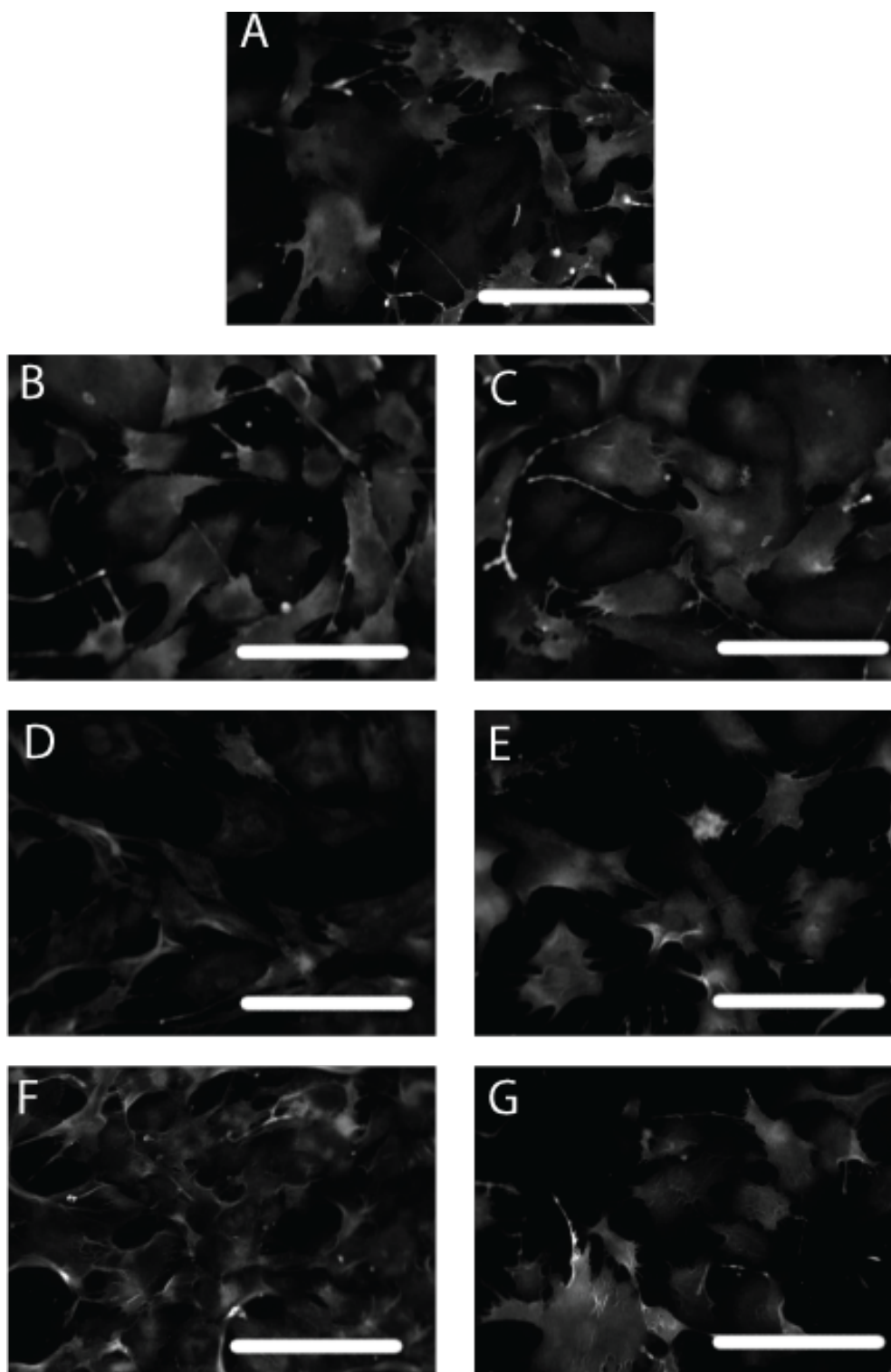


Figure 6.15: Representative images for staining of *NG2* for 10T1/2. A) 10T1/2 cells, B) 10T1/2+2ng/ml *TGF-β1*, C) 10T1/2+2ng/ml *TGF-β1* and fibronectin coated well, D) 10T1/2 cells in *MFC188* conditioned media, E) 10T1/2 in *MFC188* conditioned media and fibronectin coated well, F) 10T1/2 cells in *SVECs* conditioned media, G) 10T1/2 in *SVECs* conditioned media and fibronectin coated well. Bar 30 $\mu$ m.

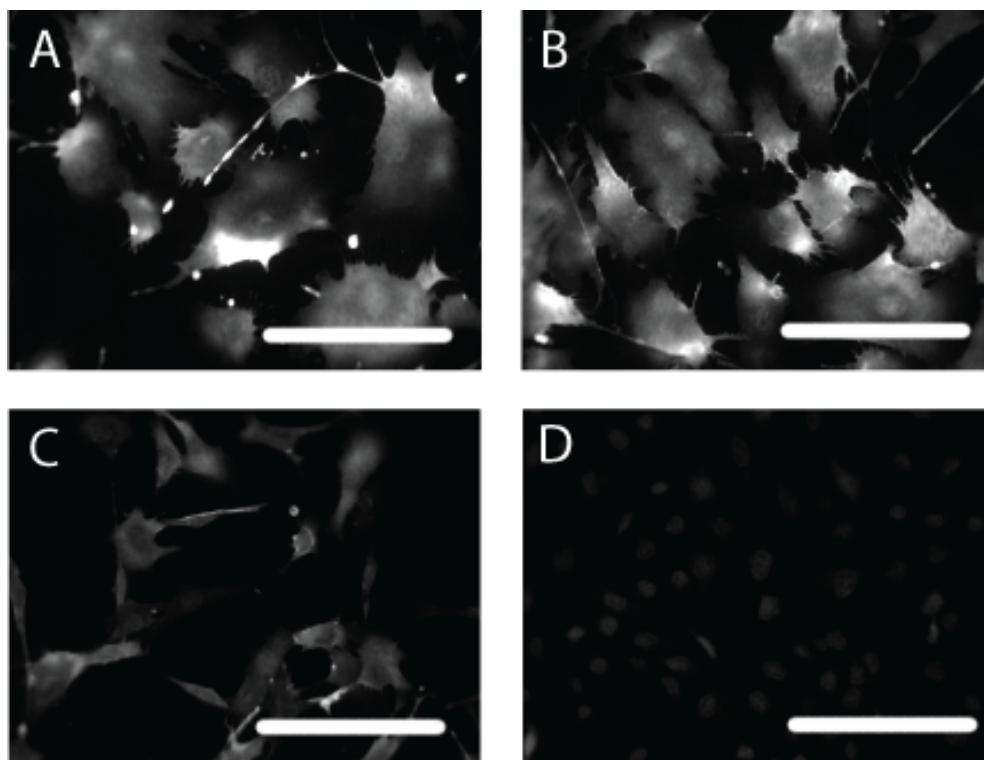


Figure 6.16: Representative images for staining of *NG2* for 10T1/2, *MFC188* and *SVECs*. A) 10T1/2 cells, B) 10T1/2+2ng/ml *TGF-β1*, C) *MFC188*, D) *SVECs*. Bar 30μm.

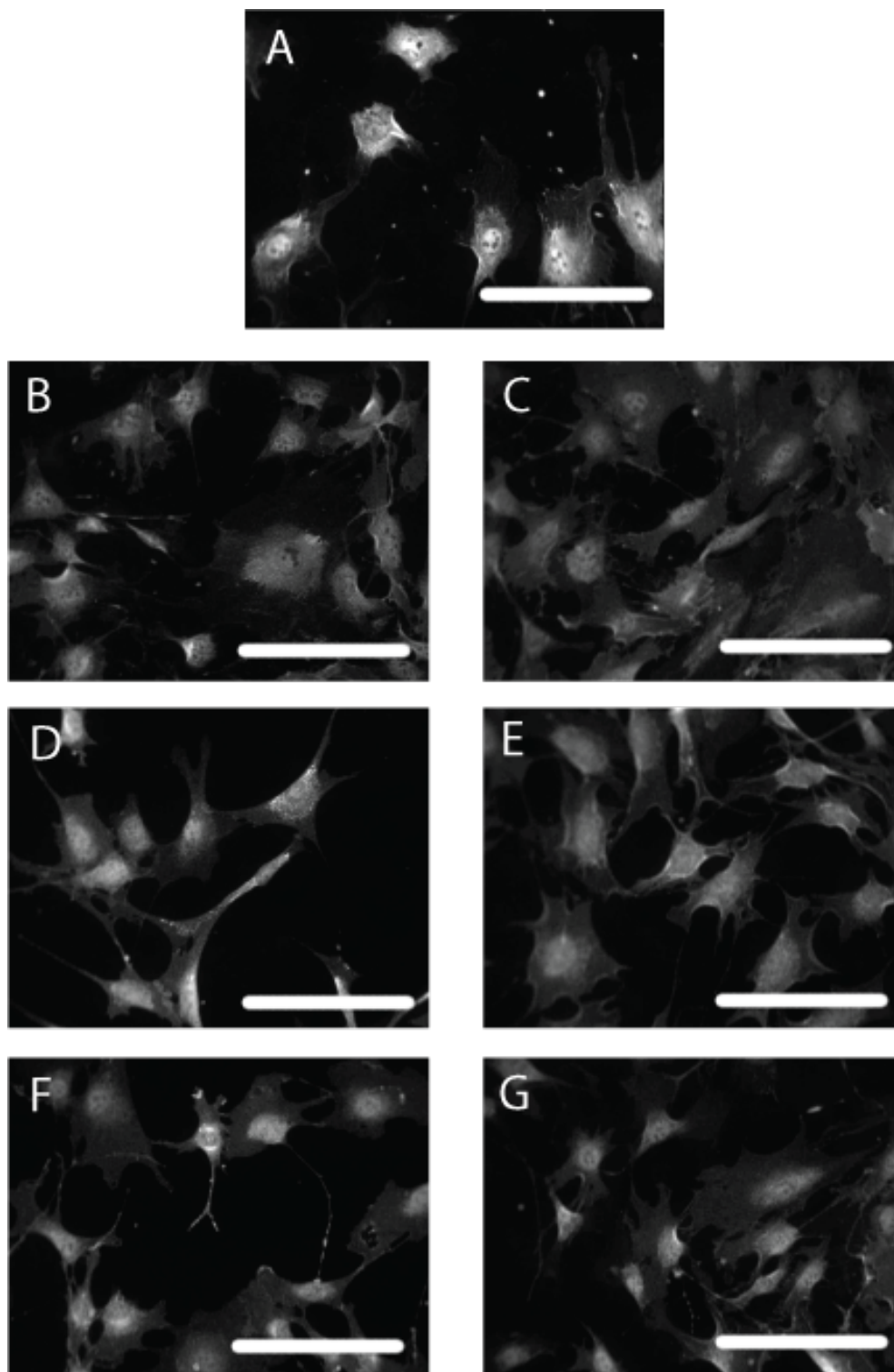


Figure 6.17: Representative images for staining of *PDGFR-β* for 10T1/2. A) 10T1/2 cells, B) 10T1/2+2ng/ml *TGF-β1*, C) 10T1/2+2ng/ml *TGF-β1* and fibronectin coated well, D) 10T1/2 cells in *MFC188* conditioned media, E) 10T1/2 in *MFC188* conditioned media and fibronectin coated well, F) 10T1/2 cells in *SVECs* conditioned media, G) 10T1/2 in *SVECs* conditioned media and fibronectin coated well. Bar 30μm.

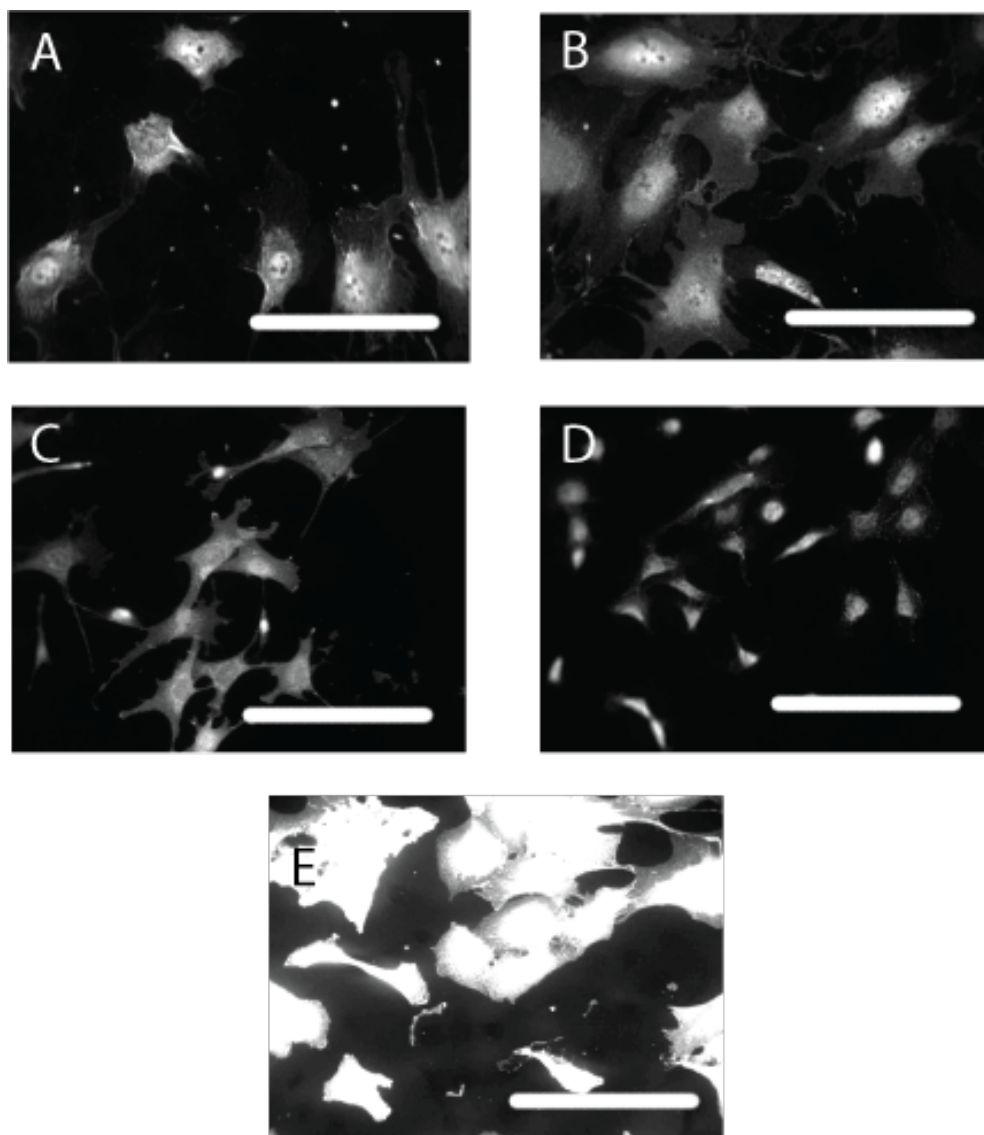


Figure 6.18: Representative images for staining of *PDGFR-β* for 10T1/2, *MFC188* and *SVECs*. A) 10T1/2 cells, B) 10T1/2+2ng/ml *TGF-β1*, C) *MFC188*, D) *SVECs*, E) 3T3 cells. Bar 30μm.

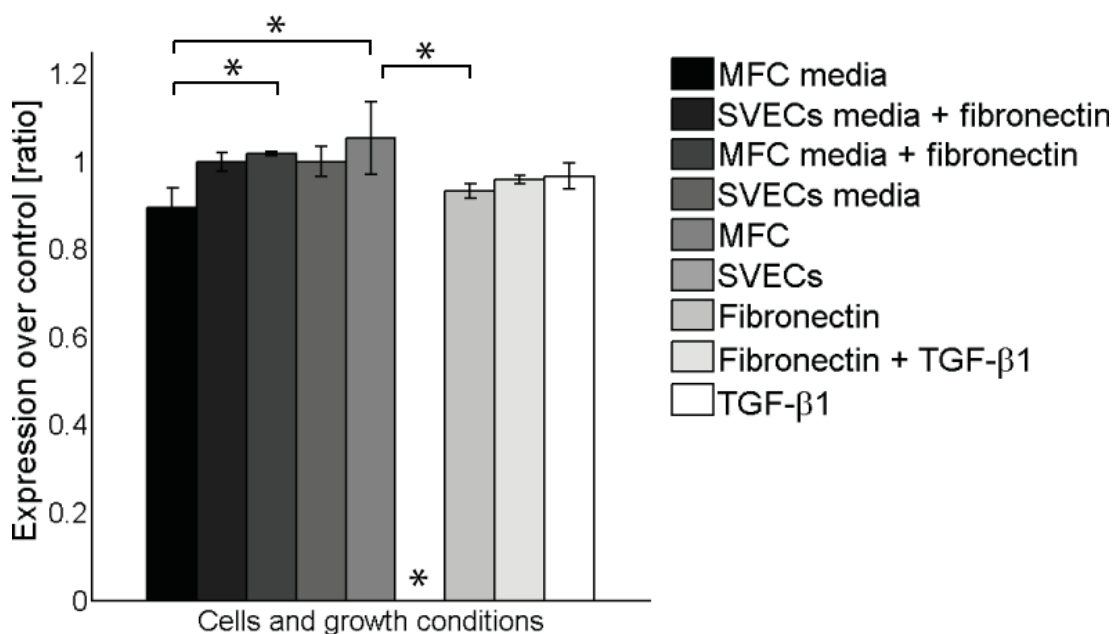
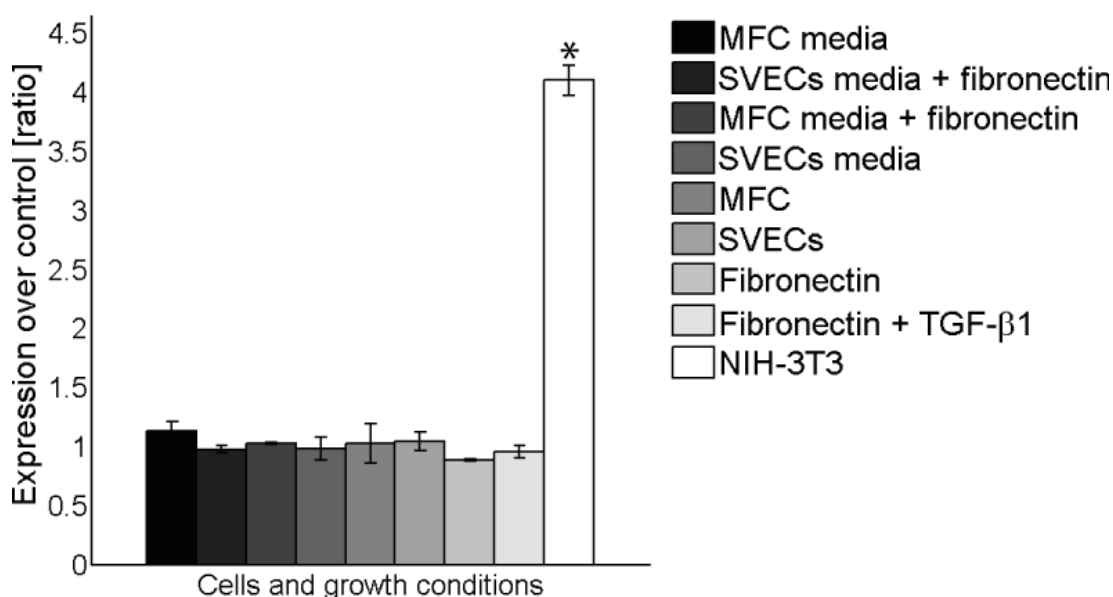
(a) *NG2*(b) *PDGFR-β*

Figure 6.19: Quantification of markers expression (*NG2* and *PDGFR-β*) in *10T1/2* cultured in different conditions and in *MFC188*, *SVECs* and *NIH/3T3*. Expression was compared to *10T1/2* cells not treated with *TGF-β1* (\*=statistical difference from untreated *10T1/2*, U-test,  $p < 0.05$ .  $N=3$ ,  $\pm SD$ ).

### 6.2.2 Western Blotting

Immunocytochemistry studies were complemented with western blot analysis for confirmation. Traditional western blot on acrylamide gel and quantitative western blot (*ProteinSimple* system) were used. In conventional western blot, *NG2* expression in *10T1/2* treated for 48h with 2ng/ml of *TGF-β1* is reduced by

50% when compared to the control, and no expression was detected in **MFC188** or **SVECs**. Using the automated western blot equipment, different concentrations of **TGF- $\beta$ 1** with 10T1/2 were evaluated, and a reduced **NG2** expression in the presence of *5ng/ml* and *10ng/ml* (0.7 and 0.9 ratio) was observed, while with *2ng/ml* there was a small increase in expression (1.05 ratio), although not significant ( $p > 0.05$ ). **MFC188** and **SVECs** had very low expression ( $\approx 0.1$ ). **PDGFR- $\beta$**  detection was also different in the two methods. In traditional western blot there is a slight decrease in expression in 10T1/2 treated with *2ng/ml* of **TGF- $\beta$ 1** for 48h compared to the control (ratio 0.9). **MFC188** has significant ( $p < 0.05$ ) reduced expression (ratio 0.4) and no expression was detected in **SVECs**. Automated western blot detected an increase in **PDGFR- $\beta$**  expression from all the 10T1/2 **TGF- $\beta$ 1** treated cells, while the receptor was found to be expressed at significantly ( $p < 0.05$ ) lower levels in **MFC188** and **SVECs** (ratio 0.35 and 0.15) (see fig. 6.20-6.21). These results suggested that both antibodies can be used to target the perivascular cells as they are expressed only (**NG2**) or at greater level (**PDGFR- $\beta$** ) by 10T1/2 compared to **SVECs** or **MFC188**. Antibody against **PDGFR- $\beta$**  will be the first one tested in polymersomes functionalisation using biotin/streptavidin chemistry.

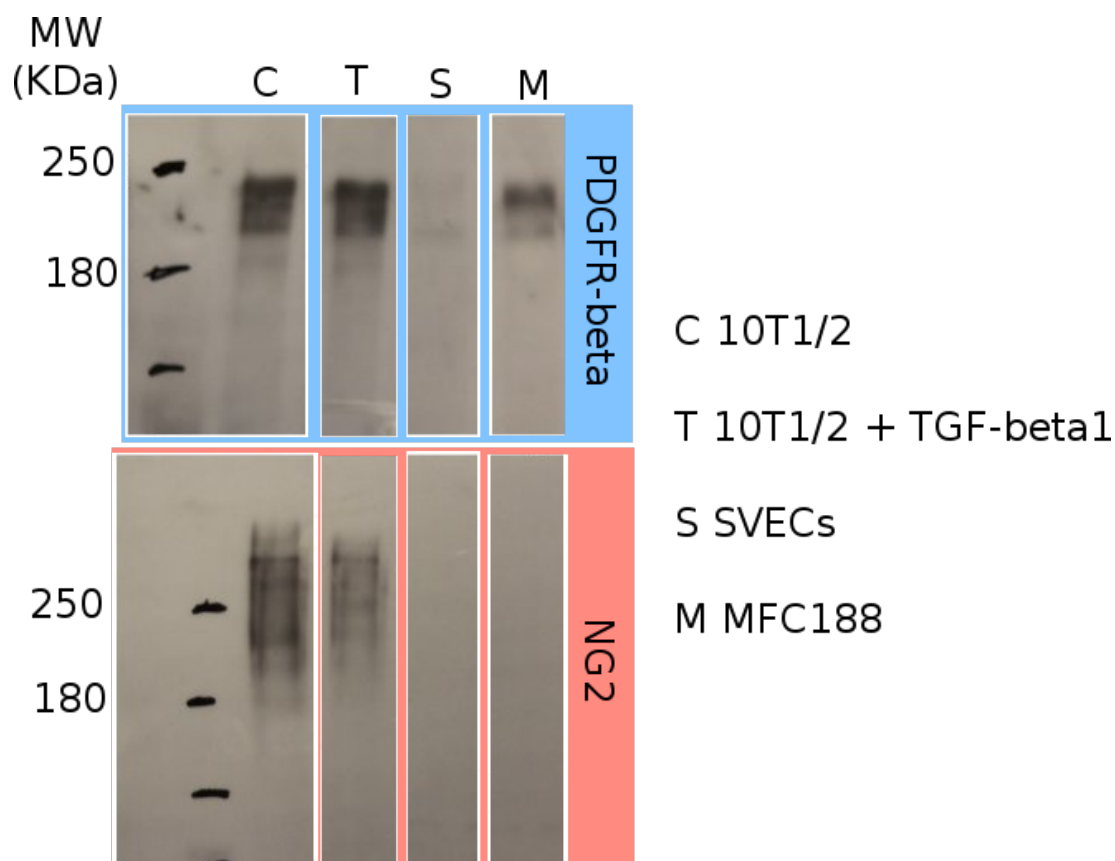


Figure 6.20: Traditional western blot results for *PDGFR-β* and *NG2*. Expression was assessed in 10T1/2, 10T1/2 treated with *TGF-β1* 2ng/ml for 48h, *MFC188* and *SVECs*.

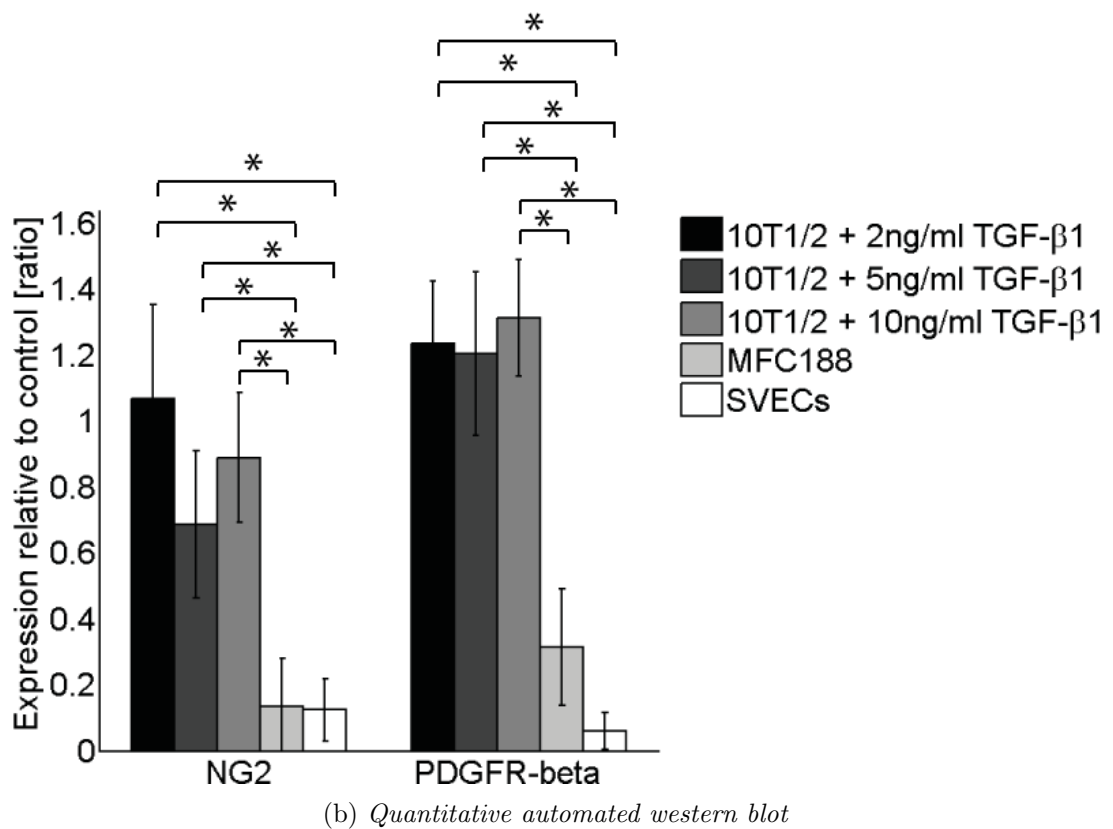
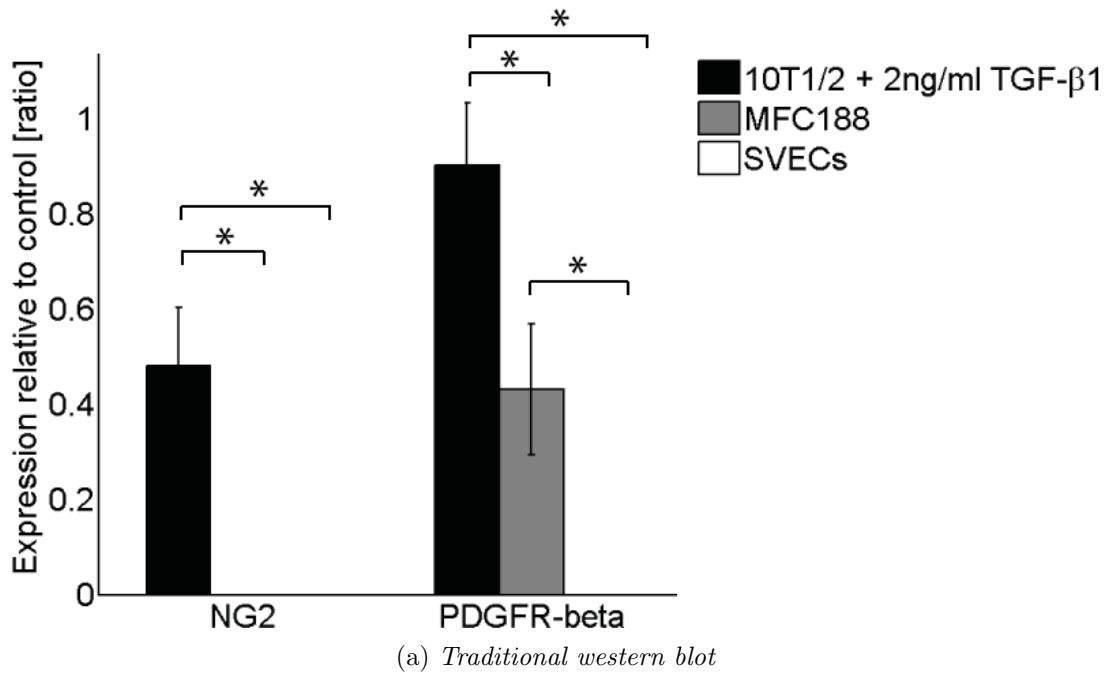


Figure 6.21: Western blot results for the traditional method (top) on acrylamide gel and the quantitative automated method (bottom). All results expressed as ratio with respect of the band intensity or signal intensity measured in the control (10T1/2 cells not treated with TGF-β1) (\*=statistical difference from untreated 10T1/2, U-test,  $p < 0.05$ .  $N=3$ ,  $\pm SD$ ).

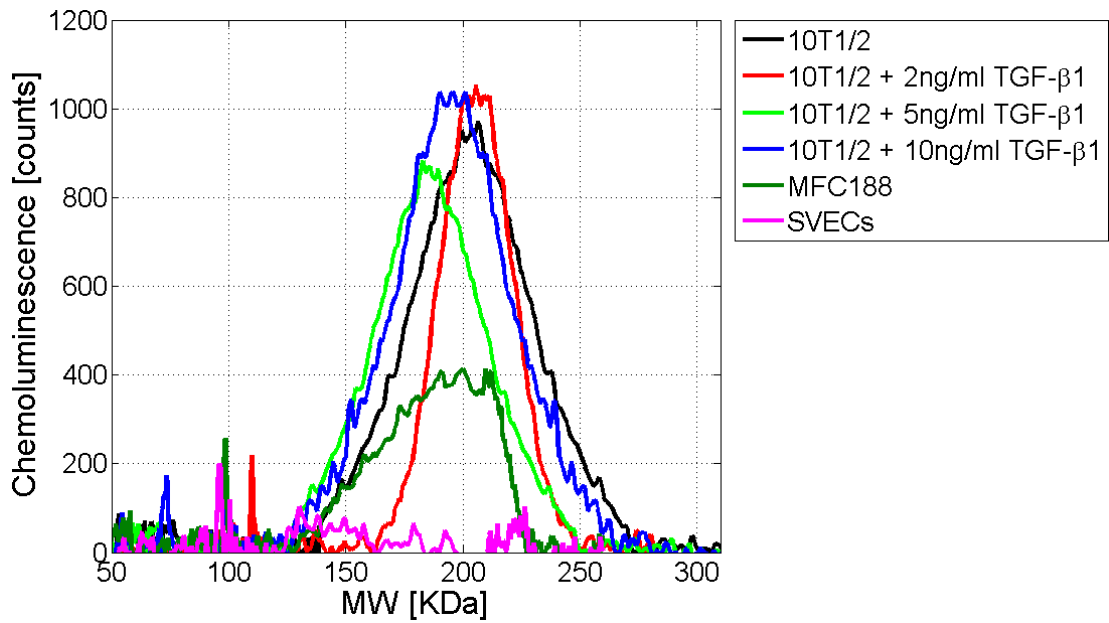
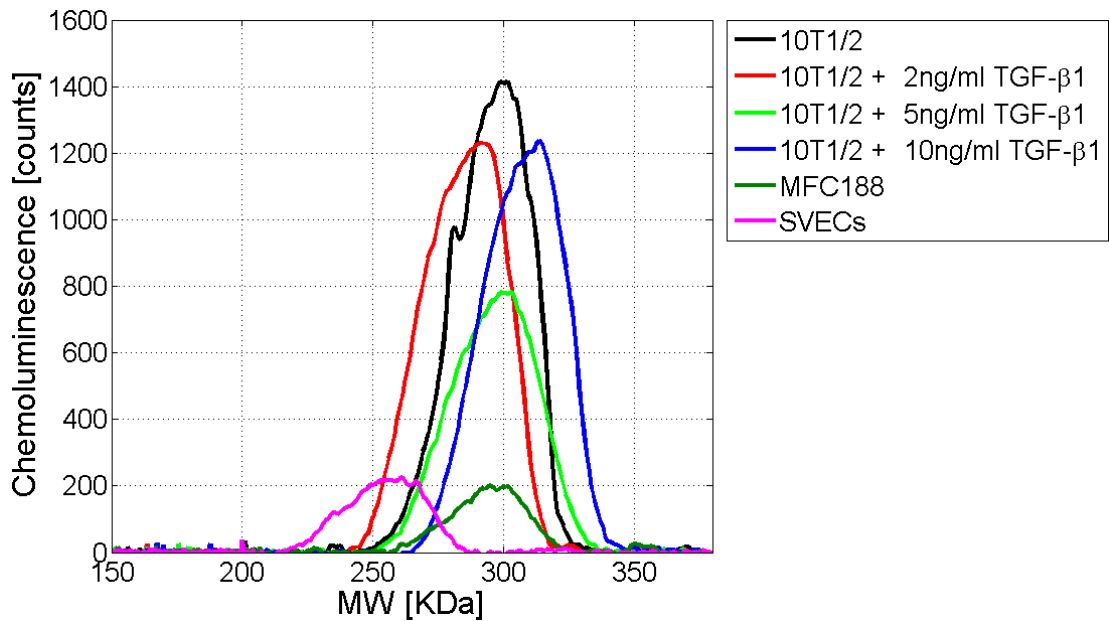
(a) *PDGFR-β*(b) *NG2*

Figure 6.22: *Quantitative western blot chromatograms. A) PDGFR-β and B) NG2 detection. Expression was assessed in 10T1/2, 10T1/2 treated with increasing concentration of TGF-β1 (2-10ng/ml) for 48h, MFC188 and SVECs. Expression is proportional to the area of the peak.*

### 6.2.3 Biotin/streptavidin conjugation

To test the control over the conjugation ratio we conjugated different formulations obtained using different molar ratios (0, 0.5, 3 and 5%) of Poly(2-methacryloxyethyl-phosphorylcholine)-poly(2-(diisopropylamino)ethyl methacrylate) (PMPC-PDPA)-biotin with the same amount of streptavidin and biotiny-

lated Texas-Red (equivalent to 2/1 molar ratio with the highest concentration of **PMPC-PDPA**-biotin). The amount of dye linked to the polymersomes after purification was quantified (see figure 6.23). Results are expressed as fluorescence intensity normalised by the amount of **PMPC-PDPA** detected. It can be observed that when no **PMPC-PDPA**-biotin was used, no Texas-red was detected, and that the concentration of Texas-red increased linearly with the concentration of **PMPC-PDPA**-biotin detected, in the range 0.5%-5% molar.

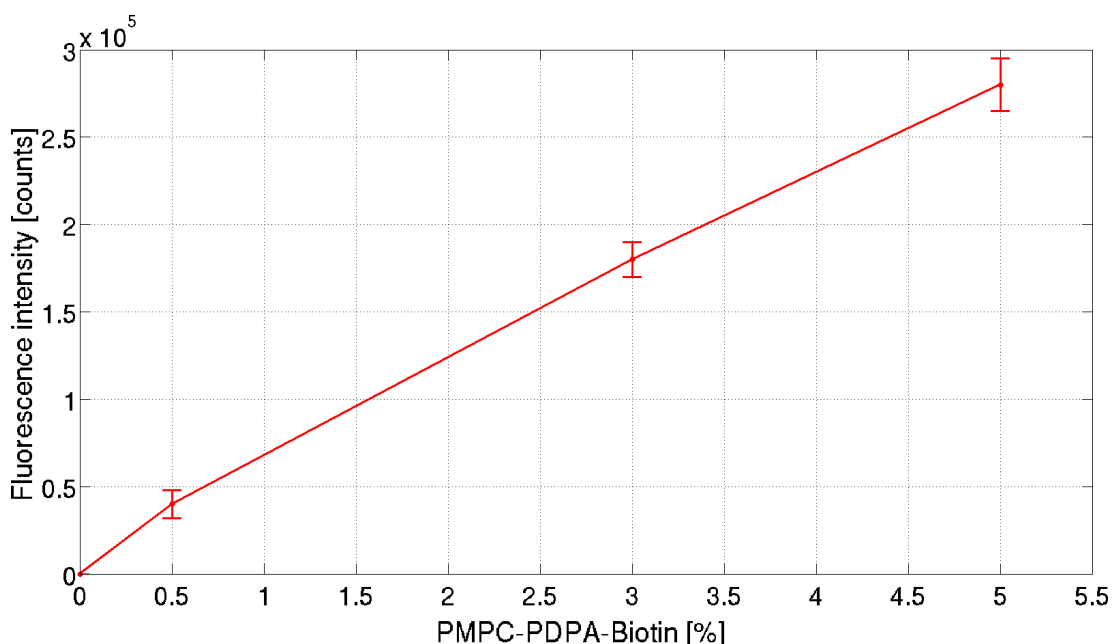


Figure 6.23: *Polymersome biotinylation. Formulations containing 0%, 0.5%, 3% and 5% of **PMPC-PDPA**-biotin were reacted with streptavidin and Texas-Red-biotin (1:1 molar ratio with biotinylated co-polymer). After purification, samples were analysed by Reverse Phase-High Pressure Liquid Chromatography (RP-HPLC) and results are expressed by fluorescence intensity, proportional to Texas red concentration, normalised by the total amount of **PMPC-PDPA** detected in the UV channel at 220nm.  $N=3$ ,  $\pm SD$ .*

The antibody against **PDGFR- $\beta$**  used in polymersome functionalisation was purchased biotinylated and it was different from the one used to evaluate marker expression. The use of this new antibody was validated using the positive control NIH-3T3 cells. In this experiment the biotinylated antibody to **PDGFR- $\beta$**  was added to living NIH-3T3 cells and FITC-avidin was used to detect the biotinylated antibody. The average intensity was measured against a control, which was 3T3 cells treated with FITC-avidin, but not with the biotinylated antibody (figure 6.24). A clear increase in signal intensity was recorded, confirming that the antibody chosen is suitable to target living cells expressing **PDGFR- $\beta$** .

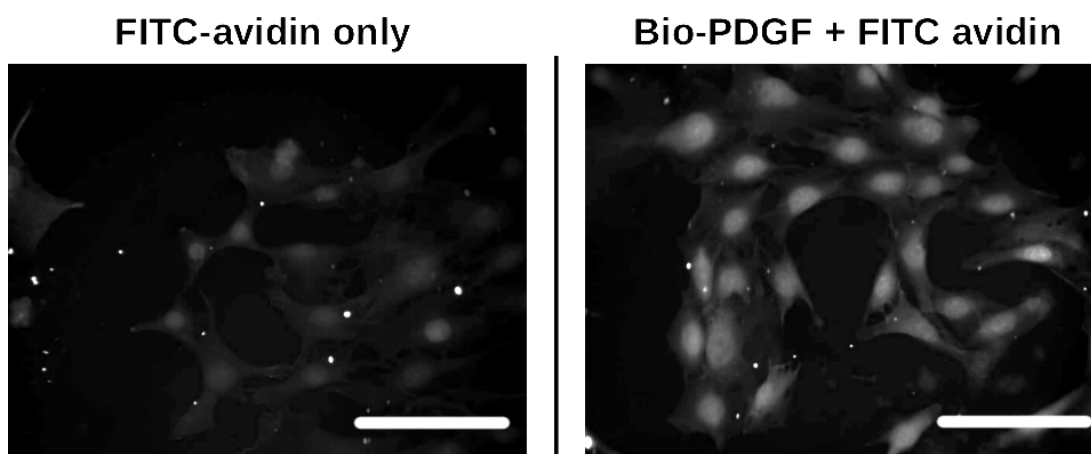
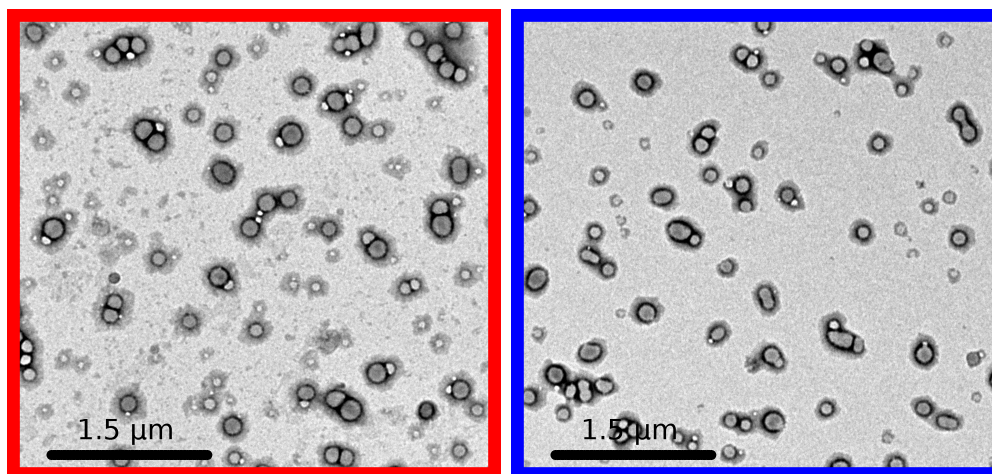


Figure 6.24: *Biotinylated antibody to PDGFR- $\beta$  testing. Living NIH-3T3 cells were treated with biotinylated antibody to PDGFR- $\beta$  (right) and FITC-avidin as a control (left). Bar 30 $\mu$ m.*

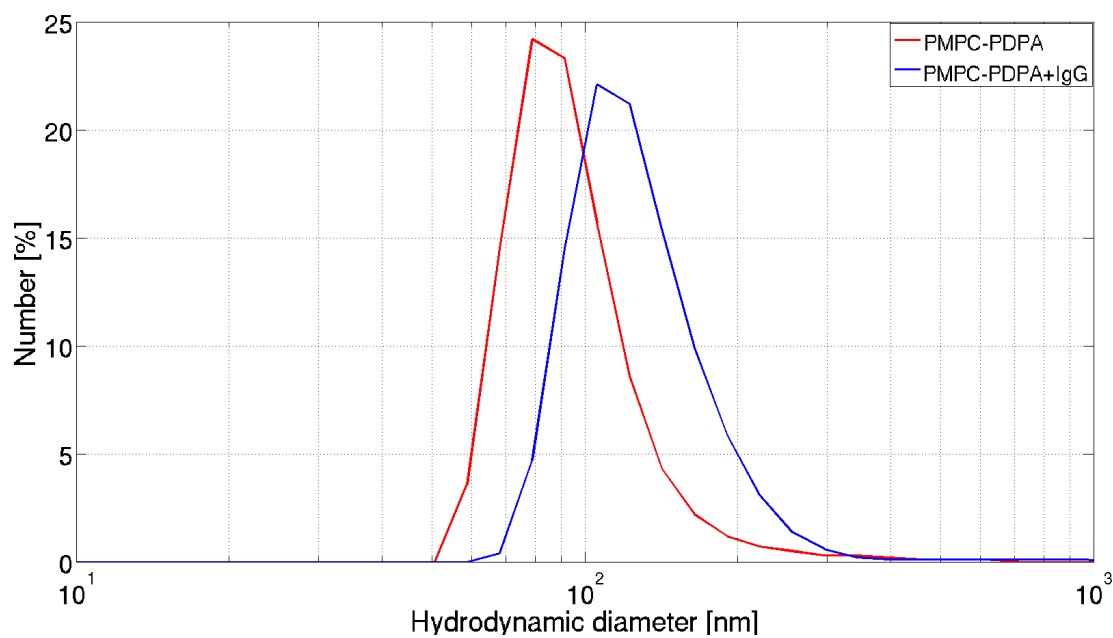
### Polymersome functionalisation

Biotinylated polymersomes were functionalised with antibody to PDGFR- $\beta$ . The antibody was purchased already biotinylated and linked to the polymersomes via a streptavidin bridge. The reaction mixture was purified by Gel Permeation Chromatography (GPC) and characterised by TEM, Dynamic Light Scattering (DLS) and RP-HPLC, as described in sections 2.1.3-2.1.4. TEM and DLS data showed that spherical size and size distribution was not altered by the synthetic protocol. A slight increase in the peak of size distribution recorded by DLS (from  $\simeq 90nm$  to  $\simeq 110nm$ ) suggesting successful conjugation which cause increase in hydrodynamic diameter of polymersomes (see fig. 6.25). RP-HPLC results indicated a molar ratio antibody/co-polymer of  $2.1 \pm 1.2 pmol/1mmol$ , demonstrating the presence of both co-polymer and antibody in the purified sample, therefore proving successful conjugation (see fig. 6.26).



(a) TEM, PMPC-PDPA

(b) TEM, PMPC-PDPA-IgG



(c) DLS

Figure 6.25: (a, b) TEM and (c) DLS of polymersomes functionalised with biotin/streptavidin. Pristine polymersomes (red) are compared to 10% functionalised polymersomes (blue). Polymersomes retained spherical shape, however the hydrodynamic diameter was  $\simeq 20\text{nm}$  after conjugation, indicating surface modification.

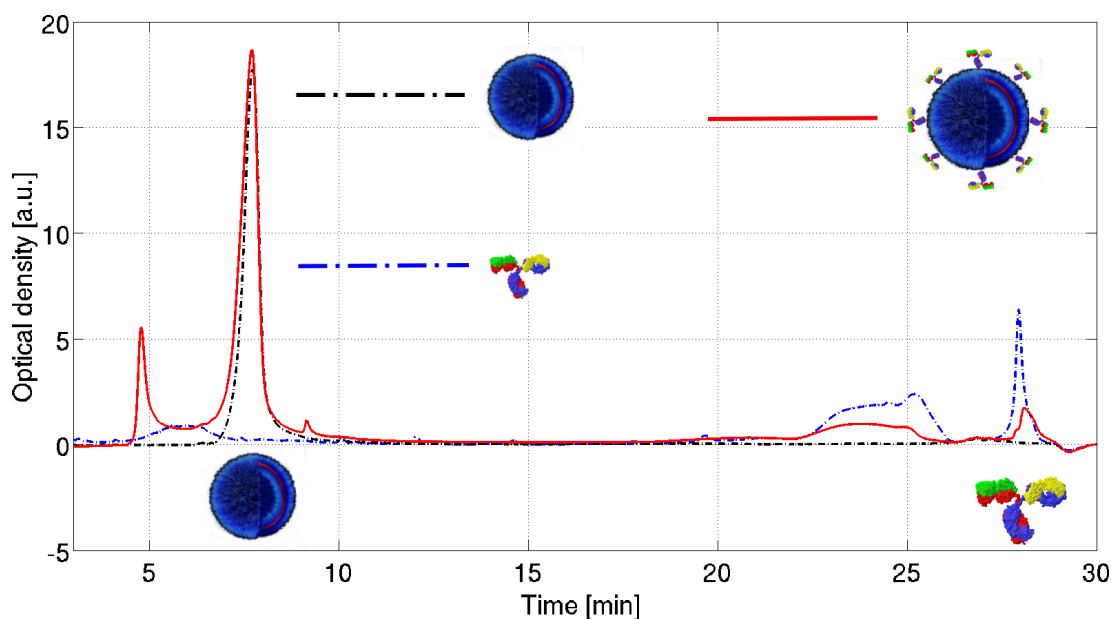


Figure 6.26: *RP-HPLC* analysis for biotin/streptavidin functionalised polymersomes. Polymersomes peak at  $\simeq 7\text{min}$ , the antibody peaks at  $\simeq 28\text{min}$ , the purified conjugate polymersome-antibody showed both peaks ( $\simeq 7\text{min}$  and  $\simeq 28\text{min}$ ).

### Flow cytometry

Uptake of functionalised formulations was evaluated by [Fluorescence Activated Cell Sorting \(FACS\)](#). The formulations tested with 10T1/2 cells were pristine Polyethylen Oxide-poly(2-(diisopropylamino)ethyl methacrylate) (PEO-PDPA), 1% functionalised PEO-PDPA, pristine PMPC-PDPA and 1% functionalised PMPC-PDPA. In this section of the work PEO-PDPA was used as a polymeric analogue of POEGMA-PDPA, which was not available in the laboratory at the time the experiments were performed. With [MFC188](#) the pristine formulations of PEO-PDPA and PMPC-PDPA were tested. In 10T1/2 there was a small increase of functionalised PMPC-PDPA formulations uptake at 6h (+10%) and at 24h for functionalised PEO-PDPA formulations (+5%). However, the uptake was lower than that of the pristine formulations at the same time points from [MFC188](#) (fig. 6.27).

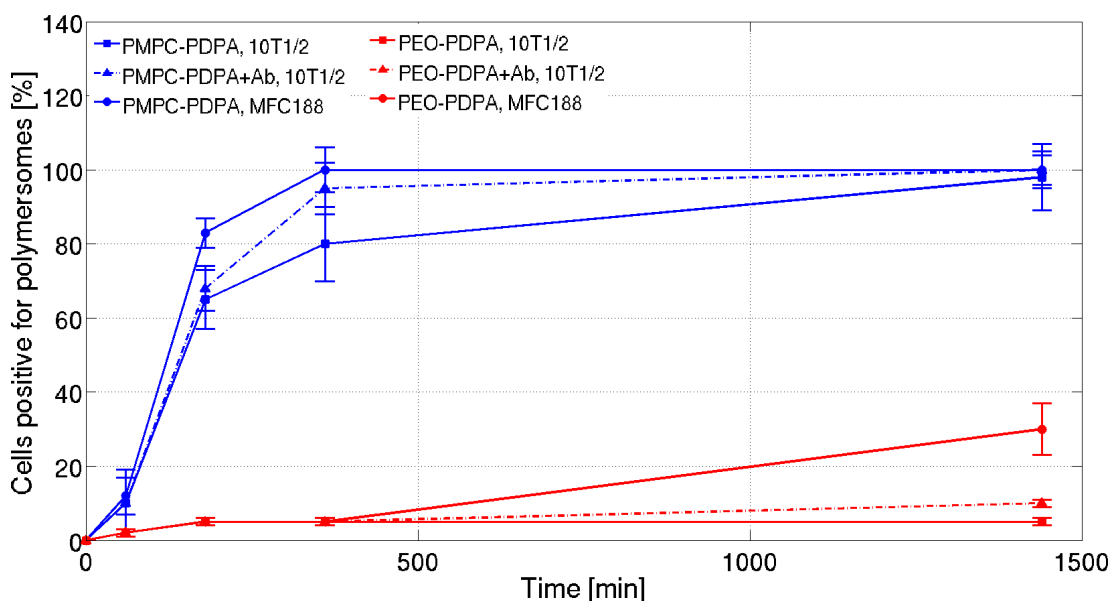


Figure 6.27: Uptake of functionalised polymersomes. Polymersomes were functionalised with 1% molar of antibody to *PDGFR- $\beta$* . Functionalised formulation did not show significant improvement in kinetic of uptake compared to the non-functionalised counterpart.  $N=3$ ,  $\pm SD$ .

#### 6.2.4 Maleimide conjugation

Maleimide reaction was performed using a generic rabbit **IgG** instead of a specific antibody to *PDGFR- $\beta$*  or *NG2*. This choice was justified considering the early developing stage of the functionalisation protocol and the consequent need for significant amount of material. A generic rabbit **IgG** represented a significantly cheaper alternative to specific antibodies. Maleimide reactivity can be shifted from thiol to primary amino groups by controlling the reaction pH (section 6.1.5). Considering the differences in amino acid abundance between cysteine and leucine in an **IgG** (fig. 6.5) the reaction was conducted at pH=7.5 (thiol groups, cysteine) and pH=8.5 (primary amino groups (leucine)). **TEM** data showed spherical vesicles suggesting that the functionalisation protocol did not affect polymersomes stability. **DLS** data showed a small shift of size distribution from  $\simeq 90\text{nm}$  to  $\simeq 100\text{nm}$ , suggesting possible conjugation (fig. 6.28). **RP-HPLC** chromatograms were characterised by the presence of both peaks for polymer (fig. 6.29a) and the antibody (fig. 6.29b). However, the ratio between the two peaks was constant, indicating that there was no significant difference ( $p > 0.05$ ) between the two reaction yield and that the degree of functionalisation was the same (antibody/co-polymer  $0.5 \pm 1.2 \text{ pmol}/1 \text{ mmol}$ ).

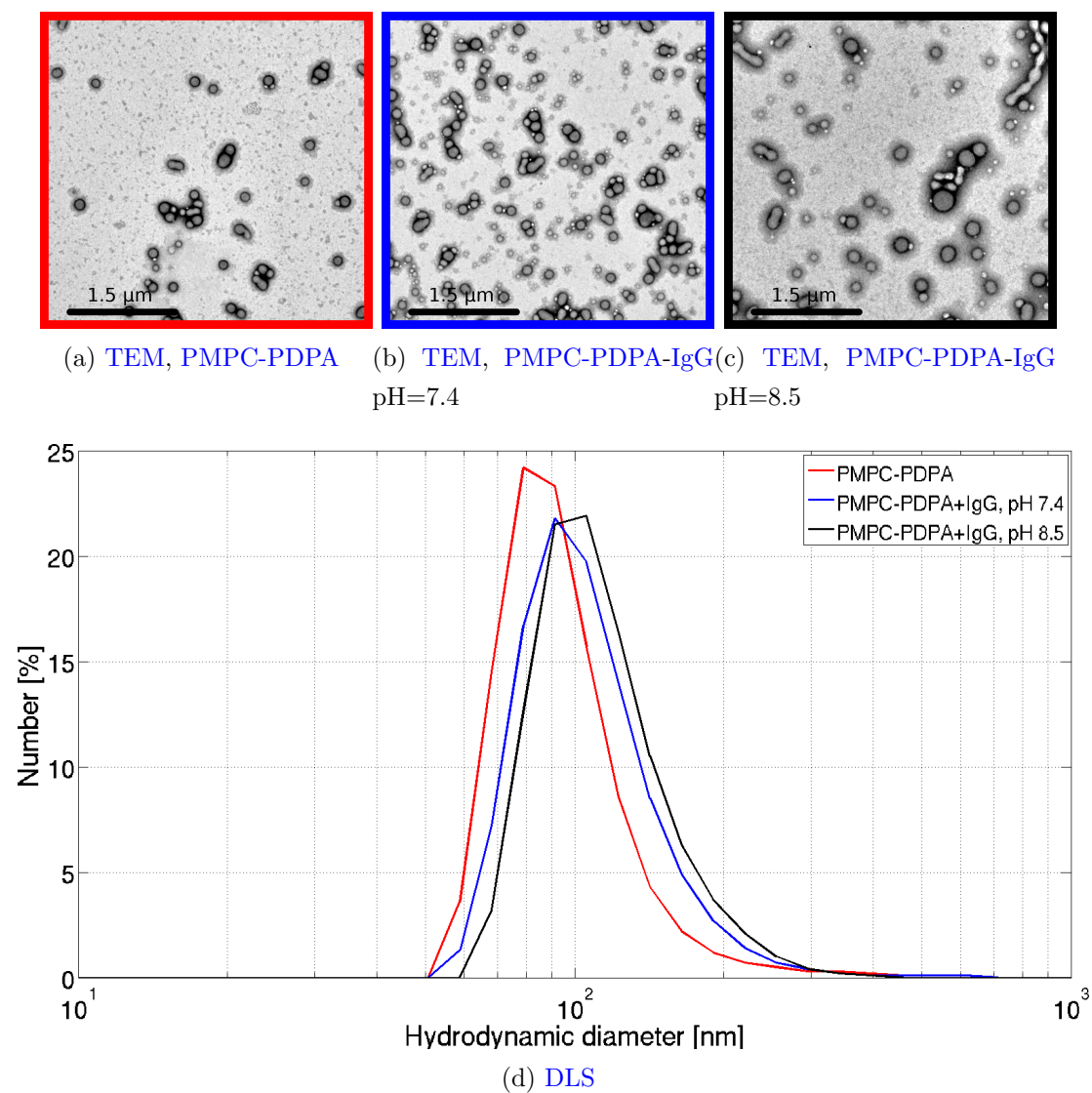
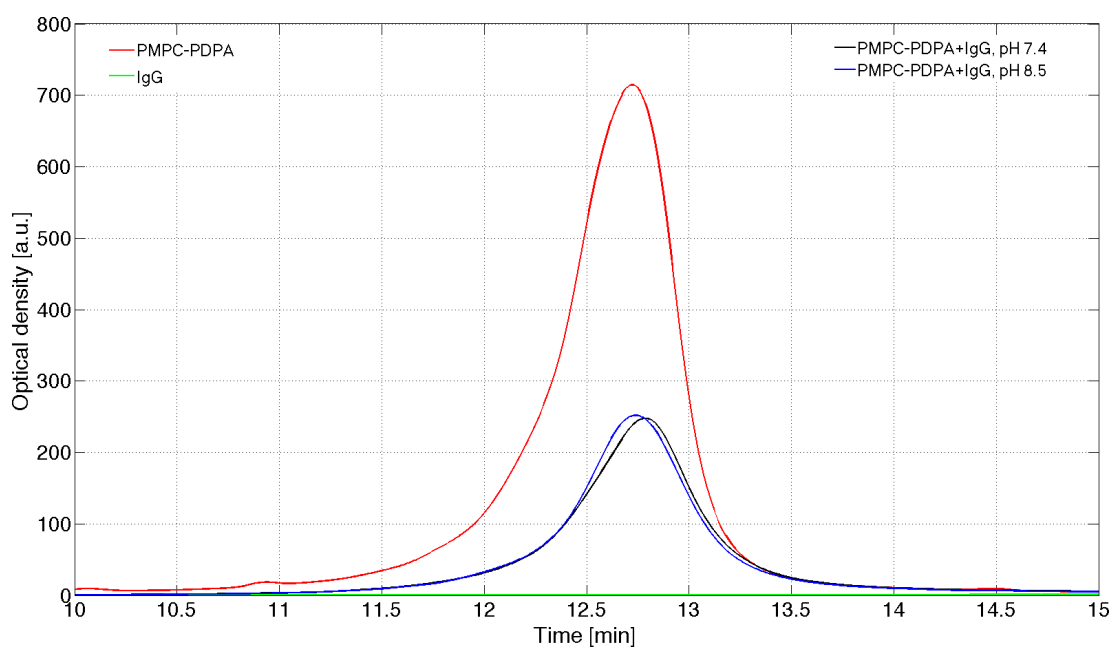
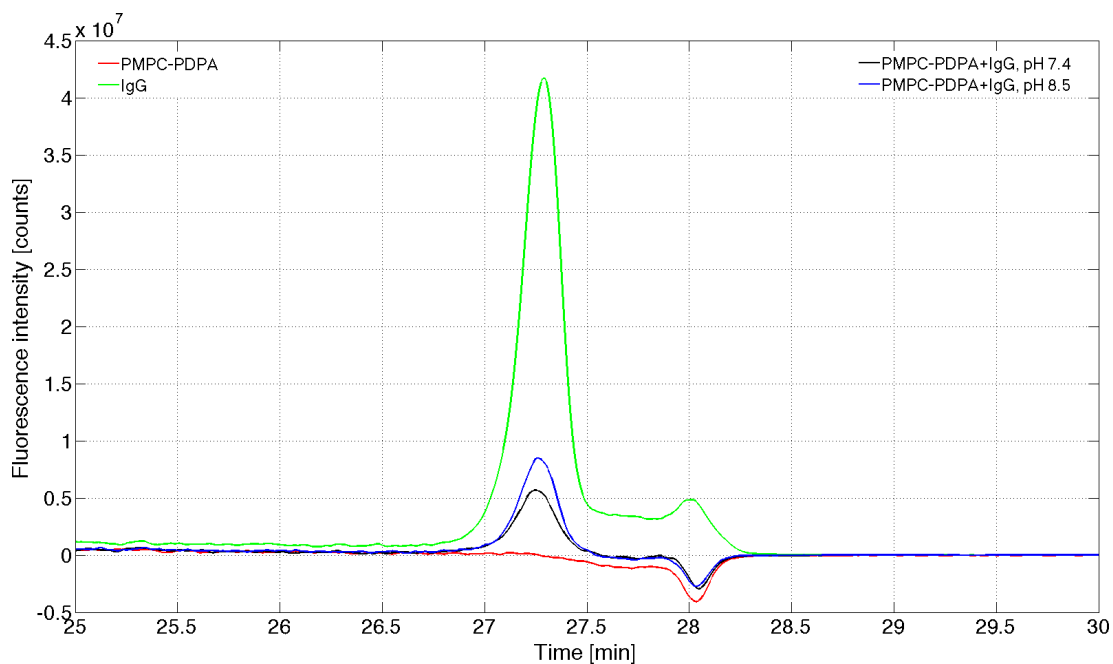


Figure 6.28: (a, b, c) *TEM* and (d) *DLS* of polymersomes functionalised with maleimide. Pristine polymersomes (red) are compared to 10% functionalised polymersomes at pH 7.4 (blue) and pH 8.5 (black). Polymersomes retained spherical shape, however the hydrodynamic diameter was  $\simeq 20\text{nm}$  after conjugation, indicating surface modification.



(a) UV, 220nm: Co-polymer



(b) EX/EM 270/340: IgG

Figure 6.29: Maleimide reaction optimisation, *RP-HPLC* analysis. (a) Co-polymer peaked at  $t \approx 12.75 \text{ min}$ . (b) *IgG* peaked at  $t \approx 27.25 \text{ min}$ . Representative *RP-HPLC* chromatograms for  $N=3$  experiment. Peaks were integrated and the amount of *IgG* per polymersomes was calculated after normalising the area of the *IgG* against the area of the polymer.

## 6.3 Discussion

A fundamental requirement in targeted delivery is the identification of a specific marker selectively expressed in the cell to target. We choose to investigate the possibility to target perivascular cells. This choice was justified by the need of a better understanding the role of perivascular cells in angiogenesis and their response to anti-angiogenic or **Vascular Disrupting Agent (VDA)** treatments. Prof. Tozer's group developed a an *in vivo* tumour model of **MFC188**, and they characterised its perivascular cell coverage *ex vivo*. Polymersomes can allow direct, *in vivo* and real-time monitoring of perivascular cells in response to combretastatin. This is of great importance in order to assess the exact mechanism of response to the treatment and vasculature normalisation. Furthermore, it has potential beneficial ethical impact as it real-time observation is not an end-point procedure, therefore one animal can be used to acquired multiple time points, as opposed to *ex vivo* examination.

In the current chapter we investigated the expression of a number of proposed perivascular cells markers in 10T1/2 cells treated with **TGF- $\beta$ 1**, a cytokine reported to induce differentiation of perivascular cells (**Hirschi et al. [1998]**). Different concentrations and exposure times of **TGF- $\beta$ 1** were tested, as well as different growing conditions. Furthermore we compared the expression of the markers in 10T1/2 cells, tumour and endothelial cells. This is of particular importance because the marker to be targeted is required to be expressed by the target cells, but not by other cell types such as tumour or endothelial cells; the aim of the study being to target perivascular cells in the tumour microenvironment.

The expression of three perivascular cells markers was assessed:  **$\alpha$ -SMA**, **PDGFR- $\beta$**  and **NG2**.  **$\alpha$ -SMA** was included in the panel because it is characteristic of perivascular cells. However, it should be noted that it is located internally, therefore it cannot be used for targeting purposes. **PDGFR- $\beta$**  and **NG2** present extracellular epitopes that can be targeted (**Shim et al. [2010]**, **Stallcup [2002]**).

Overall, **ICC** and **Western Blot (WB)** showed no significant effect of **TGF- $\beta$ 1** or tissue culturing conditions on 10T1/2 expression of **PDGFR- $\beta$** , **NG2** or  **$\alpha$ -SMA**. It is also interesting to observe that some combinations of **TGF- $\beta$ 1** exposure such as **1ng/ml** for **48h** or **72h** caused an increased expression of  **$\alpha$ -SMA** and decreased expression of **NG2**, which reflects a the phenotype of **SMC** surrounding veins ( **$\alpha$ -SMA<sup>+</sup>, NG2<sup>+/-</sup>**) rather than capillary pericytes ( **$\alpha$ -SMA<sup>-</sup>, NG2<sup>+</sup>**) (**Armulik et al. [2011]**).

Our results suggest that the pathway for differentiation of 10T1/2 in perivascular cells is likely to be dependent on other factors rather than only **TGF- $\beta$ 1**. Differentiation could be affected also by contact with endothelial cells (**Hirschi**

et al. [1998], Hirschi et al. [2003]), cell-signalling (TGF- $\beta$ 1-PDGF-B, 6.1.1), stiffness of the growth support (i.e. extracellular matrix, tubular shaped *in vivo vs* plastic well plate) unreported for 10T1/2, but well known for other stem cells systems (Park et al. [2011], Vincent et al. [2013]). Furthermore, it has been suggested that 10T1/2 might not fully differentiate into pericytes or vSMCs, but rather into myofibroblast with inconsistent markers expression (Brunelli et al. [2004], Yoshida and Owens [2005]). These conflicting reports have been explaining considering differences in protocols adopted by different laboratories (Xie et al. [2011]). Another possible explanation could be in the lack of a clear definition of pericytes and other perivascular cells, as most of the cited works referred to the differentiation of 10T1/2 in *pericytes vs* SMCs, rather than specifically in pericytes. A major limitation of the *in vitro* model is the lack of direct transferability to *in vivo*, as it is not possible to predict the expression of perivascular cells markers in the animal mode, as it would be inaccurate to assume that the endothelial cells of blood vessels found in the tumour growing in the Dorsal Skinfold Chamber (DSC) express the same markers as the SVECs used here. A better model to be adopted in future development of the targeting system would be to use histological samples from the animals. These samples have been already characterised for  $\alpha$ -SMA and other markers expression by Prof. Tozer group, and targeting effect could be validated *ex vivo* using functionalised polymerosomes instead of the primary antibody normally used in histology.

The aim of this part of the work was not to elucidate the mechanism of differentiation of 10T1/2 into pericytes or vSMCs, but to assess if expression of perivascular cell markers by 10T1/2 was higher compared to the expression of the same marker in MFC188 or SVECs. With this respect, ICC showed no significant difference in expression of PDGFR- $\beta$  or NG2 between the three cell types. WB, both the traditional acrylamide gel based and the quantitative *Simon* methods, showed significant reduced of expression of PDGFR- $\beta$  and NG2 in MFC188 and SVECs compared to 10T1/2. The difference between the two techniques could be explained by a better sensitivity of WB method compared to ICC. Considering these results it was chosen to functionalise polymerosomes with both both antibodies against PDGFR- $\beta$  and NG2, however only the first one was used in preliminary *in vitro* screening, while a cheaper generic IgG was preferred as a model of antibody in further optimisation of the conjugation method.

In principle, the functionalisation can be achieved before or after polymerosomes formation. When performed before formation, the single chain of copolymer is reacted with the desired moiety and the purified product is mixed with pristine copolymer in the second, separate step of polymerosomes formation. This approach has the advantage of being easier to control and to facilitate

the reaction between the copolymer and the functionalising molecule. However, the reaction requires the co-polymers to not aggregate, and this often involves non-biocompatible chemical solvents that will need to be purified from the final product. Furthermore, when the functionalised copolymer is mixed with the pristine copolymer during polymersome formation, statistically, half the functionalised chains will be exposed to the inner aqueous core of the polymersomes rather than the outer surface. Such positioning is useless for functionalisation and will result in lowering the yield of reaction by about 50%. The second approach is to functionalise polymersomes after their formation. In this way only the reactive chains on the outer surface of the vesicles will react. This has the advantage of reducing the waste of functionalising reagent. However, such an approach presents increased steric hindrance from the polymersomes which could affect reaction yield. In this work, functionalisation was performed following polymersome self-assembly.

We tested two different reaction methods. The first reaction exploited the strong non-covalent binding between biotin and the multivalent streptavidin to link biotinylated copolymers with biotinylated antibody to PDGFR- $\beta$  using a bridge of streptavidin. We showed that the conjugation can be controlled by changing the amount of biotinylated copolymer included in the polymersomes formulation, and that the antibody used is effective in recognising PDGFR- $\beta$ . *fac*s analysis showed increase of uptake by 10T1/2 for both PEO-PDPA and PMPC-PDPA functionalised formulations compared to the pristine formulations. However, the increased uptake was still not significantly ( $p > 0.05$ ) higher compared to the pristine formulations by MFC188. This can be explained by low efficiency of functionalisation and because PDGFR- $\beta$  is also expressed by MFC188.

Biotin/streptavidin polymersomes functionalisation required 3 steps: polymersomes self-assembly, streptavidin binding, biotinylated antibody binding. It will also involved several purification steps to eliminate intermediate unreacted reagents. These requirements have a negative impact on the cost of the production method and on the yield. To overcome these limitations we investigated the possibility using copolymers functionalised with maleimide to link directly thiol groups in the antibody (cysteine). This approach will allow to eliminate one reaction and purification step, and also to avoid the use of streptavidin, a very large protein that could potentially interfere with polymersomes stability, mechanism of reaction or antibody/antigen recognition. The generic maleimide reaction is reported in figure 2.6. Considering the high cost of the reaction due to the amount of antibody required, the method was developed using a non specific rabbit IgG. RP-HPLC analysis showed successful conjugation of the IgG, however at a very low yield (antibody/co-polymer ratio:  $0.5 \pm 1.2 \text{ pmol} / 1 \text{ mmol}$ ).

Investigation of cysteine availability on IgG showed that the amino acid is poorly represented and generally not available, for instance because thiol groups are already engaged in S-S bridges. This could explain the low yield of reaction. Leucine is a more common amino acid and it has a reactive primary amino-group. Maleimide reactivity can be shifted to primary amino groups at higher (pH>8). The effect on reaction yield was tested by performing the reaction at pH=8.5. Results did not show improvement on the yield of reaction. This can be explained considering that Poly(2 - methacryloxyethyl - phosphorylcholine) (PMPC) is a non-fouling polymers, therefore it is possible that repulsive forces between polymersomes and IgG negatively affected the reaction kinetic. This can also explain the low reaction yield obtained from biotin/streptavidin approach. Further development of the should investigate the possibility of performing the reaction before polymersomes self-assembly.

Overall, we could not prove efficient *in vitro* targeting of perivascular cells. One of the major challenges associated with the project was the lack of a specific, highly expressed pericyte marker. 10T1/2 screening identified PDGFR- $\beta$  and NG2 as possible markers, however they are not expressed only by 10T1/2, but also by tumour cells (MFC188), limiting their applicability in targeting. Furthermore, there is no proof that the marker will be expressed by tumour perivascular cells if the technology has to be translated to *in vivo* applications. Another problem was polymersomes-antibody conjugation strategy. When performed after polymersomes self-assembly, the reaction was characterised by low yield, most likely because of the steric hindrance generated by the non-fouling PMPC and Polyethylene Oxide (PEO) polymers.

Despite being negative for targeting purposes, the methods used identified the key steps in development of polymersomes for targeting: target identification, functionalisation and *in vitro* screening. The choice of alternative target (i.e. tumour cells via folic acid or RGD) and pre self-assembly conjugation can be tested in further development of the method.

A final consideration should be made on the choice of the targeting moiety. In this work we choose to work with a full IgG. This choice was made considering the commercial availability of biotinylated antibody to PDGFR- $\beta$  and the possibility to optimise the conjugation with a generic rabbit IgG. However, to respect the stoichiometric ratio 1/1 between reactive co-polymer and antibody, it was necessary to use high mass of high molecular weight IgG ( $\simeq 65KDa$ ). Considering the cost of the biotinylated antibody, a single reaction with 10% reactive co-polymer can be estimated to require  $\simeq 40,000\text{£}$  in consumable and reagents to obtain enough material for an *in vitro* uptake study. Furthermore, functionalisation with big molecules can compromise the *stealth* properties of polymersomes,

facilitating opsonisation and recognition by phagocytic cells. In future studies, IgG fragments (i.e. Fab) or smaller peptides should be considered instead of full IgG.

## 7.1 General discussion

In this work, polymersomes based on co-polymers Poly(2 - methacryloxyethyl-phosphorylcholine)-poly( 2 -(diisopropylamino)ethyl methacrylate) (PMPC-PDPA) and poly(oligo(ethylene glycol) methacrylate)-poly( 2 -(diisopropylamino)ethyl methacrylate) (POEGMA-PDPA) have been used in conjunction with the Dorsal Skinfold Chamber (DSC) to image the tumour microenvironment. The development of vesicles started with the study of uptake *in vitro*. Live cell imaging was used as a quantitative method, its results being supported by Reverse Phase-High Pressure Liquid Chromatography (RP-HPLC) and Fluorescence Activated Cell Sorting (FACS) analysis (4.1). Because of the importance of blood flow in the dynamic of polymersomes recognition and internalisation by cells, the *in vitro* system was integrated with the development of a flow bio-incubator dedicated to quantification of uptake studies via FACS and live cell imaging (fig. 4.8). Uptake studies were performed on three cell types relevant to the tumour microenvironment: tumour cells (Mouse Fibrosarcoma Cells expressing VEGF188 isoform (MFC188)), endothelial cells (Small Vessel Endothelial Cells (SVECs)) and a perivascular cell model (10T1/2). Results showed a faster uptake of PMPC-PDPA polymersomes compared to POEGMA-PDPA by all cell types, and particularly by tumour cells (fig. 4.2). In flow conditions, the differences between all cell types and polymersome formulations were significantly reduced (fig. 4.11). Differences between PMPC-PDPA and POEGMA-PDPA could be surprising considering that both poly(oligo(ethylene glycol) methacrylate) (POEGMA) and Poly(2 - methacryloxyethyl - phosphorylcholine) (PMPC) are not fouling, therefore they will not interact with circulating proteins which leads to opsonisation and rapid blood clearance. However, it has been reported that PMPC-PDPA polymersomes

uptake is mediated by scavenger receptor SR-B1 (Colley et al. [2014])). Reduced uptake in flow to a level similar to POEGMA-PDPA suggests that flow interferes with the recognition of PMPC-PDPA polymersomes by the receptors, therefore the uptake kinetic becomes similar to POEGMA-PDPA. Further development of the analysis in flow took advantage of the unique capability of imaging to focus in real time to different areas of the well. Because the device developed did not deliver perfect homogeneous flow at the cell level, the local differences were used to correlate shear stress and velocity magnitude to cellular uptake (fig. 4.12-4.14). Results suggested that shear stress had lower impact on cell uptake compared to vertical velocity. This suggests that the effect of flow on speed of the particles (therefore kinetics of ligand/receptor recognition) is higher than the effect of shear stress, which is likely to affect cell phenotype by inducing mechanical stress (Khan and Sefton [2011]), rather than ligand/receptor kinetics. Further studies are required to elucidate the effect of flow on distribution of SR-B1 at the cellular surface. Furthermore, uptake studies at this developmental stage were performed in cell media. This is a Newtonian fluid, very different to blood. It will be of interest to modify viscosity of the media to perform uptake studies in blood-like fluid. Overall, the *in vitro* findings suggested that PMPC-PDPA and POEGMA-PDPA formulations will have significantly different behaviour *in vivo*. PMPC-PDPA are expected to be cleared rapidly, while POEGMA-PDPA should have longer circulation time, which in turn will be reflected in improved accumulation within tumour.

In *in vivo* testing, the tumour vasculature was imaged in DSC using a confocal microscope equipped with a 10X objective. The tumour was implanted as a spheroid of MFC188. This particular model was chosen because it has been reported to be characterised by more vascularised tumours with a higher pericyte coverage compared to tumours obtained from Mouse Fibrosarcoma Cell (MFC) cells expressing Vascular Endothelial Growth Factor isoform 120 (VEGF120) or Vascular Endothelial Growth Factor isoform 164 (VEGF164) (Tozer et al. [2008], Akerman et al. [2013]). This tumour model was ideal to develop an imaging platform targeted to the tumour microenvironment. Image analysis was performed using a specifically developed algorithm. Both polymersome formulations were found to initially localise to the tumour vasculature, then gradually extravasate and accumulate within tumours. However, the analysis also confirmed the anticipated differences between PMPC-PDPA and POEGMA-PDPA polymersomes. POEGMA-PDPA accumulated within tumours to a greater extent compared to PMPC-PDPA polymersomes. After 16h from the injection, POEGMA-PDPA polymersomes were clearly localised in tumour stroma, with vessels visible in dark over the brighter stroma, while PMPC-PDPA polymersomes were hardly

detected in either the vessels or the stroma at the same time point (fig. 5.5, 5.6-5.6). This suggested faster clearance of PMPC-PDPA, which therefore was less efficient in accumulating within the tumour. These observations are in agreement with unpublished data from Prof. Battaglia showing longer circulating half life of PEOGMA-PDPA compared to PMPC-PDPA polymersomes, which quickly accumulate in liver and spleen, organs primarily involved in nanoparticle clearance from blood. Finally, we implemented the analysis with a method to correlate the distance travelled by the polymersomes with the diameter of the source vessel. From the results it was observed that there was greater polymersomes accumulation around higher calibre vessels, however the furthest distance travelled is recorded from smaller vessels (fig. 5.8-5.9). The accumulation around bigger calibre vessels, and specifically near vessels branches, has been already reported for liposomes (Yuan et al. [1994]). A possible explanation could be that in those areas there is a higher local density of tumour macrophages up-taking and accumulating polymersomes. At smaller vessel level extravasated polymersomes are less likely to be sequestered by phagocytic cells, therefore they can travel longer distances. This working hypothesis needs to be tested, ideally by macrophage labelling *in vivo* in the DSC followed by co-localisation study. Another possible explanation could be in the presence of bigger fenestrations in bigger calibre vessels, and local flow turbulence at the branching level facilitating polymersomes extrapolation.

The method of tumour targeting described is known as *passive targeting*. Polymersomes reach the tumour and accumulate within the stroma via **Enhanced Permeation and Retention (EPR)** effect. It is also possible to undertake active targeting to any specific tumour cell. Active targeting can be achieved by functionalising polymersomes with a moiety to recognise a specific cell marker. In the final part of the work an attempt at active targeting was introduced. The chosen target was perivascular cells. This cell type was chosen because of its key role in angiogenesis and vessels stabilisation, and the implication in development of pericyte targeted therapies. Targeting pericytes is challenging as there is no reported cellular marker specific of pericytes and uniquely expressed by pericytes. Furthermore, pericytes are not a well defined cell type. Restricting their definition to peri-capillary cells, there is still significant variation in reported markers depending on species, body location and activation status (Díaz-Flores et al. [2009]). For the *in vitro* work the embryo cell 10T1/2 was used a precursor of pericyte, as it has been reported that they can differentiate into perivascular cells in response to treatment with **Transforming Growth Factor- $\beta$ 1 (TGF- $\beta$ 1)** (Hirschi et al. [1998]). Adopting this model, the first part of the development was focused on assessing the expression of commonly accepted pericytes markers **Platelet Derived Growth**

Factor Receptor- $\beta$  (PDGFR- $\beta$ ) and Nerve Glial antigen 2 (NG2) in 10T1/2 when treated with different concentrations of TGF- $\beta$ 1, and most importantly with respect to the expression of the same markers in MFC188 and SVECs. Ideally, the marker should be expressed only by 10T1/2 to facilitate active targeting. Results indicated that 10T1/2 expression of PDGFR- $\beta$  and NG2 was not significantly affected by treatment with TGF- $\beta$ 1 alone, suggesting a more complex activation pathway, perhaps involving direct contact with endothelial cells in a co-culture system, as suggested by results reported by D'Amore and Hirschi (Hirschi et al. [1998], Hirschi et al. [1999]). However, expression of both markers, and particularly NG2, was found to be significantly higher in 10T1/2 compared to MFC188 and SVECs (fig. 6.12-6.21).

There is a vast library of chemistry available for polymer functionalisation. In this work we tested two different synthetic approaches that can be performed after polymersomes formation. The first approach is based on biotin/streptavidin chemistry, the second on maleimide reaction. In biotin/streptavidin approach a percentage of biotinylated co-polymer was included in the formulation and after polymersomes self assembly a biotinylated antibody against PDGFR- $\beta$  was linked via a bridge of streptavidin. Maleimide is commonly used to functionalise thiol groups (cysteine in proteins), however at slightly higher pH it can also undergo nucleophilic attack from primary amino groups (leucine). Both strategies were tested. RP-HPLC characterisation (fig. 6.26, 6.29) showed successful conjugation for both strategies. Biotin/streptavidin conjugate was tested *in vitro* (fig. 6.27). At 6h a slight increased uptake of PMPC-PDPA functionalised formulation was observed in 10T1/2 cells, however the uptake was still lower compared to uptake of pristine PMPC-PDPA by MFC188. A similar pattern was observed for Polyethylen Oxide-poly(2-(diisopropylamino)ethyl methacrylate) (PEO-PDPA) functionalised polymersomes at the 24h time point.

Overall, results obtained in this work represent a collection of methods developed to screen polymersomes uptake *in vitro*, also taking into account the complexity of flow mediated particles delivery. Furthermore, dedicated *in vivo* analytical methods were developed to characterise accumulation of polymersomes within tumours. Results suggested that longer circulating POEGMA-PDPA polymersomes have better chance to accumulate intra-tumour and to provide increased signal-to-noise ratio compared to PMPC-PDPA. Furthermore POEGMA-PDPA are less likely to be up-taken preferentially by tumour cells by scavenger receptors. However, PMPC-PDPA can still be considered especially for short term imaging and perhaps active targeting of cells located close to the vessels, where no significant intra-tumour accumulation is required.

## 7.2 Future directions

The work presented generated some interesting questions that can be addressed in future developments.

***In flow*** studies suggested a strong effect of flow on cellular uptake, and perhaps a more significant effect of velocity magnitude compared to shear stress. Further studies could complement the observations made by correlating uptake with topological cellular distribution of receptor involved in uptake pathways such as scavenger receptors. This is critical especially for endothelial cells, which are known to polarise receptors expression in relation to the vascular or avascular side. Formulations with receptor mediated uptake such as [PMPC-PDPA](#) could be affected by a polarisation of the receptor expression. Furthermore, it would be interesting to analyse polymersomes uptake not only as a function of the shear stress or the fluid velocity but also according to local polymersomes velocity or concentration, both quantifiable with appropriate *in silico* simulation. Polymersomes velocity is likely to be strongly correlated to fluid velocity, and to be very low at the boundaries (i.e. cell surface). Local polymersomes at the cellular level, however, is likely to be significantly higher at the inlet and outlet level compared to the rest of the well. This is because the inlet and outlet are two small points where all particles are forced to pass, while they can spread across a much bigger surface in the rest of the well. Furthermore, polymersomes concentration at the cellular level is probably very low because they are mostly quickly dragged away from the cell surface by the fluid, which has greater velocity away from the boundaries. If *in silico* simulations shows a significant effect on polymersomes drag, the device should probably be re-designed in favour of a greater surface to volume ratio compared to the current design. Finally, the introduction of a more viscous, blood-like fluid will improve the reproduction of physiological capillary flow.

***Active targeting*** attempt was not successful. Targeting of perivascular cell is made difficult by the lack of a well characterised marker and the difficulty of translating *in vitro* models to *in vivo* models. Further work could introduce the screening on *ex vivo* samples obtained from animal models bearing the same [MFC188](#) tumour model used in this work. More work can also be done in the conjugation of a targeting moiety to the polymersomes surface. In this work we choose to functionalise pre-formed polymersomes, however the formulations used are non-fouling, and this is likely to reduce the reaction yield as they will interact poorly with the [Immunoglobulin of the class G \(IgG\)](#) chosen as function-

alising molecule. Performing the reaction before the self-assembly could improve the reaction yield by reducing the steric hindrance. Furthermore, the use of a full antibody is not advisable for both stability and synthetic costs reasons. A full antibody has a relatively large hydrodynamic radius which could potentially destabilise the polymersome construct. Full antibodies could also be more easily recognised by the [Reticuloendothelial System \(RES\)](#) or opsonising proteins because of their large volume. Finally, the use of specific, full antibodies is costly, as it is necessary to use a significant amount of molecules, therefore of antibody, to perform the reaction in the ideal condition of antibody excess. The use of smaller molecules such as peptides or antibody fragments could address all the discussed issues.

Finally, *in vivo* image analysis has proved to be potentially useful in analyse a number of parameters related with polymersomes extravasation and intra-tumour accumulation. More work can be done to fully automate the masking process, which at the moment relies on the user judgement at least on the choice of the masking parameters such as intensity threshold or [Difference of gaussians \(DoG\)](#) kernel size. More animals are also required to draw significant conclusions from the analysis, as only a total of 5 animals divided across different formulations and imaging techniques were used. With respect to this, the surgical procedure necessary to implant the [DSC](#) proved to have poor outcome, with major complications arising a few hours after surgery. Some of the complication have been addressed already by changing some of the parts of the chamber, most importantly the spacers between the two frames. However, more work should be done to assure more reliable outcome, which has implication on both the ethics of the work and data quality from *in vivo* experimentation.

## CHAPTER 8

### LIST OF MATERIAL USED

#### 8.1 General *in vitro* laboratory equipment and reagents

##### Consumables

Item	Supplier
1.2ml cryogenic vials	Nalge Company, Rochester, NY, USA
0.5ml, 2.0ml eppendorf tubes	Starstedt, Ak & Co, Germany
25cm <sup>2</sup> , 75cm <sup>2</sup> tissue culture flasks	Nunc-Life Technologies Ltd, UK
3M autoclave tape	Rexam Medical Packaging, UK
5ml, 10ml and 25ml pipettes	Corning Incorporated, USA
70% (v/v) IMS	Adams Healthcare Ecolab, UK
Trigene	Medimark Scientific, UK
96, 24 well plates	Nunc-Life Technologies Ltd, UK
96 wells imaging plates	Becton, Dickinson and Company, NJ, USA
24 wells imaging plates	ibidi, Martinsried, Germany
Gilson pipette tips	Starsted Laboratory Supplies Ltd, UK
Latex examination gloves	Kimberly Clarke Ltd, UK
P2, P10, P20, P200, P1000 pipettes	Gilson Inc, USA
Paper tissue	Kimberly Clarke, USA
Presept tablets	Johnson & Johnson, UK
Sterile universal tubes	Scientific Laboratory Supplies Ltd, UK
Bijoux	Scientific Laboratory Supplies Ltd, UK
Glass vials	Scientific Laboratory Supplies Ltd, UK

1ml, 2ml, 5ml syringes	Becton Dickinson Ltd, UK
1ml insulin syringe	Becton Dickinson Ltd, UK
25G, 27G and 29G needles	Becton Dickinson Ltd
4 well slides	Nunc-Life Technologies Ltd, UK
Microscope glass slides	Fisher Scientific, UK
Coverslip	Fisher Scientific, UK
PVDF membrane	EMD Millipore Corporation, Billerica, MA, USA
Photographic film	GE Healthcare, UK
Marprene tubing	Watson-Marlow Pumps Group, UK
Elbow Luer Connector	ibidi, Martinsried, Germany
Carbon coated TEM Grids	Elektron Technology Ltd, UK
Cell scraper	Corning, NY, USA
Simon ProteinSimple consumables	ProteinSimple, Santa Clara, CA, USA

Table 8.1: *In vitro* consumables.**Equipment**

<b>Item</b>	<b>Supplier</b>
5% CO <sub>2</sub> incubator	Sanyo, UK
Autoclave	Prestige Medical Ltd, UK
Centrifuge (tissue culture)	Eppendorf 5702R
Microcentrifuge	Eppendorf 5425
Ice machine	Scotsman Ice System, UK
pH meter	Hanna Instruments, Rhode Island, USA
Plate reader	
Fluorescence microscope Pathway 855	Microscope: Becton Dickinson Ltd, UK Camera: Hammamatsu
Fluorescence microscope Leica TCS SP8	Microscope: Leica, Wetzlar, Germany Camera: CRI NuanceFX, Quorum Technologies, CA, USA
Brightfield microscope	Medline Scientific Ltd, UK
Spectrofluorometer	Jasco Inc, USA
Sterile safety cabinets/hoods	Walker Safety Cabinets Ltd, UK
Temperature control water bath	Fisher Scientific, UK
Vortex	Whirlimixer, Fisher Scientific, UK
Analytical weighting scale	Sartorius, D
Technical weighting scale	Sartorius, D

Western blot equipment	Bio-Rad Laboratories, CA, UK
Western Blot semi-dry membrane transfer	Bio-Rad Laboratories, CA, UK
FACS CellArray	Becton Dickinson Ltd, UK
TEM microscope	Microscope: Fei Tecnica Spirit Camera: Gatan1K MS600CW CCD
Glow discharger	Quorum Technologies Ltd, UK
Peristaltic pump	Watson-Marlow Pumps Group, UK
Simon ProteinSimple	ProteinSimple, Santa Clara, CA, USA
RP-HPLC Ultimate 3000	Thermo Scientific Dionex, Waltham, Massachusetts, USA
RP-HPLC column	Phenomenex, CA, USA

Table 8.2: *In vitro* equipment.**Reagents**

<b>Item</b>	<b>Supplier</b>
Streptavidin	Vector Laboratories, USA
Hydrochloric acid	Sigma-Adrich, MI, USA
Sodium hydroxide	Sigma-Adrich, MI, USA
Liquid Nitrogen	BOC, UK
Gaseous Nitrogen	BOC, UK
Phosphotungstic acid	Sigma-Adrich, MI, USA
DMEM	Lonza, Switzerland
BME	Invitrogen, CA, USA
Penicillin/streptomycin	Sigma-Adrich, MI, USA
Fungizone	Life Technologies, CA, USA
Methanol	Sigma-Adrich, MI, USA
Choloroform	Sigma-Adrich, MI, USA
Trifluoroacetic acid	Sigma-Adrich, MI, USA
PBS	Fisher Scientific, UK
FCS	Biosera, UK
Trypsin/EDTA	Sigma-Adrich, MI, USA
FACS cleaning buffer	Becton Dickinson Ltd, UK
FACS running buffer	Becton Dickinson Ltd, UK
RIPA Buffer	Thermo Scientific, MA, USA
BSA	Sigma-Adrich, MI, USA
Photographic fixative	Eastman Kodak Company, NY, USA
Photographic developer	Eastman Kodak Company, NY, USA

Simon ProteinSimple reagents	ProteinSimple, Santa Clara, CA, USA
Fibronectin	Sigma-Adrich, MI, USA
HEPES buffer	Sigma-Adrich, MI, USA
Acetone	Sigma-Adrich, MI, USA
Ethanol	Sigma-Adrich, MI, USA
ABC	Vector Laboratories, USA
DAB	Vector Laboratories, USA
DPX	Sigma-Adrich, MI, USA
Haematoxylin	Sigma-Adrich, MI, USA
Xylene	Sigma-Adrich, MI, USA
Hydrogen peroxide	Sigma-Adrich, MI, USA
Rabbit IgG	Sigma-Adrich, MI, USA
Texas red-avidin	Invitrogen, CA, USA
FITC-avidin	Invitrogen, CA, USA
Streptavidin	Vector Laboratories, USA
Normal Horse Serum	Vector Laboratories, USA
DAPI	Vector Laboratories, USA
TGF- $\beta$ 1	R&D Systems Inc, USA

Table 8.3: *In vitro* reagents.

<b>Antibody</b>	<b>Code</b>	<b>Supplier</b>
RGS5	sc-28492	Santa Cruz
Desmin	ab15200	Abcam
$\alpha$ -SMA	A2547	Sigma-Aldrich
PDGFR- $\beta$	sc-432	Santa Cruz
PDGFR- $\beta$ -Biotin	ab93533	Abcam
NG2	ab5320	Millipore
NG2	4235	Cell Signaling
NG2-Alexa488	ab5320A4	Millipore
CD31-FITC	102406	Bio Legend
DyLight-649	406406	Bio Legend
DyLight-488	406404	Bio Legend

Table 8.4: List of all the antibodies used *in vitro*.

### Consumables

<b>Item</b>	<b>Supplier</b>
Syringes	Becton Dickinson Ltd, UK
2.0ml eppendorf tubes	Sarsted AG & Co, Germany

25G and 27G needles	Becton Dickinson Ltd, UK
4/0 Ethilon	Ethicon Ltd, UK
5/0 mersilk non-adsorbable suture	Ethicon Ltd, UK
5/0 PDS II suture	Ethicon Ltd, UK
Latex examination gloves	Kimberly Clarke Ltd, UK
Microscope slides	Fisher Scientific, UK
Paper tissue	Kimberly Clarke Ltd, UK
Petri dish	Corning Inc, UK
Size 15 scalpel blade	Swann Morton, UK
Sterile Biogel gloves	Regent Medical Ltd, UK
Cotton swabs	Shermond Surgical Supply Ltd, UK

Table 8.5: *In vivo* consumables.**Equipment**

<b>Item</b>	<b>Supplier</b>
C-clamp	Medical Workshop, University of Sheffield, UK
Chamber pieces	Medical Workshop, University of Sheffield, UK
Confocal Microscope	Zeiss LSM510 NLO Upright
Epiluoescence Microscope	Nikon Eclipse E600FN
Restrainer (model 84)	IITC Life Science, USA
Incubator	Brinsea Products Ltd, UK
Sensitive warming pad	Cole-Palmer Ltd, UK
Surgical instruments	Fine Science Tools, USA

Table 8.6: IVM equipment.

**Reagents**

<b>Item</b>	<b>Supplier</b>
70% IMS	Adams Healthcare Ecolab, UK
Betadine surgical scrub	Seton Healthcare Group plc, UK
Trigene disinfectant concentrate	Medichem International, UK

Table 8.7: *In vivo* reagents.**Lysis buffer**

<b>Reagent</b>	<b>Final Concentration</b>
Tris-HCl	50mM

NaCl(150mM)	150mM
Sodium azide	0.02% (w/v)
SDS	0.1% (w/v)
Igepal CA-630 or Nonidet P-40	1%
Sodium deoxycholate	0.5%
Protease inhibitor	1 tablet for 10ml of buffer
Final pH	8.8

---

### Running buffer 10X

Reagent	Final Concentration
Tris base	25mM
Glycin	0.192M
SDS	0.1% (w/v)
Final pH	8.3

---

### Transfer buffer

Reagent	Final Concentration
Tris base	3.03g
Glycin	14.10g
SDS	2.5g
dH2O	900ml
Methanol	100ml
Final pH	8.3
SDS	2.5g

---

### Stacking gel

Reagent	Final Concentration
dH2O	3ml
tris-HCl pH 8.8	1.25ml
30% acrylamide	650μl
10% APS	50μl
TEMED	5μl

---

### Running gel

Reagent	Final Concentration
dH2O	4.85ml
tris-HCl pH 8.8	2.5ml
30% acrylamide	2.5ml
10% APS	50μl
TEMED	5μl

Table 8.8: Western blot reagents composition.

Formulation as referred to in the text	Copolymer	Amount [mg]
PMPC-PDPA	PMPC <sub>25</sub> -PDPA <sub>70</sub>	18
	Rhd-PMPC <sub>25</sub> -PDPA <sub>70</sub>	2
PEO-PDPA	PEO <sub>113</sub> -PDPA <sub>70</sub>	18
	Rhd-PEO <sub>113</sub> -PDPA <sub>70</sub>	2
POEGMA-PDPA	POEGMA-PDPA	18
	Rhd-POEGMA-PDPA	2
Biotin-PMPC-PDPA	PMPC <sub>25</sub> -PDPA <sub>70</sub>	16
	Rhd-PMPC <sub>25</sub> -PDPA <sub>70</sub>	2
	Biotin-PMPC <sub>25</sub> -PDPA <sub>70</sub>	2
Maleimide-PMPC-PDPA	PMPC <sub>25</sub> -PDPA <sub>70</sub>	16
	Rhd-PMPC <sub>25</sub> -PDPA <sub>70</sub>	2
	Maleimide-PMPC <sub>25</sub> -PDPA <sub>70</sub>	2
Maleimide-POEGMA-PDPA	POEGMA <sub>25</sub> -PDPA <sub>70</sub>	16
	Rhd-POEGMA-PDPA	2
	Maleimide-PMPC <sub>25</sub> -PDPA <sub>70</sub>	2

Table 8.9: Composition of the different polymersomes formulations use. The amounts reported are intended for the reparation of 2ml of polymeromses in film hydration or to be dissolved in 2ml of [Phosphate Buffer Saline pH 2 \(PBS<sub>2</sub>\)](#) using pH switch technique.

## 9.1 Binding efficiency (BE)

Binding efficiency (BE) was defined as the amount of polymersomes up-taken by the cells in the unit of time. BE was calculated by combining data from Reverse Phase-High Pressure Liquid Chromatography (RP-HPLC) (amount of polymersomes) and Fluorescence Activated Cell Sorting (FACS) (sorting of cell population positive for polymersomes) analysis. The work flow for the analysis is reported in figure 9.1.

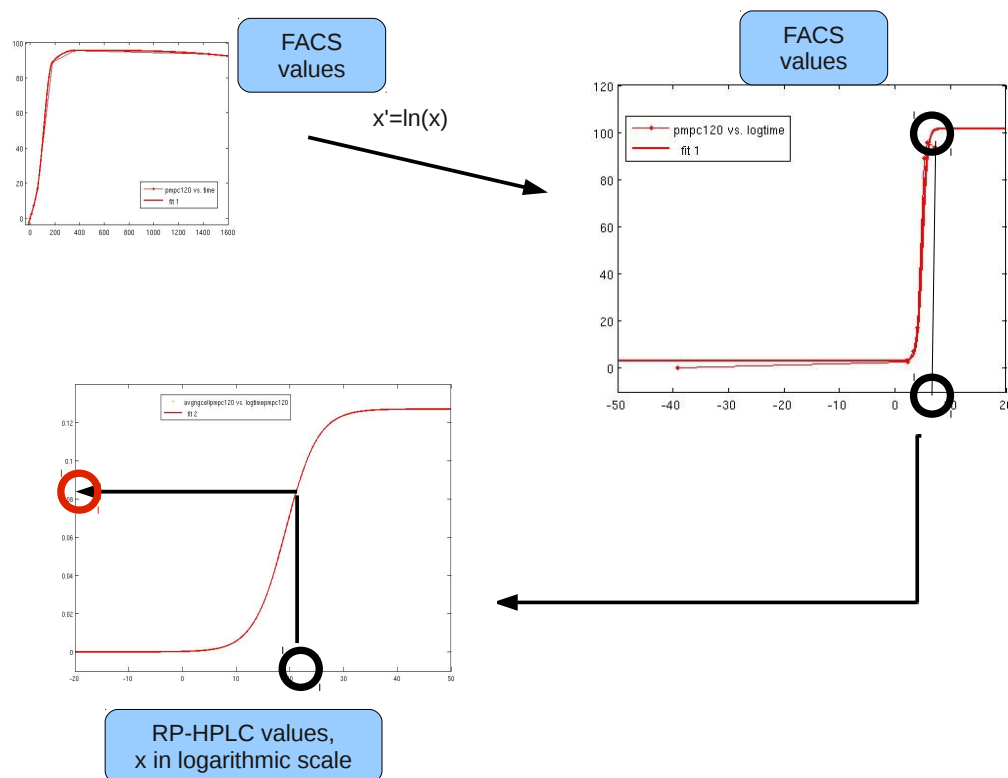


Figure 9.1: Binding efficiency calculation. *FACS* results were plotted in logarithmic scale and the time-point at which the plateau of maximal uptake was reached ( $t_p$ ) was graphically extrapolated. The number of vesicles per cell internalised was derived from *RP-HPLC* data at  $t = t_p$ .

*RP-HPLC* and *FACS* analysis were performed comparing 10% rhodamine labelled Polyethylen Oxide-poly(2-(diisopropylamino)ethyl methacrylate) (PEO-PDPA) and Poly(2 - methacryloxyethyl-phosphorylcholine)-poly( 2 -(diisopropylamino)ethyl methacrylate) (PMPC-PDPA) polymersomes. Cells used were Mouse Fibrosarcoma Cells expressing VEGF120 isoform (MFC120), Mouse Fibrosarcoma Cells expressing VEGF188 isoform (MFC188) and 10T1/2. Results are reported in figure 9.2-9.3. Consistently with the reported profile of uptake described in section 4, PMPC-PDPA polymersomes were up-taken faster than PEO-PDPA polymersomes. It was also confirmed higher uptake from Mouse Fibrosarcoma Cell (MFC) compared to 10T1/2. There was no significant difference between MFC120 and MFC188 ( $p > 0.05$ ).

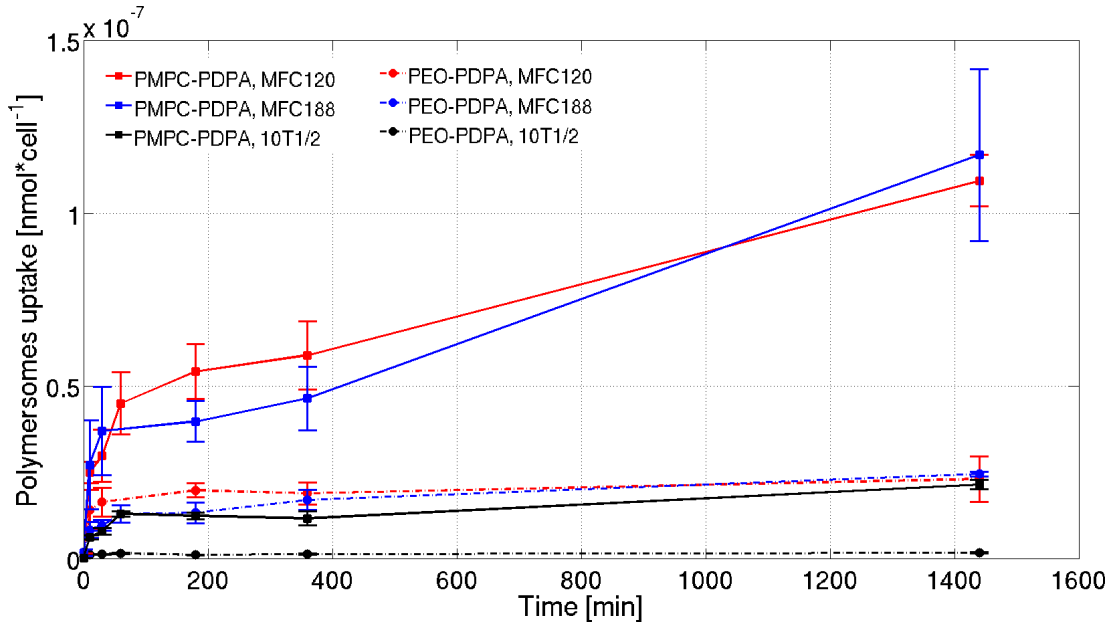


Figure 9.2: *RP-HPLC* uptake results. *PMPC-PDPA* (solid lines) is up-takes faster than *PEO-PDPA*, with no significant difference ( $p > 0.05$ ) between *MFC188* (red lines) and *MFC120* (black lines). *10T1/2* (blue lines) have very low uptake of *PEO-PDPA*, and the uptake of *PMPC-PDPA* is higher than *PEO-PDPA*, however it is lower than the uptake of the same formulation in *MFC* cell lines.  $N=3$ ,  $\pm SD$ .

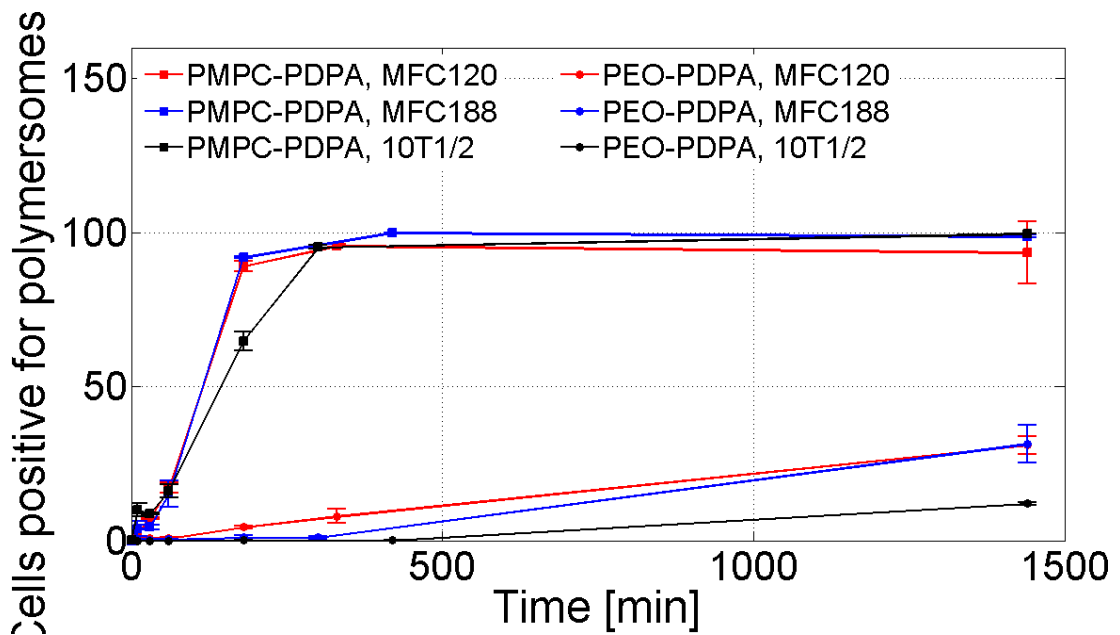


Figure 9.3: *FACS* uptake results. *PMPC-PDPA* (solid lines) is up-takes faster than *PEO-PDPA*, with no significant difference ( $p > 0.05$ ) between *MFC188* (red lines), *MFC120* (black lines) and *10T1/2* (blue lines). Uptake of *PEO-PDPA* has no significant difference ( $p > 0.05$ ) between the three cell lines up to 6h, however at 24h there is a significant difference ( $p < 0.05$ ) between *MFC* cell lines (higher uptake) and *10T1/2*.  $N=3$ ,  $\pm SD$ .

To calculate *BE*, it was critical to reach a plateau of uptake. with *PEO-PDPA*

this was not achieved in the time limit of the analysis. The value of maximal uptake can be mathematically extrapolated, however this would introduce inaccuracy. For this reason the calculation of BE was limited to the two MFC cell types. BE of PMPC-PDPA was significantly higher ( $p > 0.05$ ) than BE of PEO-PDPA polymersomes, and there was no significant difference ( $p > 0.05$ ) between MFC120 and MFC188 (9.4). The method provided a useful absolute term of comparison between uptake of different formulations from different cell types. However the technique was not developed further as it required to perform both FACS and RP-HPLC for any given combination of polymersome formulation and cell type. This was not advisable in fast, high throughput screening.

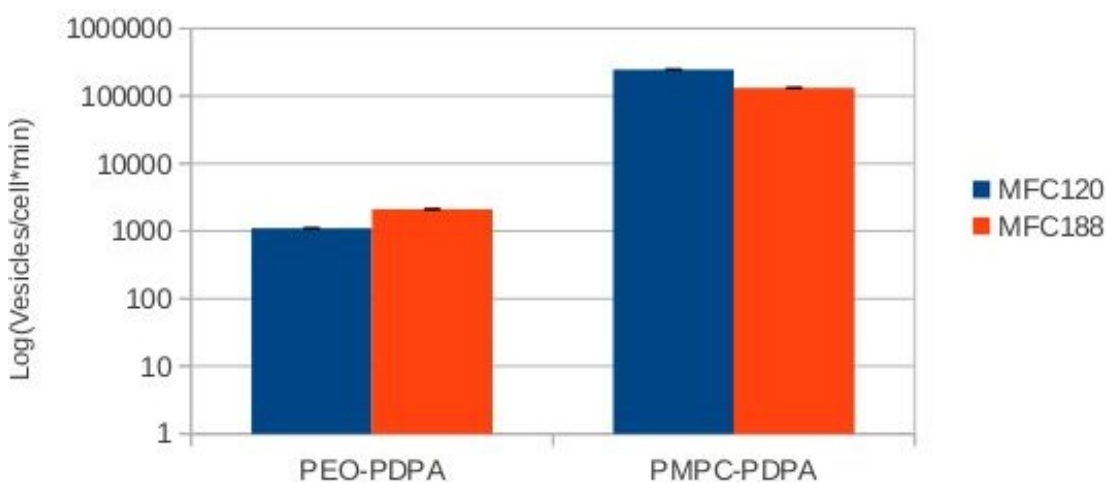


Figure 9.4: Binding efficiency for PEO-PDPA and PMPC-PDPA in MFC188 and MFC120. PMPC-PDPA had greater BE compared to PEO-PDPA, while there was no significant difference between MFC120 and MFC188.  $N=3$ ,  $\pm SD$ .

## 9.2 FACS for *in flow* uptake

In section 4 FACS results were reported as fluorescence intensity variation over time. This was useful to compare imaging and FACS results. However, FACS results can also be expressed as variation of percentage of cells positive for polymersomes over time. In this case there is no information on magnitude of uptake, but only on the percentage of cells that are up-taking polymersomes at a higher rate than a fixed threshold. For this reasons the two plots can be different, as it is possible that all cells are up-taking polymersomes, therefore the percentage of population is high, however the uptake could be slow, resulting in low magnitude of uptake. This can be observed in the plots here reported (9.5-9.7) when compared to plots 4.11, especially for cell types with low uptake (Small Vessel Endothelial Cells (SVECs) and 10T1/2). Furthermore, it can be observed how FACS uptake curves expressed as percentage of population reached a plateau

for **PMPC-PDPA** and **MFC188** and **SVECs**, but no plateau was observed in curves expressed as variation of intensity. This suggested that for fast uptake polymersomes all cells became positive for polymersomes, and vesicles continued to accumulate within the cells increasing the intensity of the fluorescence signal.

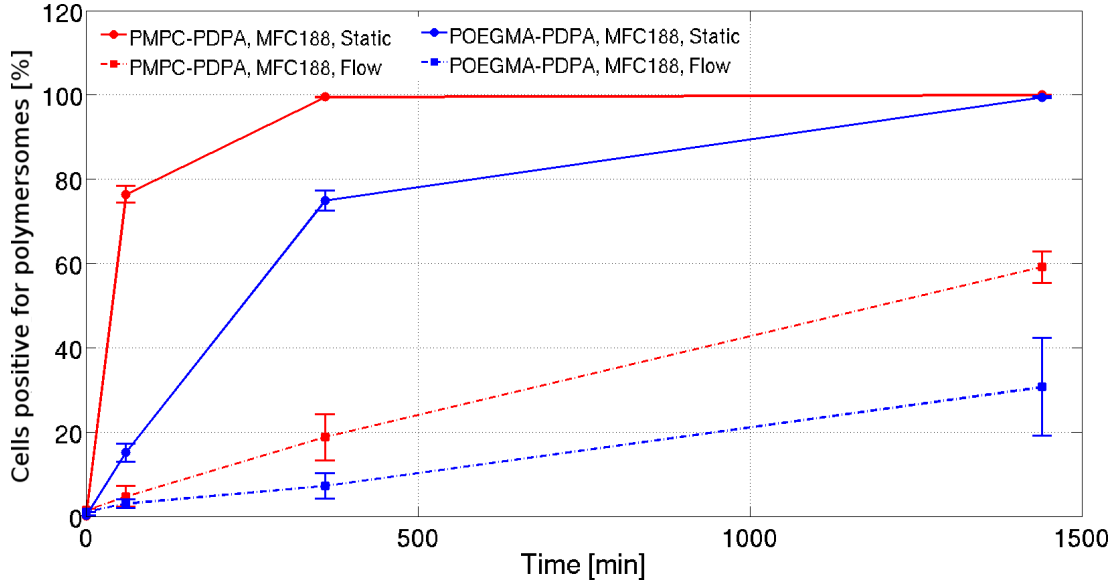


Figure 9.5: Uptake of *PMPC-PDPA* and *poly(oligo(ethylene glycol) methacrylate)-poly(2-(diisopropylamino)ethyl methacrylate)* (*POEGMA-PDPA*) rhodamine labelled polymersomes by *MFC188*. FACS data expressed as percentage of cells positive for rhodamine labelled polymersomes.  $N=3$ ,  $\pm SD$ .

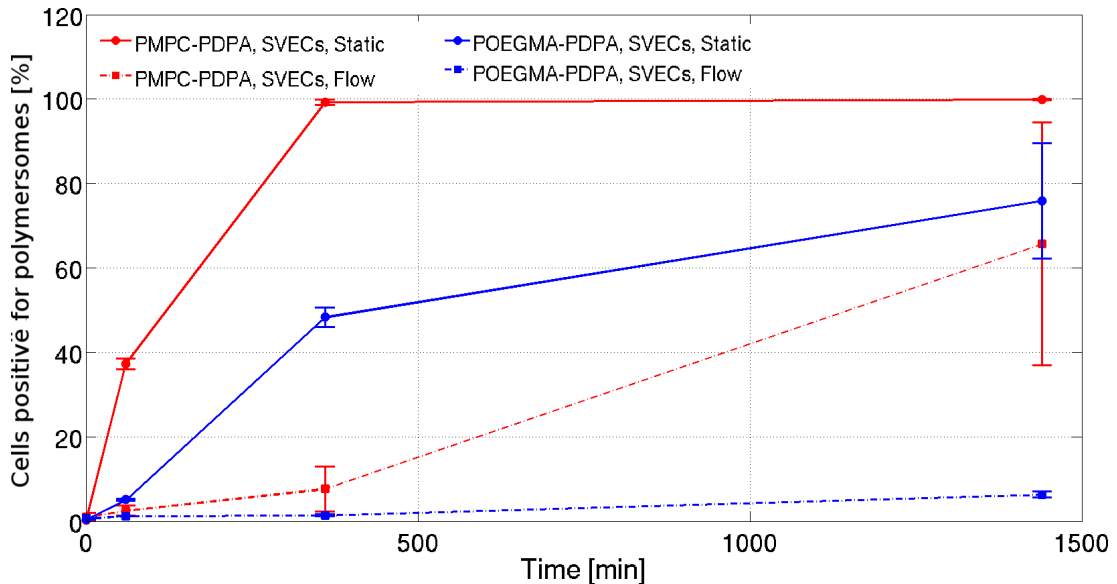


Figure 9.6: Uptake of *PMPC-PDPA* and *POEGMA-PDPA* rhodamine labelled polymersomes by *SVECs*. FACS data expressed as percentage of cells positive for rhodamine labelled polymersomes.  $N=3$ ,  $\pm SD$ .

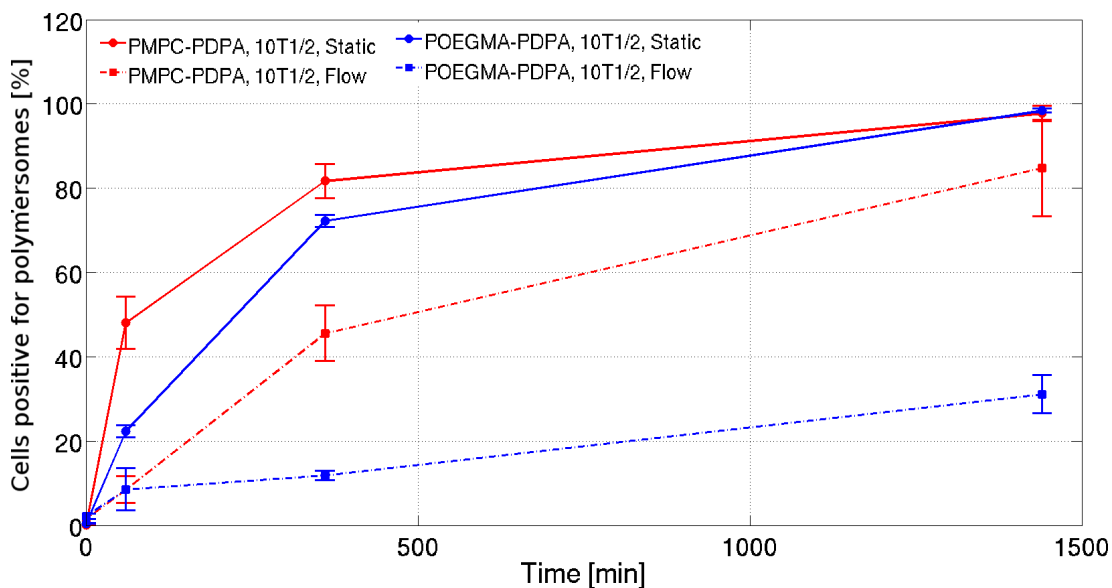


Figure 9.7: Uptake of *PMPC-PDPA* and *POEGMA-PDPA* rhodamine labelled polymersomes by 10T1/2. FACS data expressed as percentage of cells positive for rhodamine labelled polymersomes.  $N=3$ ,  $\pm SD$ .

### 9.3 *In vivo* epifluorescence imaging

The epifluorescence microscope routinely used to assess tumour establishment in *Dorsal Skinfold Chamber (DSC)* was also used to acquire fluorescence image of injected polymersomes and for image analysis. Representative images acquired equipping the microscope with a 2.5X objective and a 20X objective are reported in figure 9.8. Images were acquired 5min after the injection of rhodamine labelled *POEGMA-PDPA* polymersomes. In 2.5X and 20X transmitted light images (9.8-a,c) vessels can be observed in dark over brighter stroma, however in 20X images the contrast was significantly reduced. As was observed in confocal images (5.3), at 5min after injection vessel in rhodamine channel are highlighted in bright over dark background.

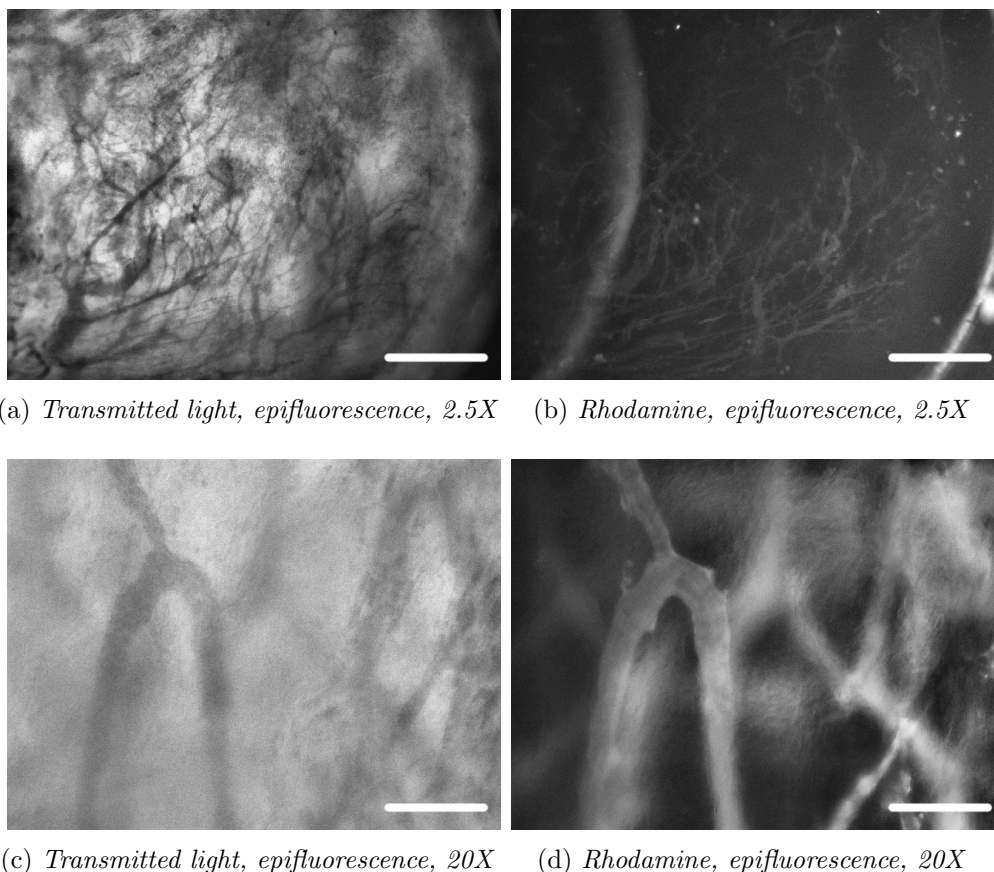


Figure 9.8: *DSC* images obtained with different magnification, epifluorescence microscopy. All images were acquired 5min after *Intra Venous (i.v.)* injection of rhodamine labelled *POEGMA-PDPA* polymersomes. On the left (a, c) transmitted light pictures, on the right (b, d) fluorescence pictures. Images (a, b) were acquired with a epifluorescence microscope equipped with a 2.5X objective, images (c, d) using the same microscope equipped with a 20X objective. Note how, in the rhodamine channel, vessels appeared bright over darker tumour stroma. Bar(a, b) 710 $\mu$ m; (c, d) 90 $\mu$ m.

A time lapse of both formulations is reported in figure 9.9-9.10 for 2.5X and 20X magnification respectively. In both cases it was observed that at early time points vessels were highlighted by polymersomes in the rhodamine channel, however at later time points vessels appeared in dark over brighter background. This supported confocal analysis results and suggested polymersomes extravasation and accumulation within tumour via [Enhanced Permeation and Retention \(EPR\)](#) effect.

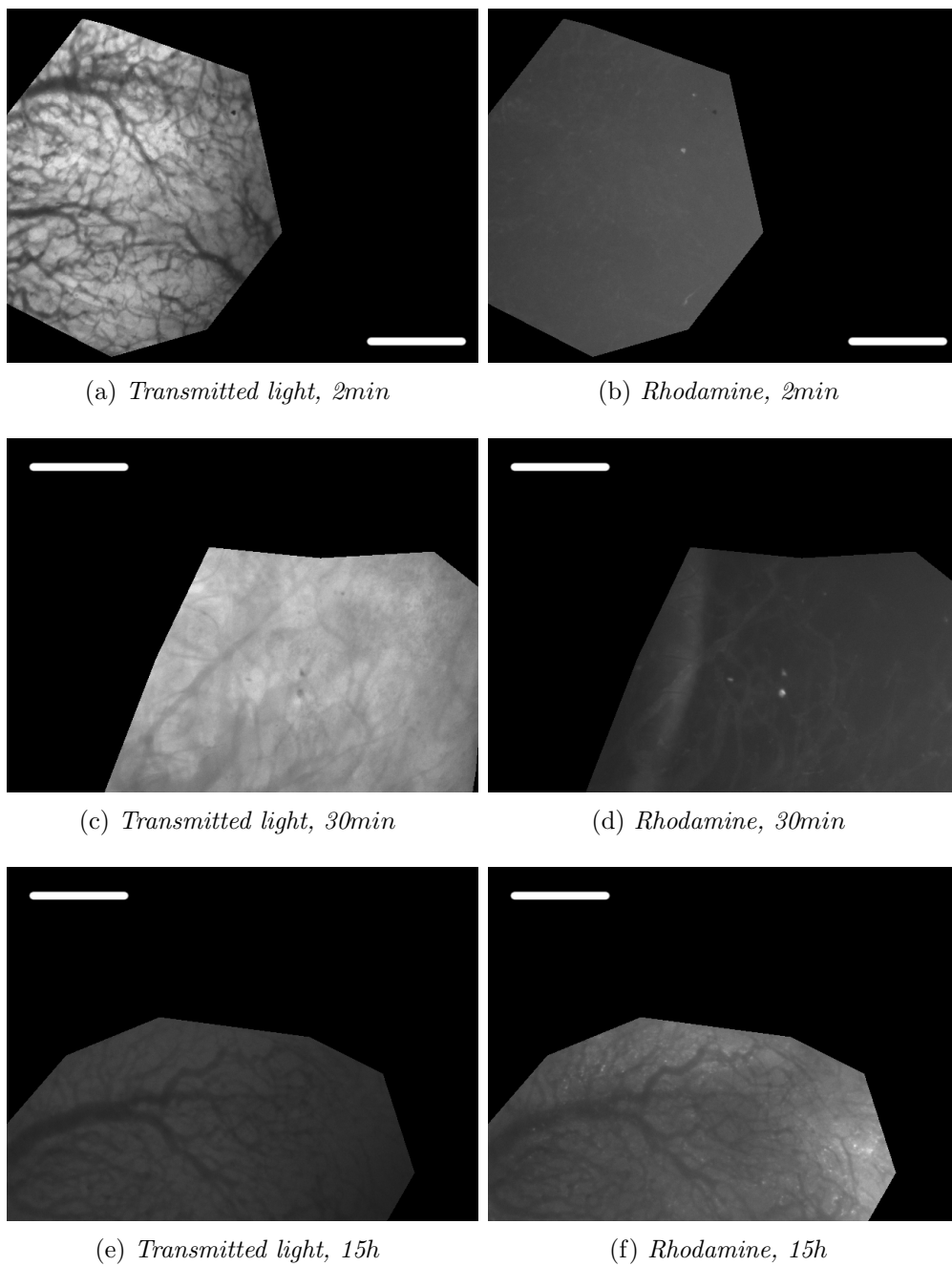


Figure 9.9: *MFC188* tumour microvasculature imaged in epifluorescence, 2.5X objective. Note how between 2min and 30min after injection the tumour vasculature gradually became brighter and the contrast increased, while at 15h vessels appeared dark over brighter stroma. Tumour region of the image was manually masked using the image analysis software developed (sec. 3.6). Bar 710 $\mu$ m.

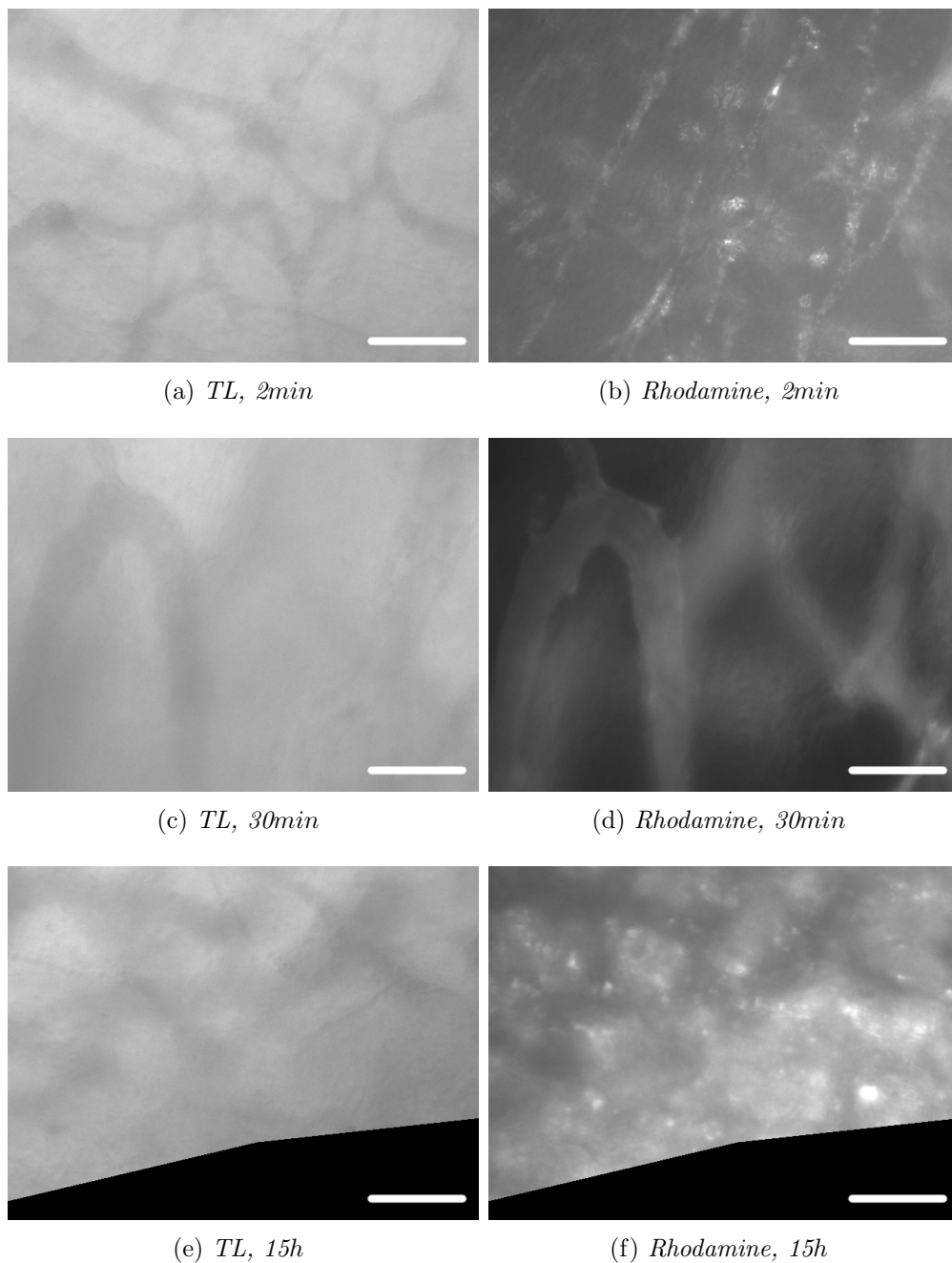


Figure 9.10: *MFC188* tumour microvasculature imaged in epifluorescence, 20X objective. Note how between 2min and 30min after injection the tumour vasculature gradually became brighter and the contrast increased, while at 15h vessels appeared dark over brighter stroma. Tumour region of the image was manually masked using the image analysis software developed (sec. 3.6). Bar 90 $\mu$ m.

Images were analysed using the algorithm described in section 3.6 to assess polymersomes intra-tumour distribution. Results for both 2.5X and 20X magnification confirmed what observed in confocal microscopy: at early time points the vessels have higher contribute to fluorescence signal strength compared to tumour stroma, while at later time point the relative contribution was reversed. However,

epifluorescence imaging was affected by out-of-focus light, limiting sensitivity and accuracy of the analysis (see 5.6-5.7 compared to 9.11-9.12).

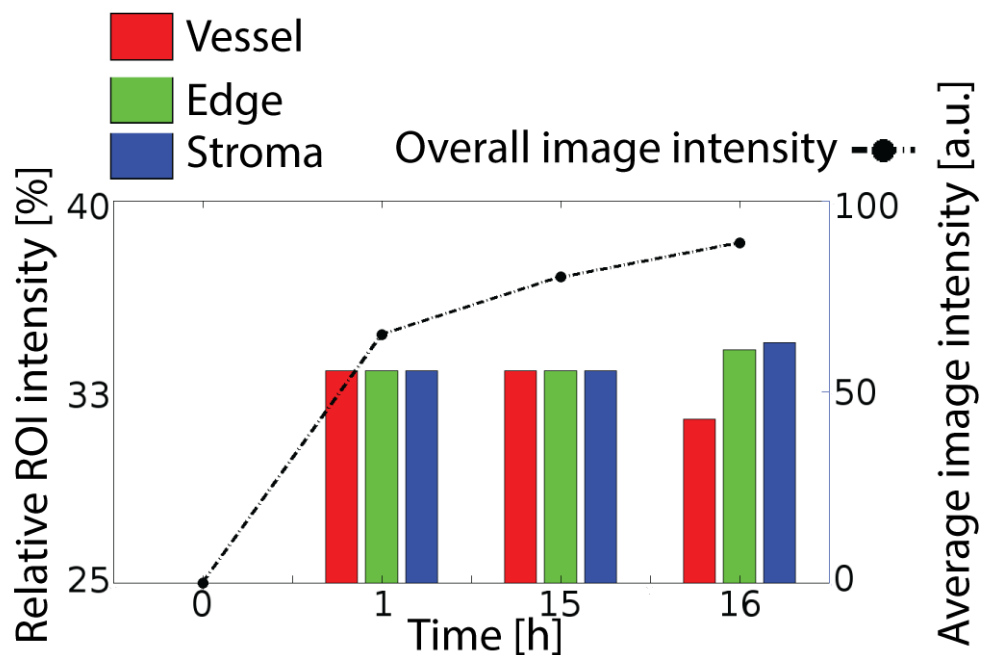


Figure 9.11: *POEGMA-PDPA* in vivo image analysis. Data are represented as overall mean intensity of rhodamine signal in the tumour area (right axis) overlaid with a break down of the relative contribution of vessels, edges and tumour stroma to the signal intensity (left axis, coloured bars). Epifluorescence microscopy, 2.5X objective.  $N=2$ .

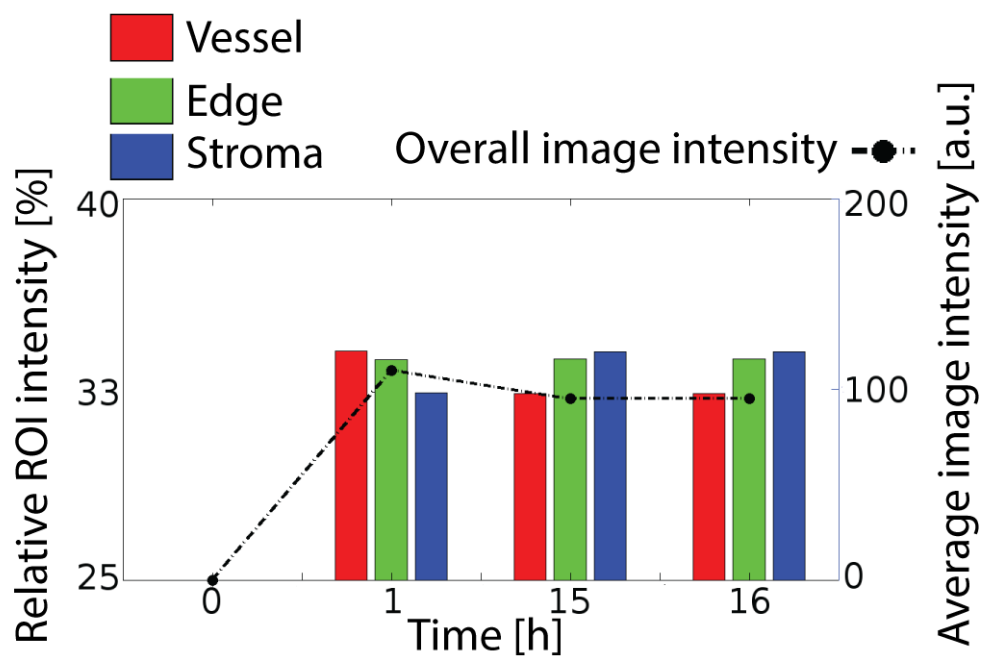


Figure 9.12: *POEGMA-PDPA* in vivo image analysis. Data are represented as overall mean intensity of rhodamine signal in the tumour area (right axis) overlaid with a break down of the relative contribution of vessels, edges and tumour stroma to the signal intensity (left axis, coloured bars). Epifluorescence microscopy, 20X objective.  $N=2$ .

## LIST OF FIGURES

1.1	Causes of death in 2011 and cancer incidence in 2010 . . . . .	2
1.2	Properties of the vascular system with respect to size . . . . .	3
1.3	Pathologies associated with unbalanced angiogenesis . . . . .	4
1.4	EPR effect . . . . .	13
1.5	Geometrical parameters governing the <i>self-assembly</i> . . . . .	17
1.6	Critical Aggregation Concentration (CAC) . . . . .	18
1.7	Multi-block co-polymers . . . . .	19
1.8	Advantages of the polymersomes . . . . .	20
1.9	Hydrophilic polymers used in this work . . . . .	23
1.10	Aim of the work . . . . .	26
2.1	PDPA pH sensitivity . . . . .	29
2.2	Typical Dynamic Light Scattering (DLS) results . . . . .	31
2.3	Typical Transmission Electron Microscopy (TEM) results . . . . .	32
2.4	Gradients used in RP-HPLC analysis . . . . .	33
2.5	Biotin/streptavidin functionalisation . . . . .	34
2.6	Maleimide reaction . . . . .	34
2.7	Automated western blot work-flow . . . . .	40
2.8	(3 - (4,5 - Dimethylthiazol - 2 - yl) - 2,5 - diphenyltetrazolium bromide (MTT) reaction . . . . .	42
2.9	Cell viability . . . . .	42
2.10	Work-flow of polymersomes extraction from cells . . . . .	43
2.11	RP-HPLC gradient and chromatogram for rhodamine labelled poly- mersomes . . . . .	44
2.12	Recovery of RhdPMPC-PDPA from cells . . . . .	44
2.13	Spheroid . . . . .	47
2.14	Window chamber parts . . . . .	48

3.1	Example of intensity thresholding masking . . . . .	52
3.2	Example of Difference of gaussians (DoG) masking . . . . .	53
3.3	Example of Local threshold entropy (LTE) . . . . .	54
3.4	Mask post processing . . . . .	55
3.5	Immunocytochemistry analysis. Masking . . . . .	56
3.6	Immunocytochemistry analysis. Data analysis . . . . .	57
3.7	Example of time-analysis . . . . .	58
3.8	Mapping a well . . . . .	59
3.9	Effect of fixation on rhodamine signal . . . . .	60
3.10	Segmentation of the flow parameter . . . . .	61
3.11	Image analysis method . . . . .	62
3.12	Mask generation in different pictures . . . . .	64
3.13	Masking blood vessels . . . . .	66
3.14	Vessel segmentation: Skeleton mask . . . . .	68
3.15	Identifying vessels, ends and branching points . . . . .	69
3.16	Vessel segmentation: Computation of vessel diameter . . . . .	70
3.17	Immunocytochemistry (ICC) and uptake software Graphic user interface (GUI) . . . . .	71
3.18	Vessel segmentation software GUI . . . . .	72
4.1	RP-HPLC, FACS and live cell imaging comparison . . . . .	78
4.2	Uptake, FACS and live cell imaging . . . . .	79
4.3	Imaging, PMPC-PDPA up-take in static . . . . .	80
4.4	Imaging, POEGMA-PDPA up-take in static . . . . .	80
4.5	Flow device modes . . . . .	82
4.6	Shear stress distribution . . . . .	83
4.7	Velocity distribution . . . . .	84
4.8	Flow device . . . . .	84
4.9	Cell viability in flow . . . . .	85
4.10	Uptake in static and flow, FACS and imaging . . . . .	87
4.11	Uptake in static and flow, FACS and imaging . . . . .	88
4.12	Image analysis of uptake, Regions of interest (ROI) shear stress . . . . .	93
4.13	Image analysis of uptake, ROI parallel velocity . . . . .	94
4.14	Image analysis of uptake, ROI perpendicular velocity . . . . .	95
5.1	Parameters observable with DSC . . . . .	104
5.2	MFC188 tumour development . . . . .	107
5.3	DSC images, 10X confocal microscopy . . . . .	108
5.4	MFC188 tumour microvasculature confocal images, 10X objective . . . . .	109

5.5	Confocal imaging comparison of POEGMA-PDPA and PMPC-PDPA . . . . .	111
5.6	PMPC-PDPA in vivo image analysis. Confocal, 10X . . . . .	112
5.7	POEGMA-PDPA in vivo image analysis. Confocal, 10X . . . . .	113
5.8	Extravasation analysis, POEGMA-PDPA . . . . .	114
5.9	Extravasation analysis, PMPC-PDPA . . . . .	115
6.1	Perivascular cell in capillary . . . . .	120
6.2	Pericytes in angiogenesis . . . . .	124
6.3	Affinity of Platelet Derived Growth Factor (PDGF) isoforms for the Platelet Derived Growth Factor Receptor (PDGFR) . . . . .	128
6.4	Immunoglobulin of the class G (IgG) structure . . . . .	129
6.5	Distribution of cysteine and leucine in IgG . . . . .	131
6.6	Polymersomes functionalisation strategies . . . . .	132
6.7	Maleimide reactivity . . . . .	133
6.8	Time analysis . . . . .	134
6.9	Platelet Derived Growth Factor Receptor- $\beta$ (PDGFR- $\beta$ ) staining examples . . . . .	136
6.10	PDGFR- $\beta$ staining examples . . . . .	137
6.11	PDGFR- $\beta$ staining examples . . . . .	138
6.12	Concentration analysis . . . . .	139
6.13	Concentration analysis . . . . .	139
6.14	Concentration analysis . . . . .	140
6.15	Nerve Glial antigen 2 (NG2) staining examples . . . . .	141
6.16	NG2 staining examples . . . . .	142
6.17	PDGFR- $\beta$ staining examples . . . . .	143
6.18	PDGFR- $\beta$ staining examples . . . . .	144
6.19	Effect of different parameters on markers expression . . . . .	145
6.20	Western Blot . . . . .	147
6.21	Western Blot . . . . .	148
6.22	Western Blot . . . . .	149
6.23	Polymersome biotinylation . . . . .	150
6.24	Biotinylated antibody to PDGFR- $\beta$ testing . . . . .	151
6.25	TEM and DLS of functionalised polymersomes, biotin/streptavidin . . . . .	152
6.26	RP-HPLC analysis for biotin/streptavidin functionalised polymersomes . . . . .	153
6.27	Uptake of functionalised polymersomes . . . . .	154
6.28	TEM and DLS of functionalised polymersomes, maleimide . . . . .	155
6.29	Maleimide reaction optimisation . . . . .	156

9.1	Binding efficiency calculation . . . . .	176
9.2	RP-HPLC uptake results . . . . .	177
9.3	FACS uptake results (1) . . . . .	177
9.4	Binding efficiency . . . . .	178
9.5	Uptake in static and flow, FACS . . . . .	179
9.6	Uptake in static and flow, FACS . . . . .	179
9.7	Uptake in static and flow, FACS . . . . .	180
9.8	DSC images obtained with different magnification, epifluorescence microscopy . . . . .	181
9.9	MFC188 tumour microvasculature imaged in epifluorescence, 2.5X objective . . . . .	182
9.10	MFC188 tumour microvasculature imaged in epifluorescence, 20X objective . . . . .	183
9.11	PMPC-PDPA <i>in vivo</i> image analysis. Epifluorescence, 2.5X . . .	184
9.12	POEGMA-PDPA <i>in vivo</i> image analysis. Epifluorescence, 20X . .	185

## LIST OF TABLES

1.1	Pro- and anti-angiogenic factors . . . . .	4
1.2	Overview of imaging techniques . . . . .	11
2.1	RP-HPLC settings used . . . . .	33
2.2	<i>In silico</i> parameters . . . . .	45
4.1	ROI segmentation for shear stress . . . . .	90
4.2	ROI segmentation xy velocity . . . . .	91
4.3	ROI segmentation for z velocity . . . . .	92
6.1	Bioconjugation of proteins . . . . .	130
8.1	<i>In vitro</i> consumables . . . . .	169
8.2	<i>In vitro</i> equipment . . . . .	170
8.3	<i>In vitro</i> reagents . . . . .	171
8.4	List of all the antibodies used <i>in vitro</i> . . . . .	171
8.5	<i>In vivo</i> consumables . . . . .	172
8.6	IVM equipment . . . . .	172
8.7	<i>In vivo</i> reagents . . . . .	172
8.8	Western blot reagents composition . . . . .	173
8.9	Polymersomes formulation . . . . .	174

- $\alpha$ -Smooth Muscle Actin ( $\alpha$ -SMA), 124  
 ICC, results, 132  
 IgG, 125  
 PDGFR- $\beta$ , 125  
 Transforming Growth Factor- $\beta$ 1 (TGF- $\beta$ 1), 124  
 10T1/2, 123  
 10T1/2, Differentiation method, 36  
 10T1/2, Tissue culture, 35  
  
 Active targeting, 13  
 Angiogenesis, mechanism, 3  
 Angiopoietin, 5  
 Animal shaving, 48  
 Animals, general experiment, 46  
 Anti-angiogenesis therapy, 7  
  
 Binding efficiency, 174  
 Bioconjugation, 127  
 Bioconjugation, Biotin/Streptavidin, 130  
 Bioconjugation, Maleimide, 130  
 Blood vessels, anatomy, 2  
  
 Cancer, 1  
 Cell viability, MTT method, 41  
 Co-polymer properties, 20  
 COMSOL Multiphysics, 45, 80  
 Confocal laser scanning microscopy, CLSM, 10  
 Critical aggregation concentration, 16  
 Difference of Gaussian, 52  
 DLS, Method, 30  
 Dorsal skinfold chamber, 100  
 DSC, After surgery animal care, 49  
 DSC, Anaesthesia, 48  
 DSC, animal welfare, 46  
 DSC, camber placement, 48  
 DSC, Spheroid preparation, 46  
 DSC, Surgery, 47  
  
 EPR effect, 12  
  
 FACS, 74  
 FACS, Method, 42  
 FACS, RP-hPLC and Imaging, 77  
 Fibronectin coating, 36  
 Flow bio-incubator, 79  
 Flow bio-incubator, modelling, 45  
 Flow bio-incubator, sterilisation, 45  
 Flow devices, 76  
 Flow, cell culture, 75  
 Flow, cell viability, 84  
 Flow, uptake, 75, 84  
 Flow, well mapping, 87  
  
 ICC, Method, 36  
 Image analysis, GUI, 70  
 Image analysis, in flow uptake, 58  
 Image analysis, in vivo masking, 63  
 Image analysis, markers expression, 55  
 Image analysis, uptake, 57  
 Image analysis, well mapping, 60

- Image post-processing, intensity thresholding, 54
- Image post-processing, size thresholding, 54
- Imaging techniques, 9
- Imaging techniques, limitations, 9
- Imaging techniques, optical imaging, 10
- IVM, method, 49
- Live cell imaging, 74
- LTE segmentation, 53
- MFC culture, 35
- MFC, Tissue culture, 35
- Multiphoton microscopy, 10
- Nanocarriers, 11
- Nanocarriers ADME, 13
- Nanocarriers ADME, Administration, 14
- nanocarriers ADME, Cargo release, 15
- Nanocarriers ADME, Distribution, 14
- Nanocarriers ADME, Extravasation, 14
- Nanocarriers ADME, Metabolism, 15
- Nanocarriers extravasation, 104
- Nanocarriers intra-tumour diffusion, 15
- ng2, 125
- Packing factor, 16
- Passive targeting, 11
- PEO, 21
- PEO-PDPA, Synthesis, 28
- Perivascular cells, 118
- Perivascular cells functions, Capillary permeability regulation, 119
- Perivascular cells functions, Contractility, 119
- Perivascular cells functions, Vessel stabilisation, 120
- Perivascular cells, Angiogenesis, 121
- PMPC, 22
- PMPC-PDPA, Synthesis, 27
- POEGMA, 21
- Polymersomes, 18
- Polymersomes applications, 19
- Polymersomes functionalisation, Maleimide method, 34
- Polymersomes functionalisation, Biotin/streptavidin method, 33
- Polymersomes synthesis, Film hydration, 29
- Polymersomes synthesis, pH switch, 29
- Polymersomes synthesis, Purification, 30
- Polymersomes, extraction from cells, 43
- Rhd-PMPC-PDPA, Synthesis, 27
- RP-HPLC, 74
- RP-HPLC, Method, 32
- Scavenger receptor SR-B1, 95
- Self-assembly, 16
- Simon, quantitative western blot method, 39
- Spheroid, preparation, 46
- Statistical analysis, 49
- SVECs culture, 35
- SVECs, Tissue culture, 35
- TEM, Method, 31
- Thresholding masking, 51
- Tumour, 1
- Tumour vasculature, 6
- Up-take, method, 41
- Uptake, Static, 77
- VEGF, 5, 103
- VEGF isoforms, 104
- Vessel segmentation, method, 66
- Western Blot, 144
- Western blot, Method, 37

- Abramsson, A., Berlin, Ö., Papayan, H., Paulin, D., Shani, M., and Betsholtz, C. (2002). Analysis of mural cell recruitment to tumor vessels. *Circulation*, 105(1):112–117.
- Adolfsson, J., Ljungqvist, A., Tornling, G., and Unge, G. (1981). Capillary increase in the skeletal muscle of trained young and adult rats. *The Journal of Physiology*, 310(1):529–532.
- Ahmed, F., Pakunlu, R. I., Srinivas, G., Brannan, A., Bates, F., Klein, M. L., Minko, T., and Discher, D. E. (2006). Shrinkage of a rapidly growing tumor by drug-loaded polymersomes: pH-triggered release through copolymer degradation. *Molecular pharmaceutics*, 3(3):340–350.
- Akerman, S., Fisher, M., Daniel, R. A., Lefley, D., Reyes-Aldasoro, C. C., Lunt, S. J., Harris, S., Bjorndahl, M., Williams, L. J., Evans, H., Barber, P. R., Prise, V. E., Vojnovic, B., Kanthou, C., and Tozer, G. M. (2013). Influence of soluble or matrix-bound isoforms of vascular endothelial growth factor-A on tumor response to vascular-targeted strategies. *International Journal of Cancer*, 133(11):2563–2576.
- Alexis, F., Pridgen, E., Molnar, L. K., and Farokhzad, O. C. (2008). Factors affecting the clearance and biodistribution of polymeric nanoparticles. *Molecular Pharmaceutics*, 5(4):505–515.
- Algire, G. (1943). An adaptation of the transparent-chamber technique to the mouse. *Journal of the National Cancer Institute*, 4(1):1–11.
- Antonelli-Orlidge, A., Saunders, K., Smith, S., and D’Amore, P. (1989). An activated form of transforming growth factor- $\beta$  is produced by cocultures of endothelial cells and pericytes. *Proceedings of the National Academy of Sciences USA*, 86(12):4544–4548.

- Armulik, A., Abramsson, A., and Betsholtz, C. (2005). Endothelial/pericyte interactions. *Circulation Research*, 97(6):512–523.
- Armulik, A., Genové, G., and Betsholtz, C. (2011). Pericytes: developmental, physiological, and pathological perspectives, problems, and promises. *Developmental Cell*, 21(2):193–215.
- Bagley, R., Weber, W., Rouleau, C., and Teicher, B. (2005). Pericytes and endothelial precursor cells: cellular interactions and contributions to malignancy. *Cancer Research*, 65(21):9741–9750.
- Baluk, P., Morikawa, S., Haskell, A., Mancuso, M., and McDonald, D. (2003). Abnormalities of basement membrane on blood vessels and endothelial sprouts in tumors. *American Journal of Pathology*, 163(5):1801–1815.
- Batchelor, T., Sorensen, A., di Tomaso, E., Zhang, W., Duda, D., Cohen, K., Kozak, K., Cahill, D., Chen, P., Zhu, M., Ancukiewicz, M., Mrugala, M., Plotkin, S., Drappatz, J., Louis, D., Ivy, P., Scadden, D., Benner, T., Loeffler, J., Wen, P., and Jain, R. (2007). AZD2171, a pan-VEGF receptor tyrosine kinase inhibitor, normalizes tumor vasculature and alleviates edema in glioblastoma patients. *Cancer Cell*, 11(1):83–95.
- Bates, F. and Fredrickson, G. (1990). Block copolymer thermodynamics: theory and experiment. *Annual Review of Physical Chemistry*, 41(1):525–557.
- Battaglia, G., LoPresti, C., Massignani, M., Warren, N., Madsen, J., Forster, S., Vasilev, C., Hobbs, J., Armes, S., Chirasatitsin, S., and Engler, A. (2011). Wet nanoscale imaging and testing of polymersomes. *Small*, 7(14):2010–2015.
- Battegay, E., Raines, E., Seifert, R., Bowen-Pope, D., and Ross, R. (1990). Tgf- $\beta$  induces bimodal proliferation of connective tissue cells via complex control of an autocrine PDGF loop. *Cell*, 63(3):515–524.
- Beckman, J. D., Grazul-Bilska, A. T., Johnson, M. L., Reynolds, L. P., and Redmel, D. A. (2006). Isolation and characterization of ovine luteal pericytes and effects of nitric oxide on pericyte expression of angiogenic factors. *Endocrine*, 29(3):467–476.
- Beerling, E., Ritsma, L., Vrisekoop, N., Derksen, P., and van Rheenen, J. (2011). Intravital microscopy: new insights into metastasis of tumors. *Journal of Cell Science*, 124(Pt 3):299–310.

- Bellou, S., Pentheroudakis, G., Murphy, C., and Fotsis, T. (2013). Anti-angiogenesis in cancer therapy: Hercules and hydra. *Cancer Letters*, 338(2):219–228.
- Benjamin, L., Hemo, I., and Keshet, E. (1998). A plasticity window for blood vessel remodelling is defined by pericyte coverage of the preformed endothelial network and is regulated by PDGF-B and VEGF. *Development*, 125(9):1591–1598.
- Berger, M., Bergers, G., Arnold, B., Hämmerling, G., and Ganss, R. (2005). Regulator of G-protein signaling-5 induction in pericytes coincides with active vessel remodeling during neovascularization. *Blood*, 105(3):1094–1101.
- Bergers, G. and Song, S. (2005). The role of pericytes in blood-vessel formation and maintenance. *Neuro-oncology*, 7(4):452–464.
- Bergers, G., Song, S., Meyer-Morse, N., Bergsland, E., and Hanahan, D. (2003). Benefits of targeting both pericytes and endothelial cells in the tumor vasculature with kinase inhibitors. *Journal of Clinical Investigation*, 111(9):1287–1295.
- Betsholtz, C. (2004). Insight into the physiological functions of pdgf through genetic studies in mice. *Cytokine & growth factor reviews*, 15(4):215–228.
- Bjarnegard, M., Enge, M., Norlin, J., Gustafsdottir, S., Fredriksson, S., Abramson, A., Takemoto, M., Gustafsson, E., Fässler, R., and Betsholtz, C. (2004). Endothelium-specific ablation of PDGFB leads to pericyte loss and glomerular, cardiac and placental abnormalities. *Development*, 131(8):1847–1857.
- Brannon-Peppas, L. and Blanchette, J. (2012). Nanoparticle and targeted systems for cancer therapy. *Advanced Drug Delivery Reviews*.
- Bremnes, R., Dønnem, T., Al-Saad, S., Al-Shibli, K., Andersen, S., Sirera, R., Camps, C., Marinez, I., and Busund, L. (2011). The role of tumor stroma in cancer progression and prognosis: emphasis on carcinoma-associated fibroblasts and non-small cell lung cancer. *Journal of Thoracic Oncology*, 6(1):209–217.
- Brewer, C. and Riehm, J. (1967). Evidence for possible nonspecific reactions between N-ethylmaleimide and proteins. *Analytical Biochemistry*, 18:248–255.
- Brindle, K. (2008). New approaches for imaging tumour responses to treatment. *Nature Reviews. Cancer*, 8(2):94–107.
- Brown, E., Campbell, R., Tsuzuki, Y., Xu, L., Carmeliet, P., Fukumura, D., and Jain, R. (2001). In vivo measurement of gene expression, angiogenesis and

- physiological function in tumors using multiphoton laser scanning microscopy. *Nature Medicine*, 7(7):864–868.
- Brož, P., Benito, S., Saw, C., Burger, P., Heider, H., Pfisterer, M., Marsch, S., Meier, W., and Hunziker, P. (2005). Cell targeting by a generic receptor-targeted polymer nanocontainer platform. *Journal of Controlled Release*, 102(2):475–488.
- Brunelli, S., Tagliafico, E., Angelis, F. G. D., Tonlorenzi, R., Baesso, S., Ferrari, S., Niinobe, M., Yoshikawa, K., Schwartz, R. J., Bozzoni, I., Ferrari, S., and Cossu, G. (2004). Msx2 and necdin combined activities are required for smooth muscle differentiation in mesoangioblast stem cells. *Circ Res*, 94(12):1571–1578.
- Bryan, B. and D’Amore, P. (2008). Pericyte isolation and use in endothelial/pericyte coculture models. *Methods in Enzymology*, 443:315–331.
- Cai, J., Jiang, W., Ahmed, A., and Boulton, M. (2006). Vascular endothelial growth factor-induced endothelial cell proliferation is regulated by interaction between VEGFR-2, SH-PTP1 and eNOS. *Microvasculature Research*, 71(1):20–31.
- Canton, I. and Battaglia, G. (2012). Endocytosis at the nanoscale. *Chemical Society Reviews*, 41(7):2718–2739.
- Canton, I. and Battaglia, G. (2013). Polymersomes-mediated delivery of fluorescent probes for targeted and long-term imaging in live cell microscopy. In *Cellular and Subcellular Nanotechnology*, pages 343–351. Springer.
- Canton, I., Massignani, M., Patikarnmonthon, N., Chierico, L., Robertson, J., Renshaw, S., Warren, N., Madsen, J., Armes, S., and Lewis, A. (2013). Fully synthetic polymer vesicles for intracellular delivery of antibodies in live cells. *The FASEB Journal*, 27(1):98–108.
- Carr, D. (2002). The handbook of analysis and purification of peptides and proteins by reversed-phase hplc. *Hesperia, CA, USA: Grace Vydac*.
- Carrow, R., Brown, R., and Van Huss, W. (1967). Fiber sizes and capillary to fiber ratios in skeletal muscle of exercised rats. *The Anatomical Record*, 159(1):33–39.
- Cha, S., Lu, S., Johnson, G., and Knopp, E. (2000). Dynamic susceptibility contrast mr imaging: correlation of signal intensity changes with cerebral blood volume measurements. *Journal of Magnetic Resonance Imaging*, 11(2):114–119.

- Chambers, A., MacDonald, I., Schmidt, E., Koop, S., Morris, V. L., Khokha, R., and Groom, A. (1995). Steps in tumor metastasis: new concepts from intravital videomicroscopy. *Cancer and Metastasis Reviews*, 14(4):279–301.
- Chaudhuri, A., Battaglia, G., and Golestanian, R. (2011). The effect of interactions on the cellular uptake of nanoparticles. *Physical Biology*, 8(4):046002.
- Cheng, Z., Thorek, D., and Tsourkas, A. (2009). Porous polymersomes with encapsulated Gd-labeled dendrimers as highly efficient MRI contrast agents. *Advanced Functional Materials*, 19(23):3753–3759.
- Chou, C., Huang, C., Lu, K.W. and Horng, T., and Lin, W. (2013). Investigation of the spatiotemporal responses of nanoparticles in tumor tissues with a small-scale mathematical model. *PloS One*, 8(4):e59135.
- Christian, D. A., Cai, S., Garbuzenko, O. B., Harada, T., Zajac, A. L., Minko, T., and Discher, D. E. (2009a). Flexible filaments for in vivo imaging and delivery: persistent circulation of filomicelles opens the dosage window for sustained tumor shrinkage. *Molecular Pharmaceutics*, 6(5):1343–1352.
- Christian, N., Benencia, F., Milone, M., Li, G., Frail, P., Therien, M., Coukos, G., and Hammer, D. (2009b). In vivo dendritic cell tracking using fluorescence lifetime imaging and near-infrared-emissive polymersomes. *Molecular Imaging and Biology*, 11(3):167–177.
- Coggan, A., Spina, R., King, D., Rogers, M., Brown, M., Nemeth, P., and Holloszy, J. (1992). Skeletal muscle adaptations to endurance training in 60-to 70-yr-old men and women. *Journal of Applied Physiology*, 72(5):1780–1786.
- Coisne, C., Lyck, R., Engelhardt, B., et al. (2013). Live cell imaging techniques to study T cell trafficking across the blood-brain barrier in vitro and in vivo. *Fluids and Barriers of the CNS*, 10(1):7.
- Colley, H. E., Hearnden, V., Avila-Olias, M., Cecchin, D., Canton, I., Madsen, J., Macneil, S., Warren, N., Hu, K., McKeating, J. A., Armes, S. P., Murdoch, C., Thornhill, M. H., and Battaglia, G. (2014). Polymersome-mediated delivery of combination anti-cancer therapy to head and neck cancer cells: 2D and 3D in vitro evaluation. *Molecular Pharmaceutics*.
- Creazzo, T. L., Godt, R. E., Leatherbury, L., Conway, S. J., and Kirby, M. L. (1998). Role of cardiac neural crest cells in cardiovascular development. *Annual Review of Physiology*, 60:267–286.

- Crisan, M., Chen, C.-W., Corselli, M., Andriolo, G., Lazzari, L., and Péault, B. (2009). Perivascular multipotent progenitor cells in human organs. *Annual New York Academy of Science*, 1176:118–123.
- Crisan, M., Yap, S., Casteilla, L., Chen, C.-W., Corselli, M., Park, T. S., Andriolo, G., Sun, B., Zheng, B., Zhang, L., Norotte, C., Teng, P.-N., Traas, J., Schugar, R., Deasy, B. M., Badylak, S., Buhring, H.-J., Jacobino, J.-P., Lazzari, L., Huard, J., and Péault, B. (2008). A perivascular origin for mesenchymal stem cells in multiple human organs. *Cell Stem Cell*, 3(3):301–313.
- Darland, D. and D'Amore, P. (2001). TGF- $\beta$ 1 is required for the formation of capillary-like structures in three-dimensional cocultures of 10T1/2 and endothelial cells. *Angiogenesis*, 4(1):11–20.
- Díaz-Flores, L., Gutiérrez, R., Madrid, J. F., Varela, H., Valladares, F., Acosta, E., Martín-Vasallo, P., and Díaz-Flores, Jr, L. (2009). Pericytes. morphofunction, interactions and pathology in a quiescent and activated mesenchymal cell niche. *Histology & Histopathology*, 24(7):909–969.
- Decuzzi, P. and Ferrari, M. (2006). The adhesive strength of non-spherical particles mediated by specific interactions. *Biomaterials*, 27(30):5307–5314.
- Dellian, M., Yuan, F., Trubetskoy, V., Torchilin, V., and Jain, R. (2000). Vascular permeability in a human tumour xenograft: molecular charge dependence. *British Journal of Cancer*, 82(9):1513.
- Denk, W., Strickler, J. H., and Webb, W. W. (1990). Two-photon laser scanning fluorescence microscopy. *Science*, 248(4951):73–76.
- Denk, W. and Webb, W. W. (1990). Optical measurement of picometer displacements of transparent microscopic objects. *Applied Optics*, 29(16):2382–2391.
- Diaz-Flores, L., Gutierrez, R., and Varela, H. (1992). Behavior of postcapillary venule pericytes during postnatal angiogenesis. *Journal of Morphology*, 213(1):33–45.
- Dickson, M. C., Martin, J. S., Cousins, F. M., Kulkarni, A. B., Karlsson, S., and Akhurst, R. J. (1995). Defective haematopoiesis and vasculogenesis in transforming growth factor- $\beta$ 1 knock out mice. *Development*, 121(6):1845–1854.
- Discher, D. E. and Ahmed, F. (2006). Polymersomes. *Annual Review Biomedical Engineering*, 8:323–341.

- Discher, D. E., Pajerowski, J. D., and Kim, Y. (2008). Polymersome delivery of siRNA and antisense oligonucleotides. In *The 2008 Annual Meeting*.
- Dittrich, W. M. and Gohde, W. H. (1973). Flow-through chamber for photometers to measure and count particles in a dispersion medium. US Patent 3,761,187.
- Dore-Duffy, P. (2003). Isolation and characterization of cerebral microvascular pericytes. In *The Blood-Brain Barrier*, pages 375–382. Springer.
- Dreher, M. R., Liu, W., Michelich, C. R., Dewhirst, M. W., Yuan, F., and Chilkoti, A. (2006). Tumor vascular permeability, accumulation, and penetration of macromolecular drug carriers. *Journal of the National Cancer Institute*, 98(5):335–344.
- Du, J., Tang, Y., Lewis, A. L., and Armes, S. P. (2005). pH-sensitive vesicles based on a biocompatible zwitterionic diblock copolymer. *Journal of the American Chemical Society*, 127(51):17982–17983.
- Dudley, A. C. (2012). Tumor endothelial cells. *Cold Spring Harbor Perspectives in Medicine*, 2(3).
- Dumont, K., Yperman, J., Verbeken, E., Segers, P., Meuris, B., Vandenberghe, S., Flameng, W., and Verdonck, P. R. (2002). Design of a new pulsatile bioreactor for tissue engineered aortic heart valve formation. *Artificial Organs*, 26(8):710–714.
- Duncan, R., Ringsdorf, H., and Satchi-Fainaro, R. (2006). Polymer therapeutics-polymers as drugs, drug and protein conjugates and gene delivery systems: Past, present and future opportunities. *Journal of Drug Targeting*, 14(6):337–341.
- Dvorak, H. (1986). Tumors: wounds that do not heal. similarities between tumor stroma generation and wound healing. *New England Journal of Medicine*, 325, Issue 26:1650–1659.
- Ebos, J. M. L., Lee, C. R., Cruz-Munoz, W., Bjarnason, G. A., Christensen, J. G., and Kerbel, R. S. (2009). Accelerated metastasis after short-term treatment with a potent inhibitor of tumor angiogenesis. *Cancer Cell*, 15(3):232–239.
- Edelman, D. A., Jiang, Y., Tyburski, J., Wilson, R. F., and Steffes, C. (2006a). Pericytes and their role in microvasculature homeostasis. *Journal of Surgical Research*, 135(2):305–311.

- Edelman, D. A., Jiang, Y., Tyburski, J., Wilson, R. F., and Steffes, C. (2006b). Toll-like receptor-4 message is up-regulated in lipopolysaccharide-exposed rat lung pericytes. *Journal of Surgical Research*, 134(1):22–27.
- Ema, M., Faloon, P., Zhang, W. J., Hirashima, M., Reid, T., Stanford, W. L., Orkin, S., Choi, K., and Rossant, J. (2003). Combinatorial effects of *flk1* and *tall1* on vascular and hematopoietic development in the mouse. *Genes Development*, 17(3):380–393.
- Endrich, B., Intaglietta, M., Reinhold, H. S., and Gross, J. F. (1979). Hemodynamic characteristics in microcirculatory blood channels during early tumor growth. *Cancer Research*, 39(1):17–23.
- Erber, R., Thurnher, A., Katsen, A. D., Groth, G., Kerger, H., Hammes, H.-P., Menger, M. D., Ullrich, A., and Vajkoczy, P. (2004). Combined inhibition of VEGF and PDGF signaling enforces tumor vessel regression by interfering with pericyte-mediated endothelial cell survival mechanisms. *The FASEB Journal*, 18(2):338–340.
- Fagiani, E. and Christofori, G. (2013). Angiopoietins in angiogenesis. *Cancer Letters*, 328(1):18–26.
- Felnerova, D., Viret, J.-F., Glück, R., and Moser, C. (2004). Liposomes and virosomes as delivery systems for antigens, nucleic acids and drugs. *Current Opinion in Biotechnology*, 15(6):518–529.
- Ferrara, N. (2004). Vascular endothelial growth factor: basic science and clinical progress. *Endocrine Reviews*, 25(4):581–611.
- Folkman, J. (1971). Tumor angiogenesis: therapeutic implications. *New England Journal of Medicine*, 285(21):1182–1186.
- Folkman, J. and Kalluri, R. (2004). Cancer without disease. *Nature*, 427(6977):787.
- Folkman, J., Watson, K., Ingber, D., and Hanahan, D. (1989). Induction of angiogenesis during the transition from hyperplasia to neoplasia. *Nature*, 339(6219):58–61.
- Fong, G. H., Rossant, J., Gertsenstein, M., and Breitman, M. L. (1995). Role of the Flt-1 receptor tyrosine kinase in regulating the assembly of vascular endothelium. *Nature*, 376(6535):66–70.
- Fredrickson, G. H. and Bates, F. S. (1996). Dynamics of block copolymers: Theory and experiment. *Annual Review of Materials Science*, 26(1):501–550.

- Frieboes, H. B., Wu, M., Lowengrub, J., Decuzzi, P., and Cristini, V. (2013). A computational model for predicting nanoparticle accumulation in tumor vasculature. *PLoS One*, 8(2):e56876.
- Fukumura, D., Xavier, R., Sugiura, T., Chen, Y., Park, E.-C., Lu, N., Selig, M., Nielsen, G., Taksir, T., Jain, R. K., et al. (1998). Tumor induction of VEGF promoter activity in stromal cells. *Cell*, 94(6):715–725.
- Fulton, G. P., Jackson, R. G., and Lutz, B. R. (1947). Cinephotomicroscopy of normal blood circulation in the cheek pouch of the hamster. *Science*, 105(2727):361–362.
- Fuyuhiko, Y., Yashiro, M., Noda, S., Kashiwagi, S., Matsuoka, J., Doi, Y., Kato, Y., Hasegawa, T., Sawada, T., and Hirakawa, K. (2011). Upregulation of cancer-associated myofibroblasts by TGF- $\beta$  from scirrhous gastric carcinoma cells. *British Journal of Cancer*, 105(7):996–1001.
- Gale, N. W., Thurston, G., Hackett, S. F., Renard, R., Wang, Q., McClain, J., Martin, C., Witte, C., Witte, M. H., Jackson, D., Suri, C., Campochiaro, P. A., Wiegand, S. J., and Yancopoulos, G. D. (2002). Angiopoietin-2 is required for postnatal angiogenesis and lymphatic patterning, and only the latter role is rescued by angiopoietin-1. *Development Cell*, 3(3):411–423.
- Gaustad, J.-V., Brurberg, K. G., Simonsen, T. G., Mollatt, C. S., and Rofstad, E. K. (2008). Tumor vascularity assessed by magnetic resonance imaging and intravital microscopy imaging. *Neoplasia*, 10(4):354–362.
- Gedde, U. (1996). *Polymer Physics*. Chapman & Hall, London.
- Geng, Y., Dalhaimer, P., Cai, S., Tsai, R., Tewari, M., Minko, T., and Disher, D. (2007). Shape effects of filaments versus spherical particles in flow and drug delivery. *Nature Nanotechnology*, 2:249–255.
- Gerber, F., Krummen, M., Potgeter, H., Roth, A., Siffrin, C., and Spoendlin, C. (2004). Practical aspects of fast reversed-phase high-performance liquid chromatography using 3 $\mu$ m particle packed columns and monolithic columns in pharmaceutical development and production working under current good manufacturing practice. *Journal of Chromatography A*, 1036(2):127–133.
- Ghoroghchian, P. P., Frail, P. R., Susumu, K., Blessington, D., Brannan, A. K., Bates, F. S., Chance, B., Hammer, D. A., and Therien, M. J. (2005). Near-infrared-emissive polymersomes: Self-assembled soft matter for in vivo optical imaging. *Proceedings of the National Academy of Sciences U.S.A.*, 102(8):2922–2927.

- Gielen, S., Schuler, G., and Adams, V. (2010). Cardiovascular effects of exercise training: molecular mechanisms. *Circulation*, 122(12):1221–1238.
- Greco, O. and Coralli, C. and Dachs, G. (2005). Role of VEGF in tumour response to vascular disrupting agents. *Microcirculation*, 12:681.
- Grinstaff, M. W., Soon-Shiong, P., Wong, M., Sandford, P. A., Suslick, K. S., and Desai, N. P. (1997). Methods for the preparation of nucleic acids for in vivo delivery. US Patent 5,639,473.
- Grothey, A., A., Sugrue, M. M., Purdie, D. M., Dong, W., Sargent, D., Hedrick, E., and Kozloff, M. (2008). Bevacizumab beyond first progression is associated with prolonged overall survival in metastatic colorectal cancer: results from a large observational cohort study. *Journal of Clinical Oncology*, 26(33):5326–5334.
- Hainsworth, J. D., Spigel, D. R., Sosman, J. A., Burris, 3rd, H. A., Farley, C., Cucullu, H., Yost, K., Hart, L. L., Sylvester, L., Waterhouse, D. M., and Greco, F. A. (2007). Treatment of advanced renal cell carcinoma with the combination bevacizumab/erlotinib/imatinib: a phase i/ii trial. *Clinical Genitourinary Cancer*, 5(7):427–432.
- Hammer, D. A., Robbins, G. P., Haun, J. B., Lin, J. J., Qi, W., Smith, L. A., Ghoroghchian, P. P., Therien, M. J., and Bates, F. S. (2008). Leukopolymersomes. *Faraday Discussions*, 139:129–141.
- Harris, A. L. (2002). Hypoxia: a key regulatory factor in tumour growth. *Nature Reviews Cancer*, 2(1):38–47.
- Harris, L. J., Larson, S. B., Hasel, K. W., and McPherson, A. (1997). Refined structure of an intact IgG2a monoclonal antibody. *Biochemistry*, 36(7):1581–1597.
- Hayden, M. R., Karuparthi, P. R., Habibi, J., Wasekar, C., Lastra, G., Manrique, C., Stas, S., and Sowers, J. R. (2007). Ultrastructural islet study of early fibrosis in the Ren2 rat model of hypertension. emerging role of the islet pancreatic pericyte-stellate cell. *Journal of the Pancreas*, 8(6):725–738.
- Hell, S. W. and Wichmann, J. (1994). Breaking the diffraction resolution limit by stimulated emission: stimulated-emission-depletion fluorescence microscopy. *Optics Letters*, 19(11):780–782.

- Hellstroem, M., Gerhardt, H., Kalén, M., Li, X., Eriksson, U., Wolburg, H., and Betsholtz, C. (2001). Lack of pericytes leads to endothelial hyperplasia and abnormal vascular morphogenesis. *Journal of Cell Biology*, 153(3):543–553.
- Hellstroem, M., Kalen, M., Lindahl, P., Abramsson, A., and Betsholtz, C. (1999). Role of PDGF-B and PDGFR- $\beta$  in recruitment of vascular smooth muscle cells and pericytes during embryonic blood vessel formation in the mouse. *Development*, 126(14):3047–3055.
- Helmlinger, G., Yuan, F., Dellian, M., and Jain, R. K. (1997). Interstitial pH and pO<sub>2</sub> gradients in solid tumors in vivo: high-resolution measurements reveal a lack of correlation. *Nature Medicine*, 3(2):177–182.
- Hida, K., Hida, Y., Amin, D., Flint, A., Panigrahy, D., Morton, C., and Klagsbrun, M. (2004). Tumor-associated endothelial cells with cytogenetic abnormalities. *Cancer Research*, 64(22):8249–8255.
- Hinz, B., Celetta, G., Tomasek, J. J., Gabbiani, G., and Chaponnier, C. (2001).  $\alpha$ -smooth muscle actin expression upregulates fibroblast contractile activity. *Molecular Biology of the Cell*, 12(9):2730–2741.
- Hirschi, K. K., Burt, J. M., Hirschi, K. D., and Dai, C. (2003). Gap junction communication mediates transforming growth factor- $\beta$  activation and endothelial-induced mural cell differentiation. *Circulation Research*, 93(5):429–437.
- Hirschi, K. K. and D’Amore, P. A. (1996). Pericytes in the microvasculature. *Cardiovascular Research*, 32(4):687–698.
- Hirschi, K. K., Rohovsky, S. A., Beck, L. H., Smith, S. R., and D’Amore, P. A. (1999). Endothelial cells modulate the proliferation of mural cell precursors via platelet-derived growth factor-BB and heterotypic cell contact. *Circulation Research*, 84(3):298–305.
- Hirschi, K. K., Rohovsky, S. A., and D’Amore, P. A. (1997). Cell-cell interactions in vessel assembly: a model for the fundamentals of vascular remodelling. *Transplantation Immunology*, 5(3):177–178.
- Hirschi, K. K., Rohovsky, S. A., and D’Amore, P. A. (1998). PDGF, TGF- $\beta$ , and heterotypic cell-cell interactions mediate endothelial cell-induced recruitment of 10T1/2 cells and their differentiation to a smooth muscle fate. *Journal of Cell Biology*, 141(3):805–814.
- Hobbs, S. K., Monsky, W. L., Yuan, F., Roberts, W. G., Griffith, L., Torchilin, V. P., and Jain, R. K. (1998). Regulation of transport pathways in tumor

- vessels: role of tumor type and microenvironment. *Proceedings of the National Academy of Sciences U.S.A.*, 95(8):4607–4612.
- Hoffmann, J., Feng, Y., vom Hagen, F., Hillenbrand, A., Lin, J., Erber, R., Vajkoczy, P., Gourzoulidou, E., Waldmann, H., Giannis, A., Wolburg, H., Shani, M., Jaeger, V., Weich, H. A., Preissner, K. T., Hoffmann, S., Deutsch, U., and Hammes, H.-P. (2005). Endothelial survival factors and spatial completion, but not pericyte coverage of retinal capillaries determine vessel plasticity. *The FASEB Journal*, 19(14):2035–2036.
- Horton, N. G., Wang, K., Kobat, D., Clark, C. G., Wise, F. W., Schaffer, C. B., and Xu, C. (2013). In vivo three-photon microscopy of subcortical structures within an intact mouse brain. *Nature Photonics*, 7(3):205–209.
- Horvath, C. G., Preiss, B., and Lipsky, S. R. (1967). Fast liquid chromatography. investigation of operating parameters and the separation of nucleotides on pellicular ion exchangers. *Analytical chemistry*, 39(12):1422–1428.
- Howard, S. S., Straub, A., Horton, N., Kobat, D., and Xu, C. (2013). Frequency multiplexed in vivo multiphoton phosphorescence lifetime microscopy. *Nature Photonics*, 7(1):33–37.
- Hurwitz, H., Fehrenbacher, L., Novotny, W., Cartwright, T., Hainsworth, J., Heim, W., Berlin, J., Baron, A., Griffing, S., Holmgren, E., Ferrara, N., Fyfe, G., Rogers, B., Ross, R., and Kabbinavar, F. (2004). Bevacizumab plus irinotecan, fluorouracil, and leucovorin for metastatic colorectal cancer. *The New England Journal of Medicine*, 350:2335–2342.
- Ichioka, S., Shibata, M., Kosaki, K., Sato, Y., Harii, K., and Kamiya, A. (1997). Effects of shear stress on wound-healing angiogenesis in the rabbit ear chamber. *Journal of Surgical Research*, 72(1):29–35.
- Jain, R. (2001). Delivery of molecular medicine to solid tumors: lessons from in vivo imaging of gene expression and function. *Journal of Controlled Release*, 74(1):7–25.
- Jain, R. K. (1988). Determinants of tumor blood flow: a review. *Cancer Research*, 48(10):2641–2658.
- Jain, R. K. (2003). Molecular regulation of vessel maturation. *Nature Medicine*, 9(6):685–693.
- Jain, R. K., Munn, L. L., and Fukumura, D. (2002). Dissecting tumour pathophysiology using intravital microscopy. *Nature Reviews Cancer*, 2(4):266–276.

- Kataoka, K., Ishii, T., Osada, K., Chen, Q., Itaka, K., and Uchida, S. (2013). Nucleic acid delivery composition and carrier composition, pharmaceutical composition using the same, and method for delivering nucleic acid. US Patent 20,130,109,743.
- Khan, O. F. and Sefton, M. V. (2011). Endothelial cell behaviour within a microfluidic mimic of the flow channels of a modular tissue engineered construct. *Biomed Microdevices*, 13(1):69–87.
- Kim, J. and Ma, T. (2012). Perfusion regulation of hMSC microenvironment and osteogenic differentiation in 3D scaffold. *Biotechnology & Bioengineering*, 109(1):252–261.
- Kim, Y., Tewari, M., Pajeroski, J. D., Cai, S., Sen, S., Williams, J., Sirsi, S., Lutz, G., and Discher, D. E. (2009). Polymersome delivery of sirna and antisense oligonucleotides. *Journal of Controlled Release*, 134(2):132–140.
- Kiziltepe, T., Ashley, J., Stefanick, J., Qi, Y., Alves, N., Handlogten, M., Suckow, M., Navari, R., and Bilgicer, B. (2012). Rationally engineered nanoparticles target multiple myeloma cells, overcome cell-adhesion-mediated drug resistance, and show enhanced efficacy in vivo. *Blood cancer journal*, 2(4):e64.
- Koehl, G. E., Gaumann, A., and Geissler, E. K. (2009). Intravital microscopy of tumor angiogenesis and regression in the dorsal skin fold chamber: mechanistic insights and preclinical testing of therapeutic strategies. *Clinical & Experimental Metastasis*, 26(4):329–344.
- Kratz, F., Müller, I. A., Ryppa, C., and Warnecke, A. (2008). Prodrug strategies in anticancer chemotherapy. *Chemmedchem*, 3(1):20–53.
- Krishnan, A. S., Neves, A. A., de Backer, M. M., Hu, D.-E., Davletov, B., Kettunen, M. I., and Brindle, K. M. (2008). Detection of cell death in tumors by using MR imaging and a gadolinium-based targeted contrast agent. *Radiology*, 246(3):854–862.
- Kuhnert, F., Tam, B. Y., Sennino, B., Gray, J. T., Yuan, J., Jocson, A., Nayak, N. R., Mulligan, R. C., McDonald, D. M., and Kuo, C. J. (2008). Soluble receptor-mediated selective inhibition of VEGFR and PDGFR $\beta$  signaling during physiologic and tumor angiogenesis. *Proceedings of the National Academy of Sciences U.S.A.*, 105(29):10185–10190.
- Kutcher, M. E., Kolyada, A. Y., Surks, H. K., and Herman, I. M. (2007). Pericyte Rho GTPase mediates both pericyte contractile phenotype and capillary endothelial growth state. *American Journal of Pathology*, 171(2):693–701.

- Larsson, J., Goumans, M. J., Sjöstrand, L. J., van Rooijen, M. A., Ward, D., Levéen, P., Xu, X., ten Dijke, P., Mummery, C. L., and Karlsson, S. (2001). Abnormal angiogenesis but intact hematopoietic potential in TGF- $\beta$  type 1 receptor-deficient mice. *The EMBO Journal*, 20(7):1663–1673.
- Laschke, M. W., Vollmar, B., and Menger, M. D. (2011). The dorsal skinfold chamber: window into the dynamic interaction of biomaterials with their surrounding host tissue. *European Cell & Materials*, 22:147–64; discussion 164–7.
- Law, M., Yang, S., Babb, J. S., Knopp, E. A., Golfinos, J. G., Zagzag, D., and Johnson, G. (2004). Comparison of cerebral blood volume and vascular permeability from dynamic susceptibility contrast-enhanced perfusion MR imaging with glioma grade. *American Journal of Neuroradiology*, 25(5):746–755.
- Lee, B. S., Yoon, O. J., Cho, W. K., Lee, N.-E., Yoon, K. R., and Choi, I. S. (2009). Construction of protein-resistant pOEGMA films by helicon plasma-enhanced chemical vapor deposition. *Journal of Biomaterial Science Polymer Edition*, 20(11):1579–1586.
- Lee, J. S. and Tung, C.-H. (2011). Enhanced cellular uptake and metabolic stability of lipo-oligoarginine peptides. *Peptide Science*, 96(6):772–779.
- Lehr, H.-A., Leunig, M., Menger, M. D., Nolte, D., and Messmer, K. (1993). Dorsal skinfold chamber technique for intravital microscopy in nude mice. *The American Journal of Pathology*, 143(4):1055.
- Leong, C. M., Voorhees, A., Nackman, G. B., and Wei, T. (2013). Flow bioreactor design for quantitative measurements over endothelial cells using micro-particle image velocimetry. *Review Scientific Instrumentation*, 84(4):045109.
- Leung, D. W., Cachianes, G., Kuang, W.-J., Goeddel, D. V., and Ferrara, N. (1989). Vascular endothelial growth factor is a secreted angiogenic mitogen. *Science*, 246(4935):1306–1309.
- Levéen, P., Pekny, M., Gebre-Medhin, S., Swolin, B., Larsson, E., and Betsholtz, C. (1994). Mice deficient for PDGF-B show renal, cardiovascular, and hematological abnormalities. *Genesis & Development*, 8(16):1875–1887.
- Li, W. and Szoka Jr, F. C. (2007). Lipid-based nanoparticles for nucleic acid delivery. *Pharmaceutical Research*, 24(3):438–449.
- Liby, T. A., Spyropoulos, P., Buff Lindner, H., Eldridge, J., Beeson, C., Hsu, T., and Muise-Helmericks, R. C. (2012). Akt3 controls vascular endothelial growth

- factor secretion and angiogenesis in ovarian cancer cells. *International Journal of Cancer*, 130(3):532–543.
- Lien, S.-C., Usami, S., Chien, S., and Chiu, J.-J. (2006). Phosphatidylinositol 3-kinase/Akt pathway is involved in transforming growth factor- $\beta$ 1-induced phenotypic modulation of 10T1/2 cells to smooth muscle cells. *Cellular Signalling*, 18(8):1270–1278.
- Lin, Y., Salek, M. F., Jennings, N., and Gmitro, A. F. (2008). An optical imaging system for window chambers in MRI system. In *Biomedical Optics (BiOS) 2008*, pages 684907–684907. International Society for Optics and Photonics.
- Lindner, J. R. (2004). Microbubbles in medical imaging: current applications and future directions. *Nature Reviews Drug Discovery*, 3(6):527–533.
- Lomas, H., Du, J., Canton, I., Madsen, J., Warren, N., Armes, S. P., Lewis, A. L., and Battaglia, G. (2010). Efficient encapsulation of plasmid DNA in pH-sensitive PMPC-PDPA polymersomes: study of the effect of PDPA block length on copolymer-DNA binding affinity. *Macromolecules Biosciences*, 10(5):513–530.
- LoPresti, C., Lomas, H., Massignani, M., Smart, T., and Battaglia, G. (2009). Polymersomes: nature inspired nanometer sized compartments. *Journal of Materials Chemistry*, 19(22):3576–3590.
- LoPresti, C., Massignani, M., Fernyhough, C., Blanz, A., Ryan, A. J., Madsen, J., Warren, N. J., Armes, S. P., Lewis, A. L., Chirasatitsin, S., et al. (2011). Controlling polymersome surface topology at the nanoscale by membrane confined polymer/polymer phase separation. *American Chemistry Society Nano*, 5(3):1775–1784.
- Lundholt, B. K., Scudder, K. M., and Pagliaro, L. (2003). A simple technique for reducing edge effect in cell-based assays. *Journal of Biomolecular Screening*, 8(5):566–570.
- Lunt, S. J., Gray, C., Reyes-Aldasoro, C. C., Matcher, S. J., and Tozer, G. M. (2010). Application of intravital microscopy in studies of tumor microcirculation. *Journal of Biomedical Optics*, 15(1):011113–011113.
- Ma, J. and Waxman, D. J. (2008). Combination of antiangiogenesis with chemotherapy for more effective cancer treatment. *Molecular Cancer Therapeutics*, 7(12):3670–3684.

- Madsen, J. (2009). *Temperature-responsive Biocompatible Block Copolymers based on 2-(Methacryloyloxy)ethyl Phosphorylcholine*. PhD thesis, University of Sheffield.
- Madsen, J., Canton, I., Warren, N. J., Themistou, E., Blanazs, A., Ustbas, B., Tian, X., Pearson, R., Battaglia, G., Lewis, A. L., et al. (2013). Nile blue-based nano-sized pH sensors for simultaneous far-red and near-infrared live bioimaging. *Journal of the American Chemical Society*.
- Marqués-Gallego, P. and de Kroon, A. I. (2014). Ligation strategies for targeting liposomal nanocarriers. *BioMed Research International*.
- Marr, D. and Hildreth, E. (1980). Theory of edge detection. *Proceedings of the Royal Society of London. Series B, Biological Sciences*, 207(1167):187–217.
- Marsh, T., Pietras, K., and McAllister, S. S. (2013). Fibroblasts as architects of cancer pathogenesis. *Biochimica et Biophysica Acta*, 1832(7):1070–1078.
- Massignani, M., Canton, I., Sun, T., Hearnden, V., MacNeil, S., Blanazs, A., Armes, S. P., Lewis, A., and Battaglia, G. (2010). Enhanced fluorescence imaging of live cells by effective cytosolic delivery of probes. *PLoS One*, 5(5):e10459.
- Massignani, M., LoPresti, C., Blanazs, A., Madsen, J., Armes, S. P., Lewis, A. L., and Battaglia, G. (2009). Controlling cellular uptake by surface chemistry, size, and surface topology at the nanoscale. *Small*, 5(21):2424–2432.
- Matsen, M. and Bates, F. S. (1996a). Unifying weak-and strong-segregation block copolymer theories. *Macromolecules*, 29(4):1091–1098.
- Matsen, M. W. and Bates, F. (1996b). Origins of complex self-assembly in block copolymers. *Macromolecules*, 29(23):7641–7644.
- Matsumura, Y. and Maeda, H. (1986). A new concept for macromolecular therapeutics in cancer chemotherapy: mechanism of tumortropic accumulation of proteins and the antitumor agent smancs. *Cancer Research*, 46(12 Pt 1):6387–6392.
- Mazzei, D., Guzzardi, M., S., G., and A., A. (2010). A low shear stress modular bioreactor for connected cell culture under high flow rates. *Biotechnology and Bioengineering*, 106, 1:127–137.
- McDonald, D. M. and Choyke, P. L. (2003). Imaging of angiogenesis: from microscope to clinic. *Nature medicine*, 9(6):713–725.

- Mehta, J. and Dhalla, N. S. (2013). *Biochemical Basis and Therapeutic Implications of Angiogenesis*. Springer.
- Mehvar, R. (2000). Dextran for targeted and sustained delivery of therapeutic and imaging agents. *Journal of controlled release*, 69(1):1–25.
- Miyakawa, A. A., Dallan, L. A. O., Lacchini, S., Borin, T. F., and Krieger, J. E. (2008). Human saphenous vein organ culture under controlled hemodynamic conditions. *Clinics (Sao Paulo)*, 63(5):683–688.
- Moeller, B. J., Cao, Y., Vujaskovic, Z., Li, C. Y., Haroon, Z. A., and Dewhirst, M. W. (2004). The relationship between hypoxia and angiogenesis. In *Seminars in radiation oncology*, volume 14, pages 215–221. Elsevier.
- Mogensen, C., Bergner, B., Wallner, S., Ritter, A., dAvis, S., Ninichuk, V., Kameritsch, P., Gloe, T., Nagel, W., and Pohl, U. (2011). Isolation and functional characterization of pericytes derived from hamster skeletal muscle. *Acta Physiologica*, 201(4):413–426.
- Moghimi, S. M., Hunter, A. C., and Murray, J. C. (2001). Long-circulating and target-specific nanoparticles: theory to practice. *Pharmacological Reviews*, 53(2):283–318.
- Monti, M., Donnini, S., Morbidelli, L., Giachetti, A., Mochly-Rosen, D., Mignatti, P., and Ziche, M. (2013). PKC- $\epsilon$  activation promotes FGF-2 exocytosis and induces endothelial cell proliferation and sprouting. *Journal of Molecular and Cellular Cardiology*, 63C:107–117.
- Murdoch, C., Reeves, K. J., Hearnden, V., Colley, H., Massignani, M., Canton, I., Madsen, J., Blanazs, A., Armes, S. P., Lewis, A. L., et al. (2010). Internalization and biodistribution of polymersomes into oral squamous cell carcinoma cells in vitro and in vivo. *Nanomedicine*, 5(7):1025–1036.
- Muthiah, M., Lee, S. J., Moon, M., Lee, H. J., Bae, W. K., Chung, I. J., Jeong, Y. Y., and Park, I.-K. (2013). Surface tunable polymersomes loaded with magnetic contrast agent and drug for image guided cancer therapy. *Journal of Nanoscience and Nanotechnology*, 13(3):1626–1630.
- Nagarajan, R. (2002). Molecular packing parameter and surfactant self-assembly: the neglected role of the surfactant tail. *Langmuir*, 18(1):31–38.
- Neeman, M., Dafni, H., Bukhari, O., Braun, R. D., and Dewhirst, M. W. (2001). In vivo BOLD contrast MRI mapping of subcutaneous vascular func-

- tion and maturation: validation by intravital microscopy. *Magnetic Resonance in Medicine*, 45(5):887–898.
- Nehls, V. and Drenckhahn, D. (1991). Heterogeneity of microvascular pericytes for smooth muscle type  $\alpha$ -actin. *The Journal of Cell Biology*, 113(1):147–154.
- Neng, L., Zhang, W., Hassan, A., Zemla, M., Kachelmeier, A., Fridberger, A., Auer, M., and Shi, X. (2013). Isolation and culture of endothelial cells, pericytes and perivascular resident macrophage-like melanocytes from the young mouse ear. *Nature Protocols*, 8(4):709–720.
- Nisancioglu, M. H., Betsholtz, C., and Genové, G. (2010). The absence of pericytes does not increase the sensitivity of tumor vasculature to vascular endothelial growth factor-A blockade. *Cancer Research*, 70(12):5109–5115.
- Øye, K. S., Gulati, G., Graff, B. A., Gaustad, J.-V., Brurberg, K. G., and Rofstad, E. K. (2008). A novel method for mapping the heterogeneity in blood supply to normal and malignant tissues in the mouse dorsal window chamber. *Microvascular Research*, 75(2):179–187.
- Ozawa, M. G., Yao, V. J., Chantry, Y. H., Troncoso, P., Uemura, A., Varner, A. S., Kasman, I. M., Pasqualini, R., Arap, W., and McDonald, D. M. (2005). Angiogenesis with pericyte abnormalities in a transgenic model of prostate carcinoma. *Cancer*, 104(10):2104–2115.
- Ozerdem, U., Alitalo, K., Salven, P., and Li, A. (2005). Contribution of bone marrow-derived pericyte precursor cells to corneal vasculogenesis. *Investigative Ophthalmology and Visual Science*, 46(10):3502–3506.
- Ozerdem, U., Monosov, E., and Stallcup, W. B. (2002). NG2 proteoglycan expression by pericytes in pathological microvasculature. *Microvascular Research*, 63(1):129–134.
- Ozerdem, U. and Stallcup, W. B. (2003). Early contribution of pericytes to angiogenic sprouting and tube formation. *Angiogenesis*, 6(3):241–249.
- Ozerdem, U. and Stallcup, W. B. (2004). Pathological angiogenesis is reduced by targeting pericytes via the NG2 proteoglycan. *Angiogenesis*, 7(3):269–276.
- Pacheco-Torres, J., López-Larrubia, P., Ballesteros, P., and Cerdán, S. (2011). Imaging tumor hypoxia by magnetic resonance methods. *NMR in Biomedicine*, 24(1):1–16.

- Paez-Ribes, M., Allen, E., Hudock, J., Takeda, T., Okuyama, H., Viñals, F., Inoue, M., Bergers, G., Hanahan, D., and Casanovas, O. (2009). Antiangiogenic therapy elicits malignant progression of tumors to increased local invasion and distant metastasis. *Cancer Cell*, 15(3):220–231.
- Park, J. S., Chu, J. S., Tsou, A. D., Diop, R., Tang, Z., Wang, A., and Li, S. (2011). The effect of matrix stiffness on the differentiation of mesenchymal stem cells in response to  $\text{tgf-}\beta$ . *Biomaterials*, 32(16):3921–3930.
- Pasut, G. and Veronese, F. M. (2012). State of the art in PEGylation: the great versatility achieved after forty years of research. *Journal of Controlled Release*, 161(2):461–472.
- Pawley, J. (2006). *Handbook of biological confocal microscopy*. Springer.
- Pegoraro, C., Madsen, J., Macneil, S., Warren, N., Armes, S. P., Battaglia, G., Cecchin, D., and Lewis, A. (2014). Translocation of flexible polymersomes across pores at the nanoscale. *Biomaterials Science*, 2(5):680–692.
- Penate Medina, O., Haikola, M., Tahtinen, M., Simpura, I., Kaukinen, S., Valtanen, H., Zhu, Y., Kuosmanen, S., Cao, W., Reunanen, J., et al. (2010). Liposomal tumor targeting in drug delivery utilizing MMP-2-and MMP-9-binding ligands. *Journal of Drug Delivery*, 2011.
- Pepper, M. S., Vassalli, J.-D., Orci, L., and Montesano, R. (1993). Biphasic effect of transforming growth factor- $\beta$ 1 on in vitro angiogenesis. *Experimental Cell Research*, 204(2):356–363.
- Peppiatt, C. M., Howarth, C., Mobbs, P., and Attwell, D. (2006). Bidirectional control of CNS capillary diameter by pericytes. *Nature*, 443(7112):700–704.
- Perrault, S. D., Walkey, C., Jennings, T., Fischer, H. C., and Chan, W. C. (2009). Mediating tumor targeting efficiency of nanoparticles through design. *Nano Letters*, 9(5):1909–1915.
- Petros, R. A. and DeSimone, J. M. (2010). Strategies in the design of nanoparticles for therapeutic applications. *Nature Reviews Drug Discovery*, 9(8):615–627.
- Pinto, M. P., Badtke, M. M., Dudevoir, M. L., Harrell, J. C., Jacobsen, B. M., and Horwitz, K. B. (2010). Vascular endothelial growth factor secreted by activated stroma enhances angiogenesis and hormone-independent growth of estrogen receptor-positive breast cancer. *Cancer research*, 70(7):2655–2664.

- Pourtau, L., Oliveira, H., Thevenot, J., Wan, Y., Brisson, A. R., Sandre, O., Miraux, S., Thiaudiere, E., and Lecommandoux, S. (2013). Antibody-functionalized magnetic polymersomes: In vivo targeting and imaging of bone metastases using high resolution MRI. *Advanced healthcare materials*.
- Powers, M. J., Janigian, D. M., Wack, K. E., Baker, C. S., Beer Stolz, D., and Griffith, L. G. (2002). Functional behavior of primary rat liver cells in a three-dimensional perfused microarray bioreactor. *Tissue Engineering*, 8(3):499–513.
- Qian, B.-Z. and Pollard, J. W. (2010). Macrophage diversity enhances tumor progression and metastasis. *Cell*, 141(1):39–51.
- Raesanen, K. and Vaheri, A. (2010). Activation of fibroblasts in cancer stroma. *Experimental Cell Research*, 316(17):2713–2722.
- Rajantie, I., Ilmonen, M., Alminaitte, A., Ozerdem, U., Alitalo, K., and Salven, P. (2004). Adult bone marrow-derived cells recruited during angiogenesis comprise precursors for periendothelial vascular mural cells. *Blood*, 104(7):2084–2086.
- Ramsauer, M. and D’Amore, P. A. (2007). Contextual role for angiopoietins and TGF- $\beta$ 1 in blood vessel stabilization. *Journal of Cell Science*, 120(Pt 10):1810–1817.
- Raza, A., Franklin, M. J., and Dudek, A. Z. (2010). Pericytes and vessel maturation during tumor angiogenesis and metastasis. *American Journal of Hematology*, 85(8):593–598.
- Reeves, K., van der Pluijm, G., Cecchini, M., Eaton, C., Hamdy, F., and Brown, N. (2009). Prostate cancer cells home to bone in a new in vivo model of bone metastasis. *The FASEB Journal*, 23(927.11).
- Reeves, K. J., Brookes, Z. L. S., Reed, M. W. R., and Brown, N. J. (2012). Evaluation of fluorescent plasma markers for in vivo microscopy of the microcirculation. *Journal of Vascular Research*, 49(2):132–143.
- Reinmuth, N., Liu, W., Jung, Y. D., Ahmad, S. A., Shaheen, R. M., Fan, F., Bucana, C. D., McMahon, G., Gallick, G. E., and Ellis, L. M. (2001). Induction of VEGF in perivascular cells defines a potential paracrine mechanism for endothelial cell survival. *The FASEB Journal*, 15(7):1239–1241.
- Reyes-Aldasoro, C. C., Akerman, S., and Tozer, G. (2008). Measuring the velocity of fluorescently labelled red blood cells with a keyhole tracking algorithm. *Journal of Microscopy*, 229(1):162–173.

- Reynolds, L. P., Grazul-Bilska, A. T., and Redmer, D. A. (2000). Angiogenesis in the corpus luteum. *Endocrine*, 12(1):1–9.
- Reznikoff, C. A., Bertram, J. S., Brankow, D. W., and Heidelberger, C. (1973a). Quantitative and qualitative studies of chemical transformation of cloned C3H mouse embryo cells sensitive to postconfluence inhibition of cell division. *Cancer Research*, 33(12):3239–3249.
- Reznikoff, C. A., Brankow, D. W., and Heidelberger, C. (1973b). Establishment and characterization of a cloned line of C3H mouse embryo cells sensitive to postconfluence inhibition of division. *Cancer Research*, 33(12):3231–3238.
- Ribatti, D. (2010). The inefficacy of antiangiogenic therapies. *Journal of Angiogenesis Research*, 2:27.
- Riihimaki, M., Thomsen, H., Hemminki, A., Sundquist, K., and Hemminki, K. (2013). Comparison of survival of patients with metastases from known versus unknown primaries: survival in metastatic cancer. *BMC Cancer*, 13:36.
- Ringsdorf, H. (1975). Structure and properties of pharmacologically active polymers. *Journal of Polymer Science: Polymer Symposia*, 51(1):135–153.
- Ritsma, L., Steller, E. J., Ellenbroek, S. I., Kranenburg, O., Rinkes, I. H. B., and van Rheejen, J. (2013). Surgical implantation of an abdominal imaging window for intravital microscopy. *Nature Protocols*, 8(3):583–594.
- Roberts, H. C., Roberts, T. P., Brasch, R. C., and Dillon, W. P. (2000). Quantitative measurement of microvascular permeability in human brain tumors achieved using dynamic contrast-enhanced MR imaging: correlation with histologic grade. *American Journal of Neuroradiology*, 21(5):891–899.
- Rouget, C. (1873). Memoire sur le developpement, la structure et les proprietes des capillaires sanguins and lymphatiques. *Archives of Physiology & Pathology*, 5:603–633.
- Rucker, H. K., Wynder, H. J., and Thomas, W. E. (2000). Cellular mechanisms of CNS pericytes. *Brain Research Bulletin*, 51(5):363–369.
- Rust, M. J., Bates, M., and Zhuang, X. (2006). Sub-diffraction-limit imaging by stochastic optical reconstruction microscopy (STORM). *Nature Methods*, 3(10):793–795.
- Samuel, R., Daheron, L., Liao, S., Vardam, T., Kamoun, W. S., Batista, A., Buecker, C., Schäfer, R., Han, X., and Au, P. (2013). Generation of functionally competent and durable engineered blood vessels from human induced

- pluripotent stem cells. *Proceedings of the National Academy of Sciences*, 110(31):12774–12779.
- Samuel, S. P., Jain, N., O’Dowd, F., Paul, T., Kashanin, D., Gerard, V. A., Gun’ko, Y. K., Prina-Mello, A., and Volkov, Y. (2012). Multifactorial determinants that govern nanoparticle uptake by human endothelial cells under flow. *International Journal of Nanomedicine*, 7:2943–2956.
- Sandison, J. (1924). A new method for the microscopic study of living growing tissues by the introduction of a transparent chamber in the rabbit’s ear. *The Anatomical Record*, 28(4):281–287.
- Sanson, C., Diou, O., Thévenot, J., Ibarboure, E., Soum, A., Brûlet, A., Miraux, S., Thiaudière, E., Tan, S., Brisson, A., Dupuis, V., Sandre, O., and Lecommandoux, S. (2011). Doxorubicin loaded magnetic polymersomes: theranostic nanocarriers for MR imaging and magneto-chemotherapy. *ACS Nano*, 5(2):1122–1140.
- Sasieni, P. D., Shelton, J., Ormiston-Smith, N., Thomson, C. S., and Silcocks, P. B. (2011). What is the lifetime risk of developing cancer? The effect of adjusting for multiple primaries. *British Journal of Cancer*, 105(3):460–465.
- Sato, S., Drake, A. W., Tsuji, I., and Fan, J. (2012). A potent anti-HB-EGF monoclonal antibody inhibits cancer cell proliferation and multiple angiogenic activities of HB-EGF. *PLoS One*, 7(12):e51964.
- Sato, T. N., Tozawa, Y., Deutsch, U., Wolburg-Buchholz, K., Fujiwara, Y., Gendron-Maguire, M., Gridley, T., Wolburg, H., Risau, W., and Qin, Y. (1995). Distinct roles of the receptor tyrosine kinases Tie-1 and Tie-2 in blood vessel formation. *Nature*, 376(6535):70–74.
- Sawano, A., Takahashi, T., Yamaguchi, S., Aonuma, T., and Shibuya, M. (1996). Flt-1 but not KDR/Flk-1 tyrosine kinase is a receptor for placenta growth factor (PlGF), which is related to vascular endothelial growth factor (VEGF). *Cell Growth & Differentiation*, 7:213–221.
- Senger, D. R., Galli, S. J., Dvorak, A. M., Perruzzi, C. A., Harvey, V. S., and Dvorak, H. F. (1983). Tumor cells secrete a vascular permeability factor that promotes accumulation of ascites fluid. *Science*, 219(4587):983–985.
- Shibuya, M. (2013). Vascular endothelial growth factor and its receptor system: physiological functions in angiogenesis and pathological roles in various diseases. *Journal of Biochemistry*, 153(1):13–19.

- Shim, A. H.-R., Liu, H., Focia, P. J., Chen, X., Lin, P. C., and He, X. (2010). Structures of a platelet-derived growth factor/propeptide complex and a platelet-derived growth factor/receptor complex. *Proceedings of the National Academy of Sciences*, 107(25):11307–11312.
- Shima, D. T., Kuroki, M., Deutsch, U., Ng, Y. S., Adamis, A. P., and D'Amore, P. A. (1996). The mouse gene for vascular endothelial growth factor. Genomic structure, definition of the transcriptional unit, and characterization of transcriptional and post-transcriptional regulatory sequences. *Journal of Biological Chemistry*, 271(7):3877–3883.
- Sinek, J., Frieboes, H., Zheng, X., and Cristini, V. (2004). Two-dimensional chemotherapy simulations demonstrate fundamental transport and tumor response limitations involving nanoparticles. *Biomedical Microdevices*, 6(4):297–309.
- Song, S., Ewald, A. J., Stallcup, W., Werb, Z., and Bergers, G. (2005). PDGFR- $\beta$ + perivascular progenitor cells in tumours regulate pericyte differentiation and vascular survival. *Nature Cell Biology*, 7(9):870–879.
- Sood, N., Jenkins, W. T., Yang, X.-Y., Shah, N. N., Katz, J. S., Koch, C. J., Frail, P. R., Therien, M. J., Hammer, D. A., and Evans, S. M. (2013). Biodegradable polymersomes for the delivery of gemcitabine to Panc-1 cells. *Journal of Pharmaceutics*, 2013.
- Soriano, P. (1994). Abnormal kidney development and hematological disorders in PDGF- $\beta$ -receptor mutant mice. *Genes and Development*, 8(16):1888–1896.
- Stallcup, W. B. (2002). The NG2 proteoglycan: past insights and future prospects. *Journal of Neurocytology*, 31(6-7):423–ppl.
- Stalmans, I., Ng, Y.-S., Rohan, R., Fruttiger, M., Bouché, A., Yüce, A., Fujisawa, H., Hermans, B., Shani, M., Jansen, S., et al. (2002). Arteriolar and venular patterning in retinas of mice selectively expressing VEGF isoforms. *Journal of Clinical Investigation*, 109(3):327–336.
- Standring, S. (2008). *Gray's anatomy*. Elsevier.
- Staton, C. A., Hoh, L., Baldwin, A., Shaw, L., Globe, J., Cross, S. S., Reed, M. W., and Brown, N. J. (2011). Angiopoietins 1 and 2 and Tie-2 receptor expression in human ductal breast disease. *Histopathology*, 59(2):256–263.

- Staton, C. A., Reed, M. W. R., and Brown, N. J. (2009). A critical analysis of current in vitro and in vivo angiogenesis assays. *International Journal of Experimental Pathology*, 90(3):195–221.
- Stetsyshyn, Y., Fornal, K., Raczowska, J., Zemla, J., Kostruba, A., Ohar, H., Ohar, M., Donchak, V., Harhay, K., Awsiuk, K., et al. (2013). Temperature and pH dual-responsive POEGMA-based coatings for protein adsorption. *Journal of Colloid and Interface Science*.
- Stylianopoulos, T., Wong, C., Bawendi, M. G., Jain, R. K., and Fukumura, D. (2012). Multistage nanoparticles for improved delivery into tumor tissue. *Methods in Enzymology*, 508:109.
- Sundberg, C., Kowanetz, M., Brown, L. F., Detmar, M., and Dvorak, H. F. (2002). Stable expression of angiopoietin-1 and other markers by cultured pericytes: phenotypic similarities to a subpopulation of cells in maturing vessels during later stages of angiogenesis in vivo. *Laboratory Investigation*, 82(4):387–401.
- Suri, C., Jones, P. F., Patan, S., Bartunkova, S., Maisonpierre, P. C., Davis, S., Sato, T. N., and Yancopoulos, G. D. (1996). Requisite role of angiopoietin-1, a ligand for the TIE2 receptor, during embryonic angiogenesis. *Cell*, 87(7):1171–1180.
- Szentmáry, N., Wang, J., Stachon, T., Goebels, S., and Seitz, B. (2013). CD34 and  $\alpha$ -smooth muscle actin expression of keratocytes following photodynamic inactivation (PDI). *Klinische Monatsblätter für Augenheilkunde*, 230(6):570–574.
- Tada, H., Higuchi, H., Wanatabe, T. M., and Ohuchi, N. (2007). In vivo real-time tracking of single quantum dots conjugated with monoclonal anti-HER2 antibody in tumors of mice. *Cancer Research*, 67(3):1138–1144.
- Tallquist, M. D., French, W. J., and Soriano, P. (2003). Additive effects of PDGF receptor  $\beta$  signaling pathways in vascular smooth muscle cell development. *PLoS Biology*, 1(2):52.
- Tekade, R. K., D’Emanuele, A., Elhissi, A., Agrawal, A., Jain, A., Arafat, B. T., and Jain, N. K. (2013). Extraction and rp-hplc determination of taxol in rat plasma, cell culture and quality control samples. *Journal of biomedical research*, 27(5):394.

- Thitiporn, C. and Guoliang, F. (2003). An efficient blood vessel detection algorithm for retinal images using local entropy thresholding. *Proceedings of the 2003 International Symposium on Circuits and Systems*, 5:21–24.
- Thorpe, P. E. (2004). Vascular targeting agents as cancer therapeutics. *Clinical Cancer Research*, 10(2):415–427.
- Tingley, S. (2006). High-throughput cell culture: a real-world evaluation. *Innovations on Pharmacological Thecnology*, 02:54–58.
- Tozer, G. M., Akerman, S., Cross, N. A., Barber, P. R., Björndahl, M. A., Greco, O., Harris, S., Hill, S. A., Honess, D. J., Ireson, C. R., Pettyjohn, K. L., Prise, V. E., Reyes-Aldasoro, C. C., Ruhrberg, C., Shima, D. T., and Kanthou, C. (2008). Blood vessel maturation and response to vascular-disrupting therapy in single vascular endothelial growth factor-A isoform-producing tumors. *Cancer Research*, 68(7):2301–2311.
- Tsai, R. K. and Discher, D. E. (2008). Inhibition of self engulfment through deactivation of myosin-ii at the phagocytic synapse between human cells. *The Journal of Cell Biology*, 180(5):989–1003.
- Valenti, R., Huber, V., Iero, M., Filipazzi, P., Parmiani, G., and Rivoltini, L. (2007). Tumor-released microvesicles as vehicles of immunosuppression. *Cancer Research*, 67(7):2912–2915.
- Valluru, M., Staton, C. A., Reed, M. W., and Brown, N. J. (2011). Transforming growth factor- $\beta$  and endoglin signaling orchestrate wound healing. *Frontiers in physiology*, 2.
- Vincent, L. G., Choi, Y. S., Alonso-Latorre, B., del Álamo, J. C., and Engler, A. J. (2013). Mesenchymal stem cell durotaxis depends on substrate stiffness gradient strength. *Biotechnology Journal*, 8(4):472–484.
- Vonarbourg, A., Passirani, C., Saulnier, P., and Benoit, J.-P. (2006). Parameters influencing the stealthiness of colloidal drug delivery systems. *Biomaterials*, 27(24):4356–4373.
- Wagner, R. and Hossler, F. (1992). SEM of capillary pericytes prepared by ultrasonic microdissection: Evidence for the existence of a pericapillary syncytium. *The Anatomical Record*, 234:249–254.
- Wang, S., Cao, C., Chen, Z., Bankaitis, V., Tzima, E., Sheibani, N., and Burridge, K. (2012). Pericytes regulate vascular basement membrane remodeling and govern neutrophil extravasation during inflammation. *PLoS One*, 7(9):e45499.

- Webster, R., Didier, E., Harris, P., Siegel, N., Stadler, J., Tilbury, L., and Smith, D. (2007). PEGylated proteins: evaluation of their safety in the absence of definitive metabolism studies. *Drug Metabolism and Disposition*, 35(1):9–16.
- Weinberg, R. (2013). *The Biology of Cancer*. Garland Publishing Inc.
- Weissleder, R. and Pittet, M. J. (2008). Imaging in the era of molecular oncology. *Nature*, 452(7187):580–589.
- Wright, W. S., Singh Yadav, A., McElhatten, R. M., and Harris, N. R. (2012). Retinal blood flow abnormalities following six months of hyperglycemia in the Ins2 (Akita) mouse. *Experimental Eye Research*, 98:9–15.
- Xian, X., Håkansson, J., Ståhlberg, A., Lindblom, P., Betsholtz, C., Gerhardt, H., and Semb, H. (2006). Pericytes limit tumor cell metastasis. *Journal of Clinical Investigation*, 116(3):642–651.
- Xie, C., Ritchie, R. P., Huang, H., Zhang, J., and Chen, Y. E. (2011). Smooth muscle cell differentiation in vitro: models and underlying molecular mechanisms. *Arterioscler Thromb Vasc Biol*, 31(7):1485–1494.
- Xing, Z., Wang, J., Ke, H., Zhao, B., Yue, X., Dai, Z., and Liu, J. (2010). The fabrication of novel nanobubble ultrasound contrast agent for potential tumor imaging. *Nanotechnology*, 21(14):145607.
- Yin, T., Wang, P., Zheng, R., Zheng, B., Cheng, D., Zhang, X., and Shuai, X. (2012). Nanobubbles for enhanced ultrasound imaging of tumors. *International Journal of Nanomedicine*, 7:895.
- Yoshida, T. and Owens, G. K. (2005). Molecular determinants of vascular smooth muscle cell diversity. *Circ Res*, 96(3):280–291.
- You, W.-K., Yotsumoto, F., Sakimura, K., Adams, R. H., and Stallcup, W. B. (2013). NG2 proteoglycan promotes tumor vascularization via integrin-dependent effects on pericyte function. *Angiogenesis*, pages 1–16.
- Yu, J. L., Rak, J. W., Klement, G., and Kerbel, R. S. (2002). Vascular endothelial growth factor isoform expression as a determinant of blood vessel patterning in human melanoma xenografts. *Cancer Research*, 62(6):1838–1846.
- Yuan, F., Leunig, M., Huang, S. K., Berk, D. A., Papahadjopoulos, D., and Jain, R. K. (1994). Microvascular permeability and interstitial penetration of sterically stabilized (stealth) liposomes in a human tumor xenograft. *Cancer Research*, 54(13):3352–3356.

- Zhang, J., Cao, R., Zhang, Y., Jia, T., Cao, Y., and Wahlberg, E. (2009). Differential roles of PDGFR- $\alpha$  and PDGFR-*beta* in angiogenesis and vessel stability. *The FASEB Journal*, 23(1):153–163.
- Zhang, L., Yang, N., Park, J.-W., Katsaros, D., Fracchioli, S., Cao, G., O'Brien-Jenkins, A., Randall, T. C., Rubin, S. C., and Coukos, G. (2003). Tumor-derived vascular endothelial growth factor up-regulates angiopoietin-2 in host endothelium and destabilizes host vasculature, supporting angiogenesis in ovarian cancer. *Cancer Research*, 63(12):3403–3412.
- Zimmermann, K. (1923). Der feinere bau der blutcapillares. *Zeitschrift fur Anatomie und Entwicklungsgeschichte*, 68:3–109.